Rational Design of Microalloyed High Strength-Low Alloy (HSLA) Plate and Strip Steels

by

Rami A. Almatani

B.S. in Mechanical Engineering, King Abdulaziz University, 2011

M.S. in Materials Science and Engineering, University of Kentucky, 2017

Submitted to the Graduate Faculty of the

Swanson School of Engineering in partial fulfillment

of the requirements for the degree of

Doctor of Philosophy

University of Pittsburgh

2022

UNIVERSITY OF PITTSBURGH

SWANSON SCHOOL OF ENGINEERING

This dissertation was presented

by

Rami A. Almatani

It was defended on

May 19, 2022

and approved by

Wei Xiong, Ph.D., Assistant Professor, Department of Mechanical Engineering and Materials Science

Patrick Smolinski, Ph.D., Associate Professor, Department of Mechanical Engineering and Materials Science

John Oyler, Ph.D., Associate Professor, Department of Civil and Environmental Engineering

Dissertation Director: Anthony J. DeArdo, Ph.D., Professor, Department of Mechanical Engineering and Materials Science

Dissertation Co-director: Brian Gleeson, Ph.D., Professor, Department of Mechanical Engineering and Materials Science

Rational Design of Microalloyed High Strength-Low Alloy (HSLA) Plate and Strip Steels

Rami A. Almatani PhD

University of Pittsburgh, 2022

The central purpose of this investigation was to understand the practical limits of Nb microalloying in controlled rolled low carbon plate and strip steels. More specifically, the influence of the high Nb addition exhibited in the so-called high-temperature processing (HTP) steels (*i.e.*, 0.08 to 0.1 wt. pct. Nb) on the austenite recrystallization behavior at high deformation temperatures and the subsequent final transformation products.

Six candidate steels, each of the same nominal base composition, with 0.03/0.06 wt. pct. C and 0/0.04/0.08 wt. pct. Nb were designed and melted based on an established solubility equation and a modified Zener pinning force model (*i.e.*, subgrain boundary model). Extensive experimental studies on the progress of the microstructure through reheating and subsequent rough rolling, finish rolling and accelerated cooling simulations were conducted. Of these conducted experiments, double-hit tests were critical to better understanding the extent of austenite recrystallization in the temperature range of roughing and finishing passes of a 5-m wide reversing plate rolling mill, namely, between 1150 °C and 900 °C.

Double-hit test results indicated that as the Nb content is increased, the extent of austenite recrystallization is decreased. Additionally, there exists a plateau in the fractional softening curves of the high-Nb steels (0.08 wt. pct. Nb), which indicated that strain-induced precipitates of Nb, carbides or carbonitrides are taking place, hence, hindering further austenite recrystallization.

Roughing passes simulation revealed that doubling the amount of Nb in the steel resulted in grain refinement but mixed grain structure developed. The retardation of austenite

recrystallization could be raised to higher temperatures in HTP steels (near 1050 °C). Hence, the austenite of the high-Nb steels can enter subsequent deformation in the unrecrystallized or partially- recrystallized state instead of full recrystallization and grain refined as expected. The roughing schedule plays a role in the final mechanical properties, and subsequently, a combination of fine effective grain size, reduced area fraction of martensite-austenite (MA) microconstituents, and adequate dislocation densities could be inherited in the final microstructure from a uniformly conditioned austenite.

Table of Contents

List of Tables

List of Figures

Acknowledgments

Many people have helped me during the course of my academic studies and research. I would like to thank them all. I offer my sincere apologies to anyone who was inadvertently omitted from this list.

First and foremost, I should like to express my sincere gratitude to my advisor, Prof. Anthony J. DeArdo, who in many ways was more a good friend than supervisor through his guidance, encouragement, advice, and unconditional support. I also would like to express my gratitude to my Ph.D. committee members: Professors Brian Gleeson, Patrick Smolinski, John Oyler, and Wei Xiong for their insightful comments and discussions.

I should thank the United States Steel Corporation Research and Technology Center for supplying the steels critical to this research program. Also, I thank King Abdulaziz City for Science and Technology (KACST) for their financial support throughout my graduate studies. My sincere appreciation is extended to Mr. Juha Uusitalo of the University of OULU for supervising the Gleeble simulations for this research program, to Dr. Soumya Sridar of the PMMD group for her guidance on TC-PRISMA calculations, to my fellow members of the BAMPRI group, namely, Dr. Yingjie Wu, Aaron Stein and Xinchi Feng for their many insightful discussions, which must have contributed to the development of this study.

I warmly acknowledge the delightful support that I have always received from my family, especially my sister Maram. I also thank my wife Lujain and my lovely kids, Abdulkarim and Taliah for sharing my burden during our stay in Pittsburgh. Last but not the least, it seems to me that I owe so much to my parents (Abdulkarim and Munirah Almatani) that I cannot express my gratitude in one paragraph and, indeed, words would never felt like enough for this task.

1.0 Introduction

In a far-reaching report published in 1959, Beiser [1] marked one of the first detailed experiments to study the effects of Nb additions to semi-killed steels, though Nb addition to steel was considered as long ago as 1940. Soon after, through active research, it was realized that small additions of Nb to simple low C-Mn steels, together with careful control of hot processing and cooling, remarkably increased strength and decreased the impact transition temperature [2, 3]. These fundamental properties are improved predominately by refining the final microstructure. Because of these excellent properties achieved without the addition of large amounts of alloying elements, the name *high strength* (relative to plain carbon steel), *low alloy* (HSLA) steels is commonly used for Nb, Ti, and V microalloyed steels [4, 5]. HSLA steels are mainly used in a wide range of products such as large diameter pipelines and other structural applications such as ship building, offshore platforms, building construction, and bridges [5]. Nb steels are now commonly found in automobiles, as well.

In hot rolled HSLA plate and strip steels, the final microstructure depends primarily on the austenite grain size, the bulk composition of the steel prior to transformation, and the cooling rate through the transformation.

The major contribution of Nb to high strength is reflected in numerous papers and research studies as well as conference proceedings by grain refinement, solid solution strengthening, precipitation and dislocation-hardening [2, 6-9]. Similarly, the enhancement in depressing the ductile-brittle transition temperature (DBTT) through the addition of niobium is critically important in pipelines intended for low-temperature service [10]. This enhancement is mainly caused by the grain refinement of the austenite during hot rolling and the grain refinement of the ferrite during transformation upon cooling. Various studies have shown that strength and toughness can be improved by increasing the level of Nb from zero to the conventional 0.03-0.04 wt.%, or up to very high levels near 0.1 wt.% Nb [11-14]. However, there are drawbacks beyond cost to the use of higher levels of Nb, such as reduced weldability, coarse undissolved particles, and higher mill loads.

When a 25 mm thick plate intended for pipe applications is hot rolled on a modern 5 m plate mill, it does so in three stages after slab reheating: rough rolling, finish rolling and accelerated cooling [15]. For instance, after reheating at 1200 °C, a continuously cast slab of 250 mm thickness might be rolled to a 75 mm transfer bar in the roughing mill at a temperature from 1150–1050°C. The bar is then transported to the finishing stands, where it is further rolled to the final gauge of 25 mm at temperatures ranging from below 900 to 750 °C. Because of the large width and potentially high mill loads, the rough rolling and finishing rolling take place in numerous, light passes, often between 10 and 15 passes in each case, with pass reductions between 10–15% each in the roughing mill, and 5–10% each in the finishing mill. Since these are reversing mills, the interpass times can range from 10–30 sec. depending on conditions.

After final rolling, the plate is water spray cooled at about 30 °C/s to the water end temperature (WET) which is dictated by the continuous cooling transformation (CCT) diagram, the cooling path, and the required microstructure and properties [9]. The WET for achieving ferrite–pearlite microstructures in steels of high hardenability, *i.e.*, CE_{II} over 0.40, is in the range of 600–650 °C. When a bainitic ferrite microstructure is desired, a WET near 450–550 °C would be used. For even higher strengths, requiring martensite, a WET around 300 °C would be used. Normally, the steels are air-cooled to room temperature from the WET.

The hot processing of Nb steels is based on most of the Nb being in solution in the austenite during slab reheating and rough rolling, and some of the dissolved Nb being reprecipitated as a strain-induced precipitate in the deformed austenite during finish rolling. The nose of the C-curve for this precipitation in austenite is around 900 °C for 0.04 wt.% Nb, but is raised to 950 °C or higher at larger levels of Nb [16]. Studies of the recrystallization-stop-temperature (*i.e.*, $T_{5\%}$ or T_{nr}) show that this temperature increases with Nb content and can reach or exceed 1050 °C in typical pipe steels containing 0.1 wt.% Nb [11, 14]. Since the last roughing passes occur in this temperature range, it is quite possible that there might be strain-induced precipitation of NbC, even in the late roughing passes. Since the grain refinement expected during roughing requires multiple static recrystallization events in the interpass times, perhaps complete recrystallization may not occur by the exit of the roughing mill. Therefore, there might be consequences for the grain refinement needed during rough rolling when the bulk Nb level is too high. For example, this lack of sufficient grain refinement is important, since coarse-grained microstructures often result in failure in drop weight tear testing of plate and pipe.

Whether static recrystallization occurs or not depends on the comparison of the driving force for static recrystallization and the retarding Zener pinning force caused by the interaction of the moving austenite boundaries with particles formed earlier on the defect structure of the deformed austenite in the roll gap; these defects include grain and sub-grain boundaries and deformation bands [17].

The potential for strain-induced precipitation of NbC or NbCN will depend on the bulk composition of the steel, the relevant solubility products for NbC or NbCN in austenite and the applicable rolling practice. The carbon content will be governed by the final strength needed in the final pipe, which can be API X50–X60 for ferrite–pearlite (F–P) microstructures, API X70–X100 for bainitic microstructures and API X120 and above for martensitic microstructures [18]. While changes in %C have only a slight influence on the strength of F–P steels, they can have dramatic effects on the strength of bainite or martensite found in direct quenched steels. Therefore, the carbon content can be expected to influence both the strength of the plate or pipe through hardenability effects, and the toughness through its effect on the precipitation in austenite and the control of grain size.

The effect of hot rolling on toughness or lowering the DBTT, through grain refinement of the prior austenite grain size (PAGS), is the result of two sequential events. The first is the combination of the elimination of both the remaining as-cast structure and the large grain size that results from slab reheating. These occur during the repeated static recrystallization that takes place between the rough rolling passes that arise when the pass strains happen above the recrystallization-complete temperature, $T_{95\%}$. This leads to grain refinement during multiple waves of recrystallization, where the PAGS might be reduced from 300 µm to 50 µm going into the finishing passes where pancaking occurs.

Since the finishing passes for controlled rolling are normally considered to occur below the $T_{5\%}$, normally about 900 °C in steel containing 0.04 wt.% Nb, the final austenite will be heavily strained, elongated, or pancaked [11]. This austenite is highly deformed with high strength and contains numerous crystallographic defects, such as deformation twins, deformation bands, sub-grain boundaries, and elongated grain boundaries. These near-planar crystalline defects contribute to what is called the S_v value, an index used to estimate the effectiveness of a given rolling process in thermomechanical processing (TMP) [8]. In low hardenability or slowly cooled F–P steels, the nucleation of polygonal ferrite occurs on the S_v, where the high density of high angle ferrite grain boundaries resulting from ferrite grain refinement can act as crack arresters for potentially growing cleavage cracks. In higher hardenability or faster cooled steels, the defects themselves can act as cleavage crack arresters in bainitic or martensitic steels. In either case, these near planar defects can act as sites for crack arresters for the growth of cleavage cracks; hence, lowering the DBTT.

The central purpose of the current research program was fourfold: (i) to determine whether NbC could form during rough rolling and (ii) whether this precipitate might cause less than complete recrystallization during rough rolling (iii) therefore, leading to a slightly partial recrystallized austenite grains resulting in non-optimum final austenite microstructure prior to transformation, and (iv) explore the transformation microstructures following hot deformation schedules.

2.0 Background

Thermomechanical controlled processing (TMP) of HSLA steels can be considered a three-step process consisting of heating the material to a high temperature (*i.e.,* reheating), hot deformation (*e.g.,* roughing and finishing passes in hot rolling), and transformation via controlled cooling to a predetermined temperature. In the case of hot processing and at such high temperatures, sufficient thermal activation will be available to induce phenomena such as recovery, recrystallization, grain growth, precipitation and dissolution of second phase particles. Furthermore, these phenomena may occur concurrently with deformation or without depending on the metallurgical state of an alloy.

This chapter contains a brief discussion of the three areas mentioned above found in the literature that are relevant to this research program. Furthermore, austenite conditioning, high temperature processing (HTP), and the basic strengthening mechanisms in HSLA steels are also being reviewed.

2.1 Thermomechanical Processing of HSLA Steels

2.1.1 Definition of Thermomechanical Processing (TMP)

Thermomechanical Processing (TMP) can be defined as a hot deformation schedule chosen to achieve a predetermined microstructure in the austenite prior to transformation [19]. Hence, controlling the passes (*e.g.,* in hot rolling), and the temperatures to achieve the metallurgical objective. Probably one of the most important benefits of TMP is by far grain refinement; adequate conditioning during TMP means that both the austenite and its subsequent transformation products can exhibit grain refinement. When the austenite grain is refined, enhancements are observed in the hot ductility of the workpiece [20] and in the toughness of as-rolled [21, 22] or direct quenched (DQ) bainitic and martensitic steels [23].

In the case of the hot rolling process, the development of TMP has started with Controlled Rolling (CR) and later, Interrupted Accelerated cooling (IAC, or simply ACC) was developed [24]. Hence, TMP implies either CR followed by air cooling or CR+ACC. In the following section, the underlying metallurgical concepts of TMP will be introduced.

2.1.2 Conditioning of Austenite

Obtaining fine ferrite grain sizes from austenite upon transformation requires high ferrite nucleation rates, and low growth rates as well as low coarsening rates subsequently. Conditioning of austenite means, as defined by DeArdo [4], that the microstructure of the austenite has achieved, through controlled hot deformation, the proper predetermined metallurgical condition prior to transformation that will embody these requirements. The earliest studies have shown that high ferrite nucleation rates stem from having many potential nucleation sites [2, 3, 25]. These sites are austenite grain boundaries, incoherent twin boundaries, and deformation bands [15]. A quantitative assessment of these heterogenous sites is expressed in what is known as the total interfacial area of the near-planar boundaries per unit volume (S_v) and has the units (mm^2/mm^3). This parameter was discussed by Underwood [26] and was later adopted by Kozasu *et al.* [8] to estimate the degree of austenite conditioning. The main aim of TMP as well as austenite conditioning is to increase S_v. The effect of S_v on the final ferrite grain size is shown in Figure 2.1 [6].

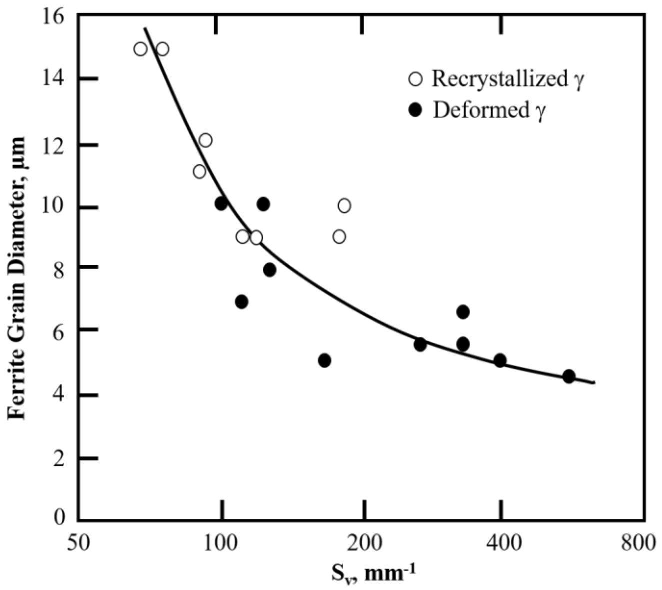

Figure 2.1 Ferrite grain size from recrystallized and deformed austenite at various S_v values; modified from reference [6].

It is crucial to recognize how austenite responds to deformations occurring over a range of temperatures. With the aid of Figure 2.2 and Figure 2.3, the behavior of austenite, for a given steel, reheat temperature, strain rate and interpass time can be visualized. For example, in Figure 2.2, at deformations temperatures down to the $T_{95\%}$, the austenite undergoes complete recrystallization between successive passes. At deformation temperatures below $T_{5\%}$, the austenite remains essentially pancaked at the end of interpass time. Finally, at deformation temperatures between $T_{95\%}$ and $T_{5\%}$, the progress of recrystallization becomes difficult, as a result, the austenite will be in partially recrystallized condition (duplex grain structure).

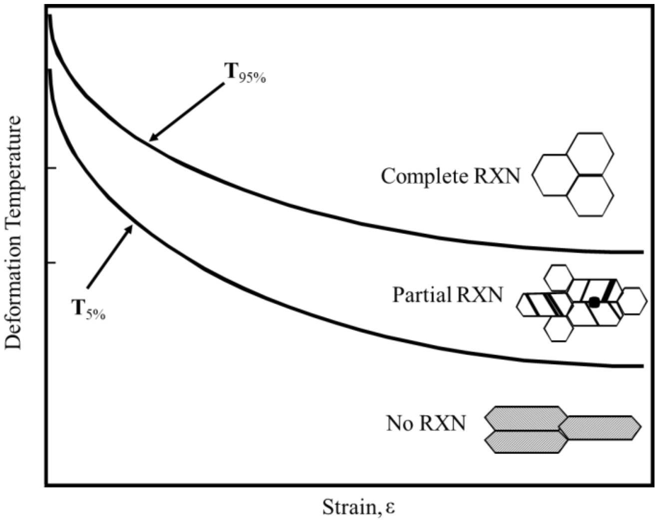

Figure 2.2 Schematic illustration of austenite microstructures resulting from various deformation conditions; after reference [17].

There are two different schedules for increasing S_v [17]. In the first, termed recrystallization-controlled rolling (RCR) where the deformation is done above $T_{95\%}$, the as-reheated austenite grains undergo repeated recrystallization during subsequent hot deformation in which the equiaxed grains are replaced by new finer equiaxed or recrystallized grains as shown in Figure 2.3. Since these fine recrystallized grains may have the tendency to coarsen during hot processing, appropriate microalloying elements are needed to suppress grain coarsening. The process simply involves repeated recrystallization and grain coarsening inhibition and was originally proposed by Sekine *et al.* [27]. Apparently, the lower the $T_{95\%}$, the larger will be the processing window between reheat temperature and finishing temperature of $T_{95\%.}$ It follows that the RCR conditioning is suited for steels having low $T_{5\%}$ and a pre-existing grain coarsening inhibition system.

The second schedule is termed conventional controlled rolling (CCR) and involves deformation below $T_{5\%}$. In this approach, the grains are deformed and remain unrecrystallized through the interpass time for all successive passes. As a result, the grains undergo repeated flattening (*i.e.*, pancaking) as can be seen in Figure 2.3. Both RCR and CCR have the same objective of resulting in structural refinement in the final plate or coil.

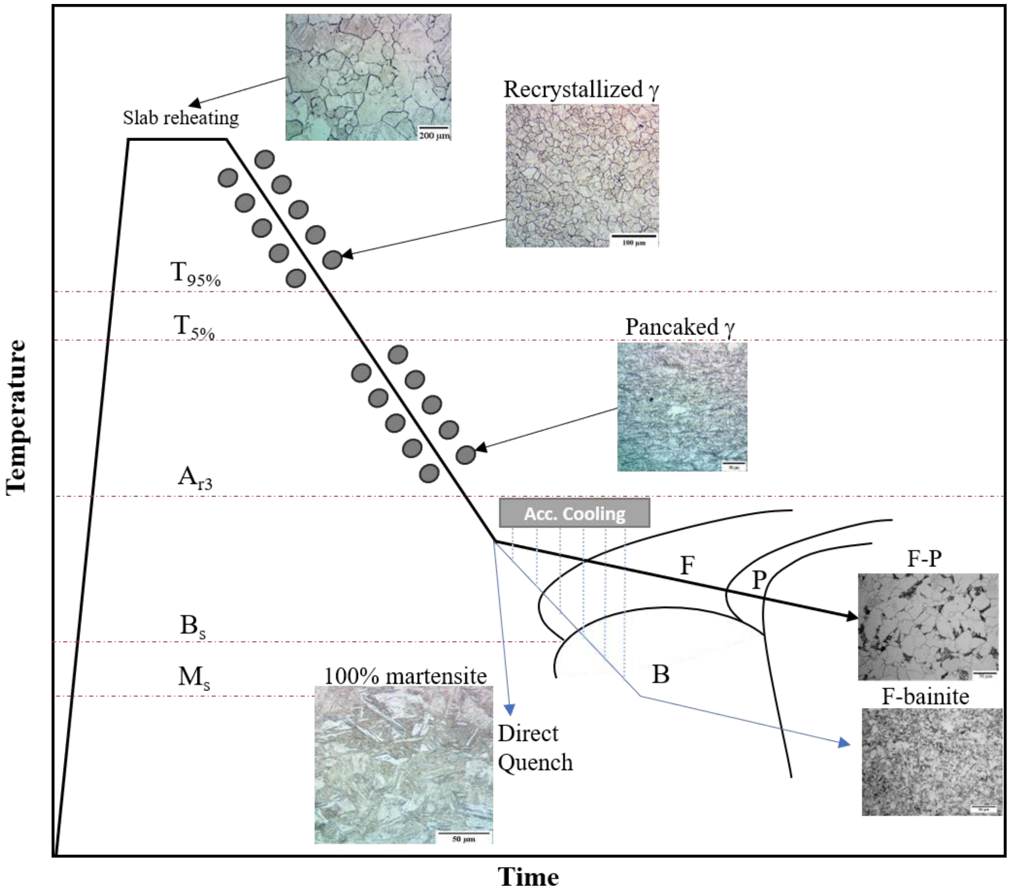

Figure 2.3 Schematic illustration of TMP and the critical temperatures as well as microstructures that result from this processing schedule; modified from reference [5].

2.1.3 High Temperature Processing of HSLA Steels

Perhaps $T_{5\%}$ is the most important concept governing the choice of TMP schedule. Raising this temperature by the appropriate microalloying element (Nb, Ti, or V) permits successive deformation in the non-recrystallization region of the austinite to be induced at uncommonly higher finishing temperatures. Although all of the microalloying additions tend to raise both $T_{5\%}$ and $T_{95\%}$, the effect of Nb is the most pronounced. Cuddy [11] studied the influence of several microalloying elements on the recrystallization temperatures in a series of microalloyed steels. In this study, $T_{95\%}$ was calculated using optical metallographic techniques and the recrystallization-stop temperature was defined, by Cuddy [11] as the first appearance of a partially recrystallized structure and it is represented by the upper limit of error bars shown in Figure 2.4. Furthermore, it was concluded from this study that $T_{5\%}$ is 50˚C lower than $T_{95\%.}$ Overall, of the four microalloying elements shown in Figure 2.4, the influence of Nb is especially pronounced. Later, Hulka and Hillenbrand [14] adapted Figure 2.4 and converted the initial solute content of microalloying elements into wt.% as can be seen in the abscissa of Figure 2.5.

For the above mentioned reason, high temperature processing (HTP) was initiated [13, 14] and its main aim is that high Nb content (between 0.08-0.11 wt.%) added to steels which elevates the finish rolling temperature by 100 ˚C as well as lowers the mill loads compared to traditional HSLA steels. The topic is scarcely found in literature and it is still undergoing development. Hence, the focus of the current research program is to further understand the factors affecting HTP.

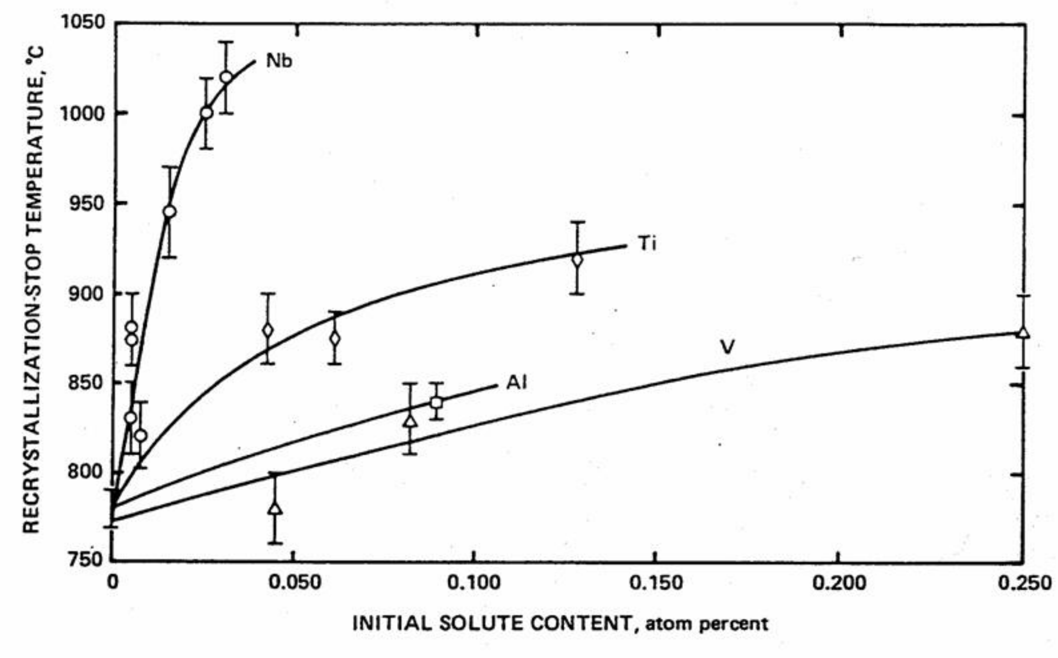

Figure 2.4 The effect of microalloy solutes on $T_{5\%}$ and $T_{95\%}$ temperatures in a 0.07C-1.4Mn-0.25 Si steel; Cuddy [11].

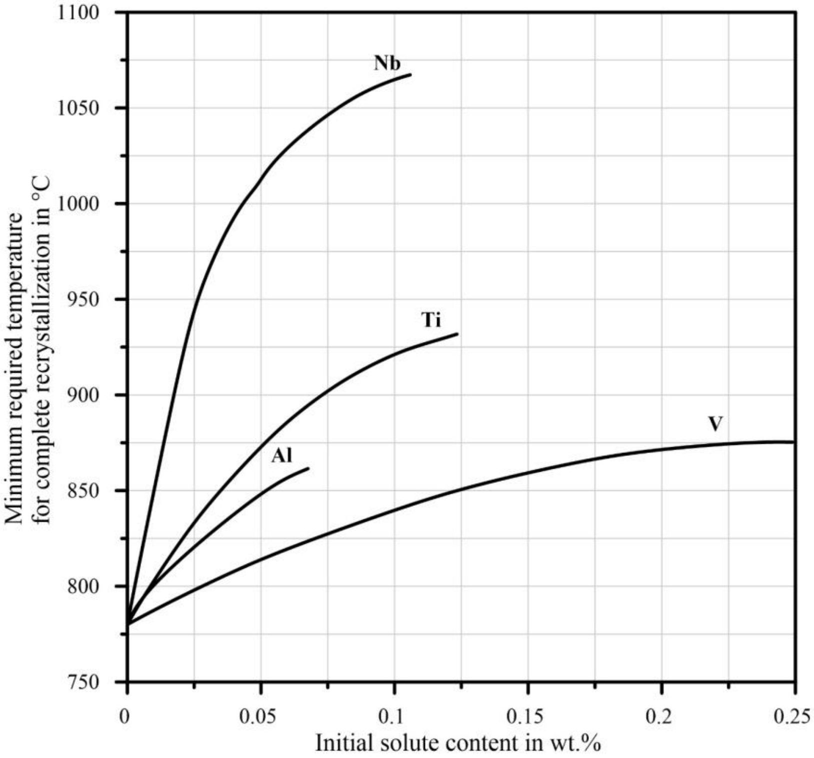

Figure 2.5 Retardation of austenite recrystallization by microalloying; after Hulka [14].

2.2 Solubility of Microalloying Elements

Basic understanding of how microalloying elements affect solid-solution and precipitation behavior in steels is of paramount importance. Since these elements in a compound form (*i.e.*, carbides, nitrides, carbonitrides) can interact with grain coarsening and recrystallization phenomena, the knowledge of the amount of these carbides, nitrides, or carbonitrides in solution and precipitation helps in better understanding. The type the compound takes can be calculated with the solubility product (the inverse of the equilibrium constant K) for the compound being investigated. If for example, the extent of solid solubility of a microalloying element, M, with an interstitial, X, in austenite is desired, the following reaction can be considered [28]:

$$[M] + [X] = MX \tag{2.1}$$

Where [M] is the concentration of M dissolved in austenite, [X] is the concentration of X dissolved in austenite, and MX represents the constituent (carbide or nitride). The concentrations herein are mainly in weight percent [wt.%] since it is considered a dilute solution. The equilibrium constant for this reaction can be written as:

$$K_s = \frac{a_{[M]} \cdot a_{[X]}}{a_{MX}} \tag{2.2}$$

Where $a_{[M]}$ is the activity of the dissolved microalloy elements, $a_{[X]}$ is the activity of dissolved interstitial (usually C or N) and a_{MX} is the activity of the compound carbide or nitride. Assuming the activity coefficients to be unity for the pure product NbC, and by using Henry's law of dilute solutions, the corresponding equilibrium constant can be expressed as:

$$K_s = [Nb]\ [C] \tag{2.3}$$

The corresponding temperature dependence of the solubility product is usually expressed by an Arrhenius relationship in a logarithmic expression:

$$\log_{10} K_s = -\left(\frac{Q}{2.303RT}\right) + \frac{C}{2.303} \tag{2.4}$$

Where Q is the heat of dissolution and R is the universal gas constant. Much of the work done on studying the solubility products of carbides and nitrides in steels has expressed the equation of the form shown by Eq. (2.4) in a generalized form:

$$\log_{10} K_s = A - \frac{B}{T} \tag{2.5}$$

coefficients A and B are found experimentally and the agreement among the reported solubility products data appears to be rather poor. The disparities in these reported solubility products are largely attributed to the different techniques employed. The techniques used in obtaining the solubility products include [29]: thermodynamic calculations, chemical separation and isolation of precipitates, hardness measurements, and statistical treatment of various solubility products. Moreover, some of the precipitates may exist in nonstoichiometric form, such as $NbC_{0.87}$. For example, Mori *et al.* [30] have studied the solubility of niobium carbide precipitates in austenite and found that the average composition is about $NbC_{0.87}$. The solubility products of some of the most important precipitates in HSLA steels are shown in Figure 2.6. The solubility products in austenite given by Turkdogan [31] were used for TiN, VN, $NbC_{0.87}$, and TiC. Other solubility products given by Irvine *et al.* [32], Akamatsu *et al.* [33], and Sawamura and Mori [34] were used for NbCN, NbC, and VC, respectively. In regards to the solubility product of NbC, one of the most accurate methods for calculating the solubility product for NbC in austenite in a steel with a nominal composition of 0.08C-1.5Mn-0·008N-0.02Nb was obtained by Palmiere *et al.* [29]. The solubility product was derived from reheated and quenched samples and measured using Atom Probe Field Ion Microscopy (APFIM), the results shown in Figure 2.6, and yielding the expression:

$$\log[Nb][C] = 2.06 - \frac{6700}{T} \tag{2.6}$$

One can see from Figure 2.6 that the higher the solubility product, the higher is the solubility of the carbide or nitride. The curves tend to decrease with decreasing temperature, signifying that the austenite will readily become supersaturated with the microalloying elements and eventually precipitation will occur. Furthermore, VC and NbC have relatively high solubility, while TiN has relatively low solubility at low concentrations in austenite. Hence, VC dissolves at the lowest temperatures while TiN remarkably remains stable even at high temperatures.

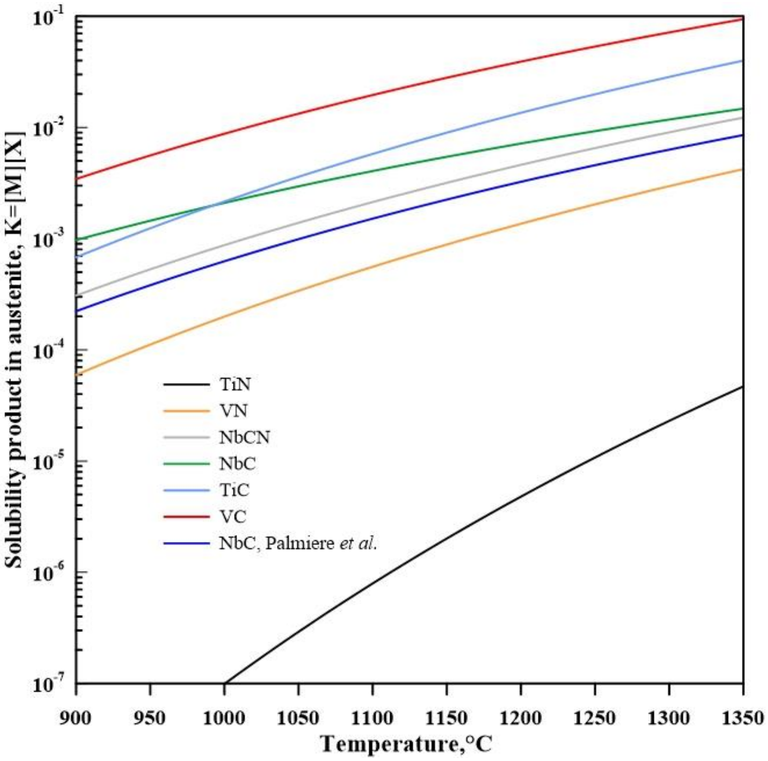

Figure 2.6 Equilibrium solubility products of carbides and nitrides in HSLA steels; adapted from [5].

2.3 Slab Reheating

Although the technology of thin-slab casting direct-rolling (TSDCR) has the advantage of eliminating reheating process and the capability of rolling thinner strip [35]. Higher grades of microalloyed steels, especially thick slab HSLA steels, proved to be very challenging to produce using this process [36]. The main difficulty arises from the existence of very coarse austenite grains in the center of the slab as well as the limited number of passes in TSDCR technology. For these reasons, thick slabs take the route: casting, reheating, controlled hot rolling, and controlled cooling.

The initial metallurgical state of the steel will have some influence on subsequent deformation as well as its final microstructure state. Hence, grain growth phenomena that occur during reheating prior to deformation should be taken into account for any microstructural investigation of hot processing. Grain growth in single phase metals and alloys can assume two basic forms as classified by Hillert [37]. Normal or continuous grain growth in which the distribution of grain size and/or shape is maintained while the mean grain size increases. This process can be relatively characterized as a uniform grain structure. Alternately, abnormal or discontinuous growth (*i.e.*, secondary recrystallization) is described by the variation of grain size and shape due to the rapid growth of certain grains at a rate much faster than others. The grain structures resulting from this process are nonuniform or duplex. The first step employed in TMCP is to control the grain size during reheating.

During reheating of slabs at elevated temperatures, grain coarsening may occur. This behavior is dictated by an important temperature which is the grain coarsening temperature (T_{GC}). The T_{GC} is defined as that temperature above which abnormal grain coarsening starts [29]. The choice of the reheating temperature relative to the T_{GC} determines the amount of microalloying element dissolved in austenite and the starting grain size. Hence, T_{GC} can be treated where an equilibrium exists between the driving force for grain coarsening and the pinning precipitate. Furthermore, the requirements of the final product also determine the choice of the reheating practice [19]. For instance, for products where toughness is very important such as plate steels, the reheating temperature can take place below the T_{GC} to keep grain coarsening to a minimum. This can be accomplished when precipitates remain relatively undissolved in austenite. On the contrary, for products where toughness is not as important as strength such as strip steels, the reheating temperature can take place above the $T_{GC.}$ In this case, some coarsening may occur since most of the microalloying elements are dissolved in austenite and will be available for precipitation strengthening during or after transformation.

There have been several investigations [38-40] showing the effect of second phase particles on grain coarsening behavior. All of these studies conclude that the extent of grain coarsening can be controlled by the pinning precipitates, though the impact of different precipitates may differ. For example, Cuddy [38] has studied the grain coursing behavior of C-Mn-Si base steels with different additions of Al, V, Ti or Nb. It was concluded from this study that steels containing the insoluble TiN coarsen at much higher temperatures than steels containing the soluble VCN. Roy *et al.* [39] investigated the grain coarsening of two continuously cast slabs, one containing Ti addition of 0.04 wt.% and the other containing 0.02 wt.% of Ti along with 0.05 wt.% Nb addition. They observed that TiN remains stable and markedly controls the austenite grain size at reheating temperatures above 1200˚C. They further showed that the Nb-containing slab exhibits a duplex austenite grain structure and noted that Ti addition of 0.02 wt.% was not sufficient to eliminate grain size bimodality. This bimodality in grain size was attributed to the variation in pinning force of Nb precipitates. A study by Fernández *et al.* [41] has also focused on the effect of microalloying elements on grain refinement in a low carbon Nb-V microalloyed steel. Their samples were solution treated at temperatures between 1050 °C and 1300 °C for times from 5 to 180 minutes and then quenched in water. The major findings of their investigation were that during normal grain growth, the grain size grows gradually until 1200 °C for times up to 30 minutes and until 1150 °C for longer times up to 180 minutes. They also noted that abnormal grain growth abruptly occurs at 1250˚C for times lower than 30 minutes. In summary, the general behavior of microalloyed austinite during reheating is illustrated in Figure 2.7 for various microalloying elements [25]. The hatched area on the curves in Figure 2.7 represents the T_{GC} for each steel.

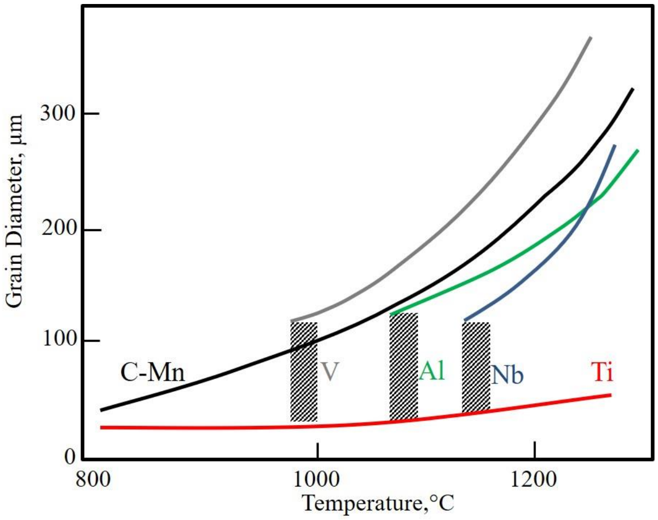

Figure 2.7 Austenite grain coarsening in microalloyed steels; modified from reference [25].

2.4 Metallurgical Phenomena Occurring During Hot Deformation

Metallurgical phenomena such as recovery and recrystallization are considered to be the basic softening (restoration) mechanisms through which cold worked metal or alloy reverts partially or completely to its condition prior to deformation [42]. These mechanisms are operative when metal is annealed at a high homologous temperature, *i.e.*, the ratio of the annealing temperature to the melting temperature on the absolute temperature scale [43]. On the one hand, in the absence of any type of stress or strain, both recovery and recrystallization can occur during annealing and are conventionally termed static. On the other hand, both recovery and recrystallization can take place during concurrent high temperature deformation. Under these specific conditions, they are conventionally termed dynamic recovery and recrystallization [44]. The dynamical events that occur during hot deformation will leave the material unstable and subsequently provide the driving force for static events to operate following deformation.

To distinguish these dynamical events for a given hot deformation process (*i.e.,* for a given deformation temperature, strain, and strain rate $\dot{\varepsilon}$), it is easier to visualize them, indirectly, on a typical flow curve. Figure 2.8 shows the ideal flow behavior of austenite during hot deformation [45]. The behavior of the flow stress, whether it be work hardening or dynamic restoration process, in the case of single-phase austenite, is dependent on strain rate and temperature. These strain rate and temperature effects are often expressed in terms of a temperature-compensated strain rate parameter, *i.e.*, the Zener-Hollomon parameter:

$$\mathrm{Z} = \dot{\varepsilon} \exp\left(\frac{\mathrm{Q}}{\mathrm{RT}}\right) \tag{2.7}$$

where Q is the apparent activation energy of deformation, R is the universal gas constant and T is the temperature in absolute scale. The structures which develop under hot deformation as well as the factors which affect these structures are commonly discussed in terms of Z [42, 44, 45]. under low temperature deformation and high strain rate (high Z), small or no softening occurs which renders the austenite grains in dislocated and elongated state. In this case, work hardening is dominant and can later be modified by the static softening process. On the other hand, under high temperature and low strain rate (low Z), dynamic recovery and dynamic recrystallization are very likely after an initial amount of work hardening. The state of austenite under these conditions at the end of hot deformation and the onset of each softening process can be understood by the critical strains for dynamic recovery (ε_C^r) and dynamic recrystallization (ε_C^R) and the strain to peak stress (ε_P). At a constant true strain rate and strains below ε_C^r, in general, the material undergoes work hardening through dislocation multiplication. However, at strains exceeding ε_C^r and less than ε_C^R, the material becomes unstable and rearrangement of defects takes place. This results in a well-defined cell walls of high dislocation density and is evident in materials with high stacking fault energy. Upon further straining, formation of new grains commences at ε_C^R which mostly nucleate at grain boundaries or deformation bands. A mixture of dynamically recrystallized grains and elongated grains exists beyond ε_C^R leading to a decrease in the flow stress after reaching a peak at ε_P. Finally, the decrease in the flow stress reaches a steady state when work hardening and dynamic recrystallization are balanced.

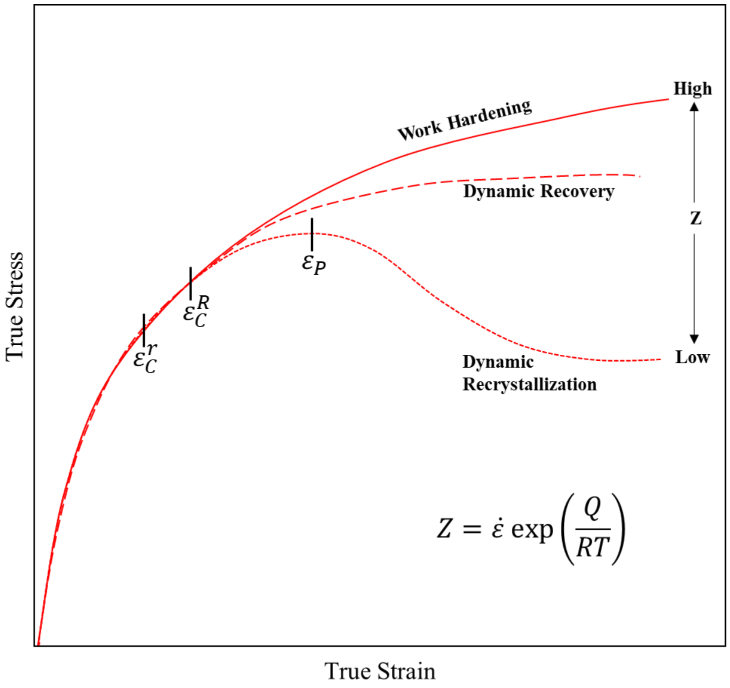

Figure 2.8 Schematic of the hot flow curve for austenite; after reference [45].

The previous discussion was a brief overview of the basic annealing phenomena occurring during hot deformation. Specific observations will now be introduced regarding the hot deformation of HSLA steels and related metallurgical phenomena.

2.4.1 Dynamic Recrystallization

Previous studies [42, 44, 46, 47] have shown that for a given X hot deformation conditions, materials of low to intermediate stacking fault energy will undergo dynamic recrystallization whereas materials of high stacking fault energy will experience dynamic recovery. For instance, copper, α-brass and austenitic stainless which have low stacking fault energies show little or no recovery due to the difficulty of dislocation climb [48]. However, in metals of high stacking fault energy such as aluminum and ferritic steels, dynamic recovery can occur readily due to the ease of dislocation climb and cross-slip.

Earlier studies on the hot deformation behavior in carbon steels or HSLA steels pointed out that dynamic recrystallization of austenite can take place [44, 49, 50]. In these studies, the strain rate used was ranging from 10^{-4} to 10^{-1} sec^{-1}, which is relatively low compared to strain rates involved in industrial hot working such as the rolling of plate or strip. The typical strain rate employed in these industrial practices ranges from 1 sec^{-1} up to 200 sec^{-1} for hot strip mill [51]. Later, Ouchi and Okita [46] have shown that dynamic recrystallization of austenite in Nb-bearing HSLA steels was not observed at the highest strain rate of 10 sec^{-1} and temperatures ranging from 900 °C to 1200 °C used in their experiments. In a more recent study, Zhao and Palmiere [52] have studied Nb-bearing HSLA steel deformed at a constant true strain rate of 10 sec^{-1} after soaking at 1250 °C and deforming respectively, at 1100 °C and 950 °C under variable strains. They observed that there is no sign of the occurrence of dynamic recrystallization.

Although seldom found in literature, however, few investigations considered the effect of initial grain size on the flow curve and the extent of dynamic recrystallization [53, 54]. It is believed that the pre-existing grain boundaries are the principal nucleation sites for dynamic recrystallization [44]. Nevertheless, there was no marked effect of initial grain size on the recrystallized grain size. What was found in these studies is that both the critical strain and peak strain increased as the initial grain size increased. Furthermore, the overall rate of dynamic recrystallization appeared to be increased with smaller initial grain size. Hence, lower strains are sufficient for the onset of dynamic recrystallization.

The effect of microalloying addition and solid solution alloying on dynamic recrystallization has been the subject of numerous studies [46, 55, 56]. It has been established from these studies that when deforming austenite at high strain rates, the initiation of dynamic recrystallization is delayed when microalloying elements (Nb, Ti, or V) are added to the steel. This is mainly attributed to the solute drag effect impeding dislocation motion since there is insufficient time for precipitate nucleation. By comparing the effectiveness of these microalloying elements in suppressing dynamic recrystallization, Nb is more effective in retarding the extent of recrystallization as pointed out by Weiss *et al*. [55].

While the subject of dynamic recrystallization is important in that it gives the opportunity to observe the progress of recrystallization under low Z conditions, it is very seldom encountered during hot working, since the strain rates are as high as 200 sec^{-1} as mentioned previously. For this reason and at such high strains, the less restored and highly work hardened austenite supplies the driving force for another technologically important softening mechanism in hot working. That is static recrystallization, which will be briefly discussed in the next section.

2.4.2 Static Recrystallization

Of the four softening mechanisms, perhaps static recrystallization is the most studied high temperature phenomena in C-Mn steels and HSLA steels [12, 46, 49-51, 57-65]. Perhaps the most popular experimental method reported in the literature for studying the progress of static softening is the isothermal double-hit mechanical testing (*i.e.*, interrupted testing). Further, the basic laboratory hot interruption methods include tension [65], torsion [50, 61-63, 66], compression [49, 51, 58, 64, 67, 68] or laboratory rolling mill [6, 60]. In the case of double-hit test, the technique consists of heating a small specimen to a given hot deformation temperature, loading to a prescribed strain, replicating the pass strain in the n-1 pass, unloading, delaying at the same deformation temperature for a prescribed time (*i.e.*, interpass time) and then reloading to a final strain, taken to be the pass strain for the nth pass. While there is a considerable amount of literature dealing with static recrystallization, it is perhaps difficult to compare the results since the mode of deformation as well as the equipment being used might influence the progress of static recrystallization.

2.4.2.1 Static Recrystallization Kinetics

The kinetics of static recrystallization and its nucleation and growth rates follow the usual Avrami type of equation as given below [69]:

$$\mathrm{X} = 1 - \exp(-\mathrm{b}\mathrm{t}^{\mathrm{n}}) \qquad \textbf{(2.8)}$$

where X is the fraction transformed (*e.g.*, recrystallized fraction), b is a constant that depends on the nucleation and growth rates, t is the time and n is the time exponent (depends on deformation parameters). Eq. (2.8) resembles a sigmoidal curve and describes a nucleation and growth event taking place under isothermal conditions.

The progress of softening can be best understood by using the flow curves obtained from the high temperature double-hit tests. This technique allows the determination of softening as a function of temperature in the time between or after deformation passes. The methods pertaining softening fraction include [70]: (i) 0.2% and 2% offset method; (ii) 5% true strain method; (iii) back extrapolation method; and (iv) mean flow stress (MFS). Utilizing one of the previous methods in interrupted testing, the softening fraction (FS) is often defined as:

$$\mathrm{FS} = \frac{\sigma_{\mathrm{m}} - \sigma_{\mathrm{r}}}{\sigma_{\mathrm{m}} - \sigma_{0}} \qquad \textbf{(2.9)}$$

where σ_{m} is the flow stress immediately before unloading as defined by one of the appropriate methods mentioned above, σ_{r} is the yield stress upon restraining at a given strain, and σ_{0} is the initial yield stress at a given strain for the first hit. The variation in determining FS mainly depends on how each stress term is defined.

2.5 The Driving Force for Recrystallization

Microscopic examination shows that the preferred sites for recrystallization nucleation are mainly grain boundaries, twin boundaries, and interfaces [48]. The main driving force for recrystallization nucleation is the difference in dislocation density between adjacent austenite subgrains. According to the model of strain-induced grain boundary migration, the driving force can be expressed by the following relation [71]:

$$F_R = \frac{\mu b^2 \Delta\rho}{2} \tag{2.10}$$

where μ is the shear modulus, b is the Burgers vector and $\Delta\rho$ is the difference in dislocation density of a recrystallized grain to a deformed grain. As mentioned earlier, controlling recrystallization is crucial in the hot processing of austenite. Thus, an inhibition system by means of particle pinning force (*i.e.*, Zener pinning force) is required to control recrystallization [4]. The following background addresses several models to quantify the Zener pinning force.

2.6 Pinning Force of Microalloying Elements

C.S. Smith, in his paper in 1948, wrote a paragraph from private communication with C. Zener [72], outlining grain growth inhibition when a particle in a material is present in the vicinity of the grain boundary. Zener proposed that the energy of the boundary would be lowered, and the energy reduction of the grain boundary is due to the surface area of the particle that replaced part of the grain boundary. Moreover, grain growth will be suppressed when the grain size reaches a critical radius which is given by Eq. (2.11):

$$R = \frac{4r}{3f} \tag{2.11}$$

where r is the radius of the pinning particle (spherical particle) and f is the volume fraction of particles. The pinning force exerted by the particle (F), can be quantified by using the diagram in Figure 2.9. It is calculated by balancing the forces and assuming an incoherent particle. The maximum drag from the spherical particle will occur when θ= 45°, and if several particles intersect a boundary, the force per unit area of migrating boundary (N/m^2) is expressed as:

$$F = \pi r n \gamma \tag{2.12}$$

where γ is the interfacial energy per unit area of grain boundary and n is the number of particles intersecting a boundary

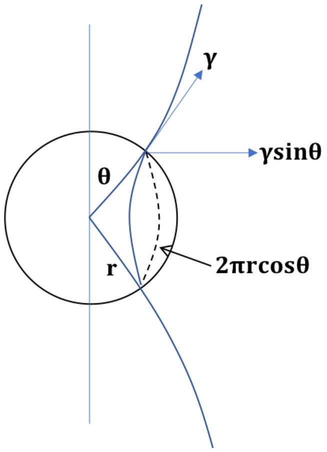

Figure 2.9 Schematic diagram showing the interaction between a spherical particle and a grain boundary; after reference [73].

The early work of Zener on the effect of particles exerting a pinning force on a migrating grain boundary has been expanded to several models and has been subject to research in microalloyed steels [51, 62]. For example, Gladman [74], assumed rigid boundary motion of grain boundaries through spherical particles and derived an expression that relates the pinning force (F) per particle and particle size by:

$$F = 4r\gamma \tag{2.13}$$

Additionally, Gladman, obtained the critical particle radius (r_c) below which grain boundaries are hindered and it is expressed as:

$$r_c = \frac{6R_0 f_v}{\pi} \left(\frac{3}{2} - \frac{2}{z}\right)^{-1} \tag{2.14}$$

Eq. (2.14) is derived by equating particle pinning force and the rates of grain boundary energy change during grain growth. In this relationship, R_0 is the mean grain radius, f_v is the volume fraction of particles, and z is the ratio of growing grains sizes to those of its neighboring grains. Eq. (2.13) can be expanded to account for more than one particle, namely, the number of particles per unit area (N) to quantify the total pinning force:

$$F = 4r\gamma N \tag{2.15}$$

Based on Eq. (2.15), several models have been proposed to quantify the total pinning force of second phase particles [62]. The differences between these pinning models were based on the criteria of calculating the number of particles per unit area N_s. The first model was attributed to Gladman, the rigid boundary model (RBM), which assumes that the number of particles per unit volume are interacting with a grain boundary within ±r distance of the grain boundary plane. From this observation, assuming spherical particles, N_s is calculated to be:

$$N_s^{RBM} = \frac{3f_v}{2\pi r^2} \tag{2.16}$$

substitution of Eq. (2.16) into Eq. (2.15) gives the total pinning force of particles:

$$F^{RBM} = \frac{6\gamma f_v}{\pi r} \tag{2.17}$$

Another model was introduced by Cuddy [11], who assumed a flexible boundary model (FBM). In this model, the boundary is assumed to be interacting with an array of distributed particles in a three-dimensional configuration until the boundary motion is completely suppressed. This model is considered to be the opposite of RBM. Hence, the number of particles per unit area is calculated as:

$$N_s^{FBM} = \frac{3f_v^{2/3}}{4\pi r^2} \tag{2.18}$$

substitution of Eq. (2.18) into Eq. (2.15) leads to the expression of the total pinning force of FBM:

$$F^{FBM} = \frac{3\gamma f_v^{\frac{2}{3}}}{\pi r} \tag{2.19}$$

Finally, Hansen *et al.* [16] introduced the subgrain boundary model (SBM). In this model, it is assumed that the particles can exist on subgrain boundaries in the hot deformed structure prior to the start of recrystallization. Taking l as the average subgrain diameter, the number of particles per unit area is expressed as:

$$N_s^{SBM} = \frac{3f_v l}{8\pi r^3} \tag{2.20}$$

thus, the corresponding pinning force of particles from this model is given by:

$$F^{SBM} = \frac{3\gamma f_v l}{2\pi r^2} \tag{2.21}$$

A summary of the aforementioned pinning forces is listed in Table 2.1.

Table 2.1 Models of pinning force.

Pinning force model	Expression	Parameters
RBM	$F^{RBM}=\frac{6\gamma f_v}{\pi r}$	γ: interfacial energy f: vol. fraction of particles r: particle radius l: subgrain size
FBM	$F^{FBM}=\frac{3\gamma f_v^{\frac{2}{3}}}{\pi r}$	
SBM	$F^{SBM}=\frac{3\gamma f_v l}{2\pi r^2}$	

2.7 Interaction Between Recrystallization and Precipitation

In Nb microalloyed steels, the microstructure of austenite during hot processing is mainly controlled by the progress of recrystallization after deformation and the strain-induced precipitation of Nb (C, N). In the case of plate hot rolling, the interpass time between passes is relatively long, thereby, the main softening mechanism is static recrystallization. However, in hot strip rolling, the interpass time, as well as the total rolling time, is short, thus, niobium can be reasonably assumed to interact with austenite as a solute (solute-drag effect) [4, 5]. The interaction between recrystallization and precipitation can be best understood by the generalized recrystallization-precipitation-temperature-time (RPTT) diagram deduced from experimental results [5, 16, 75], shown in Figure 2.10. It should be pointed out that in the absence of deformation, the interaction between recrystallization and precipitation will not be possible. However, upon deformation, recrystallization and strain-induced precipitation can simultaneously be accelerated. Furthermore, a decrease in the dislocation density of austenite by recrystallization reduces the number of precipitate nucleation sites. In Figure 2.10, T_{sol} represents the solution temperature above which Nb (C, N) precipitates are completely dissolved in austenite. $T_{95\%}$ corresponds to the temperature below which recrystallization and stain-induced precipitates compete and $T_{5\%}$ is the recrystallization-stop temperature as mentioned previously in which precipitation commences prior to recrystallization. $R_{S\text{-}5\%}$ and $R_{F\text{-}95\%}$ correspond to a 5% and 95% recrystallized fraction, signifying the onset and the completion of recrystallization.

There are three distinct regions in Figure 2.10 and can be understood by the net driving pressure between recrystallization and strain-induced precipitation (F_R-F_P). In region I, the austenite recrystallization is much faster than precipitation and it is completed before the start of precipitation (P_s). Nevertheless, in deformed austenite, the precipitation is accelerated and is noted by the shift in curves Ps and P_S^D, the latter corresponds to the start of precipitation in the deformed austenite and the former corresponds to the start of precipitation in the coarse, undeformed austenite [75]. In region II, which is between $T_{95\%}$ and $T_{5\%}$, the pinning force exerted by the strain-induced precipitates opposes the driving force for recrystallization. When the pinning force is lower than the driving force, austenite recrystallization precedes precipitation. On the other hand, when the pinning force is higher than the driving force, recrystallization progress is relatively retarded, as illustrated by the partial recrystallization lines (R_S^P and R_F^P). It should be noted that deformations in region II should be avoided due to the undesirable properties associated with duplex microstructures [11, 53]. Finally, in region III, the precipitation precedes recrystallization ($F_R < F_P$), and the recrystallization progress will completely be suppressed.

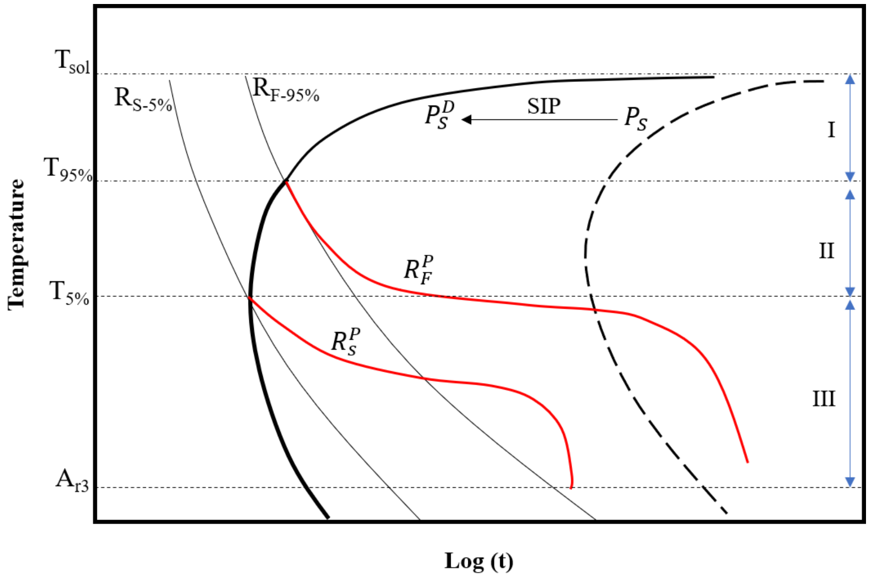

Figure 2.10 Schematic of isothermal RPTT diagram; modified from references [16, 75].

2.8 Strengthening Mechanisms

The yield strength of metal can be increased, in general, by one or more of several mechanisms. These include:

I. Solid solution strengthening
II. Precipitation strengthening
III. Grain refinement
IV. Dislocation or work hardening strengthening

All the above mechanisms share a common feature, which is the ability to hinder dislocation movements thereby increasing the yield stress required for the onset of plastic deformation. Hence, assuming linear additivity, the total yield strength of HSLA steels can be expressed in a generalized Hall-Petch equation [4]:

$$\sigma_{\mathrm{y}} = \sigma_{\mathrm{P-N}} + \Delta\sigma_{\mathrm{SS}} + \Delta\sigma_{\mathrm{Prec.}} + \Delta\sigma_{\mathrm{Dislo.}} + \sigma_{\mathrm{GB}} \qquad \textbf{(2.22)}$$

where σ_{P-N} is the iron lattice friction or Peierls-Nabarro stress; $\Delta\sigma_{\mathrm{SS}}$, $\Delta\sigma_{\mathrm{Prec.}}$, and $\Delta\sigma_{\mathrm{Dislo.}}$ are the stress increments caused by solid solution, precipitation, and dislocation; and σ_{GB} is the grain boundary strengthening, respectively. The contributions of these mechanisms to the strength of microalloyed steels will be briefly discussed in the following subsections.

2.8.1 Solid Solution Strengthening

Substitutional and interstitial atoms in solution tend to increase the yield strength. Atoms that are close to iron atom in size and do not combine to form carbides or nitrides can substitute iron atoms in austenite or ferrite and are said to be in substitutional solid solution. On the contrary, atoms that are smaller than iron atoms such as carbon and nitrogen are said to be in an interstitial solid solution. The solid solution strengthening in HSLA steels was studied by Pickering [9]. As pointed out by Pickering, the common substitutional elements are Mn, Cu, Ni, P, and Si. The incremental strength caused by substitutional and interstitial elements in HSLA steels is illustrated in Figure 2.11.

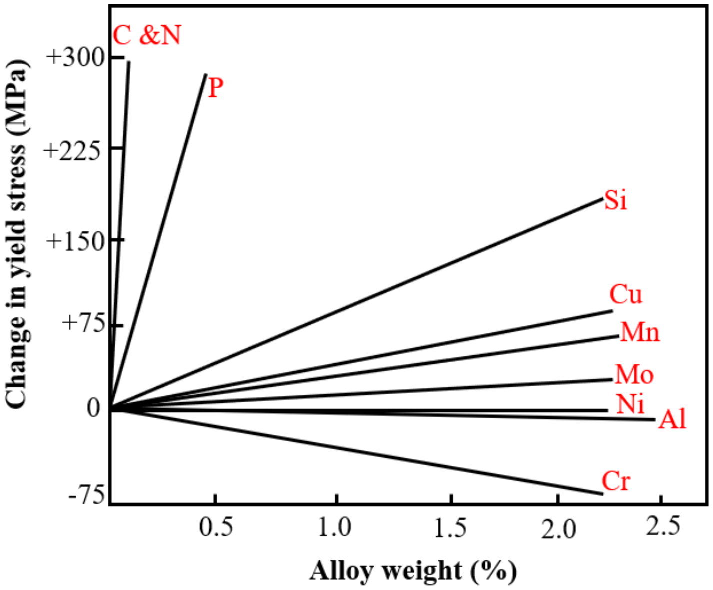

Figure 2.11 Solid solution strengthening in ferrite; after Pickering [9].

2.8.2 Precipitation Strengthening

The maximum increment increase in yield strength caused by precipitation strengthening in HSLA Nb-bearing plate and strip steels is in the range of 80-100 MPa [4]. This increase in strength is mainly attributed to the ability of precipitates to impede dislocations motions. The impedance is dependent on the morphology, size, distribution and volume fraction of precipitates. In HSLA steels, the carbides, nitrides and carbonitrides are usually incoherent or semi-coherent precipitates and follow the Orowan mechanism (dislocations loops/bypass around precipitates) [7].

2.8.3 Dislocation Strengthening

In ferrite-pearlite steels, the dislocation strengthening contribution is negligible since polygonal ferrite has a much lower dislocation density compared to acicular ferrite/bainitic steels

[9]. The dislocation strengthening increment raises with the square root of the dislocation density; the dislocation strengthening contribution can be estimated as follows [76]:

$$\Delta\sigma_{\mathrm{Dislo.}} = \alpha \mathrm{MGb}\rho^{\frac{1}{2}} \tag{2.23}$$

where α is a constant with a value of 0.3, M is the average Taylor factor (∼ 3 for BCC iron), G is the shear modulus (∼ 64 GPa) and b is the Burgers vector. It should be mentioned that the dislocation density will be decreased during TMP in steels due to the rapid recovery of ferrite at elevated temperatures.

2.8.4 Grain Refinement

Perhaps one of the most important strengthening mechanisms in HSLA is grain refinement [4]. Since grain boundaries constitute the largest obstacles for dislocation motion in a metal, increasing the grain boundary area per unit volume will increase the total yield strength. Furthermore, grain refinement is the only method to increase both strength and toughness. The yield strength contribution coming from grain refinement is best described by the Hall-Petch equation [32]:

$$\sigma_{\mathrm{GB}} = \sigma_0 + \frac{k}{d^{1/2}} \tag{2.24}$$

where σ_0 is the friction stress, d is the grain size in µm and k is a constant that depends on the steel composition. It is clear from this equation that grain coarsening should be avoided during TMP. Upon air cooling to room temperature, for example, ferrite-pearlite steels, d is dictated by the ferrite grain size. However, in bainitic or martensitic HSLA grades such as those obtained after accelerated cooling, d is determined by the effective grain size of the bainite or martensite (*i.e.*, lath or block size) [21, 52, 77, 78].

2.9 Transformation Microstructures in HSLA Steels

It is known that the mechanical properties exhibited by a steel are mainly controlled by its final microstructure [15]. In this case, the austenite conditioning, mentioned in a previous section, strongly alters the transformed microstructure and thus the final mechanical properties [4]. Ferrite-pearlite microalloyed steels result from TMP followed by air cooling to room temperature. This was a standard practice prior to 1970 for plate and strip steels and it was not until the 1980s, improvements to mechanical properties were further enhanced by TMP and the introduction of online accelerated cooling, ACC [15]. The central purpose of ACC is to suppress the formation of polygonal ferrite and enhance the non-equilibrium ferrite microstructures to be formed.

During ACC to the WET in the case of plate steels or the coiling temperature in the case of strip steels, the austenite to ferrite transformation takes place. At the end of ACC, depending on the WET, coiling temperature, and the finish rolling temperature, the final microstructure may consist of a wide range of transformation products (diffusional or displacive) [79]. The information on the types and amounts of phases, for a given cooling rate, can be obtained from the appropriate continuous-cooling transformation (CCT) diagram.

The non-equilibrium ferrite microstructures found in HSLA steels are polygonal ferrite (PF), quasi-polygonal ferrite (QF), degenerated pearlite (P’), bainitic ferrite (BF), Acicular ferrite (AF), upper or lower bainite (UB or LB) and martensite/austinite constituents (MA) [21, 80-82]. PF is characterized by equiaxed grains containing low dislocation density. QF is characterized by an irregular grain shape containing substructure with occasional MA. Any transformation products containing cementite could be P’ or classical bainite. On the other hand, bainitic ferrite usually lacks cementite and grows in the form of parallel plates or laths (packets) with MA constituents. The formation of MA in line with BF can be attributed to the partitioning of carbon from BF laths to the austenite upon cooling [80]. GB is characterized by having sheaves of elongated ferrite with low misorientations and a high dislocation density [21]. AF microstructure consists of a non-equiaxed grains with an irregular arrangement of laths [81]. Finally, there are still some controversies on the exact identification of these non-equilibrium phases, especially AF. For instance, one of the previous studies [21] classified AF as being a mixture of GB and QF. Others [83] considered AF as a mixture of GB, QF and BF.

A large body of research showed that AF-dominated microstructures have the potential to improve the strength and toughness compared to ferrite-pearlite ones [83-86]. This can be attributed to the high dislocation density, dispersion of hard particles and smaller effective grain size (*i.e.*, sheaf or packet) size found in AF. Moreover, AF microstructures exhibit higher toughness compared to BF microstructures, due to a higher density of high angle grain boundaries (HAGB) which are capable of arresting cracks or deflecting their directions [78, 83].

3.0 Motivation and Objectives

The purpose of the current study was fourfold: (i) to determine whether NbC could form during rough rolling in high Nb steels; (ii) whether this precipitate might cause less than complete recrystallization during rough rolling; (iii) whether a non-optimum final austenite microstructure prior to transformation results from a larger slightly pancaked as-roughed austenite grain size resulting; (iv) correlate different thermomechanical schedules to the final microstructure. Hence, the following research questions were specifically addressed:

i. In high Nb steel, will any of the dissolved Nb in austenite reprecipitate during roughing? And if it does
ii. Will it suppress complete recrystallization during roughing?
iii. What is the effect of Nb on $T_{95\%}$ and $T_{5\%}$ in Nb-bearing steels?
iv. What are the effects of thermomechanical histories on the austenite structure and the subsequent transformation products?

To answer these research questions, several program variations need to be taken into consideration:

a) In terms of alloy design, 0.03/ 0.06 wt.% C, and 0/ 0.04/ 0.08 wt.% Nb was adapted.
b) Reheating austenite in the range 900 °C- 1300 °C.
c) Analyzing recrystallization behavior through laboratory hot deformation experiments in a temperature range of 1150 °C to 800 °C.
d) Using Thermo-Calc software and the Dutta-Sellars model to estimate the precipitation start time.

e) Comparing transformation microstructures under different thermomechanical processing simulations.

4.0 Operating Hypotheses

i. Higher Nb additions to steel will increase both, $T_{5\%}$ and $T_{95\%}$ during hot deformation.

ii. The region of partial recrystallization of austenite in high Nb steels will be at/or close to the roughing temperatures. Consequently, deformation in this region will lead to a non-uniform austenite structure (*i.e.,* duplex grain size).

iii. The occurrence of AF-dominate microstructures is dependent on both, the amount of Nb in steel and on the thermomechanical history prior to γ-α transformation.

5.0 Experimental Procedures

5.1 Alloy Design[i]

In the current research program, the experimental steels were chosen to represent a typical linepipe steel, near X100 composition [18]. The carbon and niobium levels were chosen to demonstrate the effects of NbC pinning forces in the temperature range of rough rolling. Figure 5.1 shows the temperature profile of a modern 5 m wide reversing plate mill where the end of roughing rolling is approximately at 1050 °C [88].

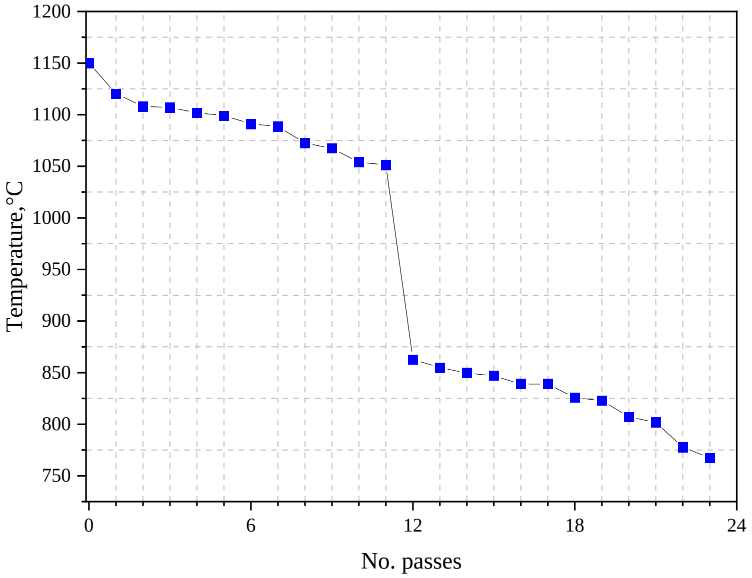

Figure 5.1 Temperature profile of a modern 5 m wide reversing plate mill; after reference [88].

---

[i] This section is part of Ref. [87] R. A. Almatani and A. J. DeArdo, "Rational Alloy Design of Niobium-Bearing HSLA Steels," *Metals*, vol. 10, no. 3, p. 413, 2020.

NbC in solution was calculated using the equilibrium solubility product proposed by Palmiere *et al.* [29], see Eq. (2.6). Figure 5.2 shows the calculated dissolution of alloys with two Nb levels, namely, 0.04Nb and 0.08Nb, in wt.%, while keeping carbon as a constant at 0.06 wt.%. It is clear that all the Nb available in 0.04 wt.% Nb steel will be dissolved at/or close to 1170 °C, whereas the higher Nb content will not be fully dissolved below a slab reheating temperature of 1265 °C, which indicates more stable precipitates at higher temperatures. It should be noted that this temperature far exceeds the normal reheating temperature of 1150–1200 °C used in industrial practice. The dashed line represents the deviation between the two alloys in terms of soluble Nb; thus, the reheating temperature is not a variable but is restricted to 1150–1200 °C in practice. Therefore, the question is how much Nb can be dissolved at perhaps 1200 °C. According to Figure 5.2, all of Nb in the 0.04Nb steel and 0.05% Nb in the 0.08Nb steel would be dissolved at 1200 °C. In normal practice with commercial steel of similar composition containing 0.04 Nb, all of the Nb is taken into solution during reheating, and very little if any is reprecipitated during rough rolling. Therefore, recrystallization goes to completion in roughing. However, in the 0.08Nb steel, only 0.055 wt.%. Nb is taken into solution and the remaining 0.025 wt.% Nb is left undissolved.

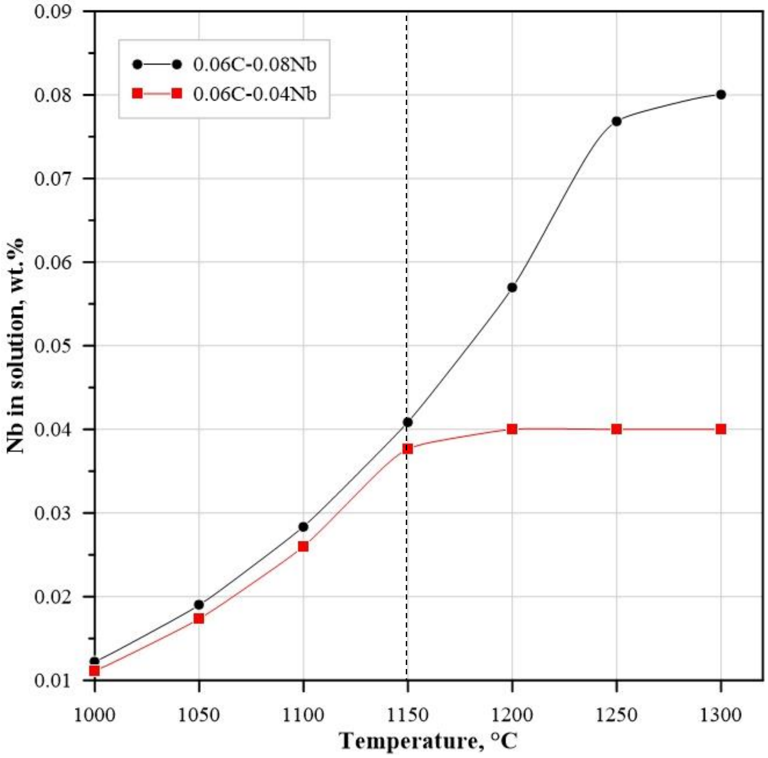

Figure 5.2 Amount of dissolved Nb in austenite as a function of temperature; based on the solubility product of Palmiere *et al.* [29].

5.1.1 Theoretical Prediction

The assumptions made here were that with the addition of Nb into the steel, the $T_{5\%}$ and $T_{95\%}$ temperatures will both be increased [11], and subsequently the processing window above $T_{95\%}$ will be reduced. In addition, the $T_{5\%}$ temperature might be increased to where it enters the later portion of the rough rolling temperature range. For example, Figure 5.3 shows a schematic of two Nb steels, namely, HTP steel (~ 0.1 Nb wt%) and TMCP steel (~ 0.04 Nb wt.%). For a given strain (*i.e.*, Σn Passes) and temperature, and as the temperature decreases, the processing window at the end of roughing for a uniform austenite grain size distribution is reduced in the HTP steel, below which only partial recrystallization and grain refinement may occur; this is shown in the hatched area above 0.1Nb $T_{95\%}$. On the other hand, the processing window for the 0.04Nb steel to produce a uniform grain size distribution is higher even below 1050 °C, which is here designated as the end of rough rolling temperature.

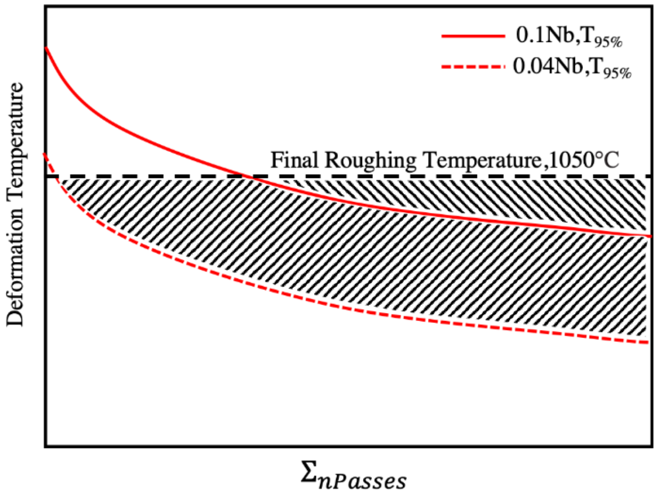

Figure 5.3 Schematic showing hypothetical processing window of high and low Nb steels; hatched areas show the window in which a uniform grain refined austenite microstructure can be obtained by rolling above the respective $T_{95\%}$ temperature.

In the context of hot rolling, the typical value of the recrystallization driving force of austenite subjected to a single low temperature rolling pass is found to be about 30 MPa. This was for 900 °C; at 1100 °C it would be much lower, near 22 MPa. Thus, to retard recrystallization, a necessary pinning force is needed and, as mentioned previously, several models were proposed to calculate the pinning force of precipitates in microalloyed steels as a result of the interaction between precipitates and austenite grain boundaries [11, 74]. However, in this study, the subgrain boundary model [16] was employed to estimate, theoretically, the pinning forces at different deformation temperatures and specifically during roughing passes. The reason for using this model is mainly that NbC particles are not randomly distributed but isolated on the subgrain boundaries of deformed austenite [17, 75].

The estimations of pinning forces caused by strain-induced precipitation of NbC were calculated using (i) the subgrain boundary model, together with (ii) the volume fractions of NbC estimated for the compositions and temperatures using the equilibrium solubility relation mentioned previously; (iii) particle sizes of NbC observed; and (iv) the dislocation cell sizes observed in the TEM in recovered austenite in earlier similar studies [16, 75]. The subgrain boundary pinning force model, given by Eq. (2.21), was used to estimate the pinning force of precipitates. The parameters used in this investigation were $\gamma = 0.8$ J/m^2, particle size = 2 nm and subgrain size = 0.5 μm; and f_v was calculated from the solubility product.

It was shown from previous studies that the measured volume fractions of NbC for subgrain and grain boundaries are higher than predicted by equilibrium considerations [16, 17]. Furthermore, it appeared that there was a segregation of Nb to the boundaries, leading to higher than expected local volume fractions of NbC. This means that the local pinning forces are actually larger than those which would be calculated from equilibrium considerations, where NbC is uniformly distributed.

Table 5.1 shows the estimated pinning forces for two Nb levels during roughing passes. The results indicate that higher Nb level gives the higher pinning force magnitudes at the end of roughing passes (*i.e.*, 41 MPa at 1050 °C), due to a higher volume fraction of NbC to precipitate at lower roughing temperature.

Table 5.1 NbC pinning force at the respective deformation temperature, MPa.

Deformation temperature, °C	0.06C, 0.08Nb	0.06C, 0.04Nb
1150	27.5	3.4
1100	35.4	10.7
1050	41.0	17.0

5.1.2 Materials

As mentioned previously, the experimental steels were chosen to represent a typical linepipe steel, near X100 composition. The experimental steels used in the present investigation are listed along with their chemical analyses in Table 5.2. The letters H and L are used to distinguish carbon levels of 0.06 wt. pct. and 0.03 wt. pct., respectively. The second digits of 0,4, and 8 are used to label niobium levels of 0 wt. pct., 0.04 wt. pct. and 0.08 wt. pct., respectively. It should be emphasized that these steels presented in Table 5.2 share the same basic nominal composition. These analyses were supplied by the United States Steel Corporation Research and Technology Center.

These steels were prepared as 45 kg vacuum melted laboratory heats and solidified in cast iron molds. Following this, the steels were homogenized at 1250 ˚C for 60 minutes, hot rolled to 25 mm thick “slabs” in five passes with finish rolling at 890 ˚C, and air cooled to room temperature. These slabs provided the starting condition for all subsequent processing. The United States Steel Corporation Research and Technology Center also supplied these slabs.

Table 5.2 Chemical compositions of the experimental steels in wt. %

Steel	C	Mn	Nb	P	S	Si	Cu	Ni	Cr	Mo	Ti	Al	N
L0	**0.032**	1.885	**0.0043**	0.010	0.002	0.303	0.020	0.204	0.499	0.101	0.0146	0.031	0.004
L4	**0.031**	1.871	**0.0429**	0.010	0.002	0.300	0.020	0.203	0.498	0.100	0.0144	0.032	0.004
L8	**0.029**	1.873	**0.0837**	0.010	0.002	0.302	0.021	0.202	0.499	0.100	0.0146	0.031	0.0035
H0	**0.061**	1.888	**0.0042**	0.008	0.003	0.305	0.020	0.204	0.498	0.101	0.0145	0.030	0.004
H4	**0.062**	1.883	**0.0413**	0.008	0.003	0.304	0.021	0.204	0.498	0.100	0.0146	0.031	0.004
H8	**0.059**	1.875	**0.0782**	0.008	0.003	0.303	0.021	0.203	0.498	0.100	0.0144	0.031	0.004

Note: embolden values represent the variables in C or Nb.

5.2 Experimental Approach

To carefully achieve the main objectives, the progress of the microstructure through reheating and subsequent processing was studied following the scheme shown in Figure 5.4.

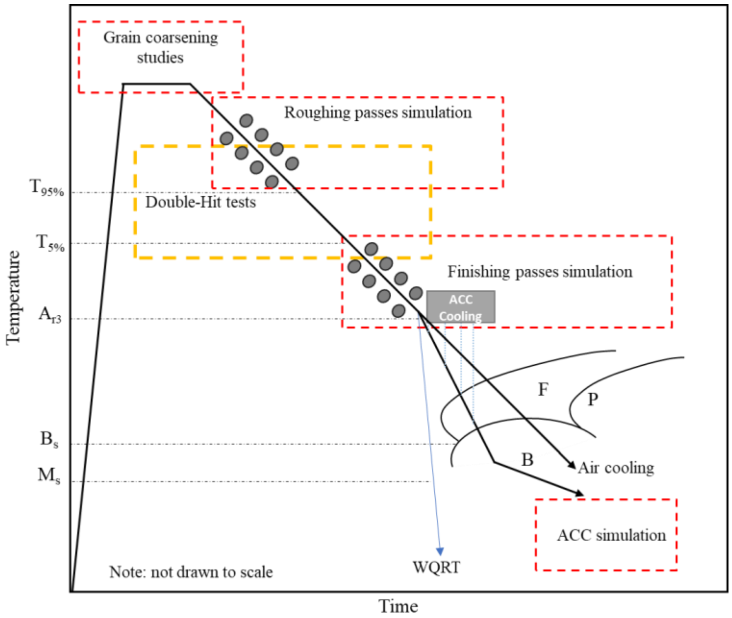

Figure 5.4 Studies performed with respect to the different stages of hot rolling.

5.2.1 Grain Coarsening Studies

To understand the behavior of austenite grain size as a function of temperature, isothermal reheating studies were performed on samples of 25 mm cube edge taken from the hot rolled slabs at about a quarter of the thickness. Special care had to be exercised prior to each soaking temperature since these austenitizing treatments were carried out at temperatures up to 1300 °C. For this reason, and to prevent any excessive oxidation, samples were encapsulated in evacuated quartz tubes and back filled with dry argon.

Encapsulated samples were placed in a box furnace and were soaked for 60 minutes at different temperatures starting from 900 °C and ending at 1300 °C in increments of 50 °C. All of the treatments were accomplished by soaking samples of the slab material directly to the specified austenitizing temperature. No prior treatments of any nature were imparted to the slab material before reheating. Following each soaking, the capsules were broken and the samples were immediately quenched in ice water.

5.2.2 Preliminary Hot Deformation Study

The central purposes of the preliminary study were to investigate the effect of deformation on the behavior of austenite in the temperature range where rough rolling would be expected and to build knowledge upon it for subsequent studies. Accordingly, the extent of austenite recrystallization was determined metallographically for different deformation schedules in the H4, H8, and L8 steels.

5.2.2.1 MTS Hot Compression Testing

Hot compression tests were performed using an MTS-458 unit designed for deformation under constant true strain rate conditions equipped with a radiation furnace (Sylvania 1200 W halogen quartz infrared bulb) and a temperature controller.

From the transverse direction of the slabs,12 mm blanks were cut for producing cylinders for hot compression testing. Selected samples were machined to right cylindrical shapes of dimensions 12 mm (diameter) × 19 mm (height), as shown in Figure 5.5. A thermocouple hole 1.6 mm in diameter and approximately 5 mm deep was drilled into the cylindrical samples to control and monitor the temperature. The shape of the compression specimen is known as modified Rastegave's design [51] where grooving is made to the geometry of the cylinders to minimize friction and the corresponding barreling effects by retaining lubricants during deformation.

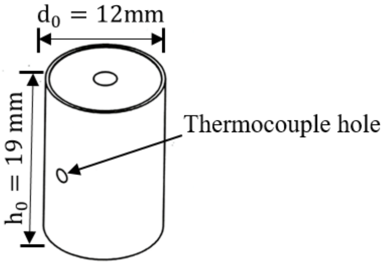

Figure 5.5 Schematic of the cylinders used in the MTS hot compression testing.

The right cylinders were reheated to 1200 °C for two minutes and then cooled to various temperatures for recrystallization studies. Glass lubricant was used to suppress barreling in the multiple hits, axisymmetric hot compression tests. Figure 5.6 shows an example of the thermomechanical path used in a series of samples to closely simulate roughing passes in a typical hot rolled plate. Two reduction levels of 15% and 25% were used in this preliminary study and the strain rate ($\dot{\varepsilon}$) was set to be 10 s^{-1} for all hot compression experiments.

Prior to each reheating in the radiation furnace, the cylinders were nickel coated to prevent any excessive oxidation. After cleaning the cylinders, the procedure consists of immersing them in an acid solution containing 20g of nickel sulfate, 27g of sodium hypophosphite and 16g of sodium succinate in one liter of distilled water. A thin layer of nickel was deposited over the surface of the cylinders after heating in this solution for 60 minutes at 90 °C

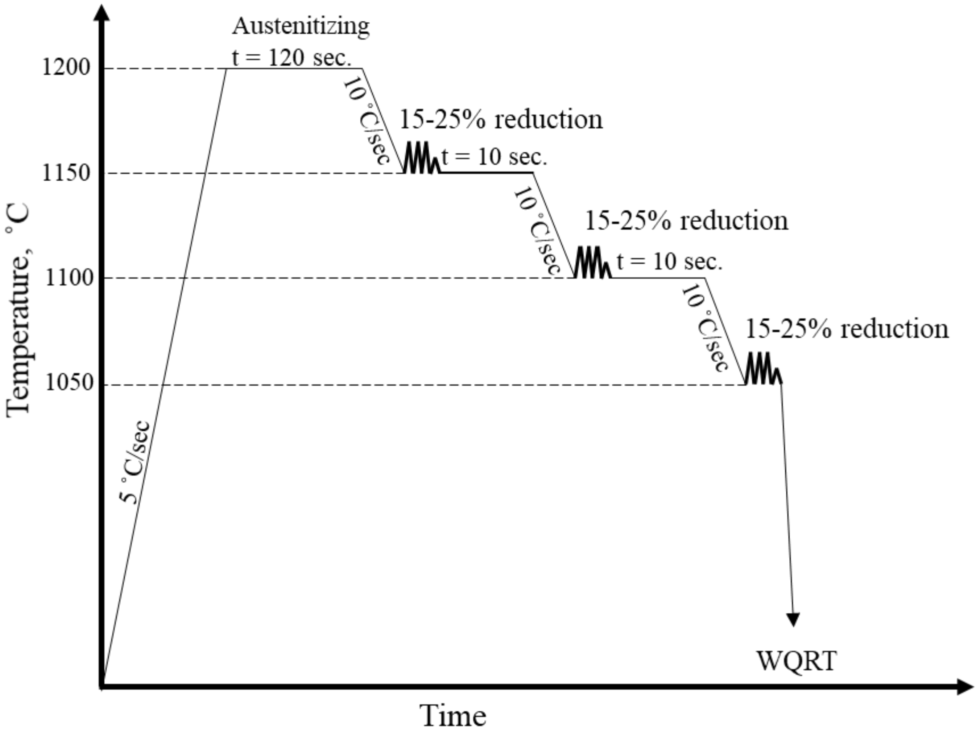

Figure 5.6 Schematic of temperature-time schedule used in the MTS hot compression testing; not drawn to scale.

5.2.3 Gleeble® 3800 Thermomechanical Simulator

5.2.3.1 $T_{5\%}$ and $T_{95\%}$ (Double-Hit Experiments)

Isothermal axisymmetric hot compression studies were conducted using Gleeble® 3800 thermomechanical simulator under a constant true strain rate. Specimens of rod-shaped taken from the transverse direction of the slabs were, initially, soaked at 1200 °C and air cooled to room temperature for homogenization. From these rods, compression samples of right circular cylinders were machined having a height of 12 mm and a diameter of 10 mm. In all tests, a graphite foil was inserted (lubricant) between two tantalum foils which were attached between the WC anvils and the sample to reduce friction effects and protect the anvils. A thermocouple was spot welded on the surface at the center of each sample for temperature control.

The isothermal double-hit test was carried out on the cylinders by following the schedules depicted in Figure 5.7. Following 180 seconds reheat at 1200 °C, each sample was forced air cooled at a rate of 30 °C sec^{-1} to one of the test temperatures at which deformation was immediately commenced. After an initial ε_1 of 0.3, the sample was unloaded and held at the same deformation temperature for some time t (interpass time). Following this holding time, the sample was loaded again to ε_2 of 0.3 and after which the sample was immediately quenched in water. The first schedule was conducted under a constant prescribed delay time of 20 seconds at decreasing temperatures starting from 1150 °C down to 900 °C in increments of 50 °C, which was intended to determine $T_{5\%}$. The other schedule was mainly carried out to observe the effect of delay time on the interaction between the progress of austenite recrystallization and the strain-induced precipitation in the experimental steels. Delay times of 5, 15, 20, 50, and 100 seconds were employed at different temperatures ranging from 1050 °C down to 900 °C in increments of 50 °C as well.

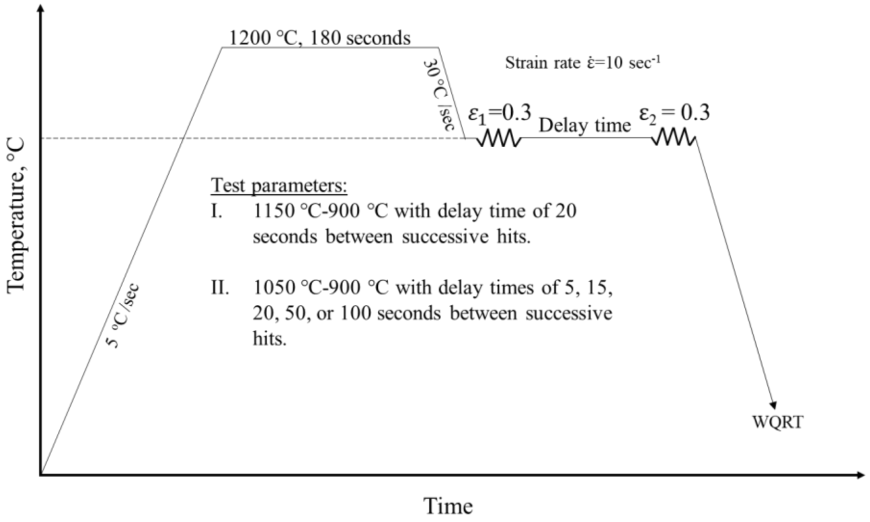

Figure 5.7 Schematic diagram of time-temperature schedules used in the double-hit experiments; not drawn to scale.

The fractional softening due to static recrystallization of austenite was measured for each sample by the net change of work hardening between the first and second hit in the hot flow curve. Several analytical methods, as mentioned earlier, are available to estimate fractional softening [70]. Previous studies have shown that it is preferred to estimate the fractional softening in double-hit tests using either the 5% true strain [68] or the 2% offset method [89] to define the flow stress. This is because these methods minimize the recovery effects, especially at lower strains. Nevertheless, the 2% offset method appears to have better sensitivity at lower strains and does not require tedious extrapolation (*i.e.*, using Ludwick-Hollomon Eq.) of the first deformation curve. For this reason, in this study, and to exclude the recovery effects, the 2% offset method was used to determine the fractional softening and it is given by [89]:

$$\mathrm{FS} = \frac{(\sigma_\mathrm{m} - \sigma_{2,2\%\,\mathrm{offset}})}{(\sigma_\mathrm{m} - \sigma_{1,2\%\,\mathrm{offset}})} \qquad \textbf{(5.1)}$$

where σ_m, is the maximum flow stress obtained from the first curve, $\sigma_{2,2\%\,\mathrm{offset}}$ and $\sigma_{2,2\%\,\mathrm{offset}}$ are the flow stresses at 2% offset of the first and second deformation curves, respectively. Figure

5.8 shows an example of flow curves obtained from a double hit test. From this figure, the main difference between the 5% true strain method and the 2% offset method is the location of the maximum stress (σ_m) in the first curve. The maximum stress of the 2% offset method is taken as the maximum stress of the first curve whereas the maximum stress of the 5% true strain method is taken from the extrapolated continuous first curve when the strain takes a value of 5% measured from the origin of the second curve.

From fractional softening curves, the deformation temperature corresponding to 20% FS was taken as $T_{5\%}$ or T_{nr} [17]. Below this value, it is expected that the steel is in the work hardening state and softening is predominately due to static recovery.

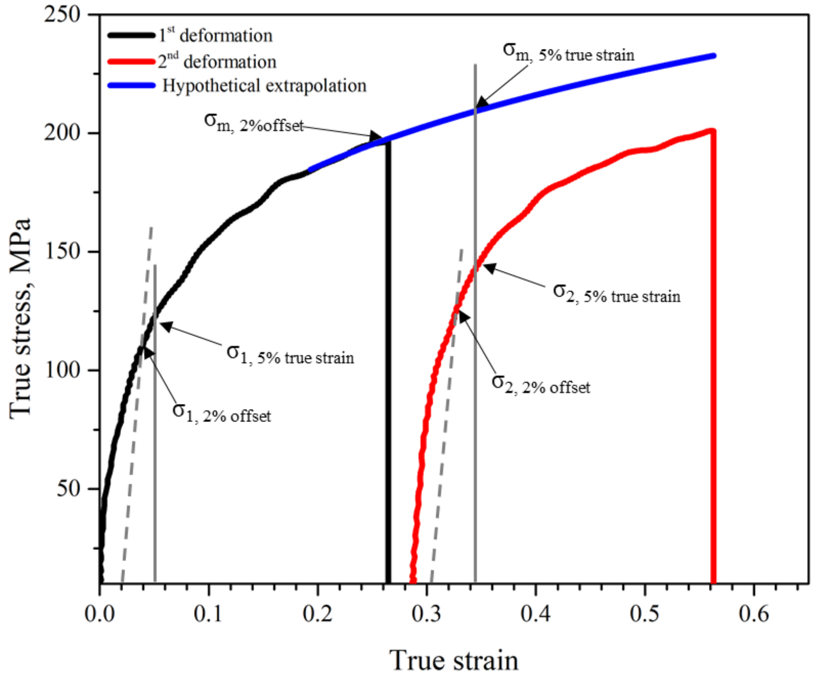

Figure 5.8 Example of the flow curves obtained from the double-hit test and the corresponding stresses used to calculate the fractional softening by 2% offset method or 5% true strain method.

5.2.3.2 Roughing Pass Simulation

The time-temperature schematic diagram shown in Figure 5.9 illustrates the roughing passes simulation used in this study. Two temperature schedules were employed to investigate the austenite structure after deformations in the roughing range. Namely, the first schedule was intended to be a high temperature roughing deformation whereas the second schedule was intended to be relatively a low temperature roughing deformation. The former consists of successive deformations at 1150 °C, 1100 °C, and 1050 °C while the latter at 1100 °C, 1050 °C, and 1000 °C.

The roughing schedules under axisymmetric hot compression were carried out in a Gleeble® 3800 thermomechanical simulator. Initially, specimens similar to those machined for double-hit tests were reheated to the soaking temperature at 1200 °C and held for 180 seconds, followed by cooling at a rate of approximately 10 °C sec^{-1} to the first deformation temperature. The deformations were conducted under a constant true strain rate of 10 sec^{-1}, where the true strain per pass is 0.287 and the interpass time is 20 seconds. The total true strain for each test was 0.86 corresponding to a 58% reduction in height. The increase in temperature resulting from adiabatic heating during deformation never exceeded 6 °C for all specimens. Following the third deformation, specimens were immediately water quenched to room temperature. For each experimental steel, except L0 steel, at least two specimens were tested per schedule.

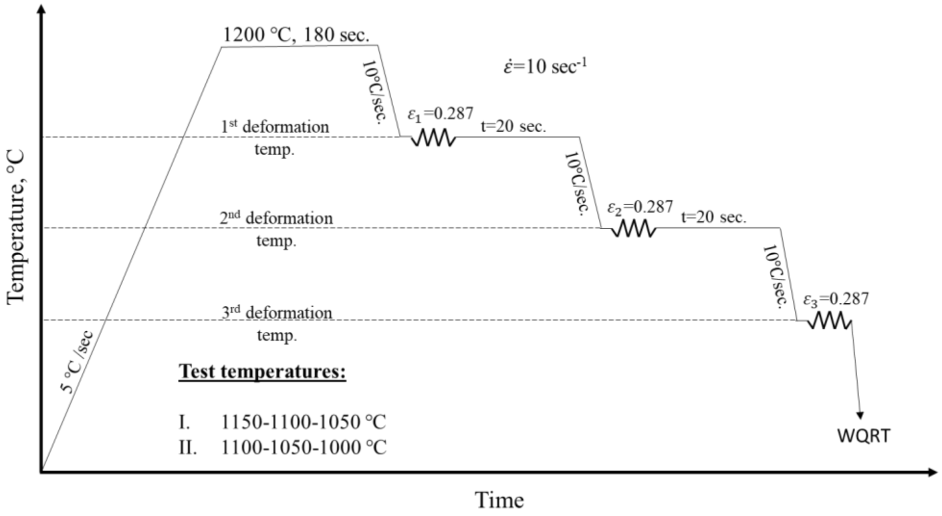

Figure 5.9 Thermomechanical schedules used for roughing passes simulation; not drawn to scale.

5.2.3.3 Finishing Pass Simulation

To investigate the effect of Nb additions on the austenite response during high temperature roughing and its final microstructure after finishing, two different roughing schedules with identical finishing schedules were adapted in this research program.

Figure 5.10 shows the thermomechanical processing route and the test parameters used in this simulation. Two roughing processing windows were employed and intended presumably to be either in the austenite recrystallization region (schedule I) or in the austinite partial recrystallization region (schedule II) depending on the steel chemistry. The test temperatures for these two schedules are listed in Table 5.3 indicating three roughing (R) and three finishing (F) temperatures for each schedule.

To simulate the aforementioned schedules, axisymmetric hot compression tests were adopted. Cylindrical specimens with dimensions of 12 mm in height and 10 mm in diameter were machined from slabs of the experimental steels, except L0 steel. All axisymmetric hot compression tests were conducted using Gleeble® 3800 thermomechanical simulator. The setup for specimen testing outlined in section 5.2.3.1 was also followed in this simulation. First, specimens were reheated to the soaking temperature at 1200 °C at a rate of 5 °C sec^{-1} and held for 180 seconds for equilibration, then cooled at a rate of approximately 10 °C sec^{-1} to the first roughing deformation (R_1) of 25 % reduction. Following this, specimens were held for 20 seconds and then cooled at a rate like the previous deformation to the second roughing deformation (R_2) at either 1100 °C (schedule I) or 1075 °C (schedule II) and, again, held for 20 seconds. Likewise, specimens subjected to R_3 had the same testing parameters as the previous deformation but deformed at either 1050 °C (schedule I) or 1000 °C (schedule II). Upon exiting the roughing stage, the specimens were cooled to the finishing passes stage and deformed at the designated finishing temperature (F) and flow curves were recorded for each deformation. For the same finishing pass, one specimen was tested and quenched in water and the second was tested and air cooled to room temperature. The reasoning for these two quenching media was to reveal the austenite microstructure at room temperature in the former, whereas to examine the transformed microstructures (*i.e.,* ferrite type, and/or bainite) in the latter. All finishing passes temperatures (*e.g.,* F_1, F_2, and F_3) were kept the same for each experimental steel.

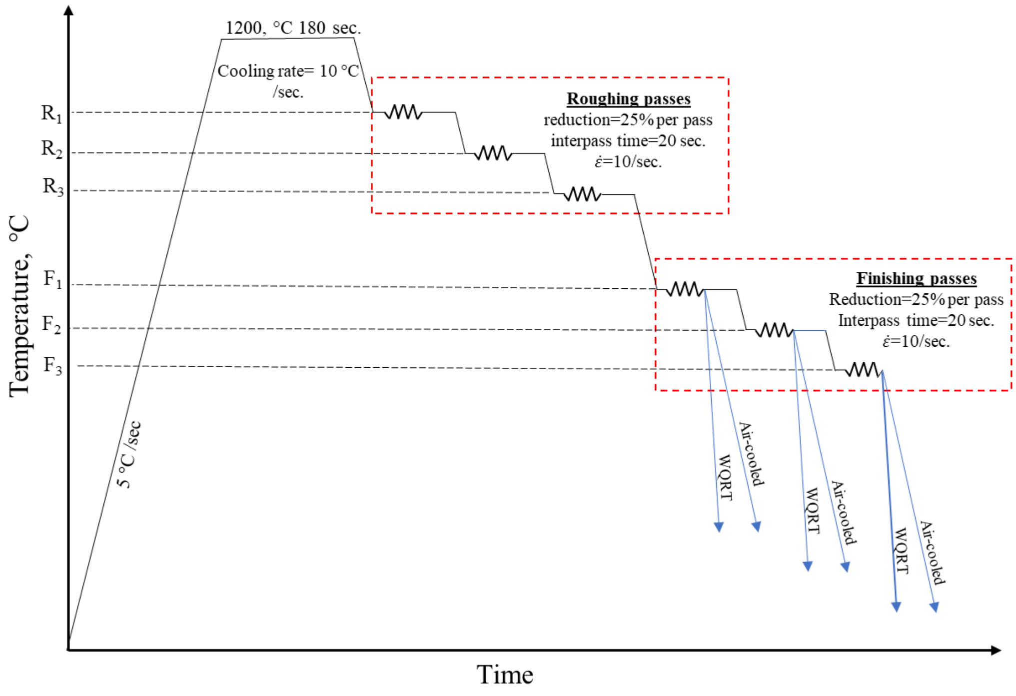

Figure 5.10 Schematic representation of the thermomechanical testing profile used in finishing simulations; not drawn to scale.

Table 5.3 Test temperatures for schedule I and schedule II, note the underlined temperatures are the main difference between the two schedules.

Schedule	Roughing pass temperature, °C			Finishing pass temperature, °C		
	R$_1$	R$_2$	R$_3$	F$_1$	F$_2$	F$_3$
I	1150	1100	1050	900	850	800
II	1150	1075	1000			

5.2.3.4 Accelerated Cooling (ACC) Studies

After roughing and finishing passes simulation, accelerated cooling to the WET or to the coiling temperature aimed to enhance nonequilibrium ferrite (*i.e.*, non-polygonal ferrite) and bainitic microstructures nucleation. To do this, specimens were subjected to roughing and finishing deformation under axisymmetric hot compression using Gleeble® 3800 thermomechanical simulator. The testing parameters were the same as those outlined in the previous section (5.2.3.3). roughing deformations were performed successively at 1150 °C, 1100°C, and 1050 °C. However, finishing deformations were carried out at 900 °C and 800 °C. Upon exiting the final finishing deformation, the specimens were forced air-cooled at a rate of 30 °C sec^{-1} to a WET at 500 °C or 400 °C and then allowed to air cool to room temperature. For each steel, at least two specimens were tested. Upon completion of the tests, the flow curves were recorded and the specimens were prepared for further analysis.

5.3 Characterization Methods

Several types of characterization techniques were used in this research program including light optical microscopy (LOM), scanning electron microscopy (SEM), and transmission electron microscopy (TEM). LOM was used to characterize the prior austenite grain size (PAGS) and morphology in the as-quenched specimens. Furthermore, LOM was used for imaging the microstructures of the air-cooled specimens. SEM was used with electron backscatter diffraction (EBSD) to characterize microstructural features and to map the various crystallographic orientations in the air-cooled specimens. TEM was used to investigate the precipitates in selected samples in the as-deformed condition.

In all the as-deformed specimens, the area of analysis under LOM, SEM, EBSD, and TEM was confined to the central area of each specimen. This was accomplished to ensure that the region being investigated had the same relative area for comparison. Figure 5.11 shows a schematic of the location of sectioning in a specimen and the area of analysis after deformation.

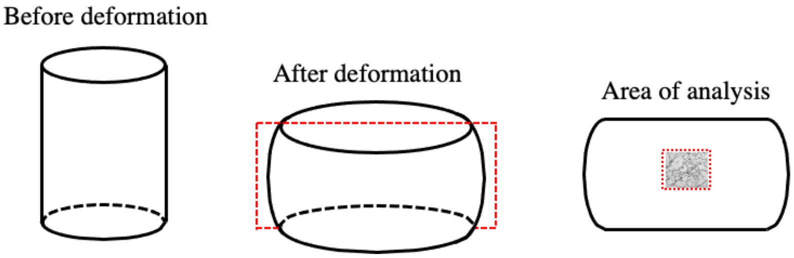

Figure 5.11 Schematic illustration showing the location of sectioning and the area of analysis.

5.3.1 Light Optical Microscopy (LOM)

Standard metallographic procedures were employed to prepare all specimens for optical metallographic investigation. The surface of interest was properly mounted in Backlite® and successively ground on silicon carbide papers to an 800-grit finish. Following this, the surface was polished on microcloth, first with a 1 µm and then a 0.05 µm alumina suspension. Between each step, the surface was cleaned with alcohol. Two different etching procedures were used to reveal the prior austenite microstructure in as-quenched and the microstructure in air-cooled specimens.

Etching of the air-cooled specimens was done using 2% nital etching solution to reveal microstructures of F, P, B, or martensite. Etching at room temperature for 10-20 seconds gives a satisfactory result.

Etching of the as-quenched specimens from both the grain coarsening and MTS/Gleeble® 3800 experiments to reveal the prior austenite grain boundaries was notoriously difficult. Prior austenite grain boundaries were revealed using either hot (*i.e.,* at 70-80 °C) or cold (at room temperature) saturated aqueous picric acid. To this reagent, 10 grams of sodium dodecylbenzene sulfonate were added as a wetting agent. After trial and error, it was found in this research program that specimens heated/deformed above 1050 °C can be etched at room temperature with this reagent by varying HCl between 0.5-2 ml until the prior austenite grain boundaries are successfully revealed. Etching was accomplished by simultaneously immersing and swabbing the specimens in this solution. After the etching solution was used for three to four samples, it was necessary to replace it with a new well mixed solution. Finally, Specimens were imaged using a Nikon FX-35WA LOM.

5.3.2 Scanning Electron Microscopy and EBSD

SEM and EBSD were used to characterize the air-cooled microstructures. specimens were prepared following the standard metallographic procedures and nital etching outlined in subsection 5.3.1. However, additional polishing was needed for EBSD analyses since the surface condition may alter the quality of the result. In this case, specimens were additionally polished by a Buehler VibroMet™ 2 vibratory polisher for 40 minutes with 0.05 µm alumina suspension. SEM imaging and EBSD mapping were carried out *via* an FEI Scios Dual-Beam SEM equipped with EDAX EBSD camera and TEAM™ software. The SEM was operated at an accelerating voltage of 20 kV, a current of 13 nA, a working distance of 14 mm, a step size of 0.2 µm, and a magnification between 1000-2500X. EBSD mapping was collected using a hexagonal pattern. All EBSD data were analyzed using OIM Analysis™ v8 software package.

5.3.3 Transmission Electron Microscopy

All TEM was conducted on selected specimens in a JEOL JEM2100F equipped with Oxford EDS and operating at an accelerated voltage of 200 kV.

Preparation of carbon extraction replica specimens began by preparing specimens using standard metallographic procedures as if LOM were to be performed. Specimens were etched for 20 seconds in 2% nital and ultrasonically cleaned using a methanol bath. After drying, all areas of the specimen were masked except the area of interest; for example, (see Figure 5.11). Following this, specimens were placed into a Denton sputter coater, and a carbon film approximately 10-20 nm thick was evaporated onto the specimen surface. After evaporation, the masking was removed and the carbon on the specimen surface was scribed into ~ 2 mm squares. Then, the specimen was immersed in a solution of 10% nital (methanol-based) and after a period of 2-6 minutes, the carbon film began to separate from the surface. The specimen was then removed from the etchant and immersed in a solution of 95% distilled water and 5% methanol whereupon the replicas floated to the surface of the solution. Finally, the replicas were lifted from the solution and collected on copper support grids. For every sample, fresh solutions were used in each step to prevent contamination.

Preparation of thin foils began by sectioning selected specimens using a low-speed cutting wheel and thinning down to ~ 0.06-0.08 mm thick foils. Discs of 3 mm in diameter were then mechanically punched out from the foil and electropolished to perforation in a Fischione twin jet electropolishing unit. The electrolyte used for polishing consisted of 5% perchloric acid and 95% acetic acid which was maintained at room temperature. A polishing voltage of 35-40 volts generally produced satisfactory results.

5.3.4 Vickers Hardness

Vickers hardness testing was conducted with a load of 300 gf and a dwell time of 10 seconds, using a LECO LM310AT hardness tester. This testing was confined to the air-cooled specimens. The mean Vickers hardness values were determined by averaging the hardness measurements of 10 random indents.

5.3.5 Nanoindentation Hardness Testing

Since there are several types of non-equilibrium ferrite microstructures, as well as different bainitic morphologies coexisting with MA constituents resulting from ACC process or air cooling, depending on the steel chemistry and thermomechanical histories, an attempt was made in this study to distinguish these microstructures. Initially, after testing, specimens were prepared by standard metallographic procedures. In the polished central region of the specimen, an array of 5 × 5 indentations was carried out using a Hysitron TI900 Triboindenter with a load of 2000 µN and 5 µm distance between each indent. The results of these indents were determined following the Oliver-Pharr method [90]. Following this, the microstructures, as well as the indents were revealed by etching in a 2% nital solution and observed under SEM.

5.4 Quantitative Metallography

The mean austenite grain size was determined using ImageJ software by manually outlining the austenite grain boundaries and calculating the equivalent grain diameter for each grain. From each sample being analyzed, at least 500 grains were measured. The mean austenite grain size and the statistical standard deviation were calculated for each sample.

For grain coarsening studies, the abnormal grain size was estimated using the criterion outlined by Fernández [41]. In this criterion, the abnormal grain size is based on grains having a size larger than the mean normal grain size by twice the standard deviation as expressed in Eq. (5.2, assuming normal distribution:

$$GS_{abnormal} = GS_{normal} + 2\sigma \qquad \textbf{(5.2)}$$

where GS_{normal} is the mean grain size of the distributions and σ is the standard deviation. If (5.2 is not fulfilled, $GS_{abnormal}$ is taken as the highest grain size.

The mean effective grain size obtained from EBSD orientation maps was determined as the mean linear intercept lengths using the minimum boundary misorientation angle of 15 degrees [21, 80].

The effective interfacial area, S_v, of austenite grains was estimated by the following equations [8]:

For elongated grains:

$$S_v = 0.429(N_L)_{\parallel} + 1.571(N_L)_{\perp} \tag{5.3}$$

For equiaxed grains:

$$S_v = 2N_L = \frac{2}{D_\gamma} \tag{5.4}$$

where $(N_L)_{\parallel}$ and $(N_L)_{\perp}$ are, respectively, the intercept numbers per unit length along the parallel and the perpendicular directions of elongated grains. In Eq (5.4), D_γ is the mean austenite grain size.

6.0 As-Received Condition

6.1 Results and Discussion

The as-received slabs provided the starting condition for subsequent studies and treatments. Thus, it is important to characterize its microstructural state.

6.1.1 As-Received Microstructures

Figure 6.1 shows the optical micrographs of the as-received slabs taken from the rolling direction plane (RD). L0 and H0 exhibited polygonal ferrite (PF) and dark etching regions whereby classical bainite aligned with a small amount of degenerate perlite (P') as seen in Figure 6.1 (a) and (b). This classification is in accordance with the *Bainite Research Committee of The Iron and Steel Institute of Japan* terminology [82]. Furthermore, the classical bainite morphology appeared to be a mixture of BII and BIII types according to those proposed by Ohmari *et al.* [91]. The BII is characterized by having sheaves of ferrite laths separated by carbon enriched layers, while BIII is characterized by having sheaves of carbon enriched platelets within the PF matrix. Although there are distinct classifications in literature for low carbon austenite decomposition products, it is rather difficult to discern the exact morphology for each microconstituent. Hence, in this study, BIII and BII types can be collectively and safely classified as granular bainite (GB) but without martensite/retained austenite (MA) microconstituents. Nevertheless, when the carbon is increased from 0.03 wt.% to 0.06 wt.% (H0), the fraction of PF is decreased and the fraction of GB is increased (Figure 6.1 (d)). Moreover, the ferrite grain size is finer in H0 compared to L0. The mean ferrite grain size of L0 was measured to be at 27 µm, while that of H0 was at about 18 µm.

Noticeable differences are apparent between L4 and its base L0. For example, The PF fraction appeared to be significantly decreased, and the faction of QF is increased, see Figure 6.1 (b), though, the PF grain size is much finer in L4 than those observed in L0. This refinement of PF is mainly attributed to the Nb addition to the steel and the controlled rolling applied and was confirmed in previous studies [2, 53]. Additionally, a small amount of MA microconstituents can also be observed. Further increase in Nb content (L8 steel) gives rise to a significant amount of QF and coarse GB with MA as shown in Figure 6.1 (c). The microstructures of GB with MA are similar to those of bainitic ferrite (BF) laths but with no clear boundaries between laths [81].

However, for H4 and H8 steels, the microstructures are different from the previously discussed. Mostly, refined QF and GB (Figure 6.1 (e) and (f)) are often termed in literature as acicular ferrite (AF) when they are transformed from heavily deformed austenite [80, 92, 93]. Bright-field TEM micrographs revealed that H4 steel yielded a refined version of QF and GB compared to that observed in L8 as shown in Figure 6.2. Furthermore, from Figure 6.2 (a), the dark regions in the TEM micrographs appeared to be GB, whereas that in Figure 6.2 (b) appeared to be MA in character.

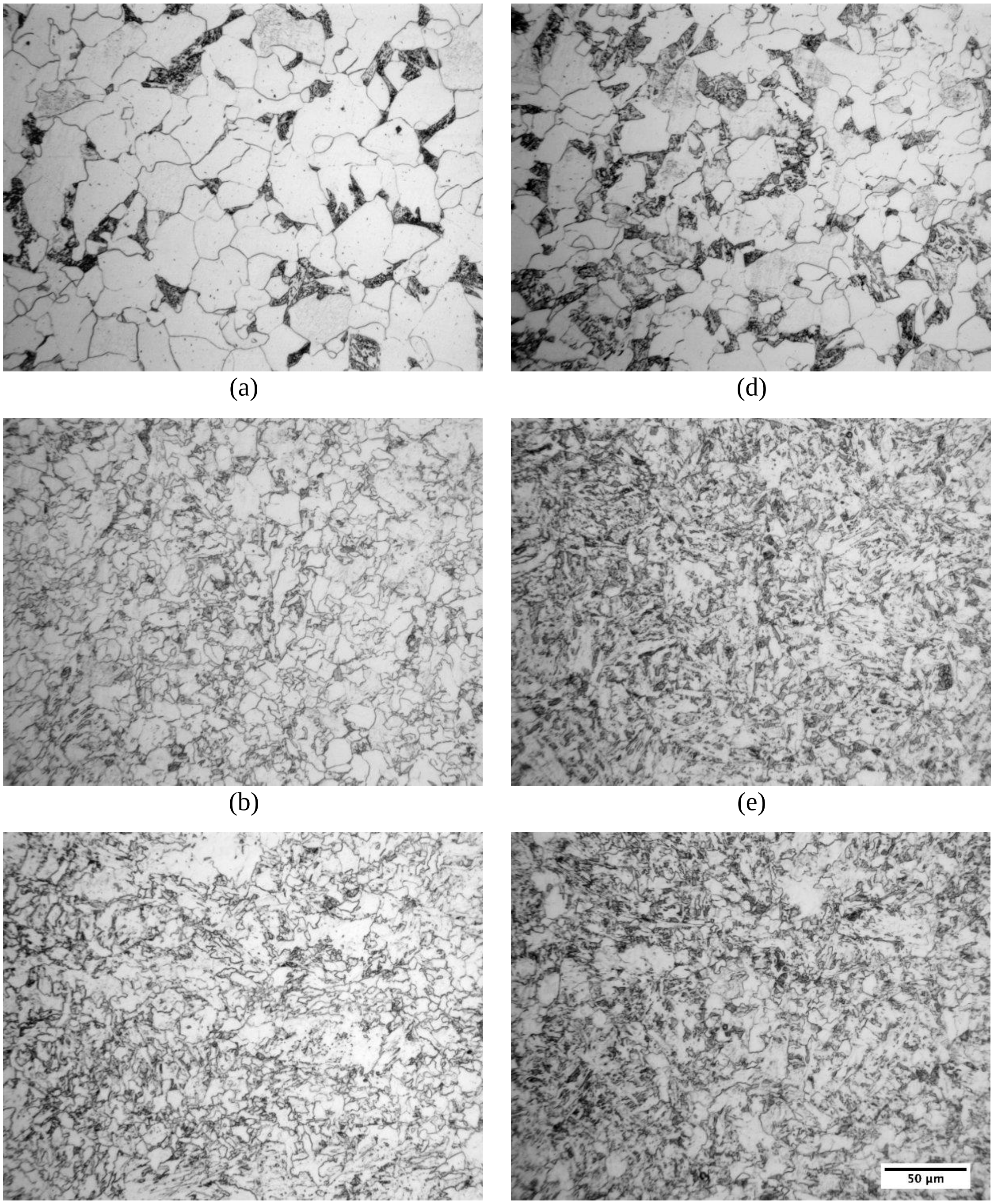

(a) (d)

(b) (e)

(c) (f)

Figure 6.1 Optical micrographs showing the microstructures of the slab materials: (a) L0, (b) L4, (c) L8, (d) H0, (e) H4, and (f) H8.

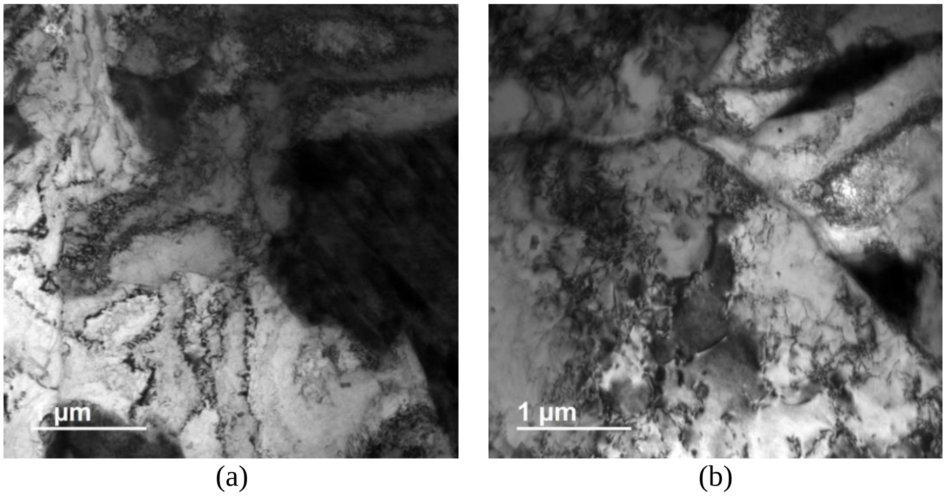

(a) (b)

Figure 6.2 Bright-field TEM micrographs of as-received steels, note the stepped boundary of QF in (a) H4; and uniform GB in (b) L8.

Although precipitates were not extensively studied in the as-received steels, a few have been examined under TEM investigation. Unfortunately, fine precipitates below 10 nm were rendered to be difficult to detect in the thin foils of the as-received steels, especially in the Nb-bearing steels. This was due in part to the complex microstructures obtained after air cooling. These fine precipitates are responsible for refining the microstructures during austenite conditions or after transformation [4]. However, few precipitates having sizes between (30- 80 nm) were examined under TEM and can be assumed to be Ti-rich NbC precipitates. For example, Figure 6.3 (a) shows a precipitate and its corresponding EDS spectrum in the as-received H4 steel. The intensity of the K_α peak of Ti at 4.52 keV is much higher than the intensity of the K_α peak of Nb at 16.6 keV, other elements are presumably coming from the matrix. This may suggest that NbC precipitates grow on a preexisting undissolved TiN particle [94, 95] or are formed either in the liquid state or during solidification [96]. These precipitates were occasionally observed in all Nb-bearing steels in this research program.

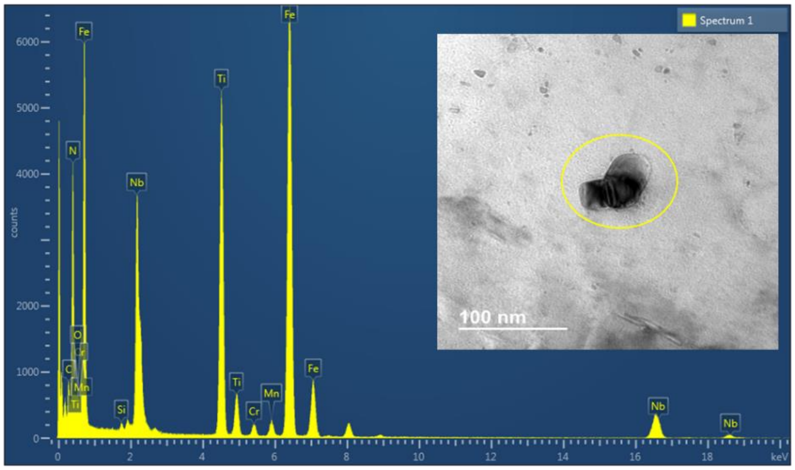

Figure 6.3 TEM micrograph of a complex carbonitride precipitate in the as-received H4 steel.

6.1.2 Vickers Hardness Measurements

Figure 6.4 displays the microhardness of the as-received steels taken from the planes in three orthogonal directions (*i.e.*, rolling direction (RD), transverse direction (TD), and normal direction (ND)). From Figure 6.4, in general, Nb addition to the base steels increases the hardness values for both L and H series steels. Taking RD as an example, the hardness values of L0, L4, and L8 are 168 VHN, 214 VHN, and 235 VHN, respectively. Compared to L0 steel, this increase in the hardness values can be attributed to the finer PF and QF exhibited in L4 steel and QF and GB observed in L8 steel. However, when the hardness values of L4 and L8 steels are compared in TD, L8 steel has a comparable value to L4 steel. The variability in L8 steel might be traced back to the steel response to austenite conditioning (in this case CCR processing), especially $T_{5\%}$ temperature, though precipitation hardening can play role in this variability. Since coarse GB microstructures can originate from recrystallized austenite grains while fine AF (*i.e.*, fine mixtures of QF and GB) can nucleate from unrecrystallized austenite grains [80].

Similarly, an increase in the hardness values is observed from H0 steel to H4 or H8 steel. This is due to the cessation of PF occurrence in H4 and H8, instead, AF-dominated microstructures are observed in these steels. Furthermore, the hardness values in the three directions for each H series steel appeared to be comparable, since the errors bars are overlapping, signifying less variability. However, a slight rise in the hardness value can be seen from H4 to H8 in the TD plane.

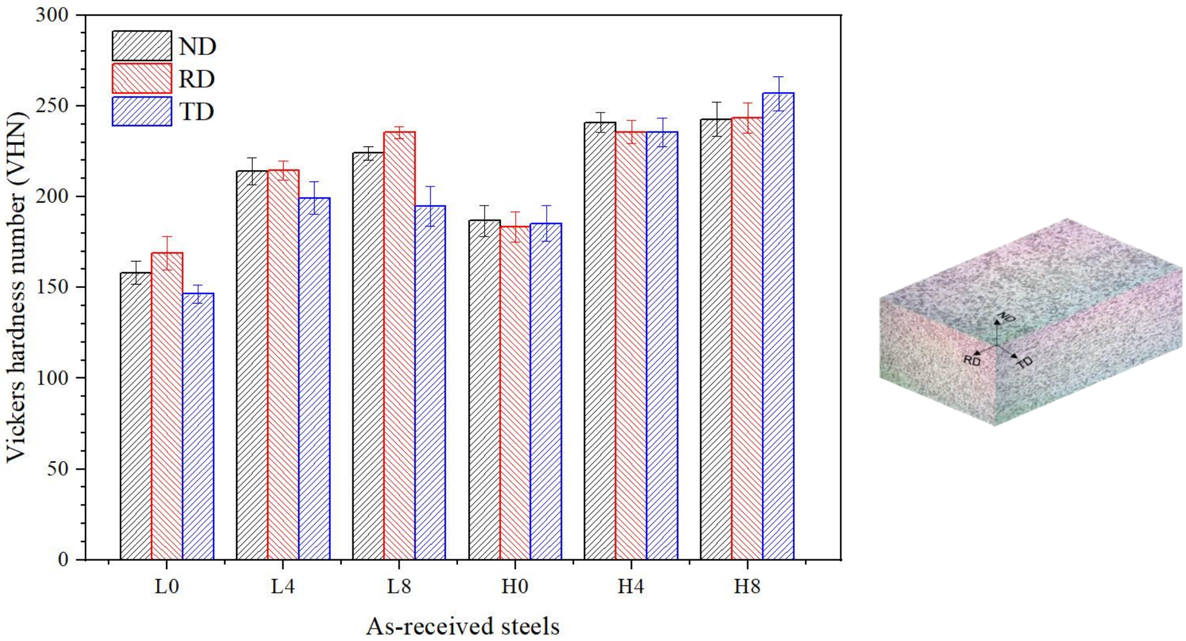

Figure 6.4 The Vickers hardness (VHN 300 gf) of the as-received steels taken from three planes; error bars represent the standard deviation.

6.2 Summary

The results presented above show the significance of Nb content as well as C content in altering the final microstructures. In the steels investigated here, the thermomechanical histories and the base compositions were essentially identical, thus, any differences in the microstructures presented above are attributed to the Nb and C contents. It was shown from a previous study that Nb, among other microalloying elements, significantly raises the $T_{5\%}$ temperature [11]. This gives different austenite conditioning responses in each steel.

Although Nb has the potential to combine with Ti to form a complex Ti-rich NbC precipitate, the Ti and N contents in all investigated steels in this study were close to the stoichiometric ratio. Any change in the precipitates type can be directly attributed to Nb and C content Furthermore, the final microstructures, in the as-received steels, are primarily expected to be dependent on the austenite microstructure prior to transformation. For example, Recrystallized and unrecrystallized austenite grains have different potential nucleation sites for non-equilibrium ferrite microstructures. Hence, it is believed that different microstructure products (*e.g.*, PF, Gb, QF, and P') are dependent on primarily whether they are nucleating from pancaked, recrystallized, or partially recrystallized austinite.

From the present investigations on the effect of Nb additions in the as-received steels in this study, the findings can be summarized as follows:

1. With no Nb addition to the steel, base steels L0 and H0, the microstructure consists of PF, classical bainite, and P'.
2. L4 and L8 steels yielded refined PF grains compared to the base steel (L0); QF and GB, however coarse GB can be seen in L8.

3. The microstructures of H4 and H8 steels mostly exhibit AF-dominated microstructures.
4. Coarse precipitates are mainly observed to be Ti-enriched NbC.
5. The bulk hardness values rise rapidly from L0 to L4 but gradually from L4 to L8, nevertheless, lower values were observed in the transverse direction in L8 steel. Similarly, this applies to H series steels with slight similarities between H4 and H8 in the transverse directions.
6. Different microstructures exhibited in the as-received steels can be linked to the state of austenite prior to transformation to room temperature.

7.0 Grain Coarsening Behavior

Isothermal reheating studies were conducted on all steels. The microstructures were obtained from soaking and holding samples (as-received condition) at temperatures spanning the austenite field for 60 minutes, after which they were quenched in water. The results and discussion of the reheating behavior are presented in the following sections.

7.1 Results

The prior austenite grain structures as a function of reheating temperature for steels L0-H8 are represented in Figure 7.1 through Figure 7.3 and Figure 7.5 through Figure 7.7. With increasing temperature, the general trend in these micrographs can be divided into three regimes:

i. A fine unimodal distribution of the reheated grains exhibiting normal grain coarsening.
ii. A bimodal distribution of fine and abnormally coarsened grains.
iii. A revert to normal grain coarsening mode exhibiting a unimodal distribution.

In L-steels (L0, L4, and L8), with increasing temperature from 900 °C to 1000 °C, the grain coarsening appeared to be continuous, resulting in a gradual increase in the size of relatively uniform equiaxed grains (*i.e.*, normal grain coarsening). Coarsening is suppressed at these lower temperatures, presumably because of the pinning of grain boundaries by alloy carbides or carbonitrides [38]. At higher temperatures, however, a breakaway from this trend is observed in L0 steel at 1050 °C, while in L4 and L8 steels are observed to be at 1100 °C and 1150 °C (Figure

7.2 and Figure 7.3), respectively. This breakaway point, which is commonly observed in microalloyed steels [29, 38, 39, 97, 98], is marked by a discontinuous growth of isolated grains at the expense of fine surrounding grains and at which, grain coarsening temperature is defined (T_{GC}). Depending on the composition of the steel being investigated, the temperature at which discontinuous growth occurs varies with the concentration and distribution of the precipitate particles. In this grain coarsening study, no direct observations of the initial particle size and distribution were made. Nevertheless, L0 steel reverts to normal grain coarsening mode at temperatures above 1100 °C while abnormal grain coarsening mode persists in L4 and L8 steels at temperatures above 1150 °C.

A further increase in the reheating temperature led to extremely large grain size in L0, presumably because the pinning particles are unable to pin the migrating boundaries. The pinning particles in this steel were assumed to be TiN precipitates since no Nb was added to this steel. The rationale behind this assumption was that when Ti is added to the steel, and upon cooling from the melt, a dispersion of very fine insoluble TiN particles forms [38]. However, it is also assumed that these TiN particles in L0 are coarse and upon reheating at high temperatures, they are ineffective in pinning grain boundaries. It is interesting to note that L4 steel exhibits a much finer grain size at high temperatures compared to L8 steel, even though it contains the double amount of Nb in terms of the initial composition. This suggests that with increasing Nb level from L4 to L8, the grain coarsening is rapid, especially at high reheating temperatures. Noticeably very coarse grains in L4 steel were observed not until a reheating temperature of 1300 °C was imparted.

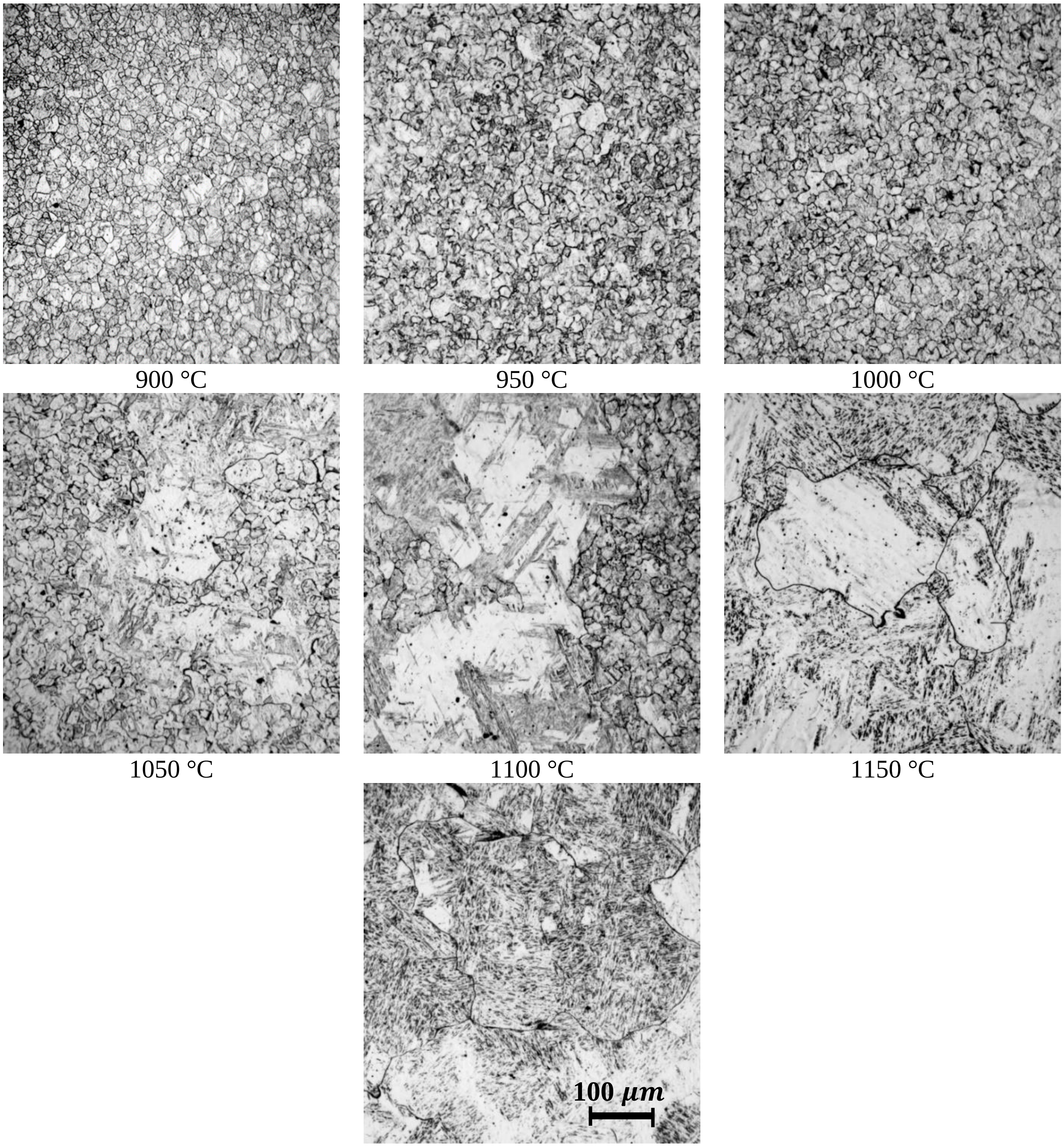

900 °C 950 °C 1000 °C

1050 °C 1100 °C 1150 °C

1200 °C

Figure 7.1 Prior austenite grains for L0 steel after isothermally reheating to the indicated temperatures and water quenching.

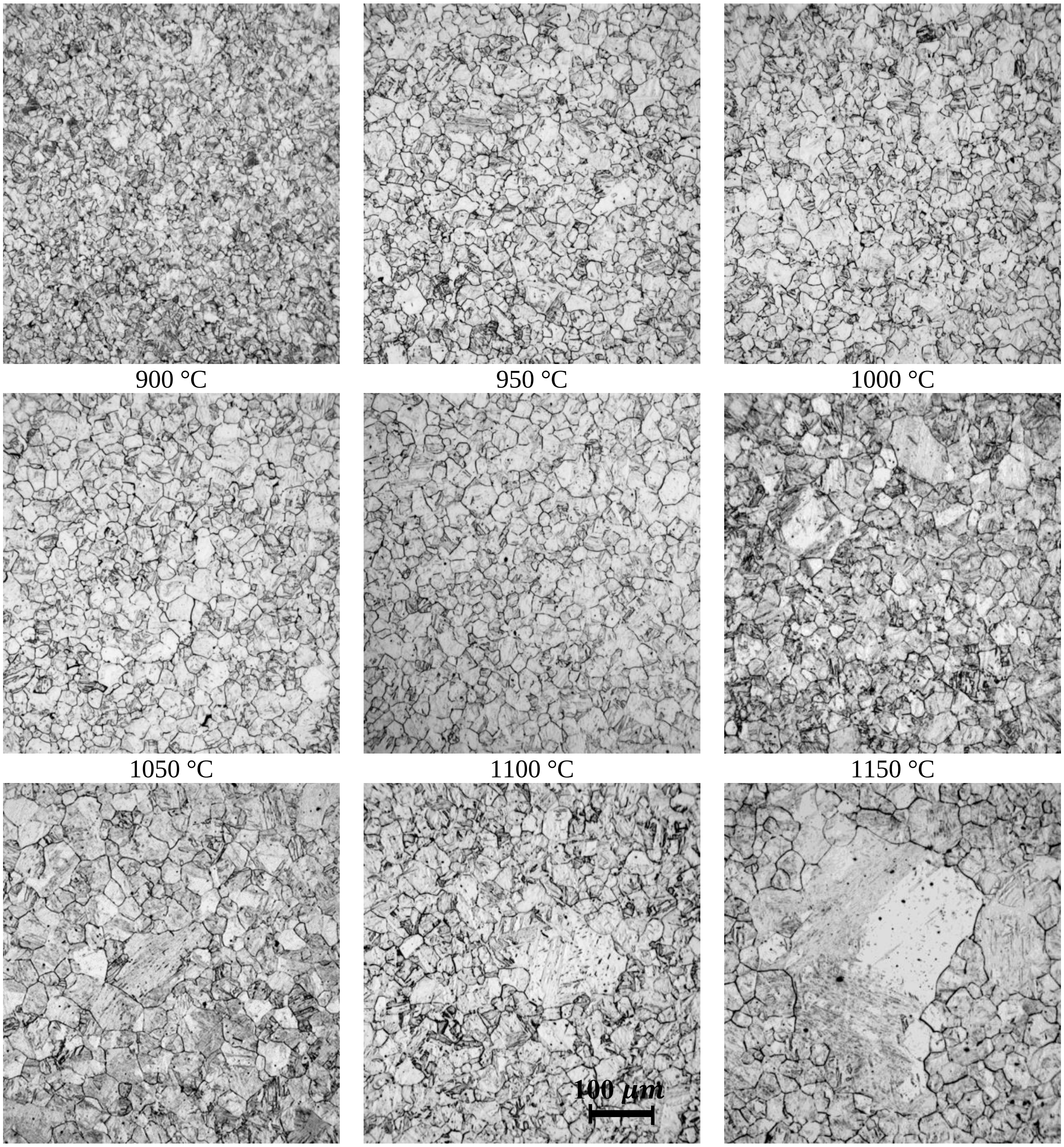

900 °C 950 °C 1000 °C

1050 °C 1100 °C 1150 °C

1200 °C 1250 °C 1300 °C

Figure 7.2 Prior austenite grains for L4 steel after isothermally reheating to the indicated temperatures and water quenching.

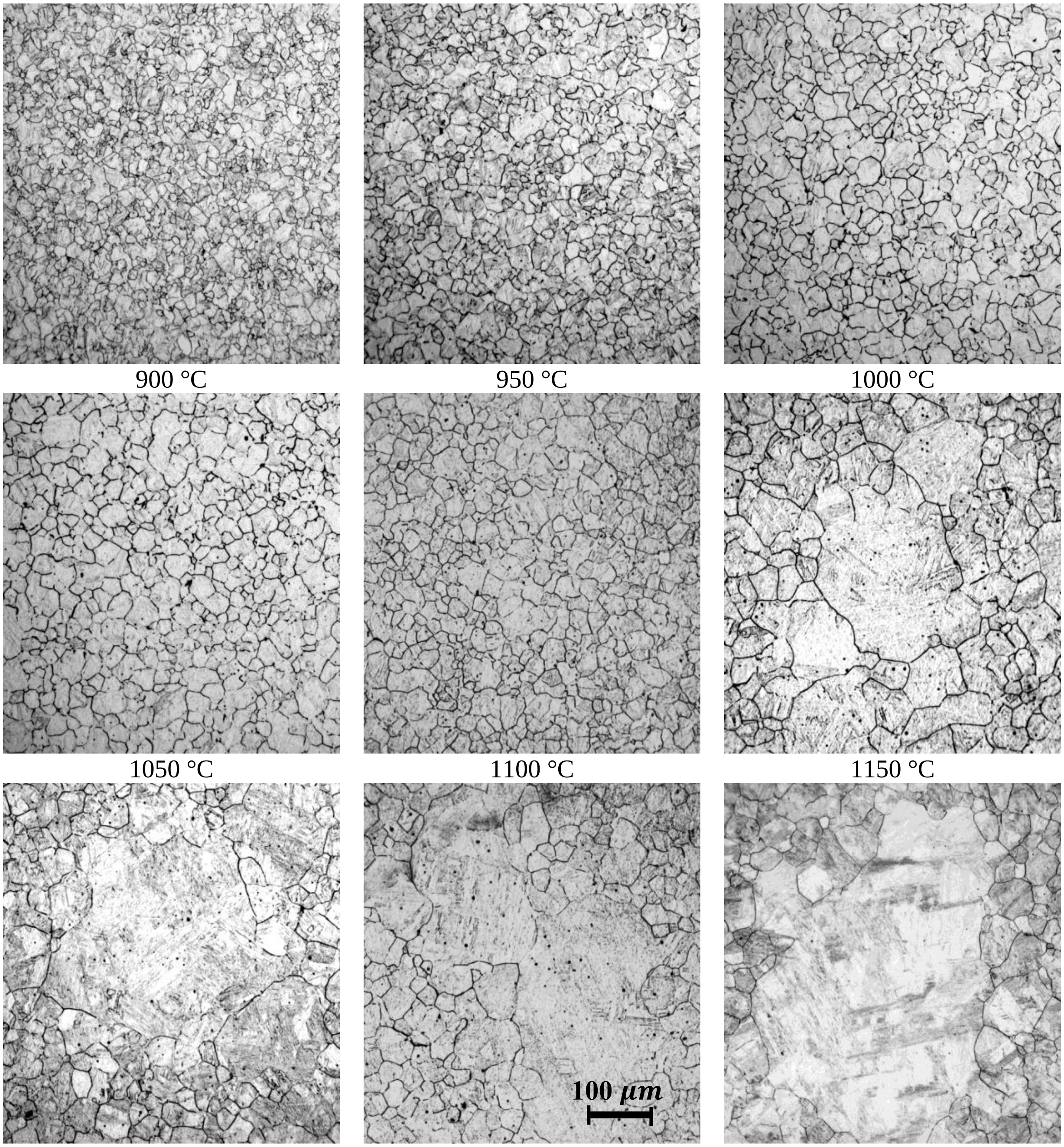

900 °C 950 °C 1000 °C

1050 °C 1100 °C 1150 °C

1200 °C 1250 °C 1300 °C

Figure 7.3 Prior austenite grains for L8 steel after isothermally reheating to the indicated temperatures and water quenching.

To show the overall grain coarsening behavior, the average grain sizes of L-series steels are quantitively depicted in Figure 7.4 and whereby the abnormal grain size for each steel was estimated using Eq. (5.2); listed previously in section 5.4. Error bars represent 95 pct. confidence interval around the average grain size.

The data presented in Figure 7.4 reveal that T_{GC} for L0 is about ~ 1050 °C, which is 100 °C lower than those observed in L4 and L8 steels. Concerning T_{GC} for L4 and L8 steels, it should be pointed out that even with the fact that they exhibit similar T_{GC}, L8 steel yielded a relatively coarser grain size at 1150 °C (upper curve of L8 in Figure 7.4). For example, at T_{GC}, the abnormal grain size for L8 steel was about 180 µm, while for L4 steel it was about 88 µm. Very few coarse grains were observed in L8 steel at 1100 °C and were not statistically significant to be considered as abnormal grain size.

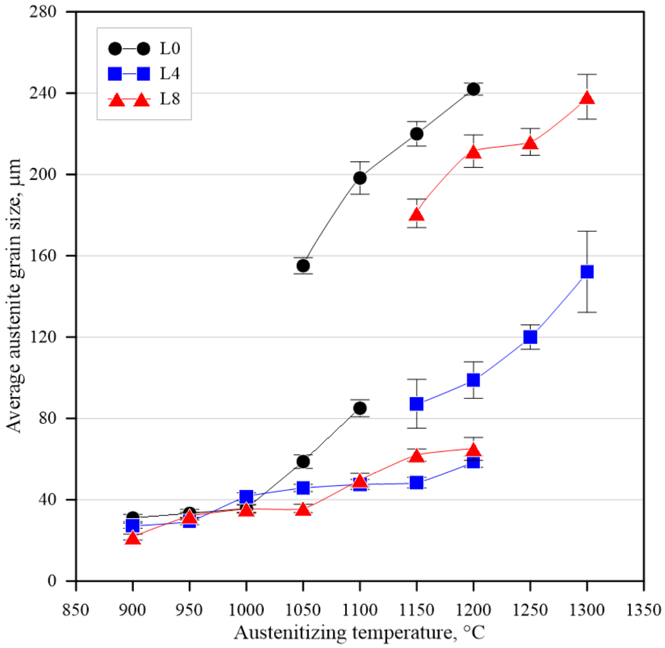

Figure 7.4 Average grain size versus reheating temperature for L0, L4, and L8 steels.

In all H-series steels (H0, H4, and H8), fine and stable austenite grain structures were observed at the lower reheating temperatures of 900 °C and 950 °C (Figures 7.5, 7.6 and 7.7). At 1050 °C, the beginning of abnormal grain coarsening is noted in H4 steel and more pronounced in H8 steel. However, in H0 steel, the abnormal grain coarsening was observed at a lower temperature of 1000 °C. The onset of this coarsening is indicative of dissolution and/or coarsening of pinning particles, resulting in a reduction in Zener pinning pressure. An increase in the reheating temperature above 1050 °C resulted in a very coarse grain structure in H0 and a more rapid coarsening in H4 and H8 steels. Normal grain coarsening (*i.e.,* regime (iii)) for H4 and H8 steel was observed at the highest reheating temperature of the current study (at 1300 °C in Figures 7.6 and 7.7). The austenite grains in H-series steels seem to grow in a similar tendency as those in L-series steels but at a relatively rapid rate.

Figure 7.8 shows the average austenite grain size for H0, H4, and H8 steels along with the error bars representing 95 pct. Confidence interval about the average austenite grain size. Upper curves are for the abnormal grain size observed in each specimen. The T_{GC} for H0 was estimated to be at 1000 °C while the T_{GC} for H4 and H8 was at 1050 °C. It is noteworthy that H-series steels exhibit lower T_{GC} compared to L-series steels. This was not expected in these steels since higher additions of C and Nb imply more stable NbC or NbCN precipitates at higher reheating temperatures [15].

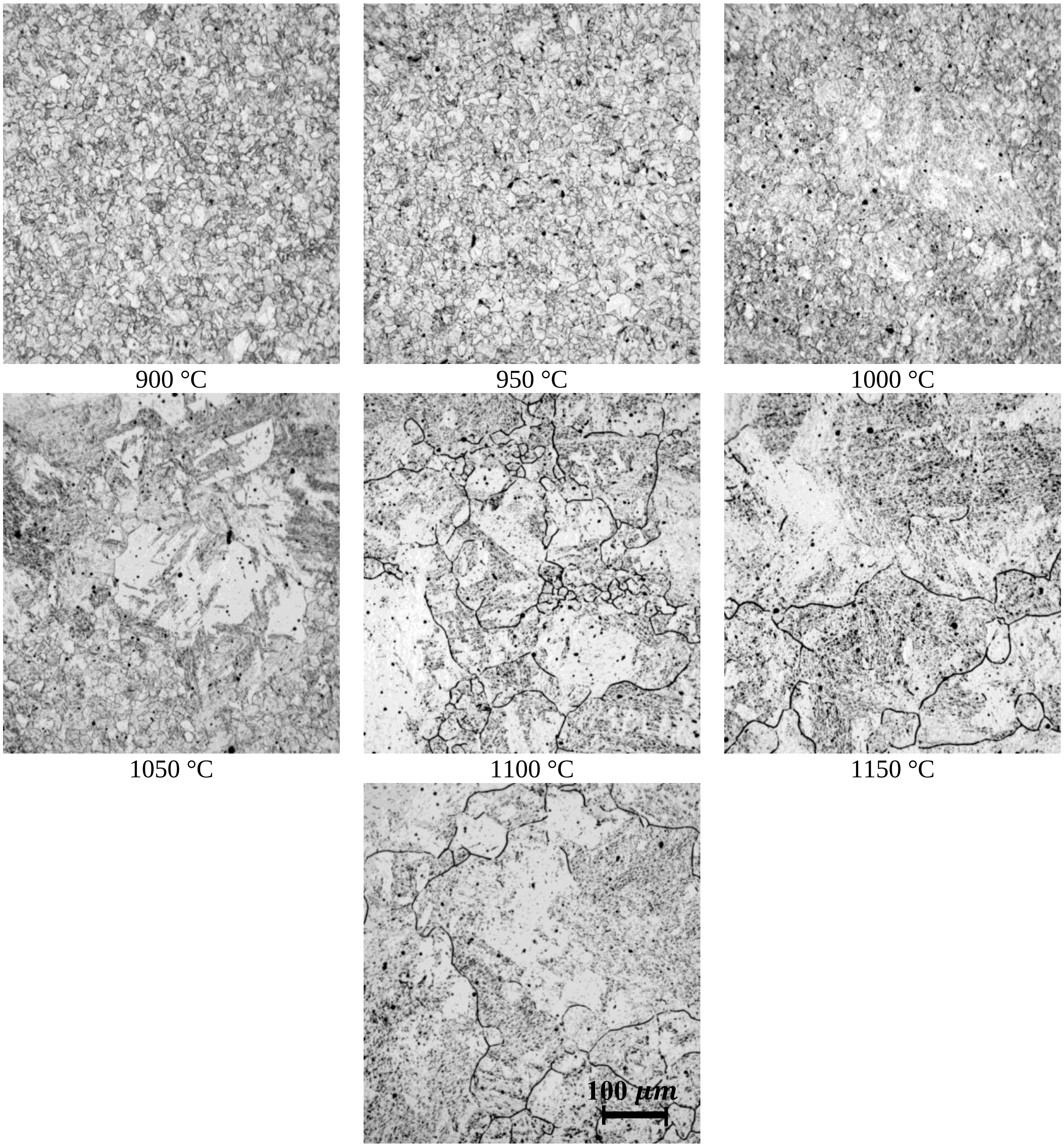

900 °C 950 °C 1000 °C

1050 °C 1100 °C 1150 °C

1200 °C

Figure 7.5 Prior austenite grains for H0 steel after isothermally reheating to the indicated temperatures and water quenching.

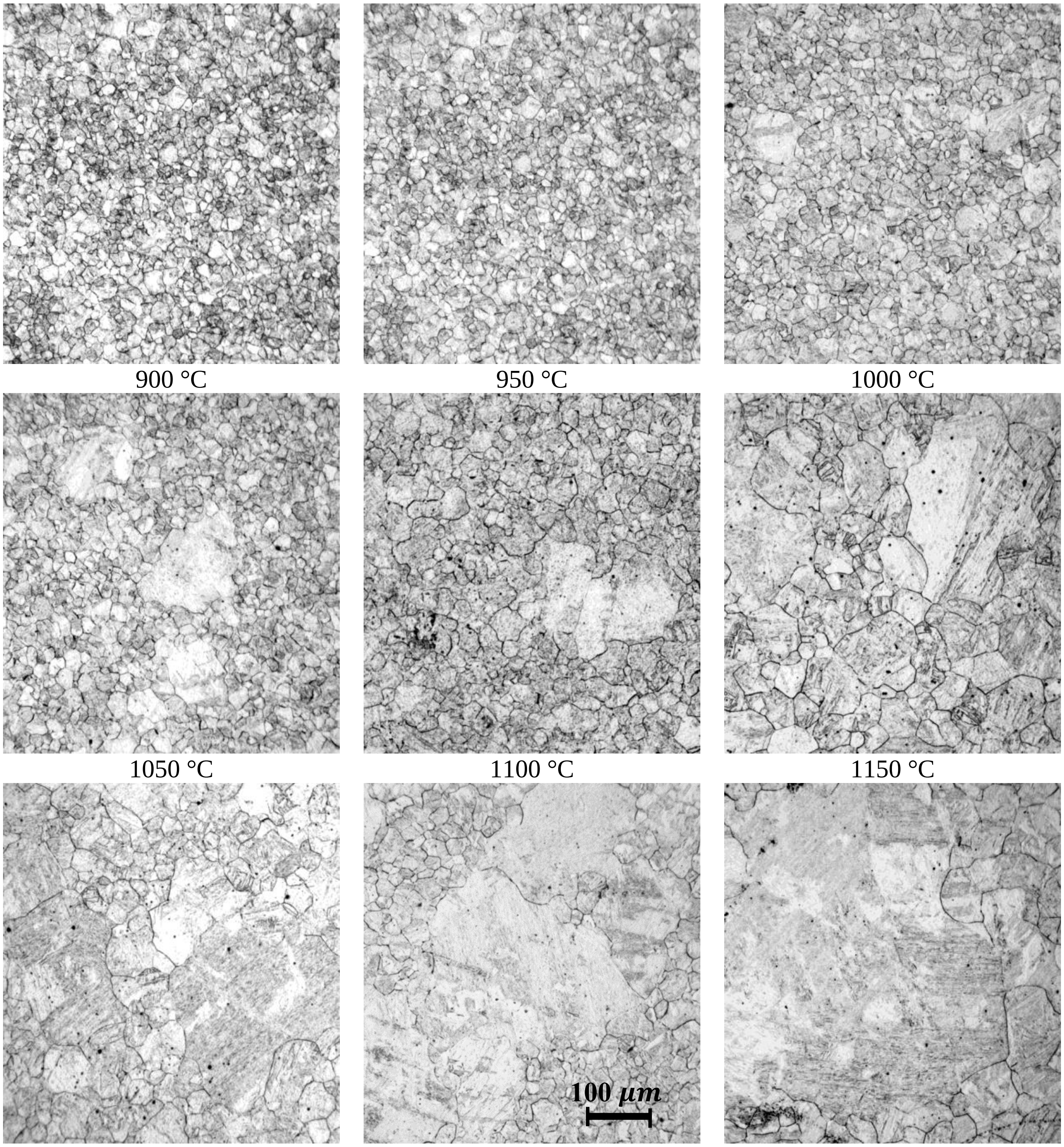

900 °C 950 °C 1000 °C

1050 °C 1100 °C 1150 °C

1200 °C 1250 °C 1300 °C

Figure 7.6 Prior austenite grains for H4 steel after isothermally reheating to the indicated temperatures and water quenching.

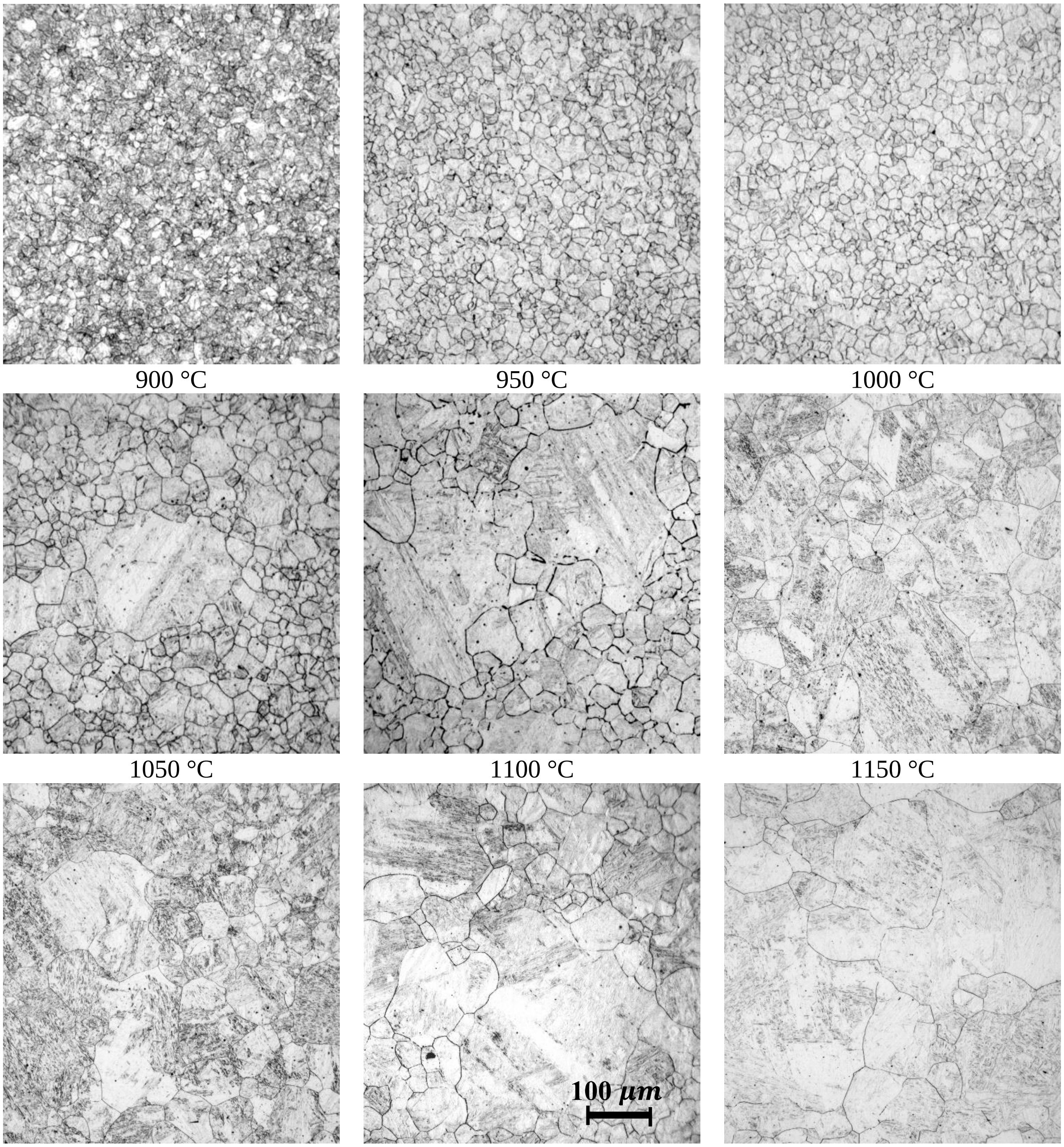

900 °C 950 °C 1000 °C

1050 °C 1100 °C 1150 °C

1200 °C 1250 °C 1300 °C

Figure 7.7 Prior austenite grains for H8 steel after isothermally reheating to the indicated temperatures and water quenching.

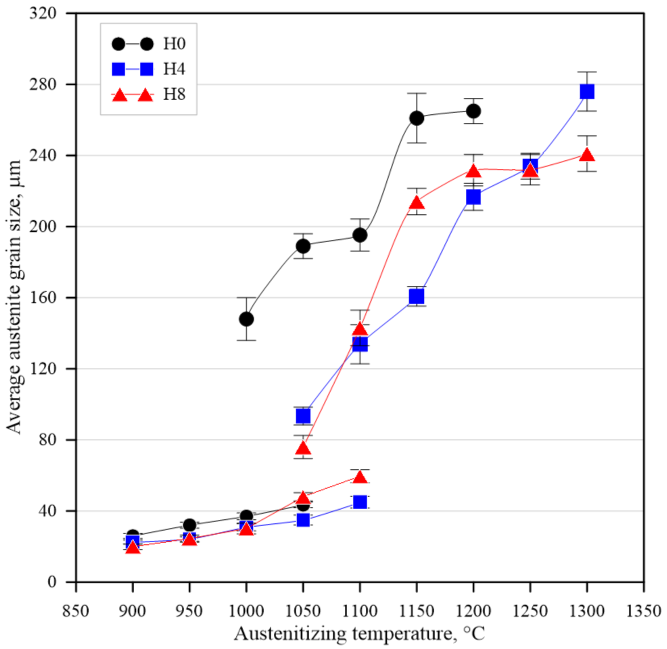

Figure 7.8 Average grain size versus reheating temperature for H0, H4, and H8 steels.

7.2 Discussion

The results presented above show the significance of microalloying in inhibiting austenite grain coarsening in steels subjected to higher austenitizing temperatures. The austenite grain coarsening behavior in this study is consistent with previous studies on the effects of second phase particles on normal and abnormal grain coarsening [29, 38, 39, 97]. Abnormal grain coarsening happens when the newly formed austenite grains are kept fine by the presence of second phase particles such as NbC, AlN, and TiN. Gladman [74] carefully considered the energy release due to grain coarsening as well as the energy of the pinning particles on grain boundaries. The critical condition occurs when the energy release rate per unit displacement of grain boundary during grain coarsening is equal in magnitude to the energy release rate due to second phase particles. This critical condition is dictated by the parameter r_c in Eq. (2.14), which gives the maximum particle size that would effectively counteract the driving force for austenite grain coarsening. From Eq. (2.14), it is apparent that the volume fraction of precipitate will influence r_c during austenite reheating. Accordingly, the volume fraction of precipitate will be sensitive to temperature as defined by the solubility relation of precipitating particles. Hence, as a result of precipitate coarsening and/or dissolution during reheating, an increase in temperature leads to the coarsening of some grains at the expense of others, while some remaining grains continue to be pinned.

Accordingly, Nb may present either as a solute [99] or as NbC precipitate [29, 100]. The former exhibits a solute drag to the moving grain boundary while the latter pins the boundary which is more pronounced in microalloyed steels. An attempt was made to compare the dissolution temperatures of NbC precipitate in all Nb-bearing steels being investigated in this study (L4, L8, H4, and H8) using both Palmiere's solubility relation [29] (see Eq. (2.6)) and Thermo-Calc simulation software. Table 7.1 lists the dissolution temperatures obtained by Palmiere's solubility relation and obtained by Thermo-Calc software (*i.e.,* austenite phase: FCC_A1). From this table, the dissolution temperatures obtained by Palmiere's equation were higher than those obtained by Thermo-Calc. For example, the solubility of NbC in L4 steel is 1084 °C using Palmiere's equation, which is about 21 °C higher than that obtained Thermo-Calc software. The difference increases in the case of H8 steel, which is about 81 °C. One explanation of these differences in dissolution temperatures is that Palmiere's equation was established based on steels without Ti addition. These differences in dissolution temperatures using different calculation methods are in agreement with a previous study [101]. Similar dissolution temperatures were obtained in H4 and L8 steels, which was expected, since C and Nb in these steels were added with a constant supersaturation (*i.e.,* constant solubility product). Figure 7.9 (a) and (b) show a comparison between L4 steel and H8 steel, respectively, which indicate that Nb and C in H8 steel exhibit higher dissolution temperature compared to L4 steel. Furthermore, Ti and N in these figures do not dissolve appreciably at low temperatures.

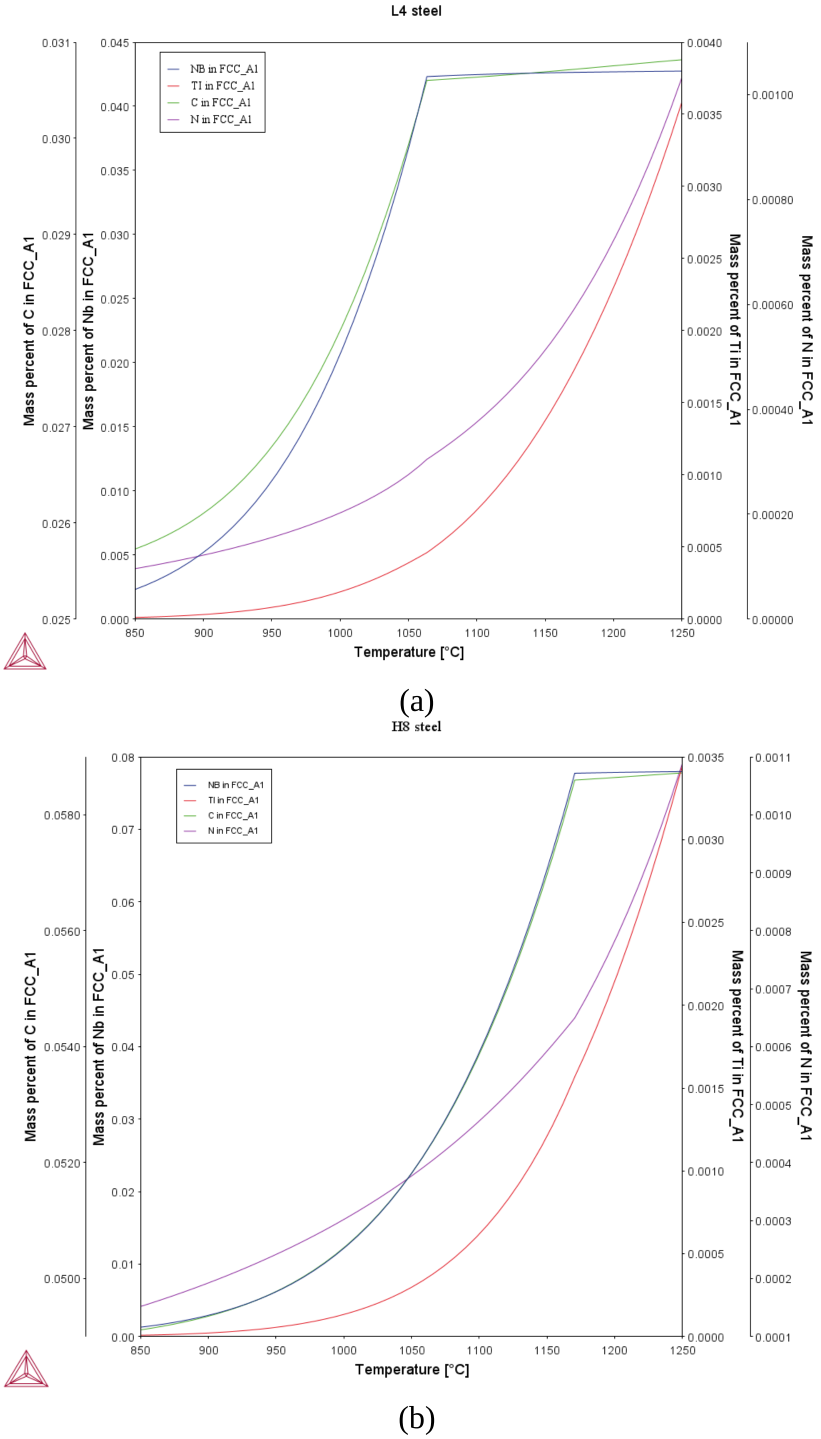

(a)

(b)

Figure 7.9 Calculated amount of Nb, C, Ti and N dissolved in austenite as a function of temperature for: (a) L4 steel and (b) H8 steel, calculated using Thermo-Calc software with TCFE11 database.

Table 7.1 Dissolution temperature of NbC precipitate.

Steel	Dissolution temperature, °C	
	Palmiere's eq., Ref. [29]	Thermo-Calc software
L4	1084	1063
L8	1160	1119
H4	1167	1114
H8	1251	1170

It was shown from earlier research that T_{GC} is lower than the dissolution temperature of NbC precipitate by approximately 40 °C to 125 °C [29, 38]. In this study, for example, T_{GC} for L8 and H4 were estimated to be at 1150 °C and 1050 °C, respectively, even though they show approximately similar dissolution temperatures. This may suggest that the solute drag effect is dissimilar between these two steels. Nevertheless, with increasing reheating temperature, the solute drag exhibited by Nb is less effective [102]. Thus, it can be assumed that the difference in austenite grain coarsening behavior between all the experimental steels is attributed to primarily the effectiveness of TiN or NbC particles in suppressing grain coarsening, especially at high temperatures, which include critical size and distribution. Furthermore, it is believed that the inhomogeneous distribution of microalloy precipitates can lead to insufficient and differential pinning force [39]. This inhomogeneous distribution of microalloy precipitates in as-cast slabs can be traced back to the interdendritic segregation during casting [98, 103]. However, verification of particles size and distribution in the current study was not established.

Since L4 steel exhibits the highest resistance to grain coarsening, which was not anticipated, the time for reheating was prolonged to 120 minutes at 1200 °C and the microstructures were compared with those obtained from H8 steel at the same reheating conditions. The reasoning for this was to observe any discrimination between these two steels in terms of austenite grain coarsening. Additionally, the reheating temperature of 1200 °C was selected to ensure complete dissolution of the highest stable NbC precipitate estimated by Thermo-Calc software; in this case, it is NbC precipitates in H8 steel. Figure 7.10 (a) and Figure 7.10 (b) show the austenite grain structure developed from this treatment condition for L4 and H8 steels, respectively. It is clear that the austenite grain size in L4 steel is finer than those observed in H8 steel. Furthermore, extensive abnormal grain coarsening is evident in H8 steel. It appears that there exists an optimal amount of TiN precipitates in the steel to fully retard grain coarsening at high temperatures. Also, the diffusivity of Nb or Ti can be an important factor contributing to the inhibition of grain coarsening through the diffusion distance. The diffusion distance $(Dt)^{1/2}$, in which D is the diffusion coefficient and t is the time, is determined mainly by the diffusivity of Nb and Ti and not by C or N [5]. Hence, it is reasonable to relate the differences in grain coarsening behavior in L4 and H8 steels to the rate of dissolution/coarsening of NbC and TiN particles.

One possible explanation of the differences in the grain coarsening behavior between L4 and H8 steels can be related to the mechanism of particle stimulated nucleation (PSN) [104, 105]. On studying the austenite of a low alloy steel, Santella [104] has shown that the undissolved NbCN particles produced significantly finer recrystallized austenite grain sizes and concluded that these undissolved particles enhanced the nucleation of statically recrystallized grains. Similarly, on studying the ferrite of heavy steel sections, Al-Hajeri *et al.* [105] noted that TiO and MnS particles enhanced the nucleation of intragranular ferrite and that the efficiency of the nucleation is associated with the size and type of particles. Hence, it is also reasonable to assume that the undissolved TiN or complex particles contributed to nucleating austenite grains and the differences in grain sizes between L4 and H8 could be related to PSN mechanism.

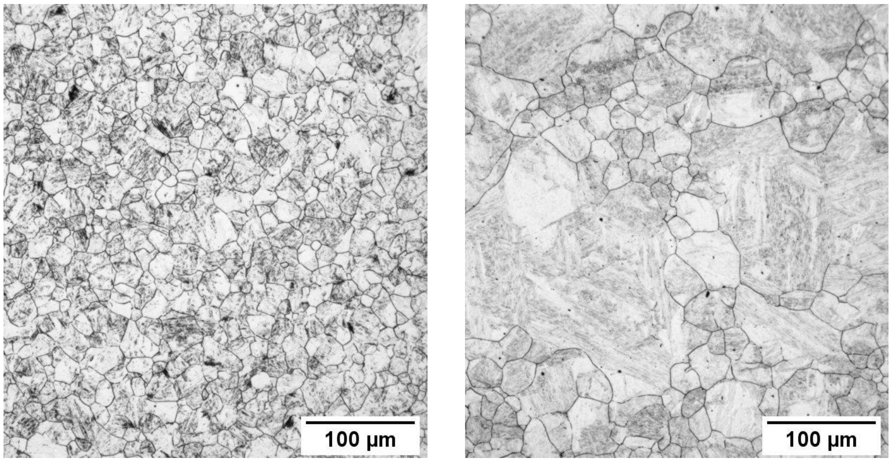

(a) (b)

Figure 7.10 Optical micrographs showing the austenite grain structure of (a) L4 steel, and (b) H8 steel; austenitized at 1200 °C for 120 minutes.

7.3 Summary

The findings presented in this chapter can be condensed as follows:

1. For austenitizing temperatures of 900, 950, and 1000 °C, L-series steels exhibit uniform austenite grain size.
2. Abnormal grain coarsening occurs in the austenite of L0 steel at 1050 °C, while it occurs in the austenite of L4 and L8 steels at 1150 °C and persists to the highest austenitizing treatment of 1300 °C
3. Reversion to normal grain coarsening in the austenite of L0 steel was at 1150 °C.
4. Among all L-series steels, L4 steel exhibits the lowest grain size at all temperatures. Apparently, this is due in part to the effectiveness of TiN and NbC precipitates in suppressing grain coarsening, especially at high austenitizing temperatures.

5. For austenitizing temperatures of 900 and 950 °C, H-series steels exhibit fine uniform austenite grain size.
6. Unlike L0 steel, H0 steel shows abnormal grain coarsening at 1000 °C while H4 and H8 steels show abnormal grain coarsening at 1050 °C and it persists up to 1250 °C.
7. It appears that the nature of NbC and TiN particles is not identical in all steels.
8. The dissolution temperatures obtained by Palmiere's solubility equation were comparable but consistently higher than those obtained by Thermo-Calc. For example, the solubility of NbC in L4 steel is 1084 °C using Palmiere's solubility equation, which is about 21 °C higher than that obtained by Thermo-Calc software. The difference increases in the case of H8 steel, which is about 81 °C.

8.0 Preliminary Hot Deformation Studies[ii]

The purpose of this study was to determine, in general, the extent of recrystallization of the austenite in the experimental steels (H4, H8, and L8 steels). The hot compression studies were employed in the temperature range where rough rolling would be expected (*i.e.*, 1150-1050 °C). The hot compression tests were conducted using an MTS testing unit. The findings from this chapter gave insights for subsequent studies in this research program.

8.1 Results and Discussion

The first series of samples were subjected to hot compression of either two passes or three passes in the temperature range between 1150 and 1050 °C, where each pass was a 15% reduction in height (see Figure 5.6). Figure 8.1 (a)—(c) show H4, H8, and L8 samples whereupon they were subjected to two-pass reduction sequentially at 1150 °C and 1100 °C. Complete recrystallization is observed in all three samples under these deformation parameters. However, more fine grains appear to be nucleated at the triple point of the austenite grains in H8 and L8 samples. It is expected from the solubility product that the fraction of NbC or NbCN precipitated in H8 steel after deformation is higher than that in H4 or L8 steels [16, 29]. Accordingly, variation in grain size among the experimental steels would be expected since strain-induced precipitates of NbC are not identical.

[ii] This chapter is part of Ref. [87]ibid.

For the three pass reduction experiments, it can be seen from Figure 8.1 (d)—(f), that the average austenite grain sizes are reduced, compared to the two-pass reduction experiments, and the maximum reduction in grain size is observed in H8 samples. However, coarse and fine grains are evident in the H8 sample, indicating some degree of nonuniformity in the recrystallization of austenite and it appears to be much less in the H4 sample.

It suggested therefore that deformation at 1050 °C may be close to the $T_{95\%}$ temperature of the steel. This is also in general accord with the L8 sample. One possibility of this nonuniform austenite grain size is that grain coarsening may occur during interpass time due to insufficient pinning of precipitates. Another possibility may be that the 15 % reduction per pass did not induce complete recrystallization of austenite in H8 or L8 steels [8]. Nevertheless, conformity of these hypotheses was not established in this study. Figure 8.2 summarizes the average austenite grain size of H4, H8, and L8 steels after reheating and deformation at each respective deformation temperature.

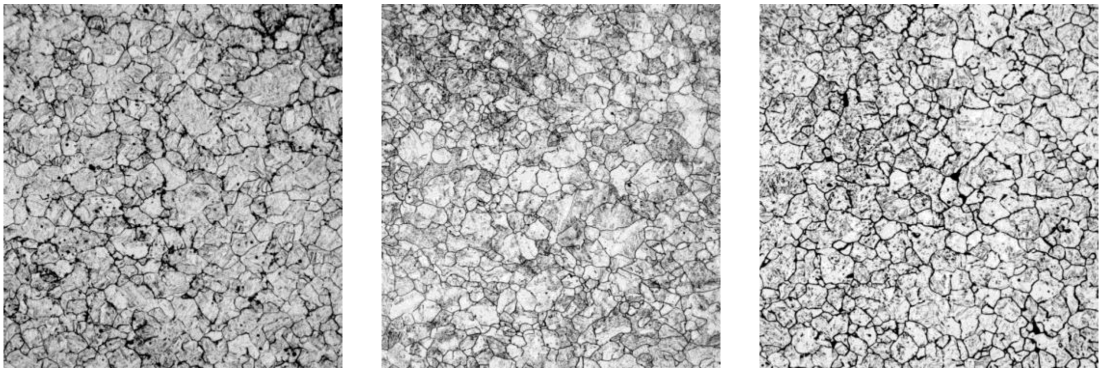

(a) Dγ=38 ± 16 μm (b) Dγ=29 ± 14 μm (c) Dγ=35 ± 17 μm

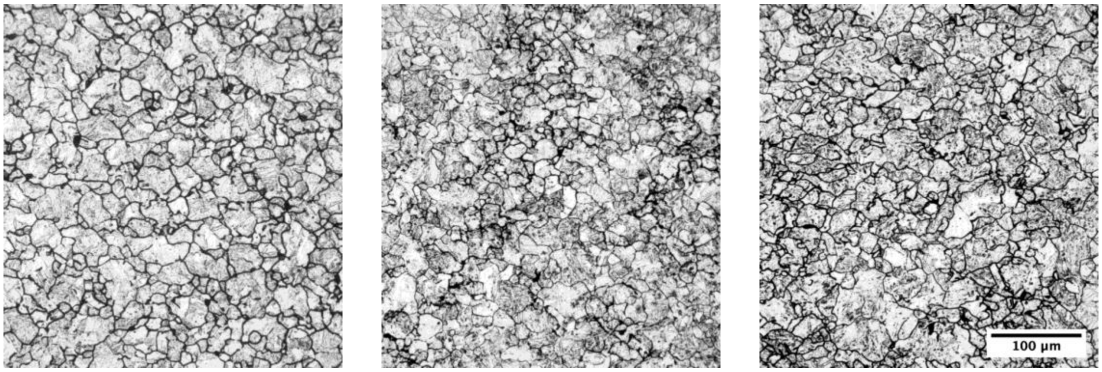

(d) Dγ=31 ± 16 μm (e) Dγ=28 ± 15 μm (f) Dγ=29 ± 16 μm

Figure 8.1 Two-pass reduction of 15% at 1150 and 1100 °C for (a) H4, (b) H8, and (c) L8; three-pass reduction at 1150, 1100, and 1050 °C for (d) H4, (e) H8, and (f) L8, compression axis is vertical.

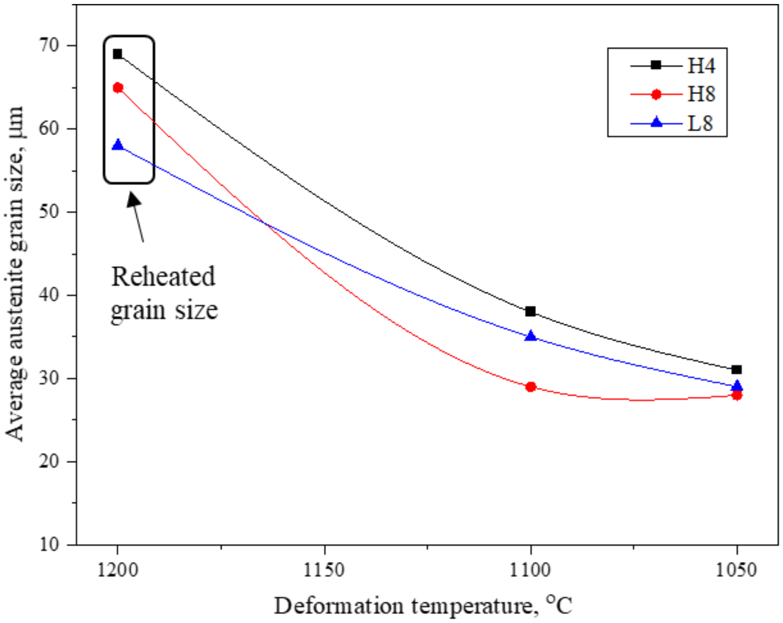

Figure 8.2 Average austenite grain size after two-pass reduction, 15% reduction/pass at the respective deformation temperature; each sample was quenched and prior austenite grain size was analyzed.

Since one of the possibilities is that a 15% reduction per pass may not induce complete recrystallization, it was decided to investigate the effect of a 25% reduction per pass on the recrystallization of austenite of the experimental steels. Figure 8.3 shows the micrographs of H4, H8, and L8 steels subjected to the aforementioned schedule. It is evident from these micrographs that the complete pancaking of austenite did not occur, even at 1050 °C. However, a non-uniform austenite grain distribution can be observed in the H8 and L8 steels. This indicates a mixture of recrystallized and unrecrystallized austenite grains (*i.e.,* duplex austenite grains).

In view of these results, the L8 sample was reheated at 1200 °C for two minutes and subjected to three passes with 25% per pass, but the last pass was conducted at 1030 °C, which is near the end of the roughing region. The interpass time was set to be 15 seconds after each pass in order to see whether complete static recrystallization could be observed. Figure 8.4 shows the prior austenite grain size of L8 subjected to the aforementioned schedule, and the fraction of unrecrystallized grains was measured to be ~15%, based on the non-circularity of the grains (measured using ImageJ software). This may show that the $T_{95\%}$ is close to the range of 1030–1000 °C temperature.

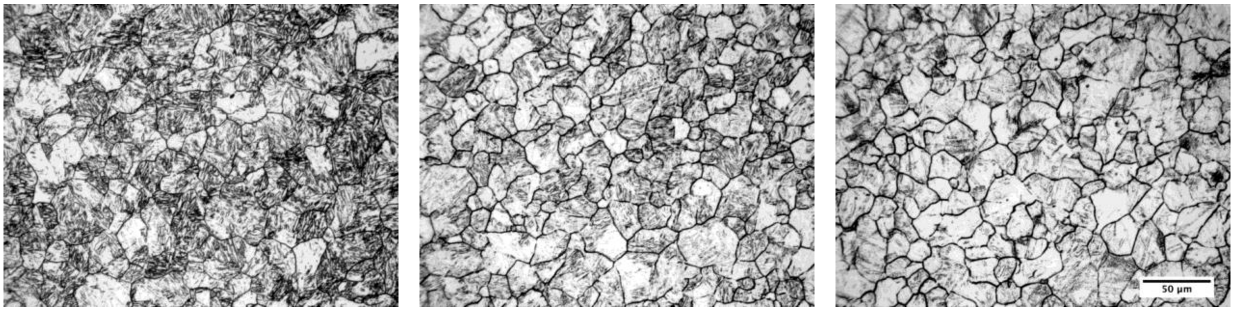

(a) $D\gamma=26 \pm 9$ µm (b) $D\gamma=20 \pm 12$ µm (c) $D\gamma=18 \pm 8$ µm

Figure 8.3 Three-pass reduction with 25% per pass at 1150-1100-1050 °C for (a) H4, (b) H8, and (c) L8 steels.

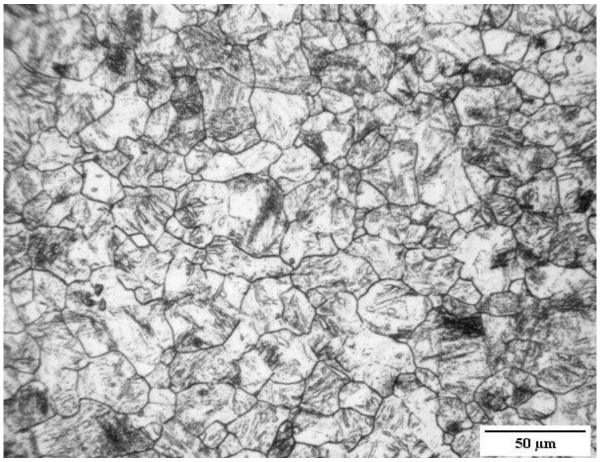

Figure 8.4 L8 sample subjected respectively to 25% reduction at 1150, 1100, and 1030 °C with the interpass time of 15 seconds. The compression axis is vertical.

This may also indicate that the NbC pinning force is large enough to retard some recrystallization of austenite close to the roughing stage. The resulting duplex microstructure at the end of the roughing passes can deteriorate strength and toughness in the final product. It is apparent that higher pinning forces of NbC on austenite grain boundaries will increase the $T_{5\%} - T_{95\%}$ range to higher temperatures, which may lead to a duplex microstructure at the end of rough rolling. This will even extrapolate more profoundly in steels with 0.1 wt.% Nb content. Hence, it is necessary to choose Nb levels perhaps well below 0.1 wt.% to have uniform austenite grain size at the end of roughing rolling. This is true for both plate mills and thin slab casting mills, where the few, if any, roughing passes or the early finishing passes acting as roughing passes occur at temperatures above 950 °C, thereby eliminating or reducing the possibility of grain refinement before experiencing the low temperature finishing passes.

While further investigation is needed to confirm the effects of C and Nb levels on grain coarsening and recrystallization behaviors based on precipitate analyses, this study draws attention to the necessity to keep Nb levels optimal to produce a uniformly refined austenite grain size during the rough rolling of plate steels.

8.2 Summary

From the present investigation, the following conclusions can be drawn:

1. Among the tested steels, H8 shows the lowest reduction in grain size. However, coarse and fine grains are evident, presumably, due to strain-induced precipitation of NbC acting to pin grain boundaries.
2. Depending on the amount of strain, the suppression of some recrystallized austenite grains would be expected to cause duplex grain structures, which are believed to be responsible for inferior mechanical properties.
3. The results presented in this study gave insight for subsequent studies which include the choice of reduction per pass, interpass time, and deformation temperature.

9.0 Determination of $T_{5\%}$ and $T_{95\%}$ Temperatures: Double-Hit Experiments

9.1 Results

9.1.1 Fractional Softening: $T_{5\%}$ and $T_{95\%}$ Temperatures

Figure 9.1 shows the flow curves plotted from double-hit tests of the experimental steels (H0, H4, H8, L4, and L8) for an interpass time of 20 seconds. In general, as the deformation temperature decreases from 1150 °C down to 900 °C, the flow stress increases (*i.e.*, work hardening). This observation is consistent with the Zener-Hollomon relationship [44]. For all steels investigated in this study, the flow curves did not exhibit signs of dynamic recrystallization since these steels are tested at a higher strain rate of 10 sec^{-1} and indicative that the critical peak strain for dynamic recrystallization was not attained in all tests.

It is evident, that Nb, as well as C, play role in increasing the flow stress (between different steels) primarily due to strain-induced precipitation of Nb (C, N), which prevents further recrystallization [63]. Steels of the same Nb level (H8 and L8) exhibit higher flow stresses compared to the other lower Nb steels (H4 and L4). On occasions, flow stress fluctuation can be observed in a few samples, and this might be due to an increase in friction between the anvils and the sample. Another possibility could be a sign of competition between hardening and recrystallization mechanisms of austenite [64, 106], especially at 1000 °C and 1050 °C flow curves. Moreover, few of the flow curves are at a lower targeted true stain of 0.6, hence, the inherited influence of the machine stiffness is apparent.

The fractional softening due to isothermal static recrystallization is determined by the net change in the work hardening between the first and the second hit of the double-hit test under a constant true strain rate. Several analytical methods, as mentioned earlier, are available to estimate fractional softening. In this study, and to exclude the recovery effects, the 2-pct. offset method was used to determine the fractional softening of austenite in the investigated steels (see Eq (5.1)). From fractional softening curves, the deformation temperature corresponding to 20 pct. FS is taken as $T_{5\%}$ or T_{nr}. Below this value, it is expected that the steel is in the work hardening state and the softening of austenite is mainly due to static recovery [49, 59, 75].

The fractional softening for all experimental steels at different deformation temperatures is depicted in Figure 9.2. Two dashed lines are drawn to indicate the limit of pancaking of austenite ($T_{5\%}$) and the complete recrystallization ($T_{95\%}$) temperatures. The value of 85 pct. softening, which is a more conservative value, was taken to be the limit for $T_{95\%}$ temperatures. The base steel for the H-series (H0 steel) exhibits full recrystallization between deformation temperatures of 1150 °C and 950 °C. Below the deformation temperature of 950 °C, the austenite is in the partial recrystallization state. On the other hand, as the Nb level increases in the steel such as in H8 and L8 steels, the fractional softening decreases for the same deformation temperature. For instance, at 1050 °C, H8 steel shows the lowest softening compared to other steels tested at the same temperature. Furthermore, the 50-pct. softening or higher is shifted to 1000 °C for H8 and L8 compared to H4 and L4 at around 950 °C. From this curve, the recrystallization- stop temperatures $T_{5\%}$, of 932 °C, 913 °C, and 900 °C were obtained for steels H8, L8, and L4, respectively. It is worth noting that L4 steel exhibits higher $T_{5\%}$ than H4 steel though the C level is higher and consequently Nb (C, N) content should be lower. To assess this finding, it is reported in a previous study on the static recrystallization behavior in Nb-Ti microalloyed steels that the initial austenite grain size before deformation plays a role in deviating $T_{5\%}$ [66]. The reasoning for this is that large austenite grain sizes yield less nucleation site density for recrystallization. The other steels (H4 and H0) exhibit presumably lower $T_{5\%}$ which was below the tested temperature of 900 °C. It can be expected that $T_{5\%}$ for H4 is between 850 °C and 900 °C and H0 is between 850 °C and 800 °C for the same deformation conditions and delay time of 20 seconds.

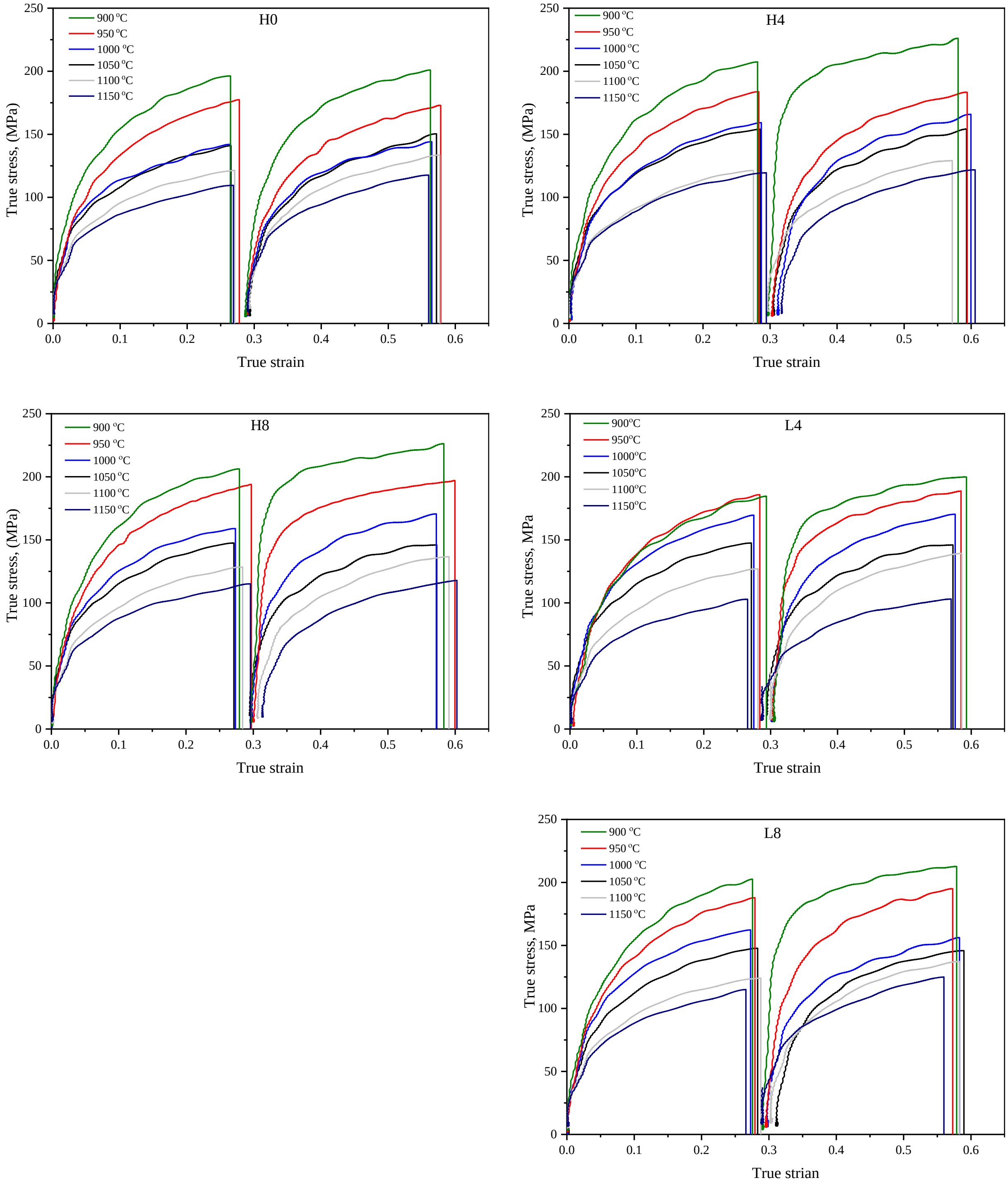

Figure 9.1 Flow curves obtained from the double-hit tests at different temperatures with a constant interpass time of 20 seconds and strain rate of 10 sec^{-1}.

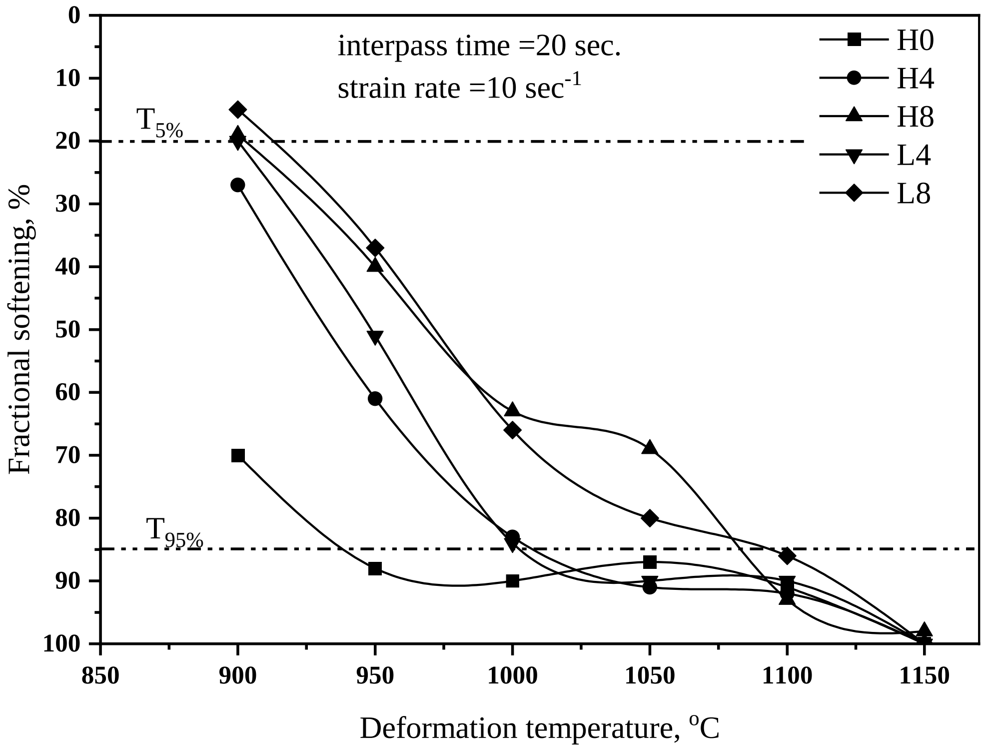

Figure 9.2 Fractional softening pct. of austenite determined using 2 pct offset method.

To support the validity of the results obtained in Figure 9.2, optical micrographs were taken from investigated steels quenched from all deformation temperatures. Tested steels in this study showed good agreement between austenite structure and the fractional softening data. At deformation temperatures between $T_{5\%}$ and $T_{95\%}$, partial recrystallization is observed. For deformations at temperatures at or close to the recrystallization-stop temperature of the respective steels, the prior austenite grains are completely unrecrystallized or pancaked. Examples of prior austenite grain structures for H4 and H8 steels at 1000 °C and 1050 °C are depicted in Figure 9.3 A complete sets of light optical micrographs for austenite grain structures are included in Appendix A. It was hypothesized that for all steels deformed at 1150 °C, fully recrystallized grains would be expected, while steels deformed at 1050 °C may or may not yield full recrystallization depending on C and Nb levels, hence, partial recrystallization is expected to begin at this temperature.

For this reason, austenite grain aspect ratios were measured, and the results are shown in Figure 9.4. Consequently, all steels have austenite aspect ratios close to 1.5 at deformation temperatures above 1050 °C, which indicates full recrystallization. At the other end of the figure, the aspect ratio scales up with Nb (C, N) content precipitated at the respective deformation temperature. In fact, H8 and L8 steels are the first to deviate from an aspect ratio of 1.5 at 1050 °C.

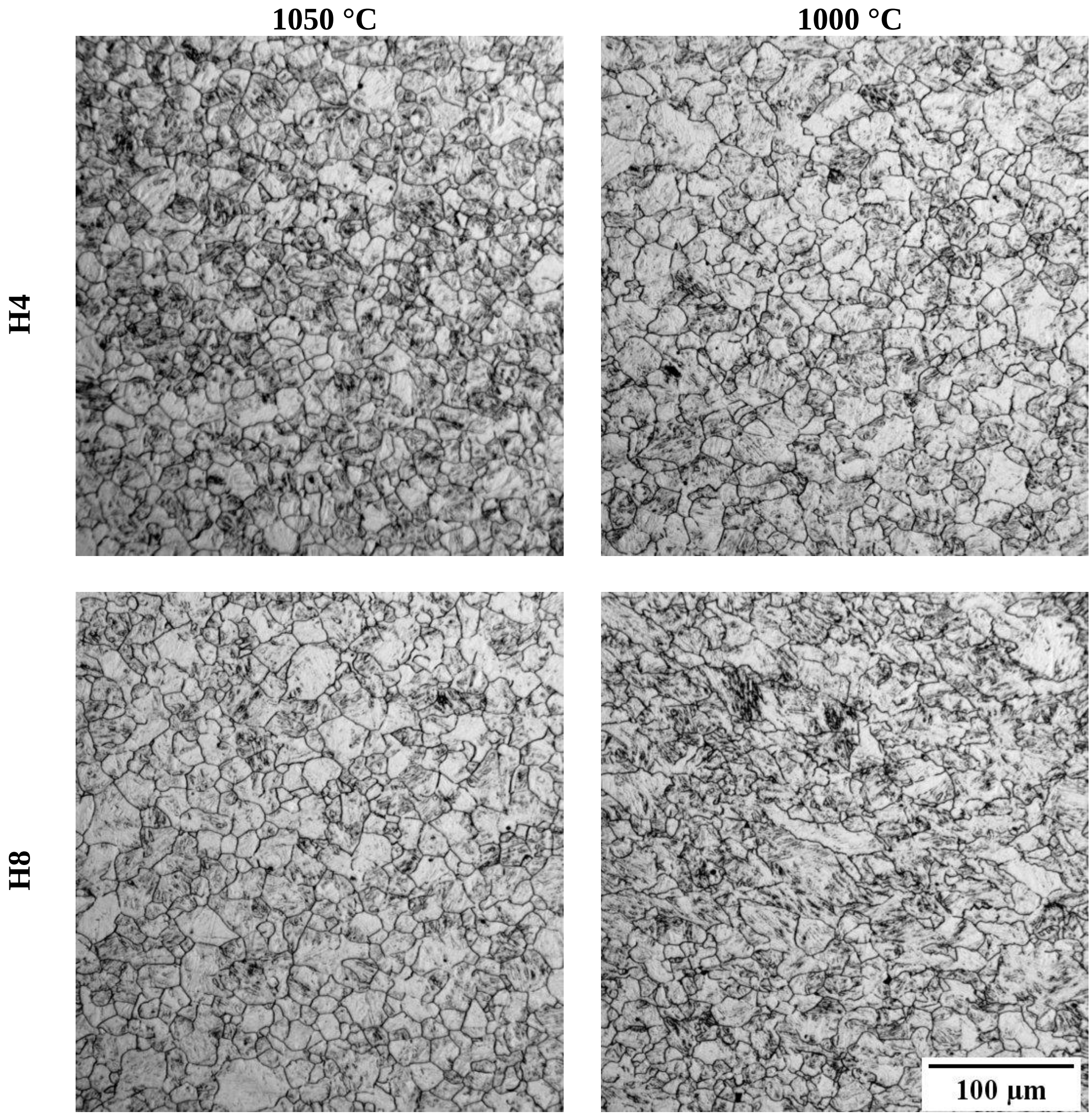

Figure 9.3 Optical micrographs of austenite grain structures for H4 and H8 steels obtained from the double-hit tests at 1050 °C and 1000 °C.

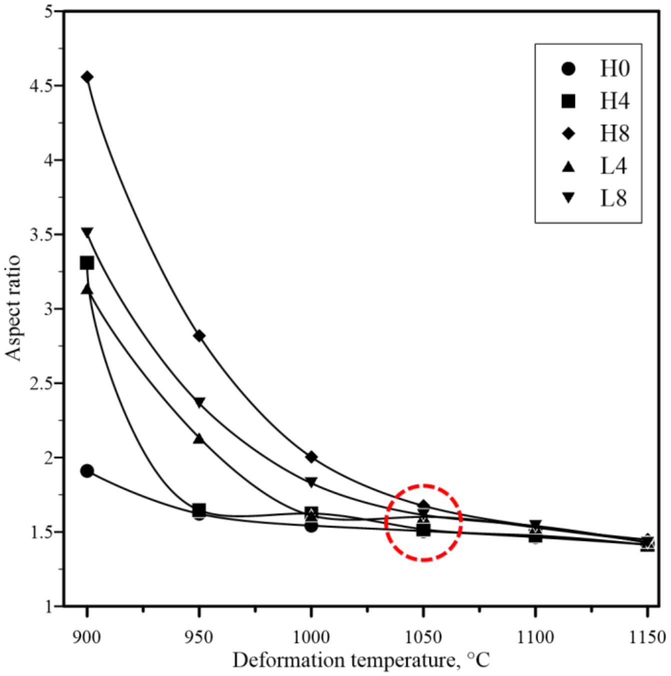

Figure 9.4 Austenite grain aspect ratios versus hot deformation temperature, dashed circle indicates what appears to be the limit of complete recrystallization.

9.1.2 Recrystallization of Austenite and Nb (C, N) Strain-Induced Precipitation

Figure 9.5 shows selected flow curves obtained at different interpass times at 950 °C (*i.e.*, schedule II in Figure 5.7) for H0, H4, and H8. In these curves, the flow stress increases at lower interpass times except, interestingly, for H8, in which the opposite of this trend can be seen. This is due to increased precipitation as the interpass time increased and it can be inferred that there is competition between strain-induced precipitation and driving force for recrystallization at interpass times of 5, 15, and 20 seconds at this respective temperature. At higher interpass times (*i.e.*, 50 and 100 seconds), the flow stress increased in this steel, indicating precipitation predominates in suppressing recrystallization.

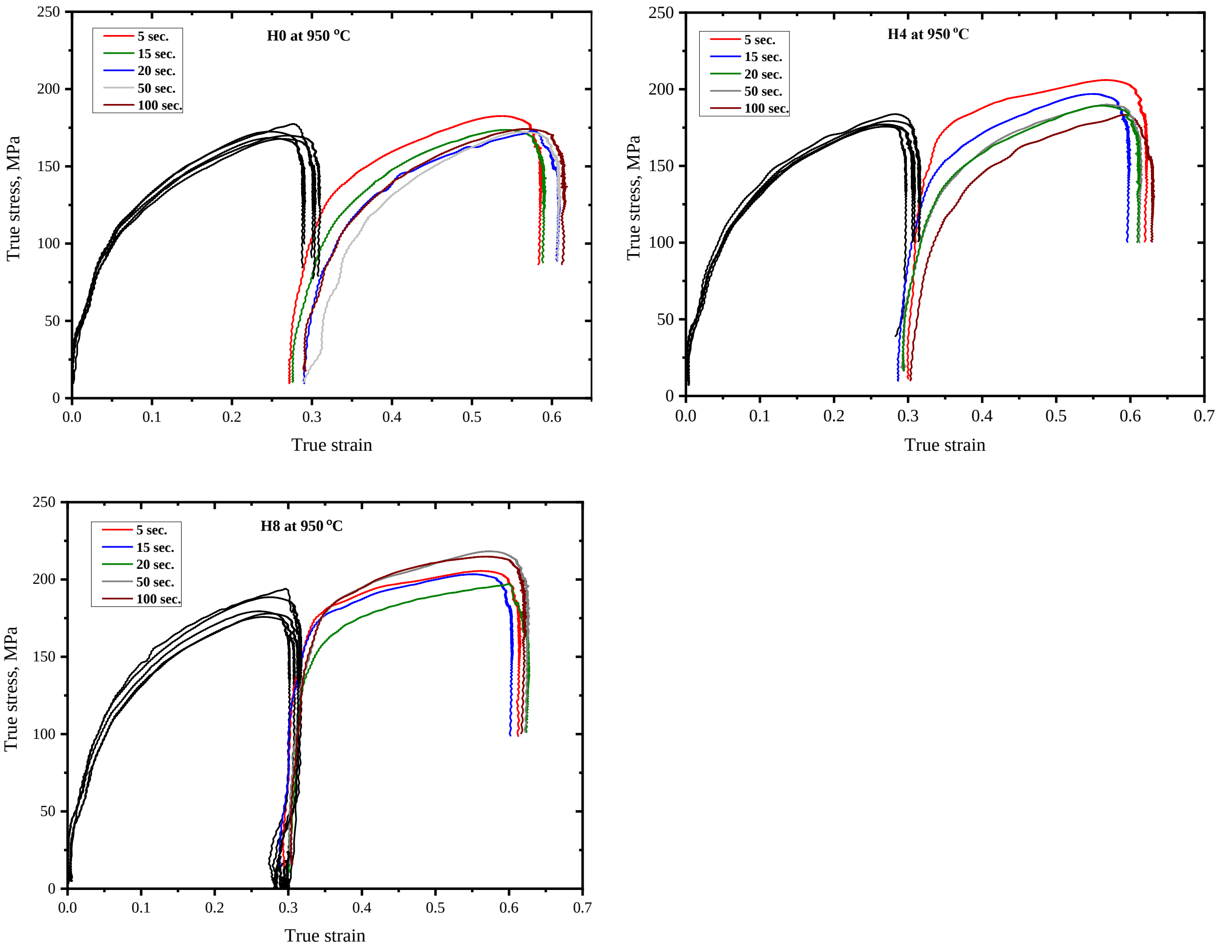

Figure 9.5 Flow curves of H- series steels obtained from the double-hit test under variable interpass times and at a strain rate of 10 sec^{-1}.

Fractional softening at different interpass times for all steel was determined at the deformation temperatures between 1050 °C and 900 °C. The reasoning for choosing this temperature range is due to the higher tendency for strain-induced precipitation to occur in this regime giving a higher pinning force over the driving force for recrystallization (*i.e.*, $F_{pin} \geq F_{RXN}$); critical in steel processing to avoid mixed austenite microstructure. The same method of 2 pct. offset, mentioned earlier, was used to determine fractional softening under different interpass times. Figure 9.6 shows the fractional softening of all steels under variable holding times. It is clear that the base steel H0 can be described by a sigmoidal curve due to Avrami’s kinetics. On the other hand, Nb-bearing steels curves show that the sigmoidal shape curves are interrupted, especially at low deformation temperatures. For instance, at 1000 °C in H8 steel (Figure 9.6 (c)), there exists a plateau which indicates that strain-induced precipitates of Nb, carbides or carbonitrides are taking place which hinders further recrystallization. The plateau in fractional softening was noted in previous studies and mainly attributed to precipitates pinning the grain boundaries motion which temporarily suppress recrystallization progress [63, 94, 107-109].

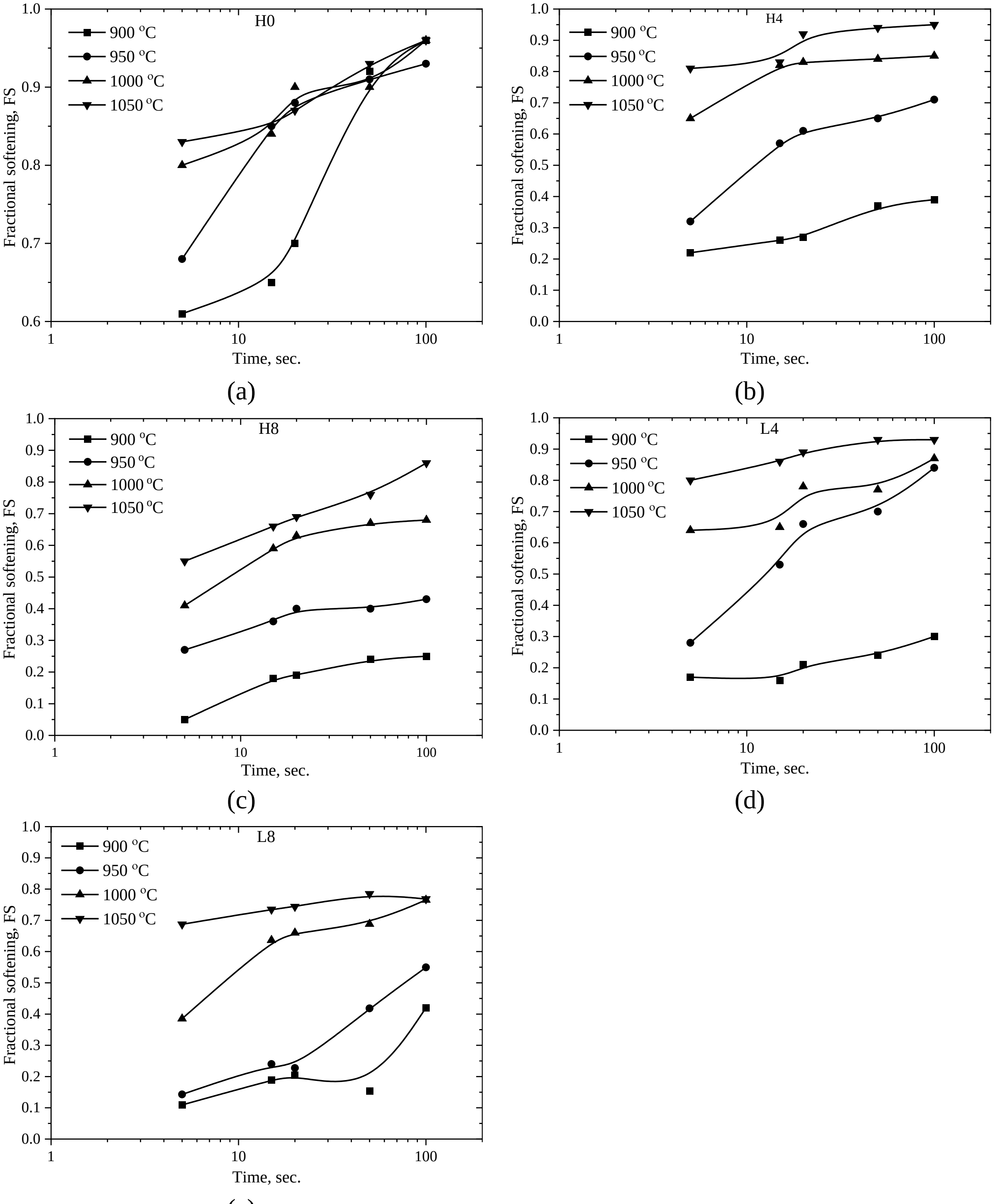

(a) (b) (c) (d) (e)

Figure 9.6 Fractional softening of austenite for (a) H0; (b) H4; (c) H8; (d) L4; and (e) L8. The fractional softening data were determined from the double-hit tests.

Figure 9.7 shows Nb (C, N) precipitates of H8 steel observed on carbon replicas under TEM. Figure 9.7 (a) shows TEM investigation for H8 sample deformed at 900 °C with a delay time of 100 seconds. Higher number density of precipitate is clearly shown and as expected higher nucleation rate of strain-induced precipitation at low temperatures. The average precipitate size measured using image processing software was about 11.9 nm. Comparing Figure 9.7 (a) with Figure 9.7 (c), the number density of precipitates of the latter is lower due to lower delay time and higher deformation temperature (Figure 9.7 (b) and (d)).

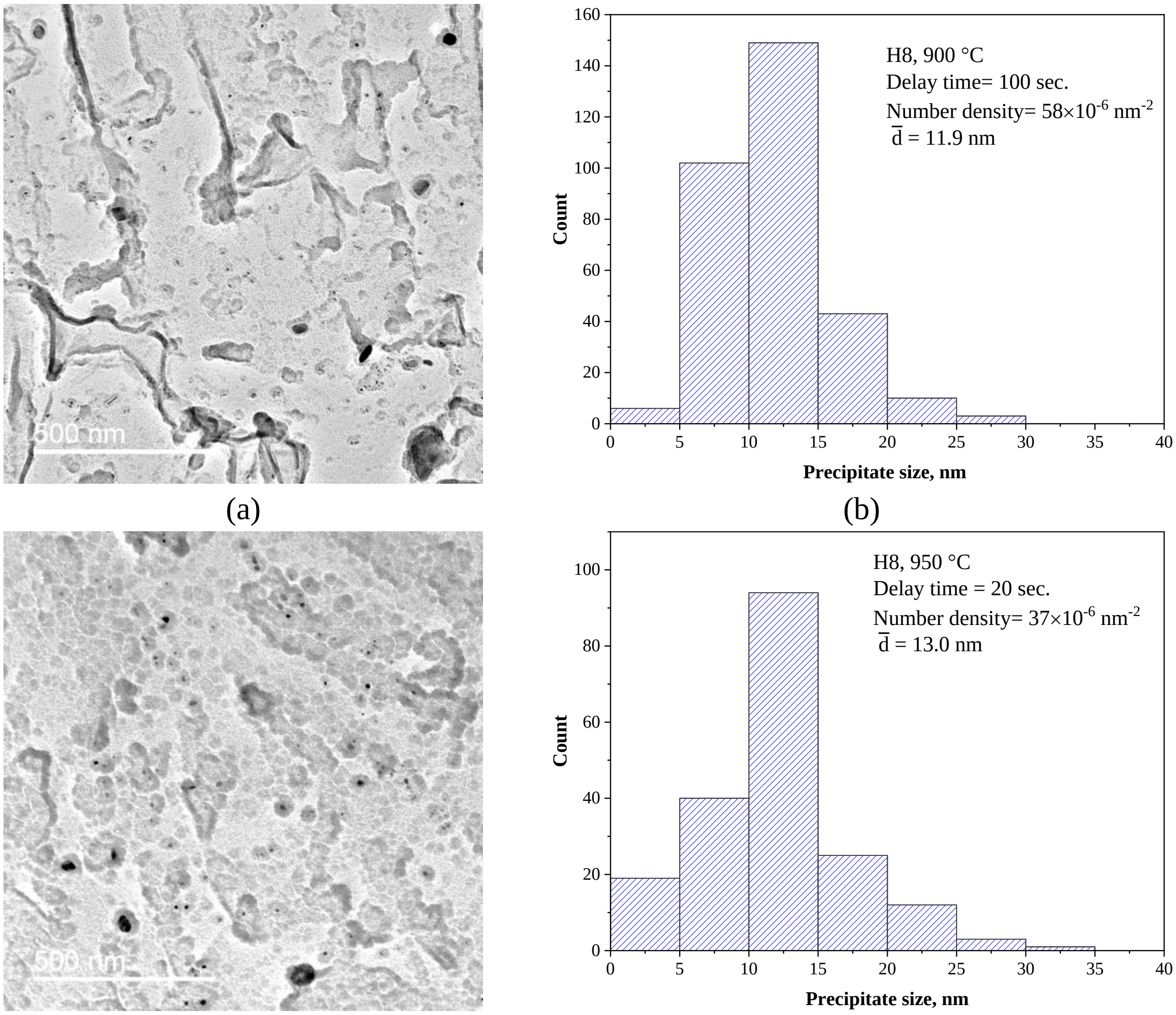

(a) (b)

(c) (d)

Figure 9.7 Carbon extraction replicas of H8 steel obtained at (a, b) 900 °C with interpass time of 100 sec. and at (c, d) 950 °C with interpass time of 20 sec.

The observation made on carbon replicas may not capture the true number density and precipitate size of the alloy steel as mentioned by previous investigators [16, 51, 62]. The reasoning was that two replicas do not necessarily have the same precipitate capture efficiency. Furthermore, the most effective precipitates in grain boundary pinning are about 2 nm in size, which are difficult to trap in the replica. Consequently, the comparison of the results can be difficult and complex. However, it is known from previous studies that strain-induced precipitation of Nb (C, N) forms on crystalline defects (*i.e.,* grain and subgrain boundaries) [4, 16]. Figure 9.8 shows Nb (C, N) precipitates forming on what appears to be a grain boundary of H8 steel deformed at 900 °C with an interpass time of 100 seconds.

Other nucleation sites of Nb (C, N) reported in the literature are the pre-existing (Ti, Nb) (C, N) particles in the steel [94]. These (Ti, Nb) (C, N) particles do not dissolve in the austenite and mainly form in the molten steels during solidification and remain stable during reheating treatment [110]. Figure 9.9 (a) and (b) show a scanning transmission electron micrograph of coarse precipitate and the corresponding EDS in H8 steel deformed at 1000 °C with an interpass time of 20 seconds. Furthermore, High-resolution TEM and Fast-Fourier transformed (FFT) diffractogram of complex precipitates of Ti-rich NbC for H8 deformed at 1000 °C -20 seconds is shown in Figure 9.9 (c) and (d). The lattice parameter was calculated using the FFT diffractogram to be 0.433 nm. It shows that these types of precipitates (*i.e.,* core-cap) are Ti-rich NbC may form on such type of complex precipitate at higher temperatures. However, it can be argued whether such precipitates are formed during melting or after deformation process. The reason for the latter assumption is believed to be that the strain energy (*i.e.,* lattice misfit) is small, leading to a decrease in the energy barrier for nucleation [94]. Nevertheless, Figure 9.7 and Figure 9.8 show that precipitates preferentially nucleate on grain boundaries and/or subgrain boundaries.

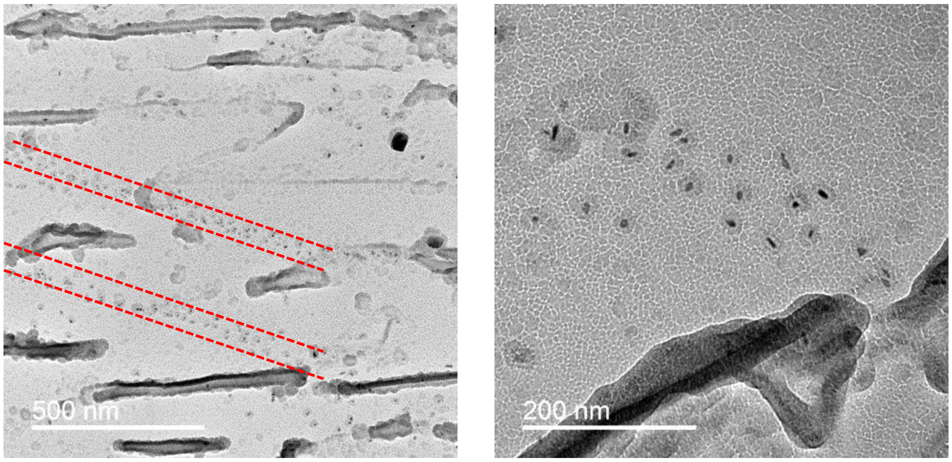

(a) (b)

Figure 9.8 Carbon extraction replicas of H8 steel at 900 ˚C for 100 sec. (a) precipitates decorate what appears to be an interlath (red dashed lines) and (b) high magnification of precipitate clusters.

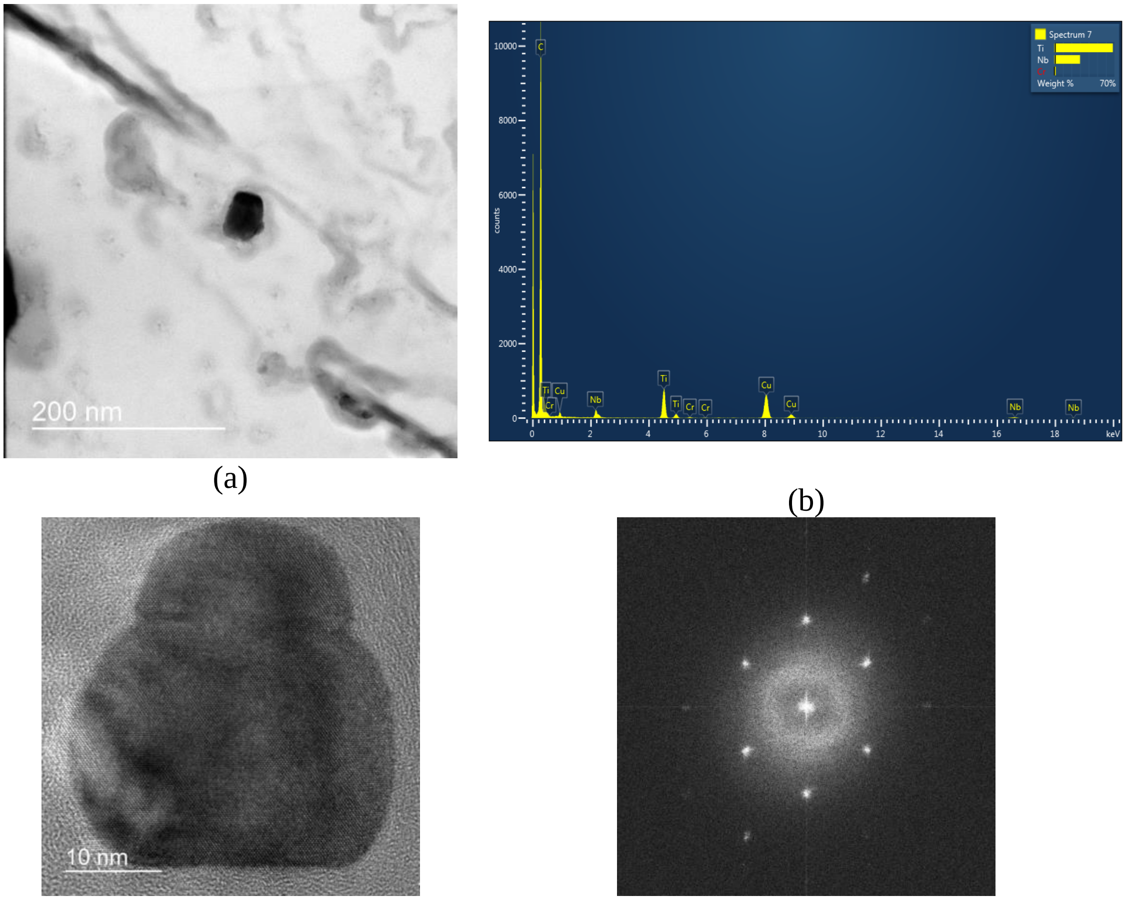

(a) (b)

(c) (d)

Figure 9.9 (a) STEM-BF of (Ti, Nb) (C, N) precipitate observed in H8 sample deformed at 1000 °C -20 seconds and (b) the corresponding EDS spectra; (c) HRTEM and (d) Fast-Fourier transform diffractogram.

Nucleation of precipitates at the interlath boundaries was observed on thin foils of H8 samples deformed at 1050 °C under a delay time of 50 seconds as shown in Figure 9.10. From this figure, the dark-field image was taken using g = 200 reflection of Nb (C, N) precipitate whereby the density of precipitates is observed at the interlath in H8 steel with a few in the matrix. Furthermore, when H4 steel was examined under TEM at the same condition (1050 °C- 50 seconds delay time), the results revealed that there is no precipitation or few occurred that there is little if any precipitation observed. Only coarse precipitates are observed as shown in Figure 9.11 (a). Similarly, Figure 9.11 (b) shows carbon extraction replica of L4 steel deformed at 1050 °C with an interpass time of 50 seconds which yields only cuboidal precipitates, mainly TiN precipitates, and no fine precipitates were observed. This may explain why recrystallization progress is delayed in H8 steel compared to H4 steel or L4 steel at 1050 °C.

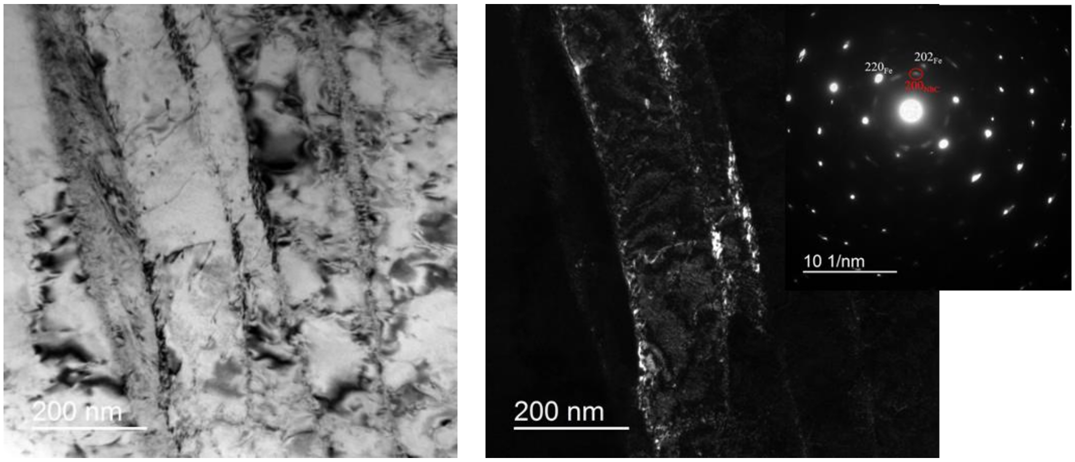

(a) (b)

Figure 9.10 Thin foil TEM images of H8 steel deformed at 1050 °C under a delay time of 50 sec. (a) Bright-field image and (b) Dark-field image with the corresponding diffraction pattern.

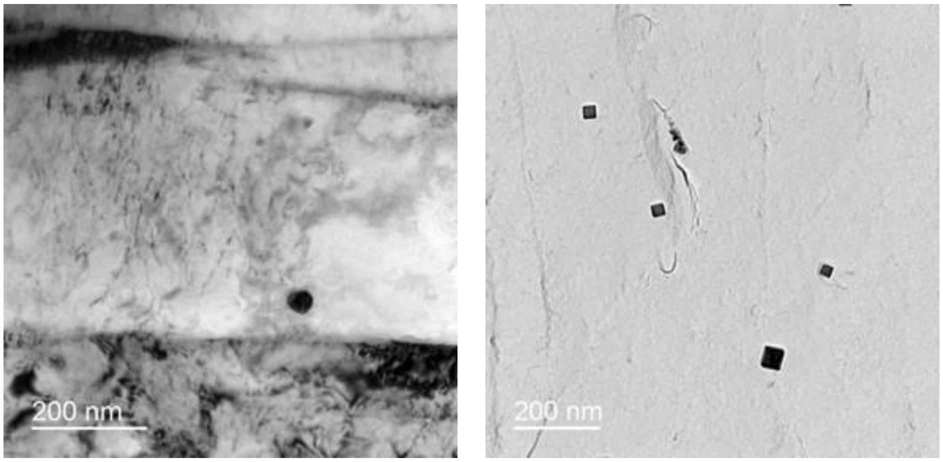

(a) (b)

Figure 9.11 TEM bright-field image of H4 steel deformed at 1050 °C under a delay time of 50 sec. and (b) carbon replica of L4 deformed at 1050 °C under a delay time of 50 sec.

9.2 Discussion

The results presented above give insight on the importance of the processing window for high temperature processing of HSLA steels. Several empirical equations appear in the literature for estimating $T_{5\%}$ or T_{nr} temperature in microalloyed steels. For instance, Barbosa *et al.* [111] developed an empirical equation to determine $T_{5\%}$ temperature by examining 17 different grades of microalloyed steels having several variations in microalloy elements such as Nb, Al, Ti and V. Of these microalloy elements, Nb strongly elevates $T_{5\%}$ and Ti, Al and V also increase $T_{5\%}$ but to a lesser extent. Barbosa's empirical equation is only applicable for microalloyed steels with Nb addition up to 0.06 wt. pct. and with no N content which is critical in carbonitride precipitation behavior. Strain-based equations for estimating $T_{5\%}$ temperature were developed by Bai *et al.* [112] for Nb microalloyed steels studied under continuously cooled conditions and later by Dutta and Palmiere [113] for Nb microalloyed steels examined under isothermal double-hit tests. A regression model for estimating $T_{5\%}$ combining various alloy content and strain variations was given by Fletcher [114, 115]:

$$T_{nr} = 203 - 310C - 149\sqrt{V} + 657\sqrt{Nb} + 683e^{-0.36\varepsilon} \quad \textbf{(9.1)}$$

where C, V, and Nb are in wt. pct. and ε is pass strain. Eq (9.3) was used to estimate $T_{5\%}$ for H0, H4, and H8 and found to be 798 °C, 929 °C, and 983 °C, respectively. For L4 and L8 steels, the values were estimated to be 938 °C and 992 °C, respectively. These $T_{5\%}$ temperature values for H-series steels are higher than those determined experimentally and this can be due to Ti addition which is not included in Eq (9.3). Furthermore, Eq (9.3) overestimates $T_{5\%}$ temperatures for L-series steels which is counterintuitive since these steels contain lower carbon contents which play a major role in carbonitride precipitation behavior. Nevertheless, for the purpose of this study, the results clearly show that the region for partial recrystallization is between 950 °C and 1050 °C for H8 and L8 steels.

Depending on C and Nb contents, the supersaturation of NbC plays a role in the subsequent precipitation of Nb (C, N) [16, 17, 63, 116]. Furthermore, Speer and Hansen [60] as well as Vervynckt *et al.* [63] showed that the strain-induced precipitation in Nb-bearing steels is more effective in retarding static recrystallization than the solute drag effects originating from the solute Nb. It was reported in previous studies that the C-curve nose depicted in the precipitation time-temperature diagram appears to be around the 900-950 °C temperature range [4, 16, 76, 117]. However, these findings were confined to low Nb-bearing steels and/or low temperature deformation. For these reasons, the Dutta-Sellars model was used to estimate the start of precipitation designated by the same authors as $t_{0.05}$. The time for the onset of (5%) of precipitation, $t_{0.05}$ can be calculated by [76]:

$$t_{0.05} = A[Nb]^{-1}\varepsilon^{-1}Z^{-0.5}\left(\exp\frac{270{,}000}{RT}\right)\left(\exp\frac{B}{T^{3}\,(\ln k_s)^{2}}\right) \quad \textbf{(9.2)}$$

where A and B are constants that depend on the thermomechanical history and have values of 3×10^{-6} and 2.5×10^{10}, respectively, [Nb] is the wt. pct. of niobium taken into solution during soaking (determined using appropriate solubility relation), ε is the true strain prior to the second deformation in the double-hit test, Z is the Zener-Hollomon parameter, T is the deformation temperature on the absolute temperature scale, and k_s is the supersaturation ratio at temperature T. Using Palmiere's solubility relation [29], k_s can be determined as:

$$k_s = [Nb][C+12N/14]_{sol} / 10^{2.06-6700/T} \tag{9.3}$$

Figure 9.12 shows the Precipitation-Time-Temperature (PPT) curves for all experimental steels in this study calculated using Eq. (9.2). The C-curve nose of H8 is close to 1000 °C while L4 steel (*i.e.,* the lowest carbide content among all experimental steels) C-curve nose is close to 850 °C. This is due to the high Nb content observed in H8 and is in line with the existing plateau shown previously in Figure 9.6 (c). A previous study shows that pre-existing Ti-rich NbCN particles delay the precipitation start time of strain-induced NbC particles in Nb-Ti steels [94]. However, in this study, all investigated steels were alloyed with the same Ti content.

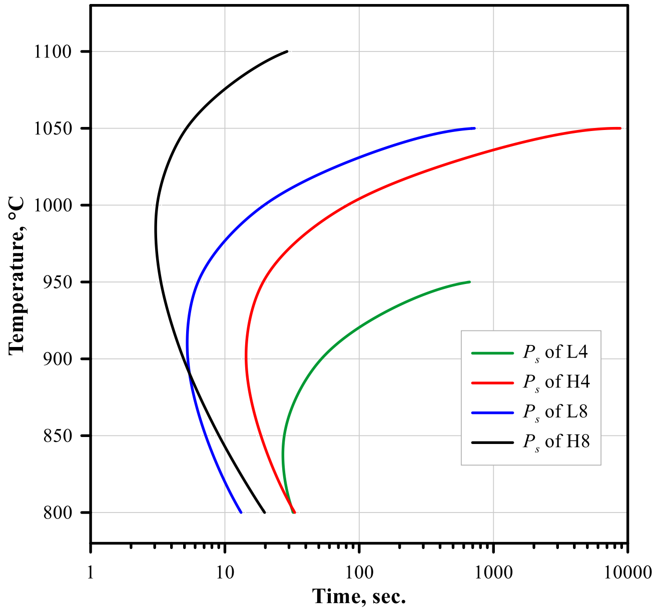

Figure 9.12 Precipitation start time-temperature curves for H8, H4, L8, and L4; determined using the Dutta-Sellars model.

Precipitation evolution was estimated using the precipitation module of Thermo-Calc (TC-PRISMA). It uses Kampmann-Wagner numerical (KWN) theory to simulate the nucleation and growth kinetics of precipitation [118, 119]. In this study, the simulation of precipitation was confined to Nb (C, N) particles and excluded the complex carbides such as (Ti, Nb) (C, N) since there is no established solubility equation for such a precipitate in the literature. From the flow curves, the dislocation density (ρ) which acts as a heterogenous nucleation site (N_0) and can be estimated as [76, 117]:

$$\rho = \left(\frac{\sigma - \sigma_y}{M\alpha G b}\right)^2 \qquad \textbf{(9.4)}$$

where σ and σ_y are the maximum and the yield stress, respectively, can be obtained from the double-hit test, M is the Taylor factor of austenite with a value of (3.1 for FCC materials), α is a constant having a value of 0.15, G is the elastic modulus at elevated temperature, taken from the study of Fukuhara and Sanpei on low carbon austenite [120], b is the Burgers vector of austenite

(= 2.59×10^{-10} m). Accordingly, from the dislocation density, the number of heterogenous nucleation sites can be estimated as follows [76]:

$$N_0 = 0.5\rho^{3/2} \qquad \textbf{(9.5)}$$

Figure 9.13 (a) and (b) show the estimated number density per unit volume and the volume fraction of precipitates, respectively, as a function of time for all investigated steels. The interfacial energy of γ/NbC used in this simulation was assumed to be 0.5 J/m^2 [119]. Two temperatures were considered, 950 °C and 1000 °C, which are in the range of the partial recrystallization region. The number density of precipitates of all steels reaches what appears to be a steady-state for as low as 7 seconds at 1000 °C and as low as 3 seconds at 950 °C. This is also reflected in Figure 9.13 (b), the volume fraction of precipitates increases with time up to 300 seconds for H8 and L8 at the two temperatures of 950 °C and 1000 °C. This emphasizes that the Zener pinning force is expected to be higher than the recrystallization driving force for the case of H8 and L8 steels as compared to H4 and L4 steels.

Therefore, from this study, the choice of Nb content is critical in TMP processing. Furthermore, the temperature and processing parameters play an important role in the choice of processing window as reported in recent studies [64, 67]. Thus, the critical temperatures of steels in the austenite (*i.e.,* $T_{95\%}$ and $T_{5\%}$) have to be designed based on the Nb level, well below 0.08 wt. pct. to avoid the partial recrystallization regime during roughing. In view of these results, it should be pointed out that the recrystallization start-finish times under industrial conditions could be somewhat shorter than what was presented in these laboratory studies. Full scale or laboratory mill studies may reflect the true times or at least verify the current data.

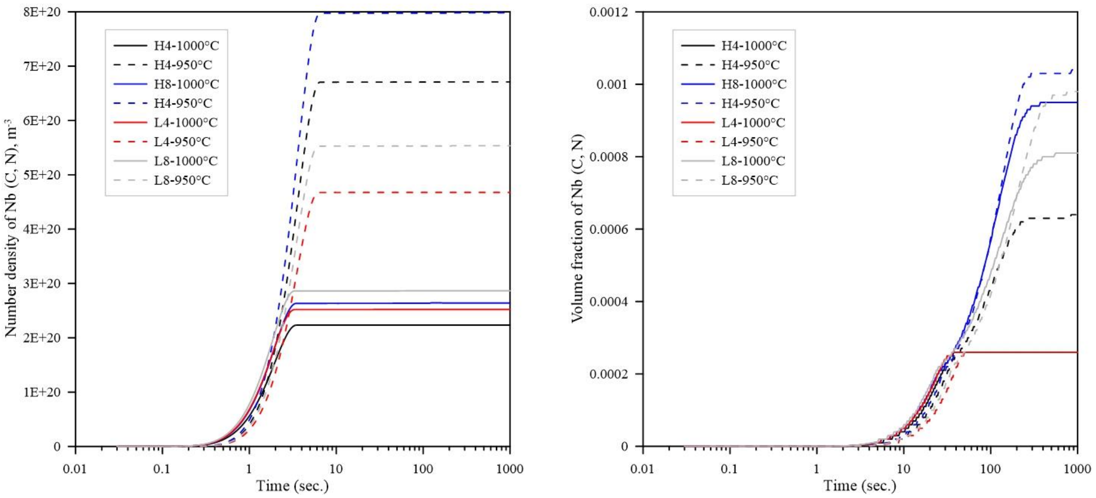

(a) (b)

Figure 9.13 Number density of Nb (C, N) (a); and volume fraction Nb (C, N) (b) estimated with TC-PRISMA module.

9.3 Summary

Recrystallization behavior of H0, H4, H8, L4, and L8 steels has been studied using a double-hit hot compression test. This study has shown that the recrystallization behavior of the experimental steels strongly depends on the precipitation state of NbC. The major findings of this study can be summarized as follows:

- The region for partial recrystallization of H8 and L8 steels were between 950 °C and 1050 °C, while H4 and L4 steels were close to 950 °C.
- The recrystallization- stop temperature, $T_{5\%}$, was estimated to be 932 °C, 913 °C, and 900 °C for steels H8, L8, and L4, respectively.
- The double-hit test results compare well with optical micrographs. The aspect ratio of austenite grains deviates from equiaxed shape at 1050 °C and more profoundly at 1000 °C for H8 and L8 steels.

- For Nb alloyed steels, a plateau is observed in the fractional softening against time curves, indicating strain-induced precipitation whereby recrystallization is temporarily halted, while the Avrami kinetics type of curve is observed in H0 steel.
- Higher Nb content led to accelerated nucleation of Nb (C, N) at crystalline defects and mainly at grain boundaries.
- The Dutta-Sellars model was used to estimate precipitation start time $t_{0.05}$. The highest C-curve nose is observed in H8 steel at 1000 °C and below 5 seconds.
- TC-PRISMA calculations indicate that higher Nb levels in H8 and L8 steels led to a higher volume fraction of precipitates which consequently lead to a higher Zener pinning force exceeding the driving force for recrystallization.

10.0 Thermomechanical Simulation Studies

The purpose of thermomechanical processing, as stated previously, is to control the structure, morphology, and grain size of the austenite in HSLA steels so that the transformation of the austenite produces the optimum ferrite, Bainite, or non-equilibrium ferrite structures. However, thermomechanical rolled HSLA steels may exhibit mixed structures consisting, for example, mainly very fine ferrite grains and/or upper bainite. As mentioned previously, it is well known that mixed grain structure could deteriorate the strength and toughness of the final product and as the mixed grain structure of the final product results from that of austenite, the formation of the former must be sought to account for the latter.

The present results and discussion describe the effects of Nb on austenite recrystallization in roughing and finishing passes and its underlying role in subsequent transformation products. Here, attempts were made to investigate these effects using hot compression tests.

10.1 Results and Discussion

10.1.1 Roughing Pass Simulation

Figure 10.1 presents examples of the flow curves obtained from roughing passes simulation using schedule I (outlined in subsection 5.2.3.2). Complete sets of flow curves for the experimental steels are included in Appendix B. Figure 10.1 (a) and (b) show the flow curves for H4 and H8 steels, respectively; tested after reheating at 1200 °C for a duration of 180 seconds, deformed consecutively at 1150-1100-1050 °C and with an interpass time of 20 seconds between passes. It can be seen from the first pass deformation at 1150 °C that the maximum true stress of H8 steel (~100 MPa) is slightly higher than H4 steel (~ 90 MPa). Decreasing the deformation temperature yielded higher true stress than the preceding passes, especially at 1050 °C for high Nb-bearing steels. For example, the maximum true stress for H8 steel at 1050 °C is approximately 167 MPa, while the maximum true stress for H4 is around 150 MPa. Similarly, this trend is observed between L4 and L8 streels; at 1050 °C, L8 steel exhibited higher flow stress than the flow stress of L4 steel. However, the flow stress for H0 steel at 1050 °C, exhibited a slightly higher value (~ 157 MPa) compared to H4 (~ 150 MPa) and L4 (~ 151 MPa) steels but lower than H8 (~ 167 MPa) and L8 (~ 164 MPa) steels.

It was reported from previous studies that the recrystallization of deformed austenite at high deformation temperatures may be retarded or controlled by dissolved solute, strain-induced precipitates, coarse grain size and the absence of second phase particles capable of nucleating recrystallization [6, 16, 53, 60, 121]. In view of the resulting flow curve of H0 steel, the initial coarse grain structure may play a role in increasing the flow stress at 1050 °C and it is likely that H0 exhibited coarse grain structure prior to deformation. Furthermore, grain coarsening between passes is more prone to occur since no NbC strain-induced precipitation is expected in H0 steel. Nevertheless, the relatively high flow stresses exhibited in high Nb-containing steels (H8 and L8) may be attributed to either the solute drag effect from solute Nb or more profoundly to the strain-induced precipitation of NbC or Nb (C, N). Hence, increasing the Nb level in the steel tends to increase the flow stress in the true stress-strain curve and it may be related to the extent of austenite recrystallization or recovery since softer austenite leads to low flow stress. The results presented here are in alignment with a previous study on the effect of Nb on the austenite strength during high temperature rolling [122]. This effect is markedly clear when deforming at temperatures in the lower austenite partial recrystallization region or in a lower temperature of the austenite field (*i.e.*, recovery region). It appeared that H8 and L8 steels were deformed close to the beginning of the partial recrystallization region. For this reason, the austenite structures of the experimental steels were examined and they are discussed below.

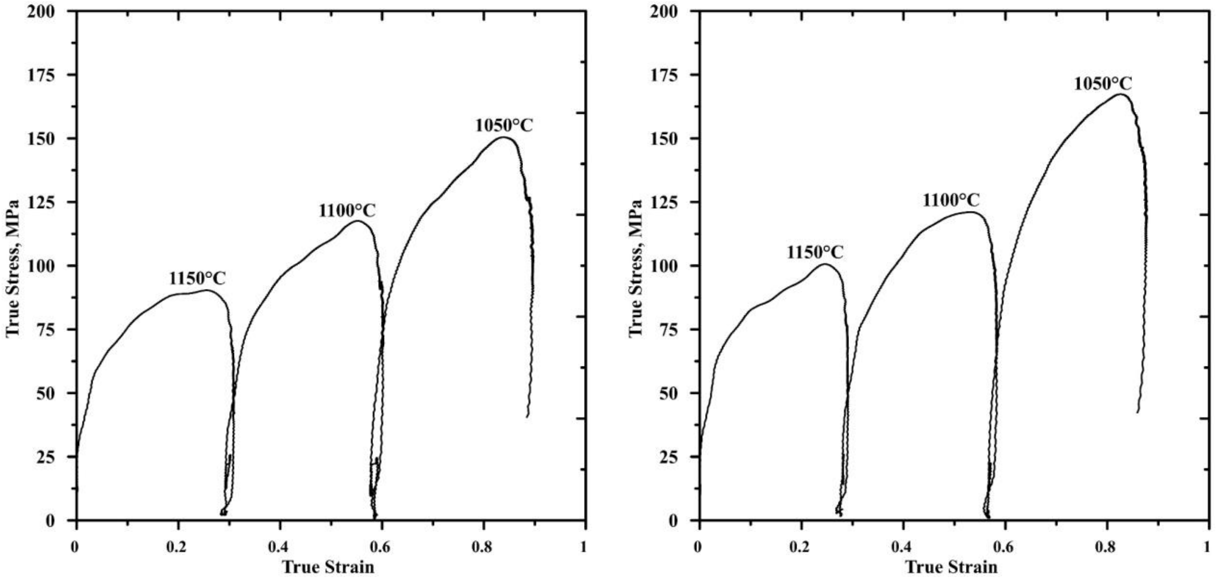

(a) (b)

Figure 10.1 True stress-true strain curves obtained from Gleeble® 3800 thermomechanical simulator for (a) H4 steel and (b) H8 steel tested at a strain rate of 10 s^{-1} and at 1150-1100-1050 °C (Schedule I in the roughing passes simulation).

Figure 10.2 depicts austenite grain structures which are obtained by three-pass reduction with 25% reduction per pass at 1150-1100-1050 °C. For H0 steel (Figure 10.2 (a)), either grain coarsening between passes occurred or the fact that initial coarse grain size caused relatively less grain refinement between deformation. This might be to the fact that the T_{GC} for H0 steel is low compared to those for Nb-containing steels and there is no preexisting inhibition system to prevent grain coarsening after static recrystallization, specifically NbC or Nb (C, N). Furthermore, it is difficult to refine an initial coarse grain size unless a high reduction or multipass reduction is employed to enhance further recrystallization. This phenomenon was studied extensively by

Tanaka and colleagues [123], who studied Nb-containing steels and found that small reductions (*e.g.,* < 6% reduction) rendered the steels in the recovery region even at high deformation temperatures. This is mainly attributed to the occurrence of selective grain-coalescence due to strain-induced grain boundary migration, creating perhaps a few coarse grains much larger than the initial size. Nevertheless, the current study employed successive reductions of 25% and it is expected that the critical reduction for partial recrystallization or complete recrystallization is attained in all the experimental steels at high deformation temperatures (*i.e.,* > 1000 °C).

In Nb-containing steels, at a given steel chemistry and deformation parameters, competition between strain-induced precipitation and static recrystallization after deformation is expected and it is rather complex to isolate each of these phenomena. Generally, recrystallization and precipitation can interact in three ways [5]: (i) recrystallization tends to decrease the dislocation density which reduces the number of precipitate nucleation sites available and hence can retard the rate of precipitation; (ii) pinning force originating from precipitate dispersion, which in turn retard or delay the progress of recrystallization; (iii) the solute drag effect affecting the grain boundary migration. Perhaps the most profound effect is the pinning force acted by strain-induced precipitation hindering recrystallization. These precipitates nucleate in austenite heterogeneously on preferential sites such as grain boundaries and dislocations. There is two schools of thought appear in the literature regarding the potential nucleation sites, Santella [104] has shown that the Nb (C, N) forms almost exclusively on grain boundaries or subgrain boundaries, while Dutta *et al.* [76] have shown that the nodes in the three-dimensional network of dislocations and the subgrain boundaries are preferential nucleation sites for Nb (C, N) precipitation. From the current research program (see Chapter 9.0), it appeared that at low deformation temperatures in the austenite field, precipitation is more favored on what were once prior austenite grain boundaries or subgrain boundaries. However, at high deformation temperatures, both nucleation sites (grain boundaries or dislocation networks) might be preferable, but the underlying mechanism is still unclear.

In the low Nb-containing steels (H4 and L4 steels), the austenite grain size was found to decrease compared to H0 steel as can be seen in Figure 10.3, and exhibited relatively uniform recrystallized grains as shown in Figure 10.2 (b) and (d). This refinement in austenite grain size may be associated directly with the Nb addition to the steels. From the solubility of NbC in H4 and L4 steels, it is expected that some strain-induced precipitation may occur allowing static recrystallization to proceed between successive deformation but at the same time preventing grain coarsening after recrystallization [6, 60]. Another effect acted on grain refinement might be associated with the solute Nb atoms, since the complete solution temperature for NbC in H4 and L4 steels are 1114 and 1063 °C, respectively. However, this conclusion could not be verified in the current study.

Figure 10.2 (c) and (e) show the austenite grain structures for H8 and L8, respectively. Doubling the amount of Nb in the steel (*i.e.,* 0.08 wt. pct.) resulted in a grain refinement but a mixed grain structure existed as in H8 steel. From the previous results obtained from the double-hit tests (Chapter 8.0), the partial recrystallization region of H8 steel was below 1050 °C and this may agree with what is observed in Figure 10.2 (c), where fine and coarse grains coexist in the austinite structure (*i.e.,* duplex microstructure). Figure 10.2 (e) shows the austenite grain structure for L8 steel obtained from the aforementioned schedule.

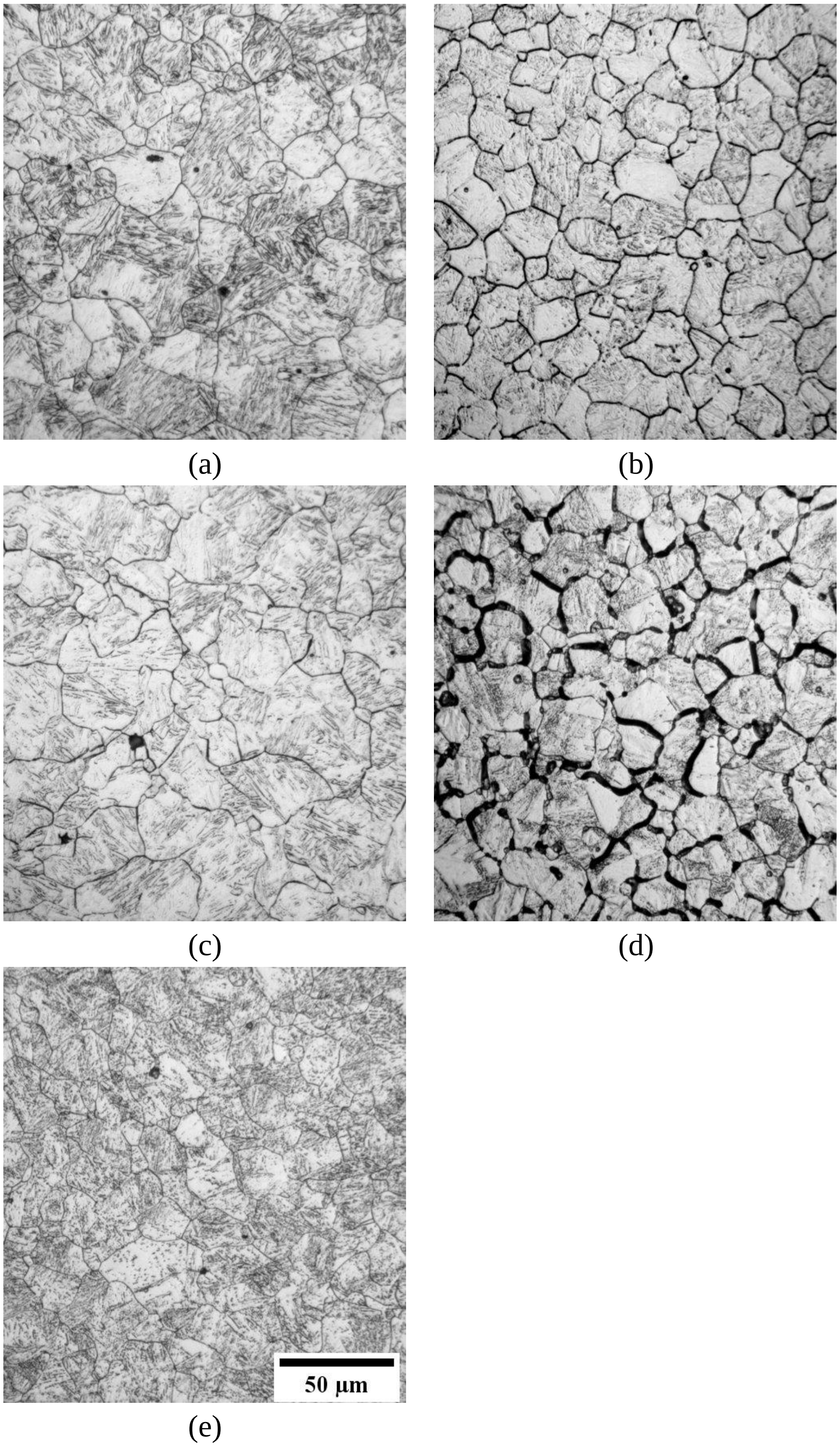

Figure 10.2 Light optical micrographs showing austenite grain structures for (a) H0, (b) H4, (c) H8, (d) L4, and (e) L8. Samples were quenched in water after hot deformation following schedule I; outlined in roughing passes simulation (Figure 5.9). Thick grain boundary lines in micrograph (d) are from the etching effect.

It appeared that the austenite grain size is comparable with H4 and L4 steels (Figure 10.3), even though the flow stress at 1050 °C for L8 steel is slightly higher compared to those for H4 or L4 steels. However, lowering the carbon content to 0.03 wt. pct. in L8 led to the same degree of grain refinement as in H4. This might represent the limit for complete recrystallization enough to cause grain refinement in L8 steel.

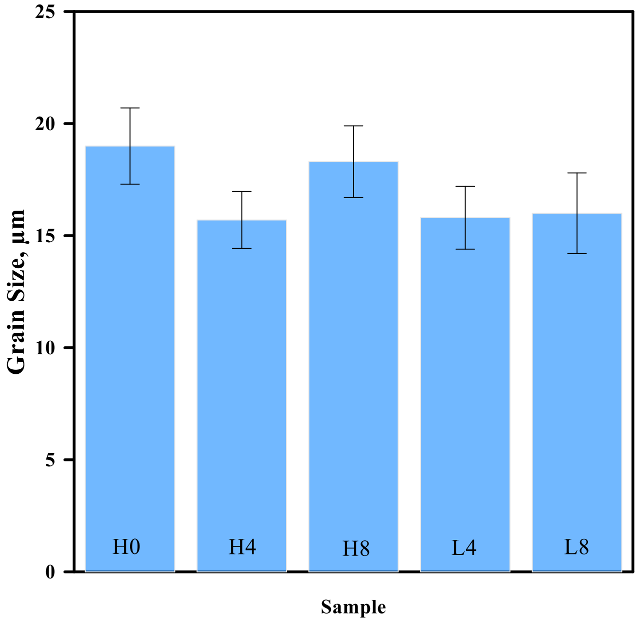

Figure 10.3 Mean austenite grain size obtained after roughing passes simulation (schedule I; 1150-1100-1050 °C). Error bars represent the 95 % confidence limit.

Roughing passes simulation was conducted at a relatively lower roughing temperature range. Figure 10.4 (a) and (b) show the true stress-true strain curves for H4 and H8 steels obtained after three-pass reduction at 1100-1050-1000 °C with an interpass time of 20 seconds. A complete set of flow curves for all tested steels is included in Appendix B. At given deformation parameters, the high temperature flow stress tends to increase gradually when temperature decrease. From the flow curves, it appeared that the peak for dynamic recrystallization was not triggered. It is well known that under low temperatures and high strain rates (*i.e.,* high Z conditions), the peak of the dynamic recrystallization becomes broad resembling a dynamic recovery curve [80]. Nevertheless, from the current investigation, the flow curve broadening was not observed since the reduction per pass was 25%. Furthermore, the flow stress curves, only yield the average and macroscopic condition of the entire samples being tested.

The peak flow stress at 1000 °C for H8 steel exhibited a slightly higher value than that for H4 steel. This might be the first indication of the difference in recrystallization behavior between H4 and H8 steels. Similar observation can be seen between L8 and L4 steels. Among all tested steels (H0, H4, H8, L4, and L8), L8 showed the maximum peak stress of 186 MPa at 1000 °C.

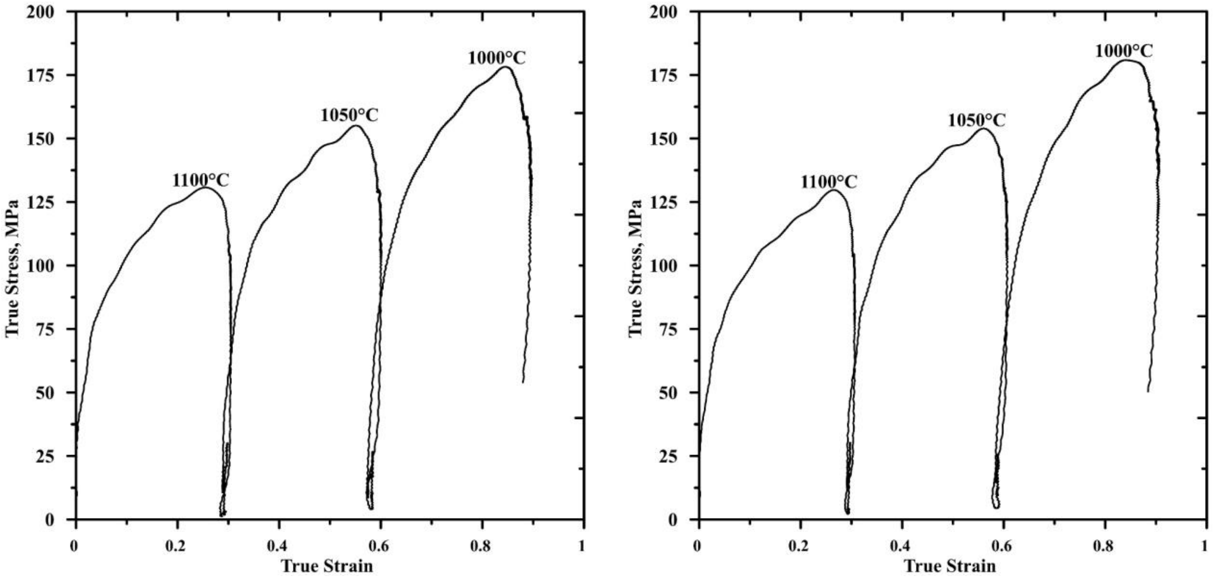

Figure 10.4 True stress-true strain curves obtained from Gleeble® 3800 thermomechanical simulator for (a) H4 steel and (b) H8 steel tested at a strain rate of 10 s-1 and at 1100-1050-1000 °C (Schedule II in the roughing passes simulation).

Figure 10.5 (a) through (e) show the austenite grain structures after quenching from the last deformation temperature at 1000 °C (schedule II). The austenite grain structures appeared to be refined compared to the previous schedule (schedule I). However, in high Nb-containing steels (H8 and L8), there are few elongated grains with highly serrated boundaries coexisting with recrystallized grains (Figure 10.5 (c) and (e)). Furthermore, in a few grains, some deformation bands were occasionally observed. On the other hand, low Nb-containing steels (H4 and L4), exhibited few coarse grains but with no indication of elongated grains. H0 steel showed grain refinement but exhibited fine and relatively coarse grains. The average grain sizes of the experimental steels are shown in Figure 10.6.

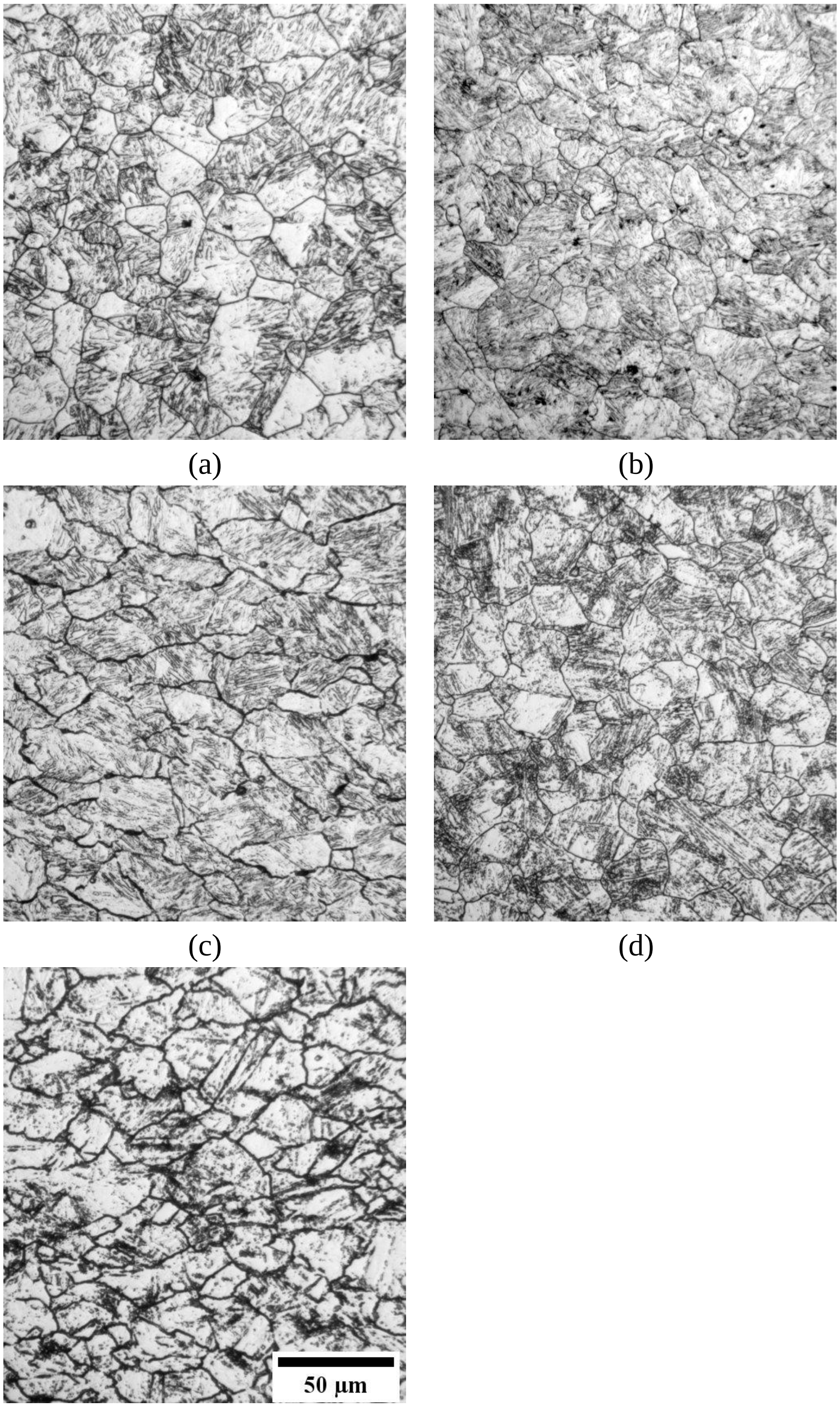

(a) (b) (c) (d) (e)

Figure 10.5 Light optical micrographs showing austenite grain structures for (a) H0, (b) H4, (c) H8, (d) L4 and (e) L8. Samples were quenched in water after hot deformation following schedule II; outlined in roughing passes simulation (Figure 5.9).

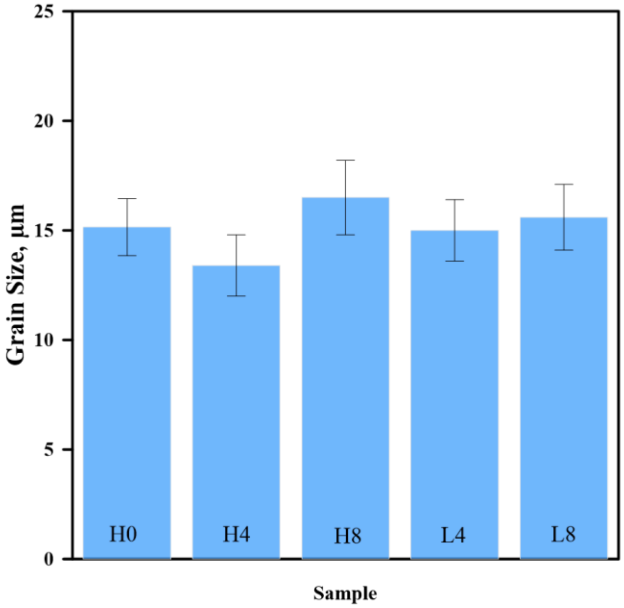

Figure 10.6 Mean austenite grain size obtained after roughing passes simulation (schedule II; 1100-1050-1000 °C). Error bars represent the 95 % confidence limit.

The preceding results suggest that there is a limiting grain size (*i.e.*, grain refinement capacity) that can be obtained in the high temperature range; for instance, a limiting grain size in rough rolling. Figure 10.2 indicates that the austenite grain structures of H4, L4, and L8 steels are more uniform than that of H8 steel. Decreasing the rouging passes temperatures (schedule II) led to duplex microstructures in H8 and L8 and less obvious microstructures in character in H4 and L4 steels.

This observation is not unreasonable since a higher tendency for strain-induced precipitation of carbides or carbonitrides is expected in H8 steel, and can be attributed to the degree of supersaturation of these precipitates in high Nb-containing steels. One possible outcome, consequently, is the occurrence of non-uniform pinning of precipitates acting on the austenite grain boundaries. This could be attributed to and originating from the competition between the driving force for recrystallization and the Zener pinning force, which in turn could yield a duplex austenite microstructure. This can be more profoundly observed in high Nb-containing steels such as HTP steels with Nb contents, nominally ≥ 0.08 wt. pct.

An important aspect of HTP steels is that they tend to be rough rolled at relatively high temperatures in order to avoid high mill loads (*i.e.*, limitation of mill load capacity) at lower temperatures. While this could be a feature, the severe retardation of recrystallization by niobium at deformation temperatures at/or below 1000 °C can results in a complex mixture of deformed and recrystallized grains (Figure 10.5 (c) and (e)) [28]. The results of the current study show that the retardation of recrystallization could be raised to higher temperatures in HTP steels (at/or below 1050 °C; Figure 10.2 (c)). Hence, the steel can enter subsequent deformation in the unrecrystallized or partially recrystallized state unless high reductions are applied to overcome partial recrystallization. Under these conditions, the unrecrystallized grains in the mixed austenite structure undergo further deformation which in turn become extremely elongated. The effective grain size of these elongated grains is similar in character to those of coarse grains.

The results of this investigation clearly demonstrate the important role of Nb on the recrystallization behavior at high deformation temperatures. Increasing the Nb content in the steel rendered the austenite in the partial recrystallization state, especially after deformation at 1100-1050-1000 °C. Elimination of such duplex grain structure in the finishing passes could be notoriously difficult and may require higher reductions in the finishing passes of hot rolling. The next section explores the effect of roughing and finishing passes on the austenite and the transformed structures.

10.1.2 Finishing Pass Simulation

10.1.2.1 Austenite and Transformation behavior

The obtained flow curves, prior austenite grains, and transformed microstructures after finishing passes simulation (Figure 5.10 and schedule I in Table 5.3) for H0 steel are presented in Figure 10.7. Finishing at 900 °C resulted in a duplex austenite microstructure as shown in Figure 10.7 (b). This was anticipated from the fact that deforming at 900 °C is within the range of partial recrystallization of H0 steel. Consequently, the transformed microstructure exhibited coarse granular bainite (GB) with few quasi-polygonal ferrites (QF) (Figure 10.7 (c)). Within these microstructures, small amounts of martensite-austenite (MA) microconstituent are observed, specifically, at the lath boundaries of GB (Figure 10.7 (d)). As pointed out by Yomamoto *et al.* [124], the GB microstructures may be regarded as a recovered bainitic ferrite microstructure accompanied by indistinct lath boundaries instead of elongated laths. Furthermore, they showed that the undeformed coarse austenite grains promote the formation of bainitic ferrite with elongated laths and preserve the austenite grain boundaries (*i.e.*, sheaf-like bainite). This was also reported by Chiou *et al.* [125] who showed that the austenite grain boundaries serve as a nucleation site for bainitic ferrite. Nevertheless, from Figure 10.7 (b), the deformed coarse austenite grains promoted bainitic ferrite but presumably, the sheaves could not be completely developed and changed to GB microstructure during air cooling. On the other hand, it appeared that the fine austenite grains promoted QF microstructure as shown in Figure 10.7 (d).

Further deformation at 850 °C brought about a different behavior in H0 steel compared to deformation at 900 °C. The coarse austenite grains become somewhat elongated while still recrystallization was not completely retarded. This is clearly shown in Figure 10.7 (f) where coarse elongated grains and fine grains coexist. The transformed microstructure, Figure 10.7 (g) and (h), show the presence of polygonal ferrite (PF) accompanied by a complex of austenite decomposition products. Depending on the cooling rate and the steel chemistry, the formation of PF by increasing the deformation of austenite is well documented in previous studies [21, 92, 126]. This is mainly attributed to the increase in austenite stored energy originating from the heavy deformation as well as the increase in the density of austenite grain boundaries and subgrain boundaries. PF predominantly nucleates at austenite grain boundaries grow inward and at the same rejecting carbon to austenite [127]. Accordingly, the remaining austinite transforms into other non-equilibrium ferrite microstructures, and the carbon-enriched region in the austenite transforms into MA constituents at much lower temperatures. The non-equilibrium ferrite microstructures can be regarded as a mixture of GB and QF, and these are referred in the literature as acicular ferrite (AF) [81, 125]. Furthermore, there is a reduction in the formation of MA constituents in H0 steel when increasing the deformation to a lower temperature.

With accumulating strain and finishing at 800 °C, the duplex microstructure still appears to be persisted and the uniform austenite grain structure (*i.e.,* proper austenite conditioning) was not attained even under such a heavy austinite deformation (Figure 10.7 (j)). Figure 10.7 (k) and (l) show the optical and SEM micrographs, respectively, of the transformed microstructure. The microstructure consists of PF, QF, classical bainite, and MA microconstituent. It is interesting to note that the size of classical bainite, as well as its fraction, are increased under these deformation conditions as shown in Figure 10.8, which is a higher magnification of Figure 10.7 (l). The increase in classical bainite fraction can be attributed to the increase of the bainite start temperature with accumulating strain [125]. Hence, qualitatively, more fraction of classical bainite would be expected upon cooling.

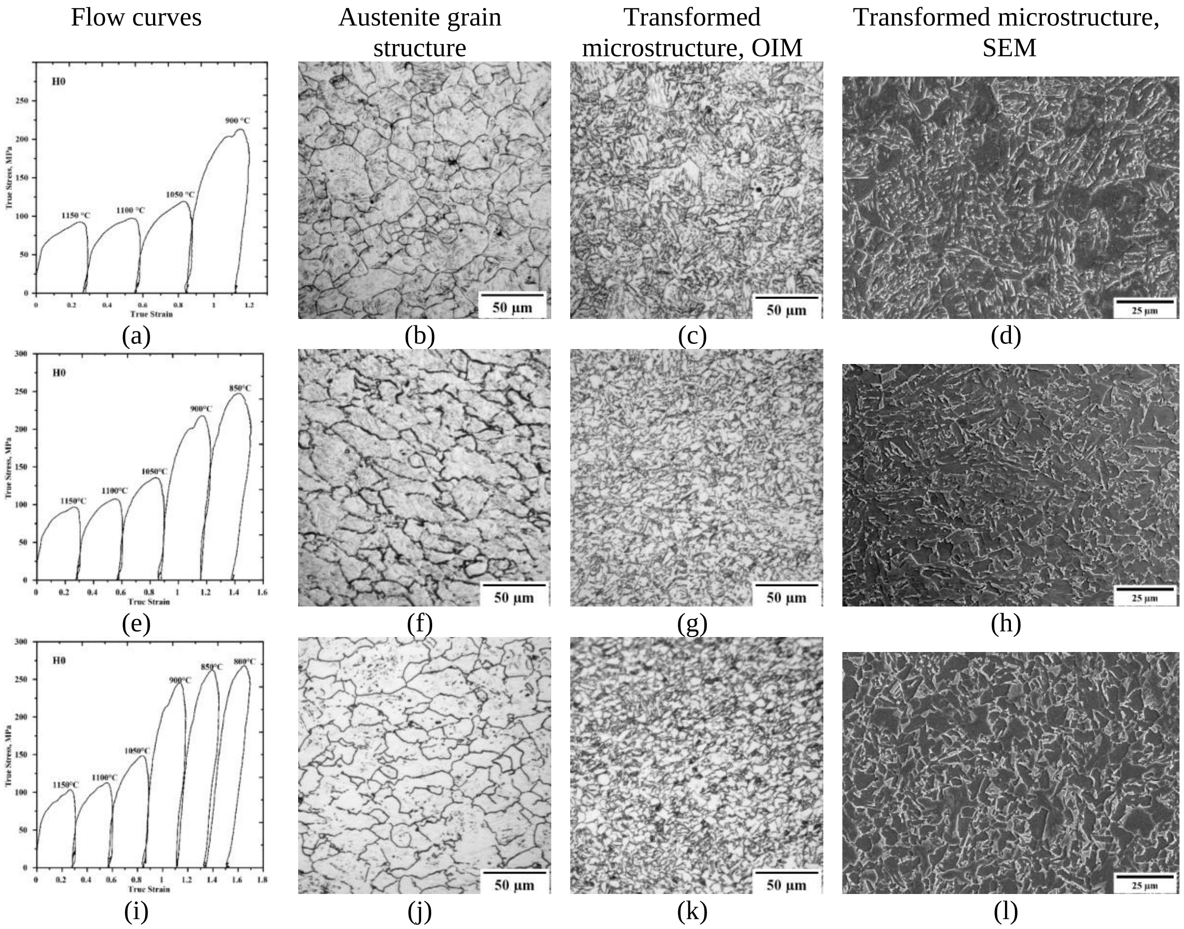

Figure 10.7 Change in the austenite and the transformed microstructure as a function of finishing temperature in H0 steel; finishing passes simulation carried out following schedule I in Table 5.3.

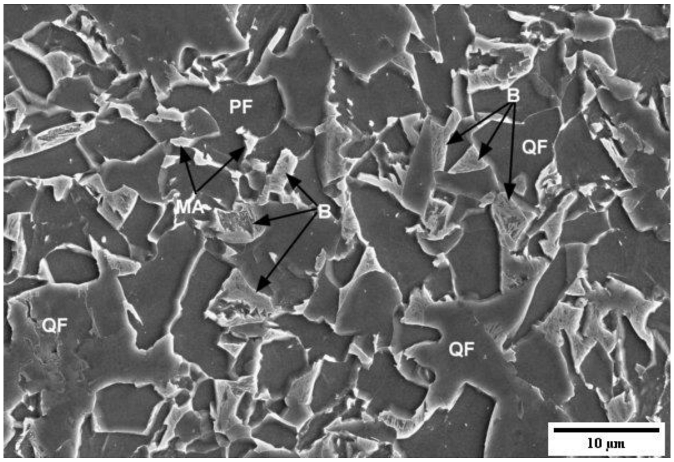

Figure 10.8 Scanning electron micrograph of H0 steel after finishing at 800 °C; Schedule I, Table 5.3.

Figure 10.9 (a) through (l) present flow curves, austenite grain structure, and transformed microstructures for H4 steel obtained after finishing passes simulation (Schedule I in Table 5.3). With decreasing deformation temperature, the flow curves tend to increase, especially at the finishing passes temperature range (Figure 10.9 (a), (e), and (i)) indicating that the austenite in the non-recrystallization region. Deforming the steel at 900 °C, which is in the range of non-recrystallization of H4 steel, produced a relatively coarse elongated austinite (17.3 ± 2.0 µm, Figure 10.9 (b)). Further deformation at 850 °C yielded fine elongated austenite grains with a size of 12.8 ± 0.6 µm (Figure 10.9 (f)). At the lowest deformation temperature of 800 °C, there appears no significant change in the austinite grain size (12.0 ± 1.2 µm).

Transformation microstructures of H4 steel show different behavior than that of H0 steel. PF is completely suppressed in H4 steel and rather, other austenite decomposition products appear. For example, finishing at 900 °C and air cooling produced non-polygonal ferrite products such as QF and GB. Also, as it can be seen from Figure 10.9 (d), some bainitic ferrite is present (*i.e.*, lath bainite), like what was observed in H0 steel (see Figure 10.7 (d)). It is believed that microalloying elements such as Nb as well as Mo tend to stabilize the ferrite phase [126, 128]. Furthermore, these elements also raise the A_{r3} temperature and hinder the decomposition of austenite predominantly by decreasing carbon diffusivity [21]. It is also believed that Nb and Mo reduce the grain boundary energy by segregating to the prior austenite grain boundary and hence, decreasing the nucleation rates of equilibrium ferrite microstructures [128].

However, it appears that the austenite and its behavior in the roughing stage are more important and have an indirect effect on the disappearance of PF microstructure. Partially recrystallized austenite grains or coarse elongated ones may produce similar microstructures (*e.g.*, Figure 10.7 (b) and (d); Figure 10.9 (b) and (d)). This is can be inferred from the fact that both H0 and H4 steels yielded a non-polygonal ferrite microstructure when cooling from 900 °C but the proportion of these non-equilibrium ferrites microstructures may differ with Nb addition. It has been shown from previous studies that austenite deformation (*i.e.,* recrystallized or unrecrystallized austenite) triggers non-equilibrium ferrite but at the same time retards its progress [80, 92, 129]. As stated previously, this is mainly attributed to the increase of the austenite stored energy and, in the case of Nb-containing steels, also, to the decrease of the amount of Nb (C, N) by strain-induced precipitation.

Cooling from 850 °C produced a fine mixture of QF and GB (*i.e.,* acicular ferrite) and MA in H4 steel and these can be seen in Figure 10.9 (g) and (h). These were originated and transformed from fully pancaked austenite. From a microstructural viewpoint, uniform grain structure (Figure 10.9 (f)); the introduction of deformation bands and other intragranular nucleation sites, enhanced the transformation microstructure and eliminated the bainitic ferrite product. However, increasing the deformation to a lower temperature of 800 °C produced an opposite trend. Some bainitic ferrite with laths appeared in the microstructure and this might be due to the heavy deformation introduced at 800 °C. Nevertheless, for H4 steel, finishing at 850 °C produced a uniform microstructure with no indication of coarse QF grains. The effective grain size and area fraction of MA will be discussed further below.

In regards to bainite and other non-polygonal ferrite formation mechanism, the subject itself has been hotly discussed over the last four decades [79, 130, 131]. There are two schools of thought on the mechanism of bainite formation. One suggests the diffusional growth mechanism [131] and the other supports the displacive formation mechanism [79]. The fundamental debate between these two schools is on the subsequent degeneration by diffusional processes. For example, the volume change occurring during transformation at low temperatures causes the steel to accommodate stresses and hence, increases the dislocation density within the lath of GB or lath bainite. The other school of thought suggested that GB or lath bainite forms through shear mechanism followed by carbon partitioning from the bainitic ferrite to the austenite [79]. In this case, regardless of volume change stresses, the dislocation density will be increased. Despite this debate on the formation of bainite, it is now agreed that the bainitic ferrite forms through displacive instead of diffusional transformation [132].

For H8 steel, the degree of pancaking increases with increasing deformation and decreasing temperature. However, a mixed microstructure exhibited after deformation at 900 °C and produced a mixture of GB, QF, and MA. With further increasing deformation and decreasing temperature, the GB is refined but some coarse QF is present as can be seen in Figure 10.10 (g) and (h). Finishing at 800 °C, yielded a finer mixture of GB and QF compared to higher finishing temperatures. This is due to the increased stored energy of the austenite and decreased hardenability in the steel [92].

One point should be emphasized regarding the austenite deformation in the H-series steels. The uniformity of the austenite, whether it be equiaxed or pancaked, should therefore produce a uniform transformed microstructure. It seems that duplex austenite grain size inherently yields coarse QF and GB microstructures. This can be seen in Figure 10.7 (b) and (d); Figure 10.10 (g) and (h). The level of bimodality in the austenite grain size could be related to the austenite conditioning and the response of Nb between successive deformation and holding. However, the level of bimodality in grain size can be subjective in nature as pointed out by Chakrabarti *et al.* [98].

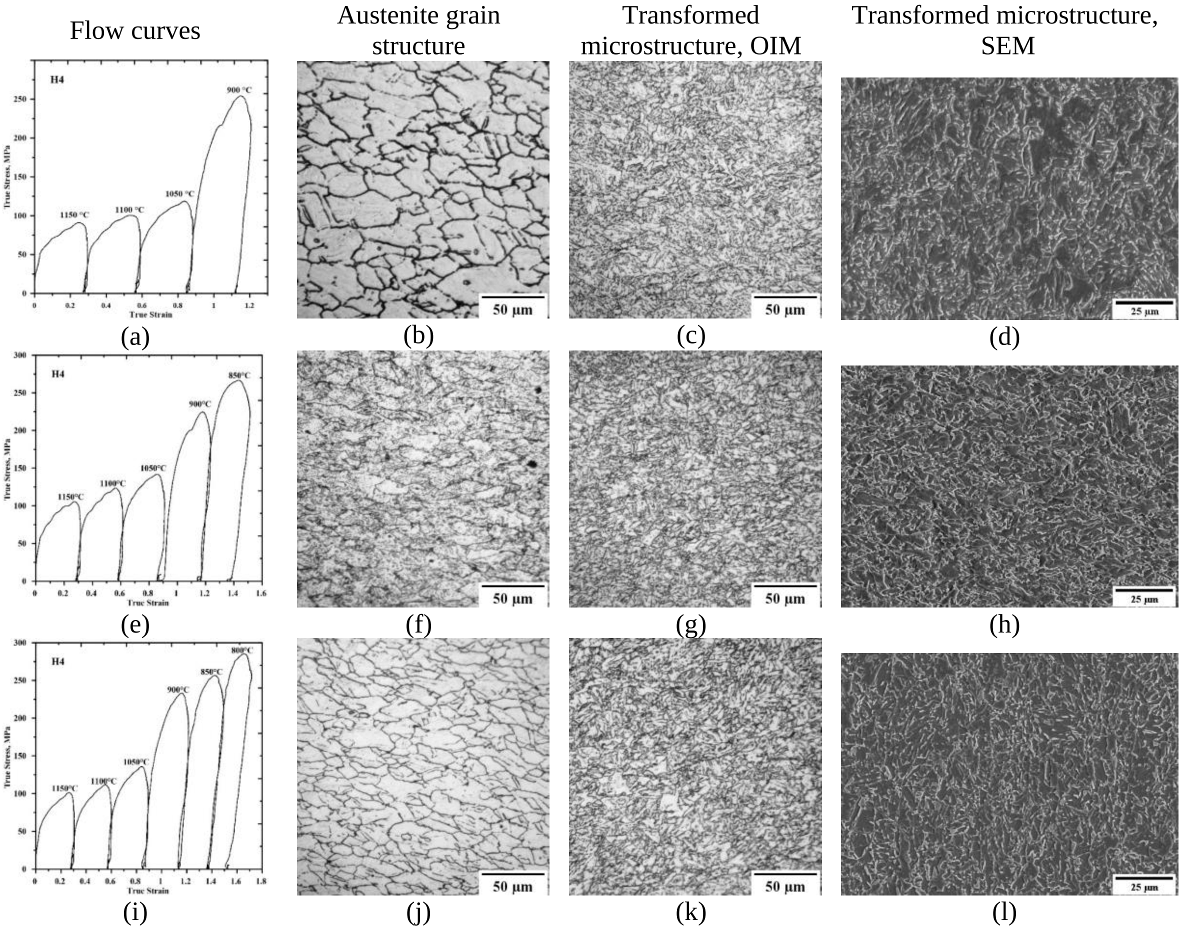

Figure 10.9 Change in the austenite and the transformed microstructure as a function of finishing temperature in H4 steel; finishing passes simulation carried out following schedule I in Table 5.3.

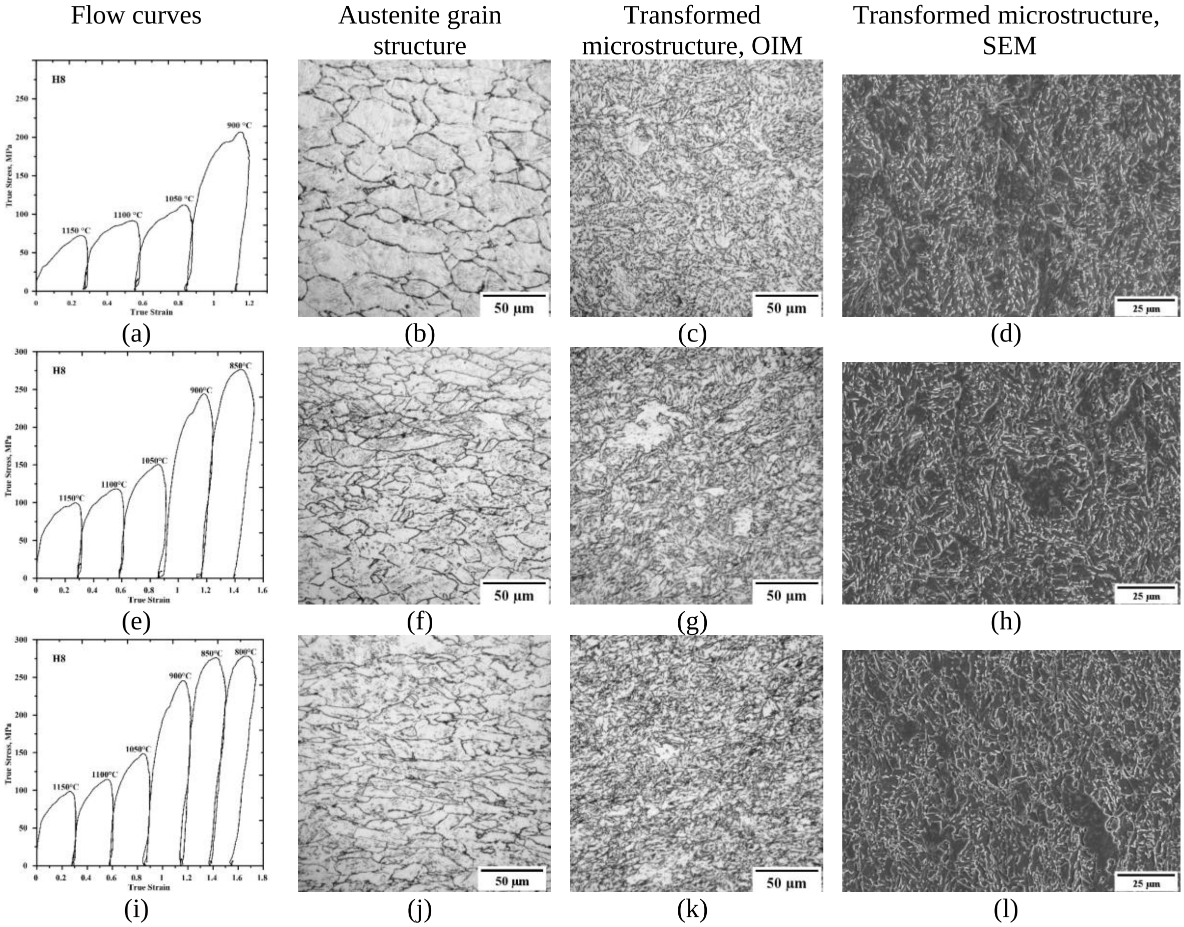

Flow curves
Austenite grain structure
Transformed microstructure, OIM
Transformed microstructure, SEM

(a) (b) (c) (d)

(e) (f) (g) (h)

(i) (j) (k) (l)

Figure 10.10 Change in the austenite and the transformed microstructure as a function of finishing temperature in H8 steel; finishing passes simulation carried out following schedule I in Table 5.3.

The flow curves, austenite grain structures, and transformed microstructures for L4 and L8 steels obtained after finishing passes simulations are presented in Figure 10.11 and Figure 10.12. Due to the low carbon content in L4 and L8 steels, the transformation behavior for both steels is somewhat different than their counterparts (H4 and H8 steels). The austenite grain size of L4 steel at 900 °C, 850 °C, and 800 °C is 16.3 ± 1.9 µm, 13.2 ± 1.5 µm, and 14.3 ± 1.7 µm, respectively. The representative austenite grain structures for L4 steels after testing at 900 °C, 850 °C, and 800 °C are shown in Figure 10.11 (b), (f), and (j), respectively. The austenite grain structures of L4 steel transformed from tested temperatures to show QF, GB, and MA microconstituents as shown in Figure 10.11 (d), (h), and (l). Similarly, a summary of the micrographs obtained for L8 steels after testing at 900 °C, 850 °C, and 800 °C is shown in Figure 10.12. It is noted from comparing the microstructures of L4 and L8 steels, the austenite grain structure of L8 steel exhibited relatively coarse elongated grains at 850 °C while L4 steel exhibited fine elongated grains at 850 °C. The coarse QF grains observed in Figure 10.12 (g) might be originated from these coarse elongated grains (Figure 10.12 (f)). While it is true that QF microstructures form at high transformation temperatures compared to other bainite microstructures, it appears that γ grain size as well as uniformity play role in the size of QF product. This can be rationalized by comparing Figure 10.11 (b) and (c); Figure 10.12 (b) and (c).

The mean austenite grain size for all experimental steels tested following schedule I are summarized in Table 10.1. It can be seen from this table, as expected, that the austenite grain size decreases with decreasing temperature and increasing total strain. It is also noted that H8 and L8 steels exhibit relatively coarser austenite grain compared to H4 and L4 steels. This is due to presumably the efficiency of austenite conditioning since recrystallization kinetic in H4 and L4 steels is accelerated at high temperatures (roughing passes) yielding more grain boundary area per unit volume. In contrast, H8 and L8 steels may show slower recrystallization kinetic, depending on the degree of strain-induced precipitation, and hence, yielding the opposite of what is in H4 and L4 steels. In the current study, other factors may affect the austenite grain size in the finishing passes. One possible factor is the isothermal holding between passes, where grain coarsening after recrystallization might occur, but this hypothesis was not tested in the current study in the region after holding at, 1050 or 1000 (*i.e.*, the austenite grain structure prior to cooling to the first finishing pass). However, the S_v value calculations show that the values for all experimental steels decrease momentarily from 1050 °C to 900 °C and then increase to 850 °C as can be seen in Figure 10.13. The drop in S_v values exhibited in H0, L4 and L8 steels at 800 °C may signify strain-induced grain boundary migration.

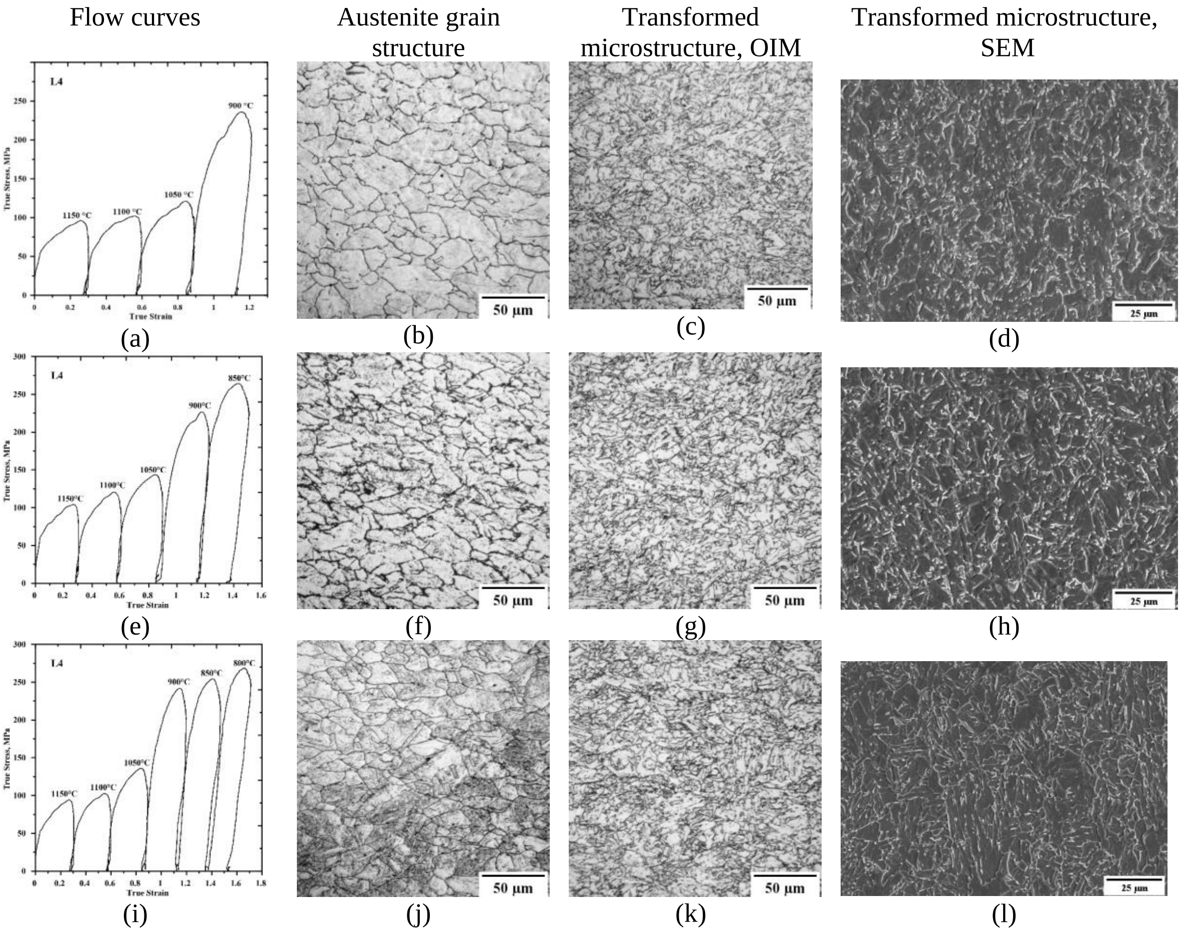

Figure 10.11 Change in the austenite and the transformed microstructure as a function of finishing temperature in L4 steel; finishing passes simulation carried out following schedule I in Table 5.3.

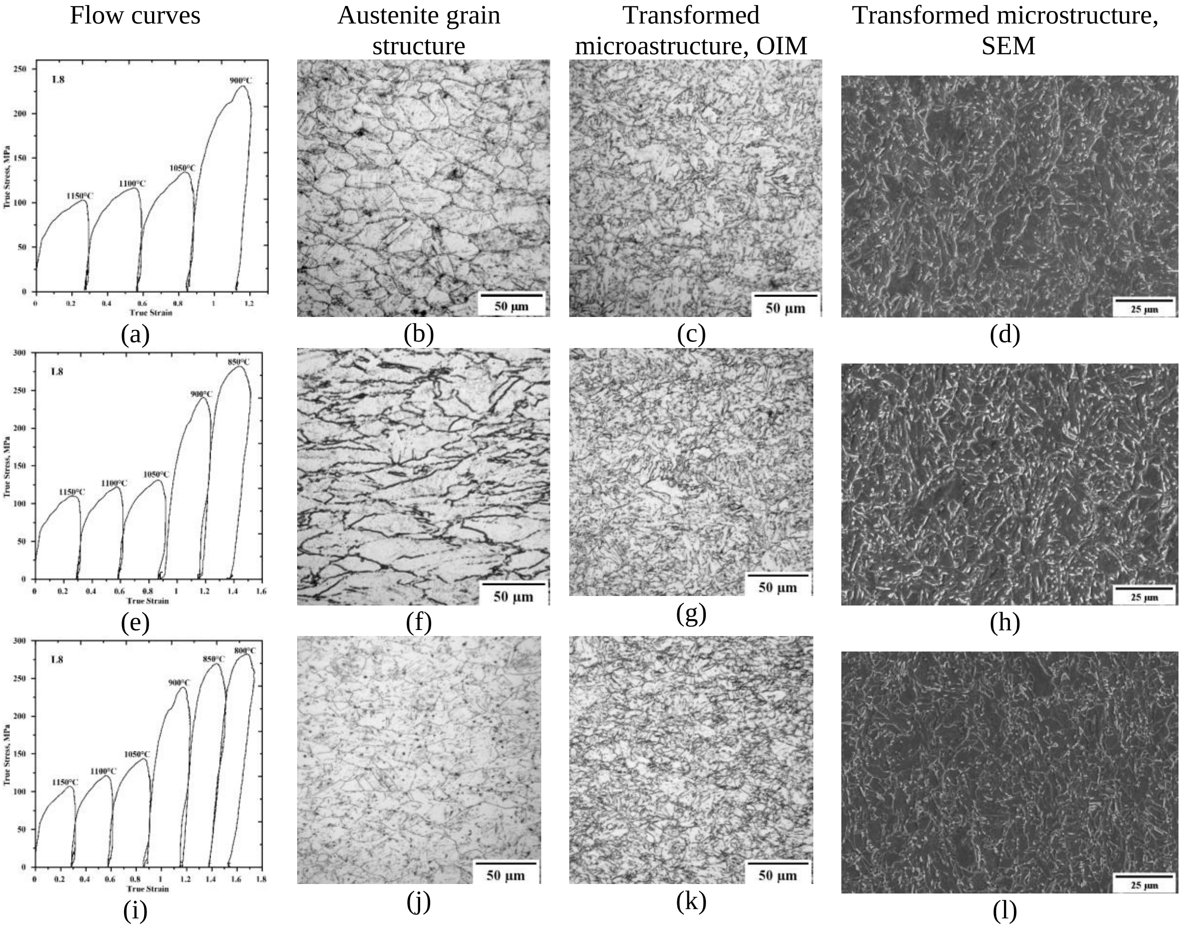

(a) (b) (c) (d)

(e) (f) (g) (h)

(i) (j) (k) (l)

Figure 10.12 Change in the austenite and the transformed microstructure as a function of finishing temperature in L8 steel; finishing passes simulation carried out following schedule I in Table 5.3.

Table 10.1 Mean austenite grain size. Finishing passes simulation carried out following schedule I in Table 5.3.

Steel	Mean austenite grain size (μm)		
	Finishing temperature		
	900 °C	850 °C	800 °C
H0	19.3 ± 2.3	15.3 ± 1.7	15.7 ± 1.6
H4	17.3 ± 2.0	12.8 ± 0.6	12.0 ± 1.2
H8	20.5 ± 3.5	15.3 ± 1.9	13.5 ± 1.7
L4	16.3 ± 1.9	13.2 ± 1.5	14.3 ± 1.7
L8	19.9 ± 2.8	15.2 ± 1.7	15.4 ± 2.2

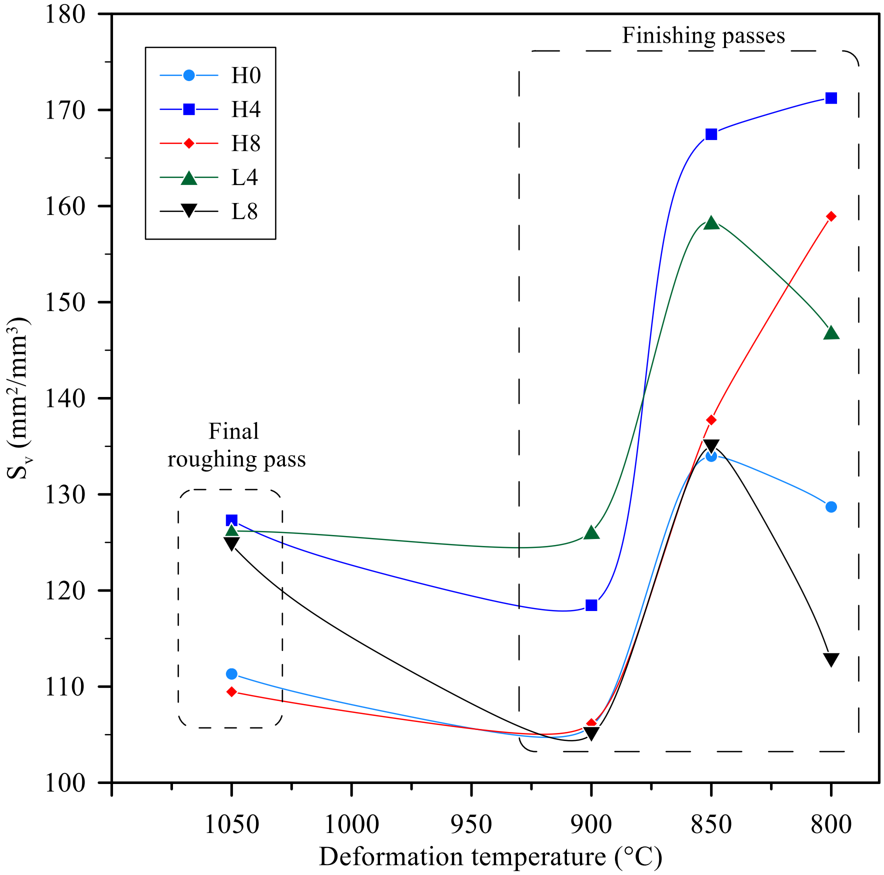

Figure 10.13 Variation of effective interfacial area (Sv) with roughing and finishing passes for the experimental steels.

Table 10.2 presents the austenite grain sizes of H0, H4, H8, L4, and L8 steels after testing a different schedule which is schedule II outlined previously in Table 5.3. A complete set of figures obtained from schedule II is included in Appendix C. The results revealed a similar trend except that the austenite grain sizes are refined not until deformation of 800 °C is induced. A slight increase in the mean austenite grain size is noted in H4 and L4 steels at 850 °C.

The transformed microstructures from schedule II are similar in characteristics to schedule I. PF microstructures are observed in air cooled H0 sample with increasing deformation, especially at 850 °C. In general, a mixture of QF and GB and MA microconstituents in other tested steels and the differences in size can be distinguished utilizing EBSD. The comparison between the two schedules carried out in this study will be discussed further below.

One important feature in these microalloyed steels is the fraction of MA microconstituents which have been shown to be detrimental to strength [133]. Table 10.3 shows the area fraction pct. of MA in the experimental steels. Also, in this table, a comparison of the area fraction pct. of MA between schedule I and schedule II. In schedule I, the area fraction pct. of MA tends to decrease with decreasing deformation. This is in agreement with the study of Chiou *et al.* [125] who reported that the fraction of MA microconstituents decreases with increasing the amount of deformation in ultra-low carbon bainitic steel. However, the area fraction pct. of MA for H8 and H8 steels after testing following schedule II shows a slight increase at 850 °C and again decrease at 800 °C. Since the cooling rate is similar, the slight increase in MA fraction might be due to the temporary increase in effective grain size at 850 °C in H4 and H8 steels.

Table 10.2 Mean austenite grain size. Finishing passes simulation carried out following schedule II in Table 5.3.

Steel	Mean austenite grain size (μm)		
	Finishing temperature		
	900 °C	850 °C	800 °C
H0	18.1 ± 2.2	15.4 ± 1.4	15.8 ± 1.3
H4	15.8 ± 2.1	17.2 ± 2.1	13.9 ± 1.7
H8	19.2 ± 2.6	18.0 ± 2.2	14.0 ± 1.5
L4	15.3 ± 1.7	17.0 ± 1.9	16.3 ± 1.8
L8	19.8 ± 2.8	19.2 ± 2.6	16.0 ± 1.7

Table 10.3 Area fraction of MA microconstituents (%),

Steel	Schedule I			Schedule II		
	900 °C	850 °C	800 °C	900 °C	850 °C	800 °C
H0	12	12.4	7.6	8.6	6.8	6.7
H4	10.5	9.2	7.8	7.7	8.9	6.8
H8	13	8.9	8.4	8.7	10.6	7.6
L4	9.7	9.2	8.3	10.8	7.3	6.9
L8	8.9	8.6	7.9	7.7	6.3	7.2

10.1.2.2 EBSD Analysis

EBSD mapping is an excellent tool to characterize microstructures in low carbon HSLA steels where nonpolygonal ferrites or complex bainitic microstructures are present [21, 80, 93, 126, 132]. This technique has been adapted in research in HSLA steels since the information gained from EBSD orientation scanning, to name one of them, enables the identification of misorientation angles of grain boundaries. Usually, 15° and 4° thresholds are used in literature to identify the effective grain size and the substructure unit size, respectively, though the true values are still being disputed in the literature. The reasoning for choosing these values is because the substructure unit size (*i.e.*, low misorientation angles) is reported to be one of the controlling factors of the yield and tensile strength and the effective grain size (*i.e.*, high misorientation angles) controls the toughness behavior by opposing cleavage fracture [22, 93, 134]. Although there is no agreed cut off value for the substructure unit size (*e.g.*, 4°, 3°, 2° or 1° normally reported in literature), 3° and 15° misorientation angles thresholds were adapted in the current study to identify the substructure unit size and the effective grain size, respectively.

Figure 10.14 and Figure 10.15 summarize the inverse pole figures and the misorientation boundary maps obtained by EBSD for the experimental steels which were tested following schedule I and schedule II, respectively. As an example, from Figure 10.14, one can see that H4 steel at 850 °C exhibits fine effective grain size and a moderate fraction of low angle misorientation. But increasing the deformation and decreasing the deformation temperature yielded relatively coarse effective grain size. In contrast, H8 steel shows a fine effective grain size at 800 °C in schedule II (see Figure 10.15, H8 at 800 °C). Similarly, this also applies to L8 steel, where it appeared to be refined at 800 °C due to the accumulated strain in schedule II, overcoming what was a coarse austenite grain structure at 850 °C. In the case of L4 steel, it is noticed that there is an increase in the fraction of low angle misorientation in the samples air cooled from 800 °C in both schedules I and II (L4 steel, 800 °C in Figure 10.14 and 10.15). This could be due to the decreased fraction of QF microstructures at the expense of BF or GB.

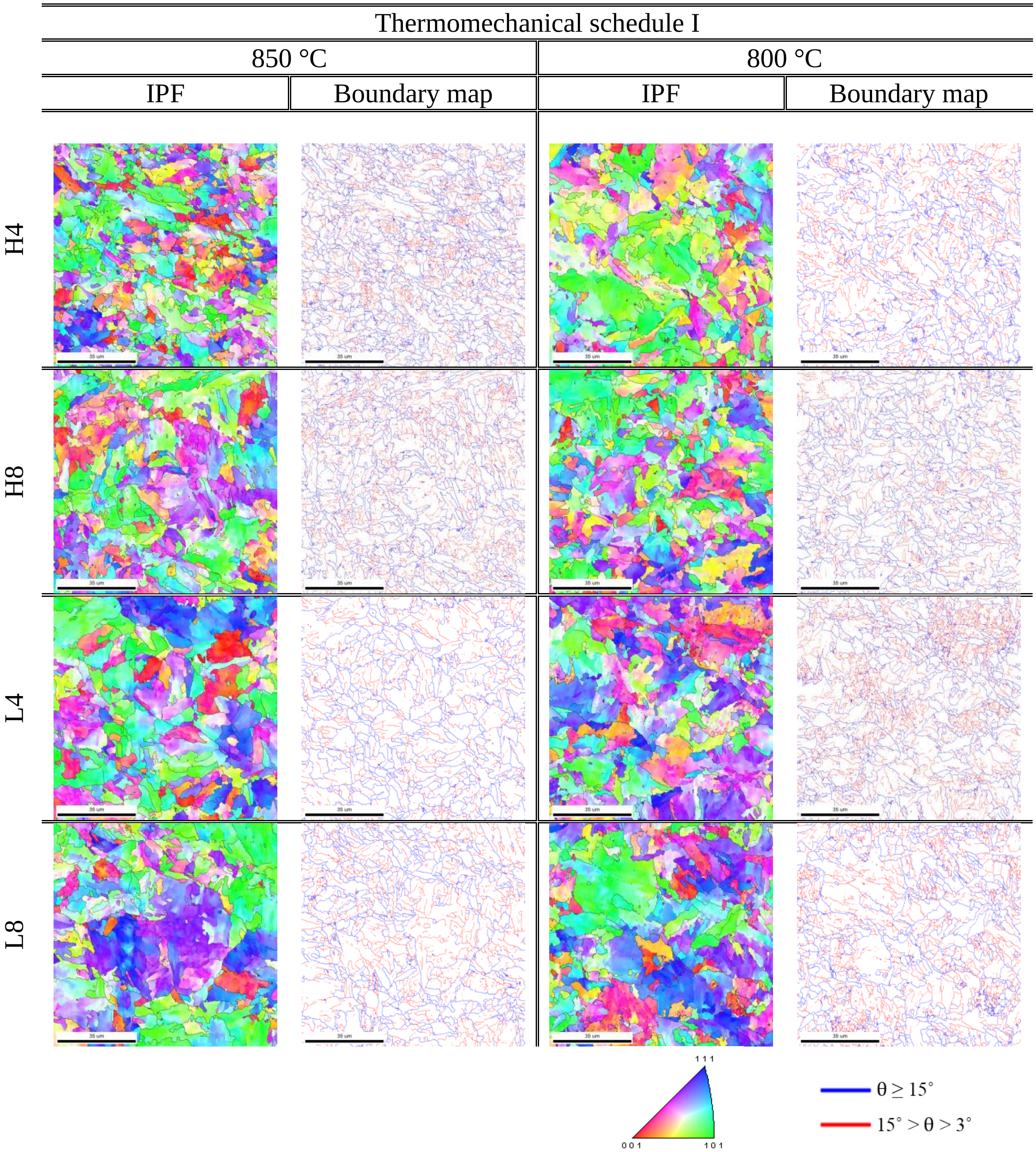

Figure 10.14 Inverse pole figures (IPF) and misorientation boundary maps obtained by EBSD for Nb-containing steels (Thermomechanical schedule I).

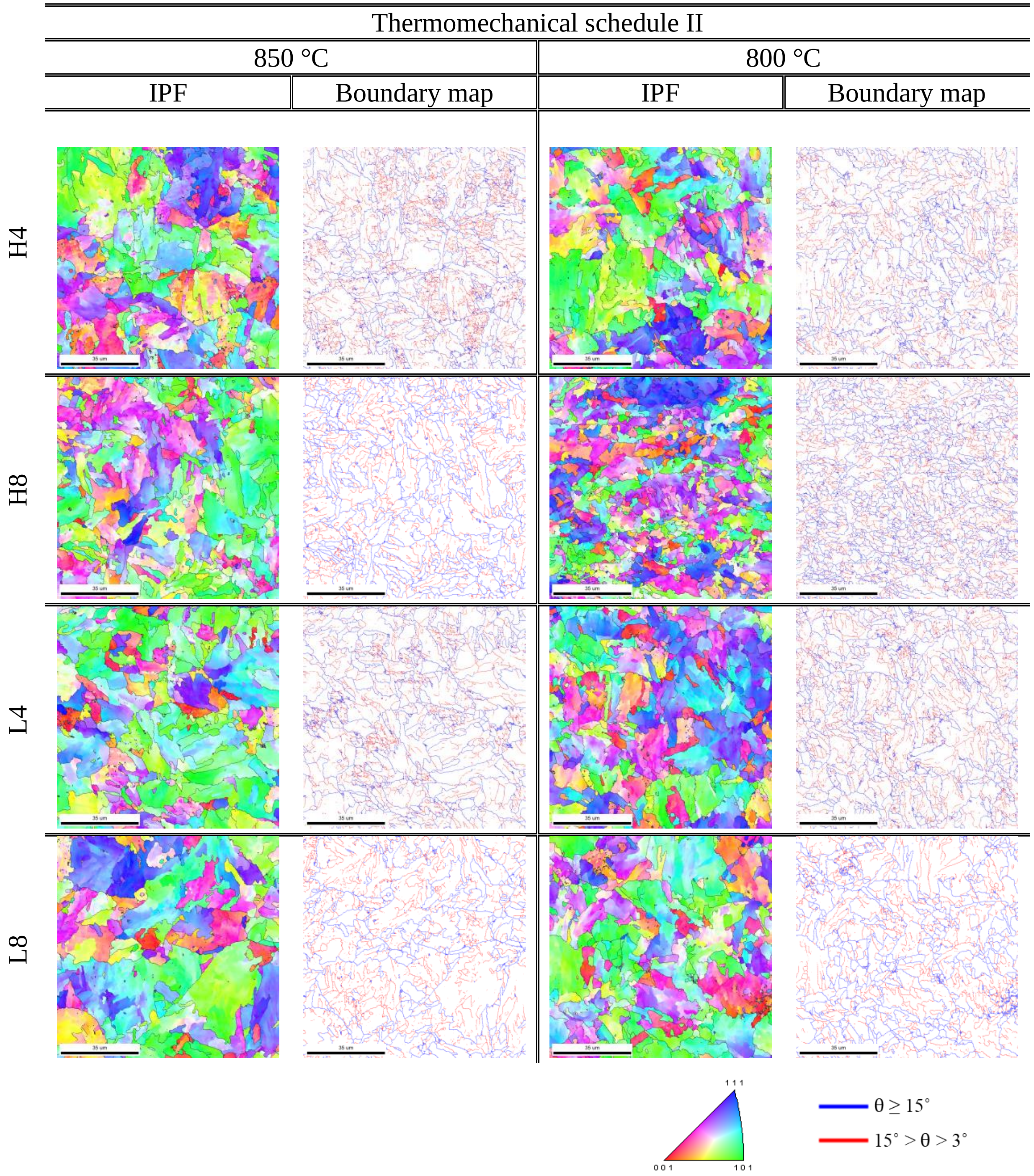

Figure 10.15 Inverse pole figures (IPF) and misorientation boundary maps obtained by EBSD for Nb-containing steels (Thermomechanical schedule II).

To assess the boundary misorientation angles, the number fraction for all boundaries was plotted. Figure 10.16 shows the distribution of misorientation angles obtained by EBSD for Nb-containing steels. The general characteristic of such figures is in the intensity of specific distribution of misorientation angles. For example, for displacive microstructures such as martensite or bainite, a higher intensity of misorientation angles following the Kurdjumov-Sachs (K-S) or Nishiyama–Wasserman (N-W) orientation relationship with the parent austenite would appear [21, 80, 129, 135]. This corresponds to high intensity of misorientation angles in the range of 50° to 60° and in the range 0° to 20°; and to a low intensity of misorientation angles in the range of 20 to 47° [80, 135]. The fraction of misorientation angles ranging from approximately 20° to 47° in H4 tested at 850 °C in schedule I is relatively increased compared to other steels (Figure 10.16 (a)). This confirms that H4 steel exhibit fine QF and GB microstructures obtained from this specific schedule. Furthermore, polygonal ferrite is suppressed in all Nb-containing steels on both schedules, since the intensity of misorientation angles in the range of 20 to 47° are generally low. When polygonal ferrite is present in the microstructure, which represents a typical diffusional-controlled product, a random distribution would appear in the range of 20 to 47° misorientation angles and low intensity distribution in the range 0° to 20° [21, 135]. Among all steels, H8 shows high intensity of misorientation angles in the range of 50 to 60°. This could be attributed to the presence of GB at the expense of QF microstructure. It is also noted that the number fraction of low angle grain boundaries in L4 steels is increased at the lowest deformation temperature (Figure 10.16 (b) and (d)). This suggests that the presence of BF with laths in which increased dislocation density led to the increase in the number fraction of low angle grain boundaries.

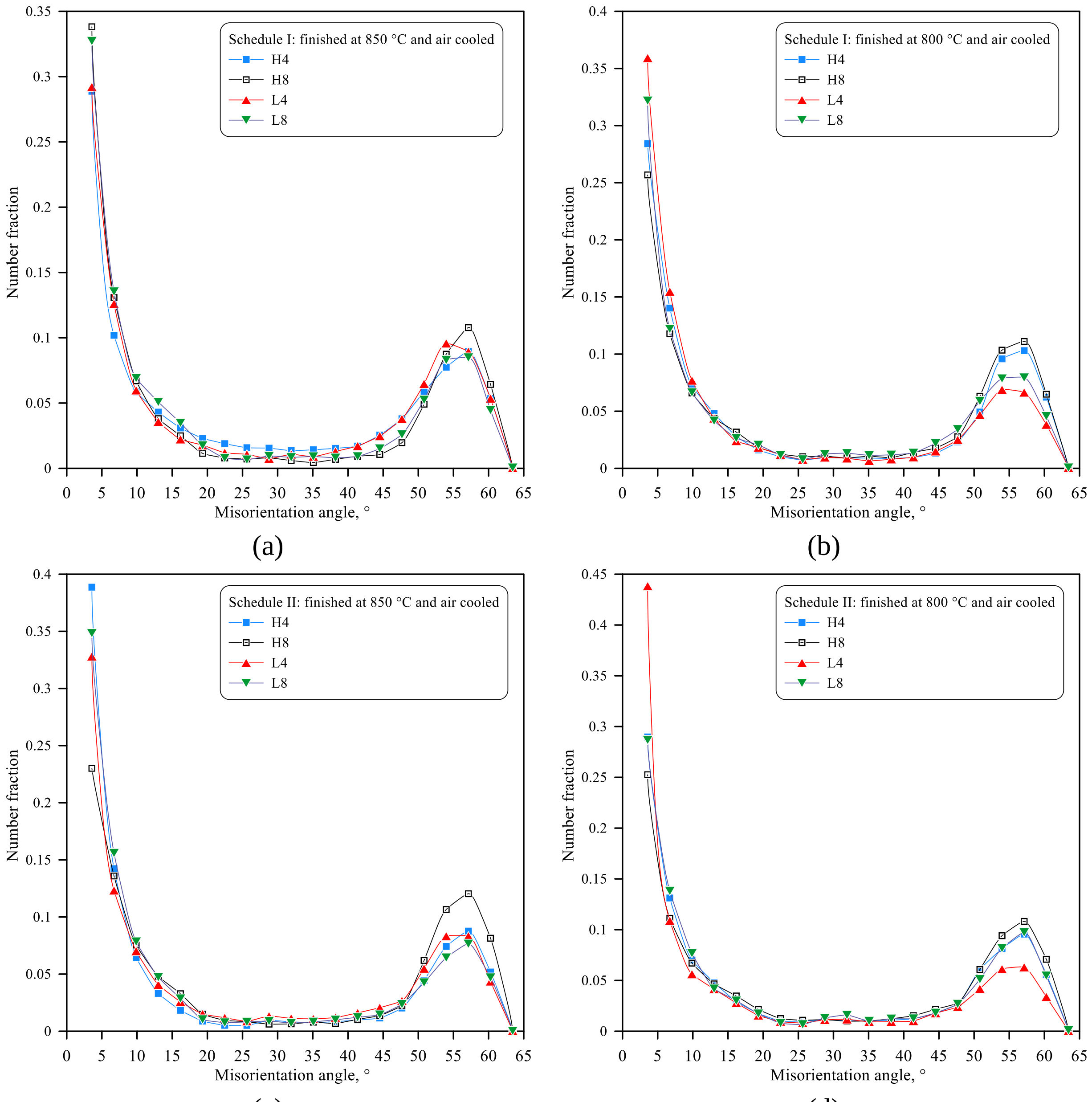

(a) (b)

(c) (d)

Figure 10.16 Distribution of boundary misorientation angles obtained for Nb containing steels following Schedule I at (a) 850 °C and (b) 800 °C; and Schedule II at (c) 850 °C and (d) 800 °C.

To further assess the misorientation angles for the purpose of comparison between the experimental steels, the effective grain size corresponding to high angle grain boundaries greater than 15° was measured. Table 10.4 displays the effective grain size of tested samples obtained from the finishing passes simulation. In general, this table reveals that the effective grain size decreases with increasing strain and decreasing temperature from 900 °C to 850 °C for all steels. However, for H4 steel cooled from 850 °C from schedule I, the effective grain size showed the lowest value of 5.6 ± 0.4 but increased to 7.6 ± 0.8 cooled from 800 °C and this could be originated from the absence of fine QF grains. For H8 steel cooled from 800 °C from schedule II, the effective grain size showed the lowest value of 5.4 ± 0.4 and this could be a suitable schedule for H8 steel to decrease the effective grain size.

Table 10.4 Effective grain size (mean linear intercept) formed from finishing passes simulation.

Steel	Schedule I			Schedule II		
	900 °C	850 °C	800 °C	900 °C	850 °C	800 °C
H0	9.1 ±1.0	7.9 ± 0.6	7.4 ± 0.6	9.0 ± 0.8	8.5 ± 0.8	7.9 ± 0.7
H4	6.2 ± 0.5	5.6 ± 0.4	7.6 ± 0.8	7.6 ± 0.7	8.4 ± 0.8	7.7 ± 0.7
H8	8.4 ± 0.8	6.4 ± 0.5	6.3 ± 0.6	8.4 ± 0.8	7.4 ± 0.7	5.4 ± 0.4
L4	9.8 ± 1.0	7.2 ± 0.7	7.4 ± 0.6	8.9 ± 0.8	8.1 ± 0.7	7.4 ± 0.7
L8	8.7 ± 0.7	7.5 ± 0.7	6.1 ± 0.5	9.4 ± 0.8	8.4 ± 0.6	7.9 ± 0.8

10.1.2.3 Vickers Hardness Measurements

Figure 10.17 (a) and (b) show the Vickers hardness values obtained from the finishing passes simulation. For a given thermomechanical schedule, increasing C and Nb contents led to an increased in the microhardness and this is clearly shown in H4 and H8 steels. The microhardness values presented here could be affected by the overall microstructures, and specifically by the amount and size of MA microconstituents, substructure unit size, and precipitation hardening increments during austenite-ferrite transformation. From schedule I and cooling from deformation temperature at 900 °C, H8 steel yielded higher microhardness values (249 ± 1.94) in comparison to other temperatures as well as to other tested steels. The decrease in the microhardness value observed at 850 °C for H8 can be attributed to the decrease in the area fraction of MA exhibited in all steels. Similarly, this is also observed in H0 steel, where the presence of PF grains with low dislocation densities led to a reduction in the microhardness from 900 to 850 °C by 6.3 % (Figure 10.17 (a)). The combination of fine effective grain size and reduced MA area fraction could be beneficial to the strength as shown by H4 steel finished at 850 °C. There is also an increase in the microhardness value for L8 steel from 850 °C to 800 °C due to the increased dislocation density and reduced effective grain size. Concerning schedule II, there is a temporary drop in the microhardness values at 850 °C in all steels except L4 as shown in (Figure 10.17 (b)). Overall, for a given steel chemistry and thermomechanical schedule, Figure 10.17 reveals that the roughing schedule plays a role in the differences in microhardness values. A combination of fine effective grain size, the reduced area fraction of MA, and adequate dislocation densities could be inherited from a uniformly conditioned austenite.

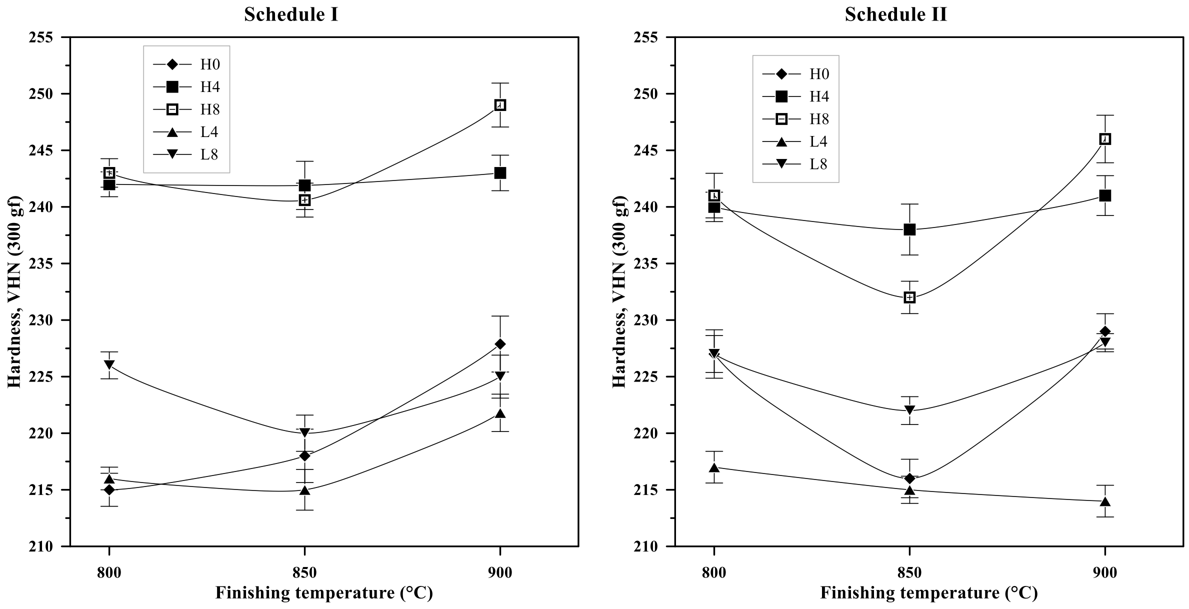

(a) (b)

Figure 10.17 Vickers hardness values of the experimental steels obtained after finishing-passes simulation: (a) schedule I and (b) schedule II, error bars represent standard deviations of ten readings.

10.1.3 Accelerated Cooling Studies

The thermomechanical schedule used in the ACC studies is listed in the upper part of Figure 10.18 (1150-1100-1050-900-800 °C + ACC to 500 °C+ air-cooled). It should be mentioned that over the temperature range of finishing passes, the deformation at 850 °C was not conducted instead, cooling from 900 °C to 800 °C then deforming samples, ACC at a rate of 30 °C sec^{-1} to 500 °C, and air cooled to room temperature. Figure 10.18 displays the inverse pole figures and misorientation boundary maps for all steels in this research program. The figure reveals that as C and Nb contents in the steel increased, the fraction of substructures is increased, being lowest in L0 steel and highest in H8 steel. This was expected since H8 exhibited lath-like bainite or BF and MA microconstituents, while L0 exhibited a mixture of PF, QF, and GB. This could be related to the austenite grain size after finishing and the decreased hardenability of the investigated steel.

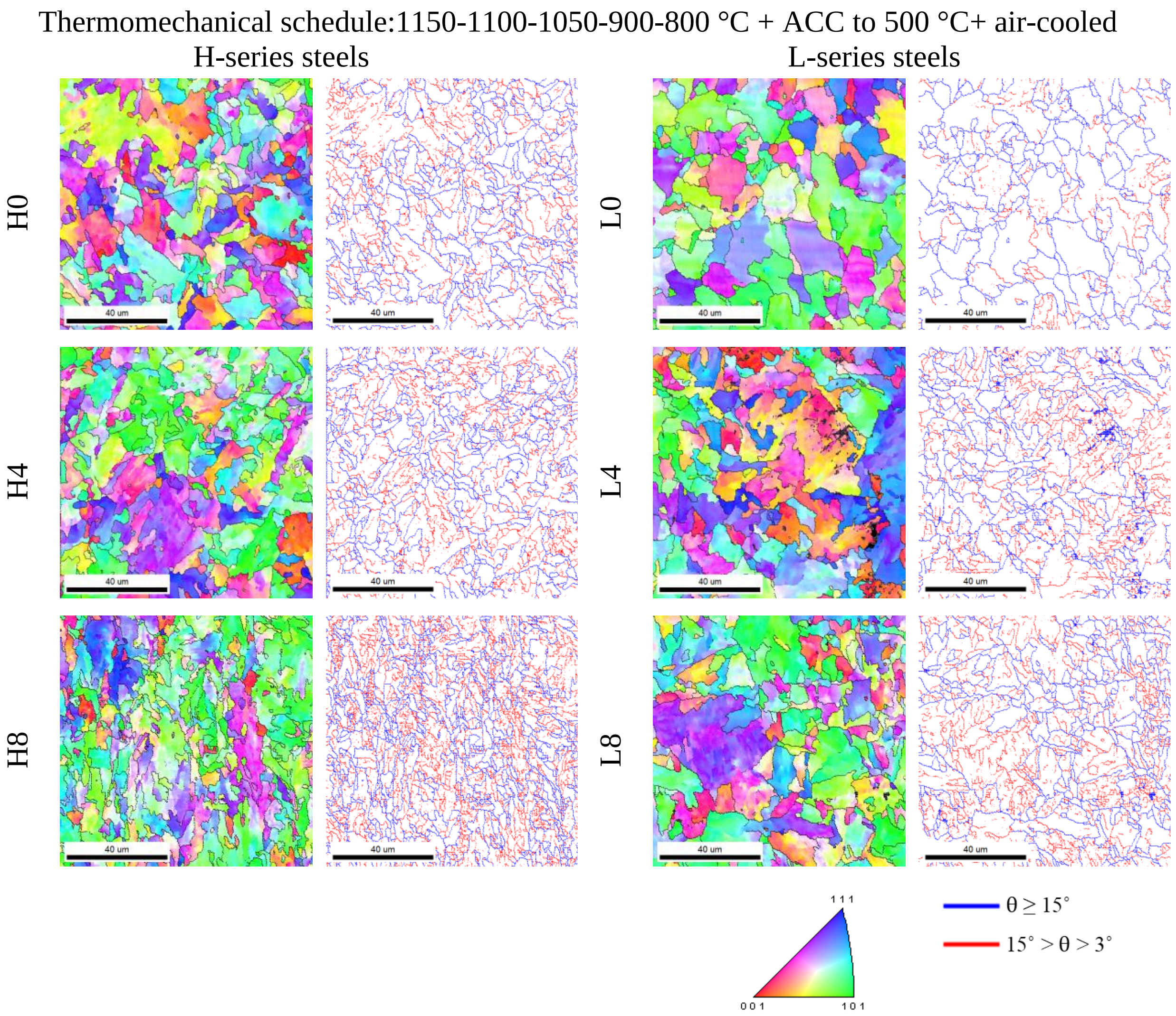

Figure 10.18 Inverse pole figures (IPF) and misorientation boundary maps obtained by EBSD of all-experimental steels obtained after ACC simulation.

The distribution of grain boundary misorientation angles of ACC cooled samples is shown in Figure 10.19. It is noted from this figure that L0 exhibits relatively much higher grain boundary misorientation angles of intermediate range (*i.e.*, 20°- 47°). This also indicates that L0 steel exhibits PF along with other microstructure products since PF-dominate microstructures would yield a random distribution of grain boundary misorientation angles. Furthermore, PF in H0 sample is reduced by ACC to 500 °C due to the reduced growth rate of PF minimizing its formation.

From an inspection of the distribution of grain boundary, misorientation angles of ACC cooled samples, the number fraction of low misorientation angles is increased, in ascending order, in L0, L4, H0, L8, H4, and H8 steels. Over the range 50°- 60° misorientation angles, the H4 sample shows the highest intensity. This indicates that an increase in C and Nb contents does not necessarily produce a monotonic increase in the number fraction of low misorientation angles and high misorientation angles. Other factors interplay such as uniform austenite grain size (from thermomechanical history) as well as precipitation behavior in the investigated steel. This is directly related to the steel hardenability where austenite stored energy and the precipitation of NbC or Nb (C, N) which lowers the amount of Nb in solid solution.

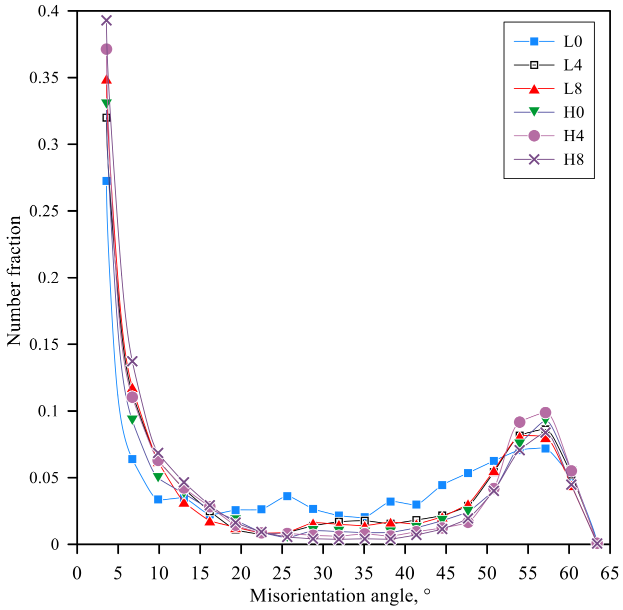

Figure 10.19 Distribution of misorientation angles obtained for all experimental steels. Steels were ACC to 500 °C after hot deformation at 1150-1100-1050-900-800 °C.

Nanoindentation technique is another method to distinguish the complex phases such as bainite and non-equilibrium ferrite that exhibit in HSLA steels [136], and ferrite-martensite that exhibit in Advanced High Strength Steels (AHSS) [137].

Figure 10.20 (a) through (f) show the SEM micrographs of the nanoindents performed (circled) on H0, L0, H4, L4, H8 and L8 steels, respectively. The base for L-series steels (L0) reveals PF microstructure with some AF and MA microconstituents as shown in Figure 10.20 (b). In contrast, the base for H0-series steels (H0), PF grains appeared to be suppressed by ACC to 500 °C. Instead, a mixture of GB and QF microstructure is observed (Figure 10.20 (a)). However, with Nb addition, the microstructure of GB and QF becomes refined and can be safely designated as AF. For simplicity, the nanoindentation measurements of PF, AF, and MA nanohadness are reported.

Table 10.5 summarizes the nanohardness values for all steels that were ACC to 500 °C. The total average of nanohardness values, from Table 10.5, increases in ascending order: L0, H0, L8, L4, H4, and H8. The total average of nanohardness values is altered by the presence of MA microconstituents and AF or PF. Taking H4 and H8 steels as an example, the average nanohardness value of MA microconstituents in H4 and H8 steels are 4.66 ± 0.53 and 5.36 ± 0.63, respectively. Furthermore, a concrete conclusion regarding the nanohardness values would be possible if large samples of nanoindents were performed, since the probability of indents landing on MA, AF or PF is expected to be different. Nevertheless, the results presented here give an insight into the importance of the thermomechanical history of the steel, especially in the roughing passes and the inherited austenite grain structure in the finishing passes.

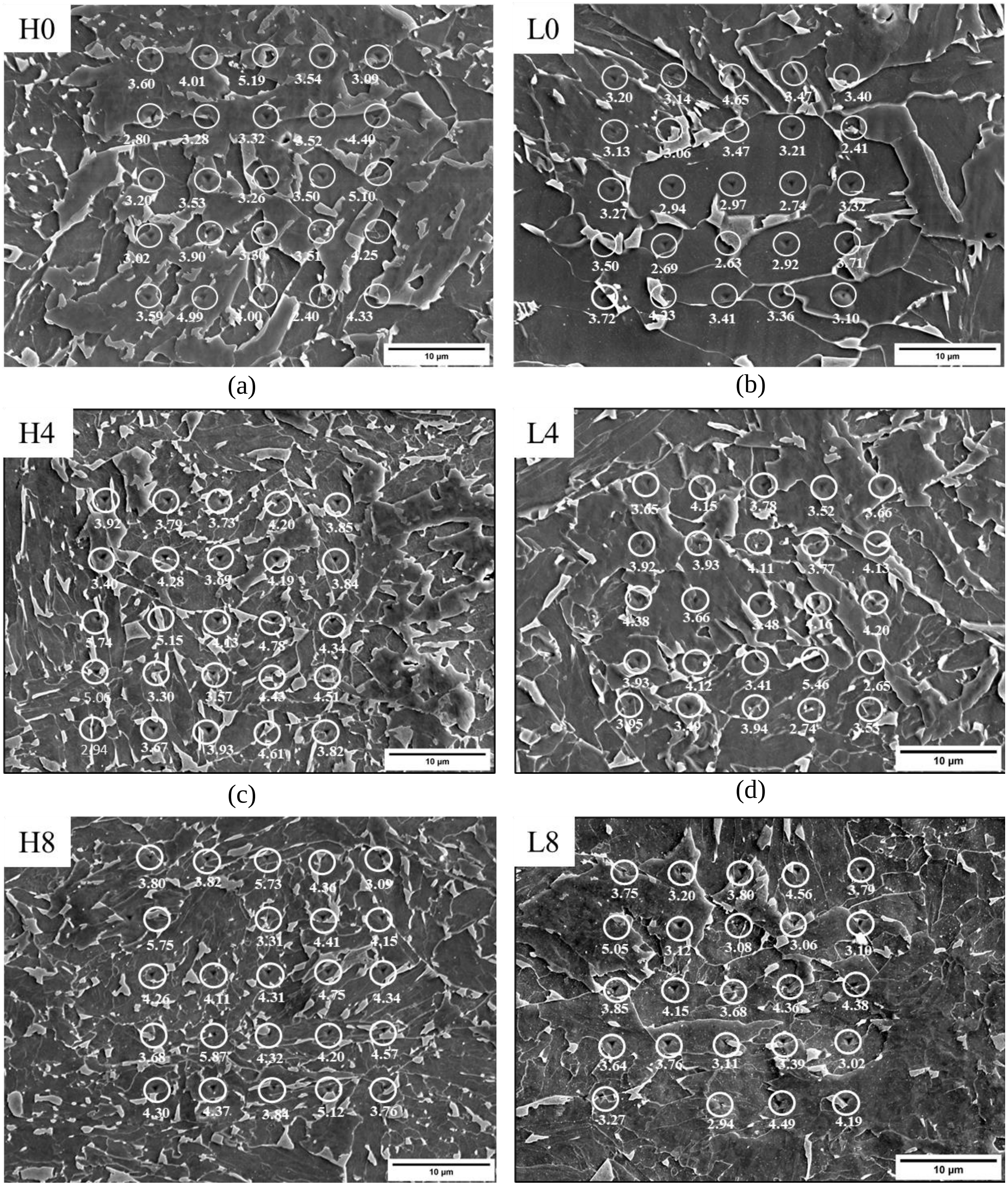

(a) (b)

(c) (d)

(e) (f)

Figure 10.20 Nanoindents performed on ACC samples to 500 °C: (a) L0, (b) H0, (c) H4, (d) L4, (e) H8 and (f) L8. Units of nanoindents measurements are in GPa.

Table 10.5 Nanohardness of the experimental steels; ACC to 500 °C

Steel	Nanohardness (GPa)		
	PF	AF	MA
H0	——	3.32 ± 0.35	4.46 ± 0.48
H4	——	3.80 ± 0.43	4.66 ± 0.53
H8	——	4.00 ± 0.40	5.36 ± 0.63
L0	2.76 ± 0.20	3.36 ± 0.19	4.44 ± 0.29
L4	——	3.60 ± 0.38	4.37 ± 0.50
L8	——	3.40 ± 0.33	4.50 ± 0.30

10.2 Summary

This study focused on thermomechanical simulation in the temperature range of roughing, finishing and ACC of the experimental steels. Mainly, the austenite state and its transformation product were emphasized. The findings from this study can be summarized as follows:

1. The maximum true stress for H8 steel at 1050 °C is approximately 167 MPa, while for H4 is around 150 MPa. This trend is also observed between L4 and L8 streels; at 1050 °C, L8 steel exhibited higher flow stress than the flow stress of L4 steel.
2. The flow stress for H0 steel at 1050 °C, exhibited a slightly higher value (~ 157 MPa) compared to H4 (~ 150 MPa) and L4 (~ 151 MPa) steels but lower than H8 (~ 167 MPa) and L8 (~ 164 MPa) steels.
3. The relatively high flow stresses exhibited in high Nb-containing steels (H8 and L8) may be attributed to either the solute drag effect from solute Nb or more

profoundly to the strain-induced precipitation of NbC or Nb (C, N). This was also associated with the extent of austenite recrystallization or recovery since softer austenite leads to low flow stress.

4. In the low Nb-containing steels (H4 and L4 steels), the austenite grain size was found to decrease compared to H0 steel.
5. Doubling the amount of Nb in the steel (*i.e.*, 0.08 wt. pct.) resulted in a grain refinement but a mixed grain structure existed as in H8 steel.
6. The retardation of recrystallization could be raised to higher temperatures (*e.g.*, at/or below 1050 °C) in HTP steels, 0.1 Nb wt pct. Hence, the steel can enter subsequent deformation in the unrecrystallized or partially recrystallized state.
7. In the temperature range of finishing pass, the transformed microstructure of H0, air cooled from 900 °C, exhibited coarse granular bainite (GB) with few quasi-polygonal ferrites (QF). Within these microstructures, small amounts of martensite-austenite (MA) microconstituent were observed. Furthermore, there is a reduction in the formation of MA constituents in H0 steel when increasing the deformation to a lower temperature.
8. In Nb containing steels, PF is completely suppressed and rather, other austenite decomposition products appeared.
9. While it is true that QF microstructures form at high transformation temperatures compared to other bainite microstructures, it appears that γ grain size as well as uniformity play role in the size of QF product.
10. the S_v value calculations show that the values for all experimental steels decrease momentarily from 1050 °C to 900 °C and then increase to 850 °C.

11. From Schedule II, H4 steel at 850 °C exhibits fine effective grain size of the transformed microstructure and a moderate fraction of low angle misorientation. But increasing the deformation and decreasing the deformation temperature yielded relatively coarse effective grain size.
12. For H4 steel cooled from 850 °C from schedule I, the effective grain size showed the lowest value of 5.6 ± 0.4 µm but increased to 7.6 ± 0.8 µm cooled from 800 °C and this could be originated from the absence of fine QF grains. For H8 steel cooled from 800 °C from schedule II, the effective grain size showed the lowest value of 5.4 ± 0.4 and this could be a suitable schedule for H8 steel to decrease the effective grain size.
13. Overall, for a given steel chemistry and thermomechanical schedule, the roughing schedule plays a role in the differences in microhardness values. A combination of fine effective grain size, the reduced area fraction of MA, and adequate dislocation densities could be inherited from a uniformly conditioned austenite.
14. ACC studies revealed that as C and Nb contents in the steel increased, the fraction of substructures is increased, being lowest in L0 steel and highest in H8 steel. This was expected since H8 exhibited lath-like bainite or BF and MA microconstituents, while L0 exhibited a mixture of PF, QF, and GB. With Nb addition, the microstructure of GB and QF becomes refined.
15. The total average of matrix nanohardness values obtained from ACC to 500 °C, increases in ascending order: L0, H0, L8, L4, H4, and H8. The total average of nanohardness values is altered by the presence of MA microconstituents and AF or PF.

11.0 Conclusions

Six HSLA steels were developed to investigate the effect of thermomechanical processing on the constituent austenite, emphasizing high temperature processing, and its subsequent transformation products. Two base steels, designated as L0 and H0, were chosen to have a respective carbon level of 0.03 pct. and 0.06 pct. and chemical composition near X100 grade. To these base steels, two Nb levels of 0.04 pct. and 0.08 pct. were added to replicate TMCP and HTP steels, respectively. The Nb-containing steels were designated as L4, L8, H4, and H8, where L8 and H8 are the high Nb ones (*i.e.,* HTP steels). Furthermore, all six steels contained addition of 0.0145 pct. Ti which is near the stoichiometric level of TiN. The choice of C and Nb levels were based on established solubility equation as well as on the modified Zener pinning force (subgrain boundary model).

Extensive experimental studies on the progress of the microstructure through reheating and subsequent roughing, finishing and accelerated cooling simulations were conducted following the schemes shown previously in section 5.2. Of these conducted experiments, double-hit tests were critical to better understanding the extent of austenite recrystallization in the temperature range of roughing and finishing pass, namely, between 1150 °C and 900°C.

Reheating experiments showed that, in general, as the Nb content increases, the grain coarsening temperature increases. However, among all the experimental steels, L4 steel exhibited the lowest grain size at all temperatures. Presumably, this is due in part to the effectiveness of TiN and NbC precipitates in suppressing grain coarsening, especially at high austenitizing temperatures. Furthermore, particle-stimulated nucleation of austenite grains might be triggered in L4 due in part to the undissolved precipitates, giving fine grain size at high reheating temperature.

Base steels, H0 and L0, exhibited the lowest grain-coarsening temperatures compared to the Nb-containing steels. The amount of dissolved NbC precipitates calculated using Thermo-Calc showed lower values in comparison with the solubility equation obtained by Palmiere *et al.* [30].

Preliminary hot-deformation studies gave insight for subsequent studies which include the choice of reduction per pass, interpass time, and deformation temperature. A 25 pct. reduction per pass and interpass time of 20 seconds were chosen for the Gleeble testing to simulate plate mill rolling on 5 m-wide plate rolling mill.

Double-hit tests results indicated that as the Nb content is increased, the extent of recrystallization is decreased. For example, steels of the same Nb level (H8 and L8) exhibited higher flow stresses compared to the other lower Nb steels (H4 and L4) and this could be a sign of competition between hardening and recrystallization mechanisms of austenite. The fractional softening due to isothermal static recrystallization was determined by the net change in the work hardening between the first and the second hit of the double-hit test under a constant true strain rate of 10 sec^{-1}. At 1050 °C, H8 steel showed the lowest softening compared to other steels tested at the same temperature. Furthermore, the 50-pct. or higher softening or higher is shifted to 1000 °C for H8 and L8 compared to H4 and L4 at around 950 °C. From the double-hit test results, the recrystallization- stop temperatures $T_{5\%}$, of 932 °C, 913 °C, and 900 °C were obtained for steels H8, L8, and L4, respectively. The other steels, H4 and H0, exhibited presumably lower $T_{5\%}$ which was below the tested temperature of 900 °C. It can be expected that $T_{5\%}$ for H4 is between 850 °C and 900 °C and H0 is between 850 °C and 800 °C for the same deformation conditions and delay time of 20 seconds. Additionally, there exists a plateau which indicated that strain-induced precipitates of Nb, carbides or carbonitrides are taking place, hence, hindering further recrystallization. The plateau in fractional softening can be attributed to precipitates pinning the grain boundaries which temporarily suppress recrystallization progress.

The Precipitation-time-temperature (PPT) curves for all experimental steels were calculated using the Dutta-Sellars model [76]. The C-curve nose of H8 was close to 1000 °C, while L4 steel the C-curve nose was close to 850 °C. This is due to the high Nb content in H8 and is in line with the existing plateau in the fractional softening curve. Precipitation evolution was estimated using the precipitation module of Thermo-Calc (TC-PRISMA). The results showed that the volume fraction of precipitates increases with time up to 300 seconds for H8 and L8 at the two temperatures of 950 °C and 1000 °C. This emphasizes that the Zener pinning force is expected to be higher than the recrystallization driving force for the case of H8 and L8 steels as compared to H4 and L4 steels. In view of these results, it should be pointed out that the recrystallization start-finish times under industrial conditions could be somewhat shorter than what was determined in these laboratory studies. Full scale or laboratory mill studies may reflect the true times or at least verify the current data.

Roughing pass simulation revealed that doubling the amount of Nb in the steel (*i.e.,* 0.08 wt. pct.) resulted in a grain refinement but a mixed grain structure developed as in H8 steel. The retardation of recrystallization could be raised to higher temperatures in HTP steels (at/or below 1050 °C). Hence, the austenite of high Nb steels can enter subsequent deformation in the unrecrystallized or partially recrystallized state instead of full recrystallization as expected.

Overall, for a given steel chemistry and thermomechanical schedule, the roughing schedule plays a role in the final mechanical properties. A combination of fine effective grain size, reduced area fraction of MA, and adequate dislocation densities could be inherited in the finishing pass or accelerated cooling processing from a uniformly conditioned austenite.

12.0 Future Work

This research program explored the influence of Nb addition (*i.e.*, 0.04 and 0.08 pct.) with different carbon levels on the austenite behavior of HSLA steels and its transformation products. Specifically, the grain coarsening behavior and the extent of austenite recrystallization were discussed. Furthermore, two different roughing pass schedules and its effect on the finishing pass as well as subsequent accelerated cooling were simulated. For future directions, several areas could be pursued:

1. Since interesting results have emerged from the grain-coarsening studies, especially from L4 and H8 steels, special attention should be considered to evaluate the precipitate nature in L4 steel during reheating. While the current reheating study explored only the reheated grain size in the full austenite field, studying precipitate volume fraction, size and composition at high reheating temperatures via systematic TEM studies would be insightful. Furthermore, whether particle-stimulated nucleation (PSN) of the preexisting precipitates play role in altering the reheated austenite grain size or not, this area needs further explanation.
2. It would be interesting to obtain via experiments, a solubility equation for the complex precipitates such as (Ti, Nb) (C, N). This might be done by utilizing Atom Probe Tomography (APT).
3. Thermomechanical simulations of roughing and finishing passes with isothermal interpass time of 20 seconds were explored in the current research program. From these simulations, it is suggested to study the effect

of roughing and finishing pass with different interpass times (*e.g.*, > 20 seconds) and continuous cooling between successive passes on the austenite grain size and the final transformation product.

4. Since the effective grain size and substructure unit size are respectively germane parameters to the strength and toughness in Nb-Ti containing steels, these parameters need to be explored in tested slabs from a laboratory mill and compare them with those obtained from the current laboratory study. Additionally, comparison between different threshold of misorientation angles could be explored. From these studies, tensile and Charpy V tests could confirm the desired thermomechanical schedule for better strength and toughness.

Appendix A Double-Hit Tests: Optical Micrographs

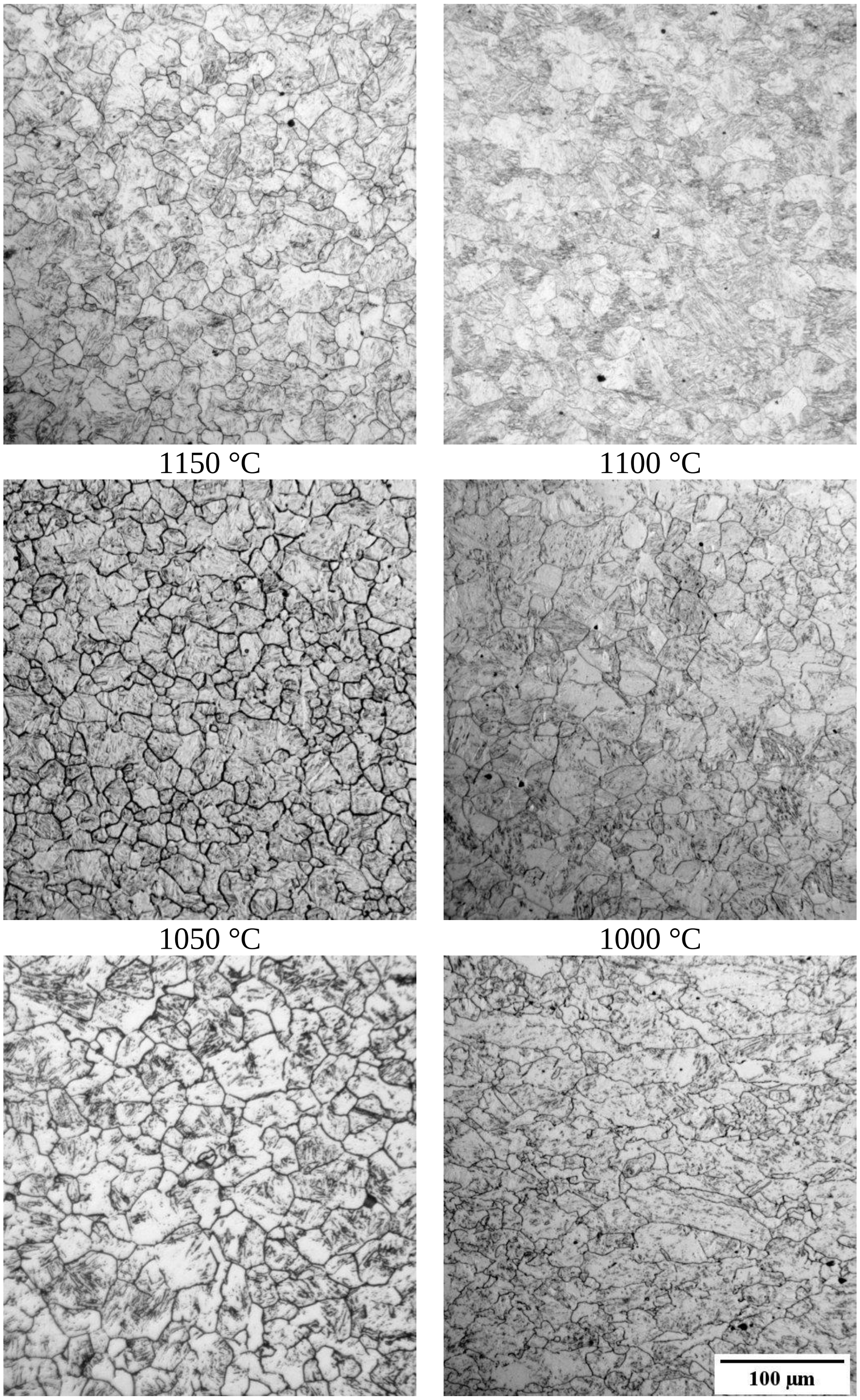

1150 °C 1100 °C

1050 °C 1000 °C

950 °C 900 °C

Figure A.1 Prior austenite grain structure of H0 at respective deformation temperatures.

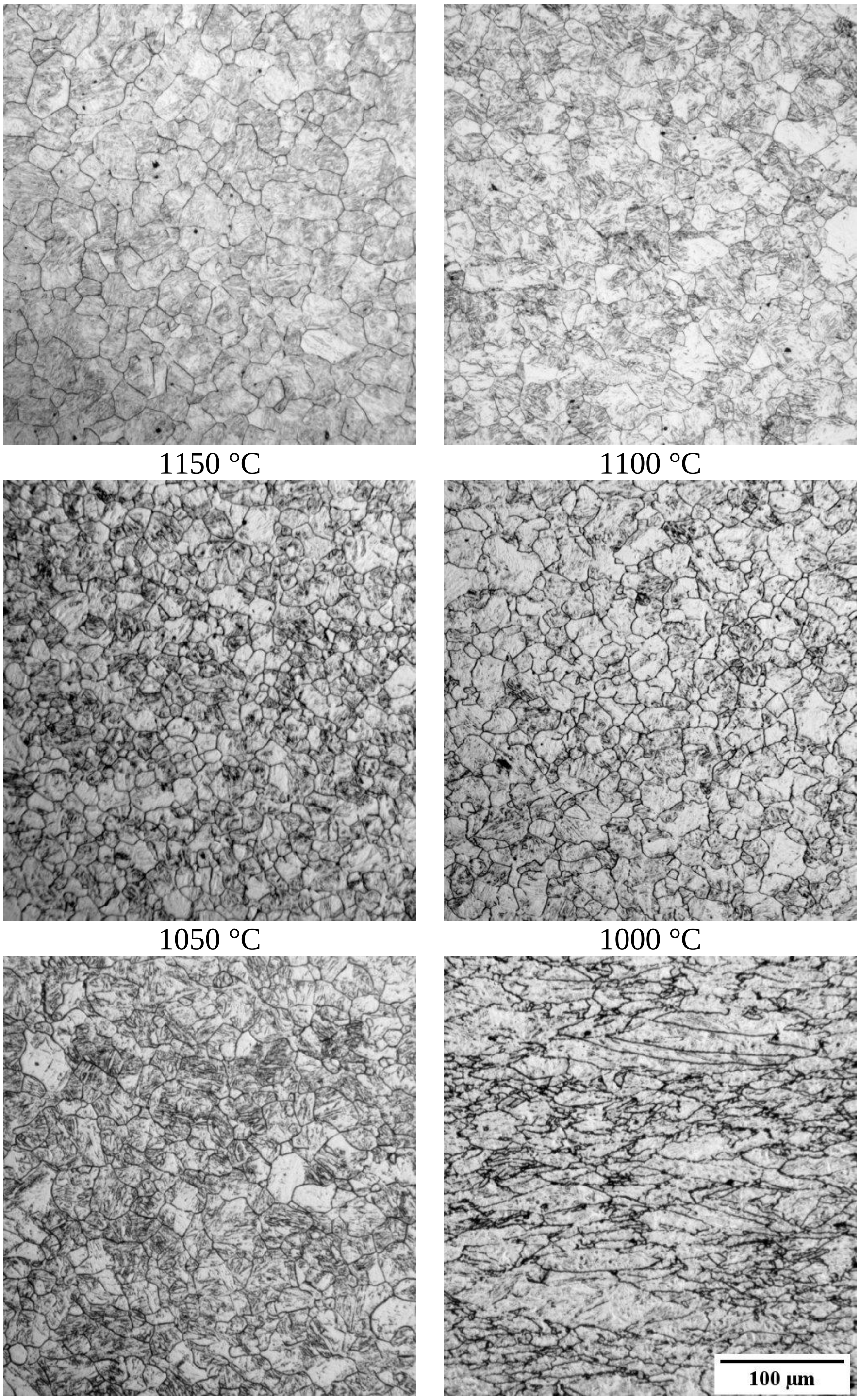

1150 °C 1100 °C

1050 °C 1000 °C

950 °C 900 °C

Figure A.2 Prior austenite grain structure of H4 at respective deformation temperatures.

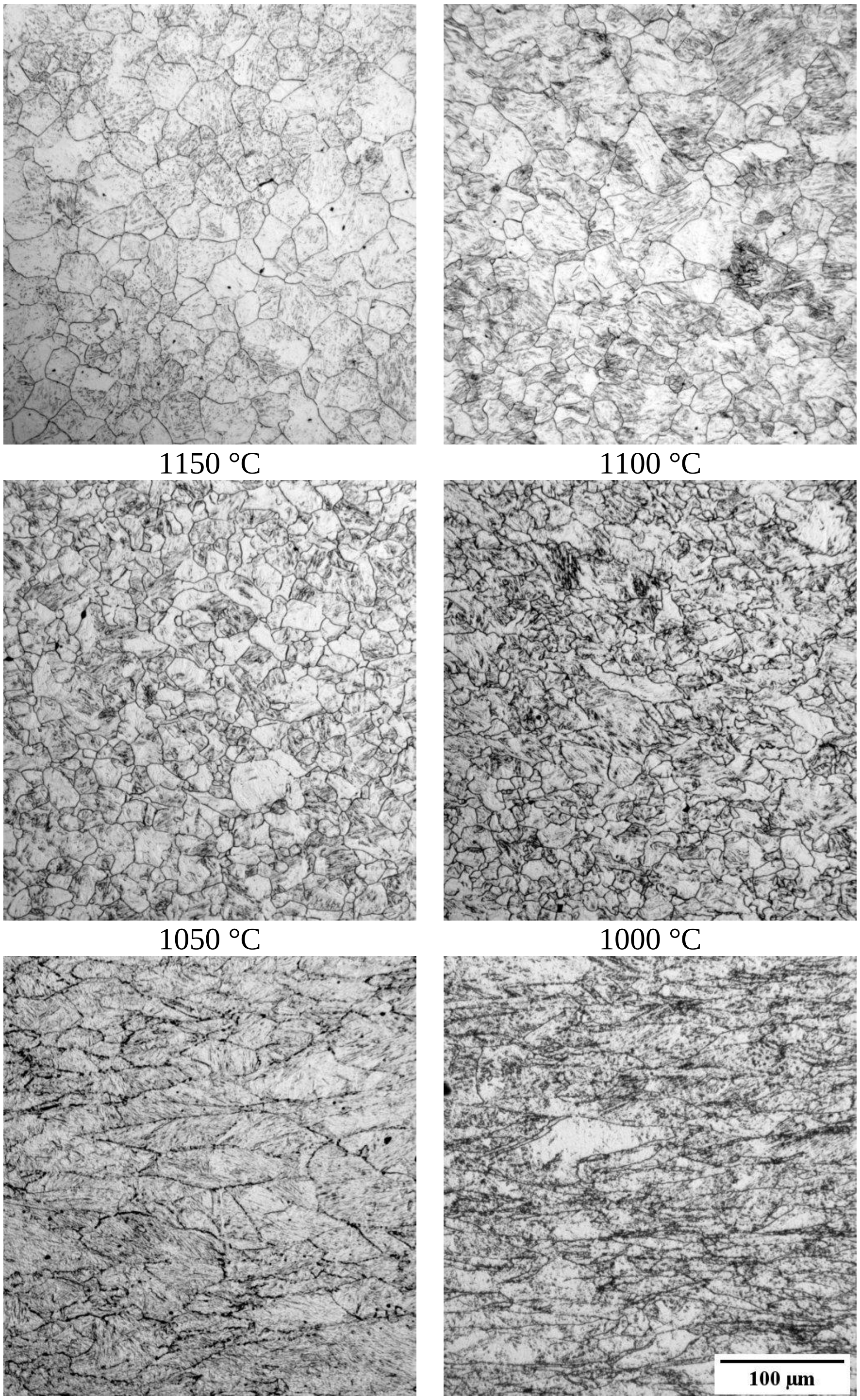

1150 °C

1100 °C

1050 °C

1000 °C

950 °C

900 °C

Figure A.3 Prior austenite grain structure of H8 at respective deformation temperatures.

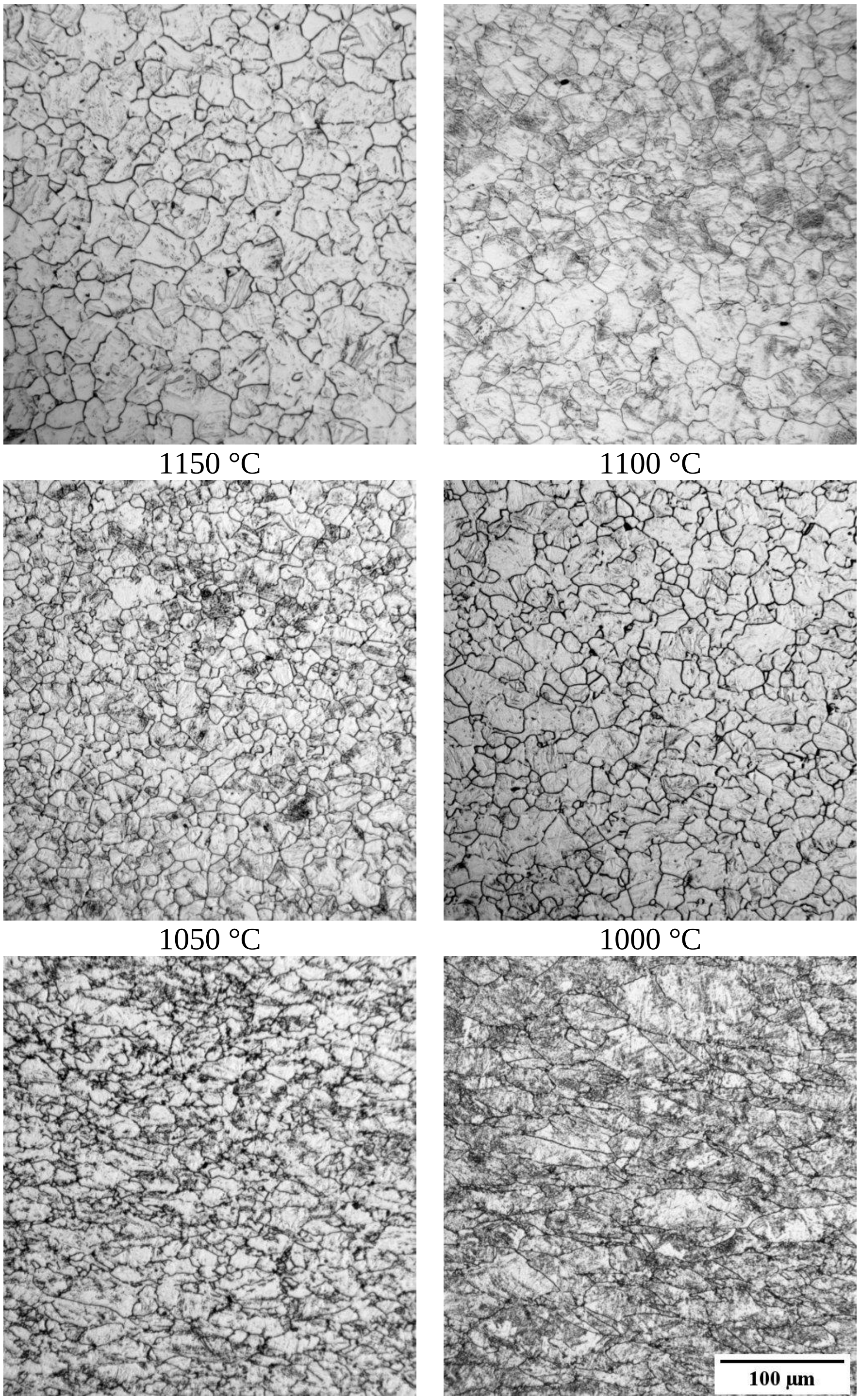

1150 °C

1100 °C

1050 °C

1000 °C

950 °C

900 °C

Figure A.4 Prior austenite grain structure of L4 at respective deformation temperatures.

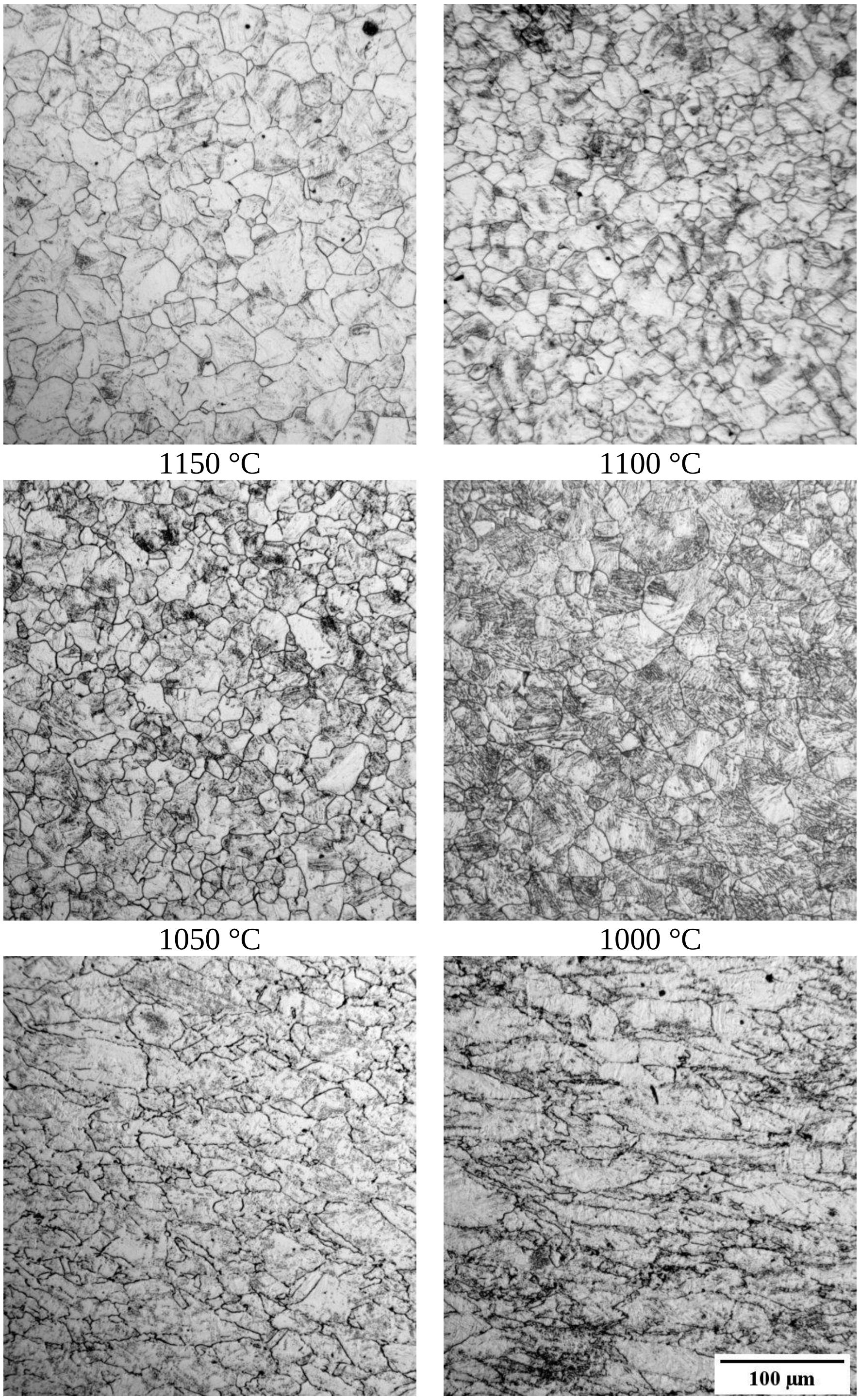

1150 °C

1100 °C

1050 °C

1000 °C

950 °C

900 °C

Figure A.5 Prior austenite grain structure of L8 at respective deformation temperatures.

Appendix B Roughing Passes Simulation: Flow Curves:

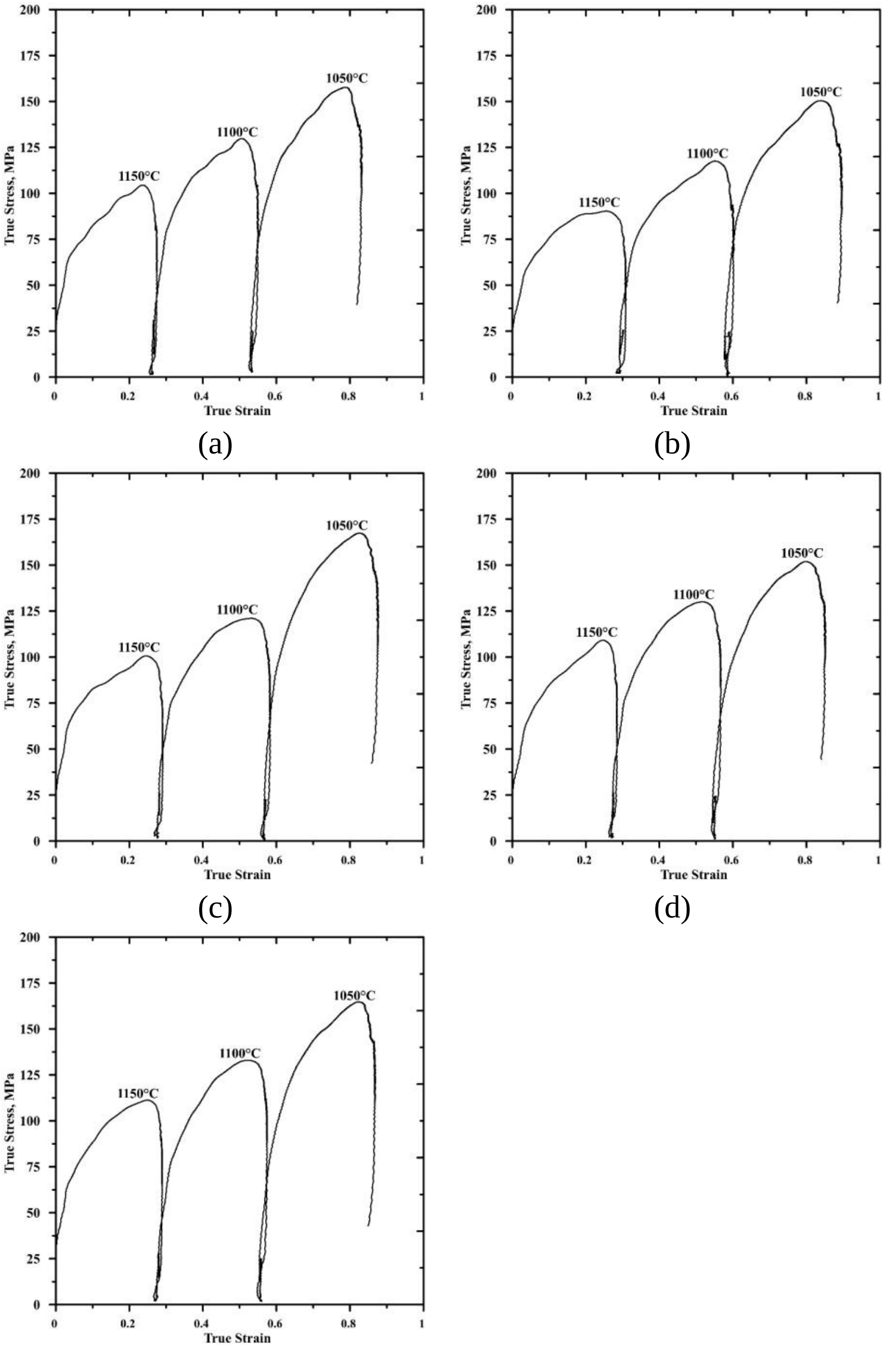

(a)

(b)

(c)

(d)

(e)

Figure B.1 True stress-true strain curves obtained from Gleeble® 3800 thermomechanical simulator (Roughing passes simulation) for (a) H0, (b) H4, (c) H8, (d) L4, and (e) L8.

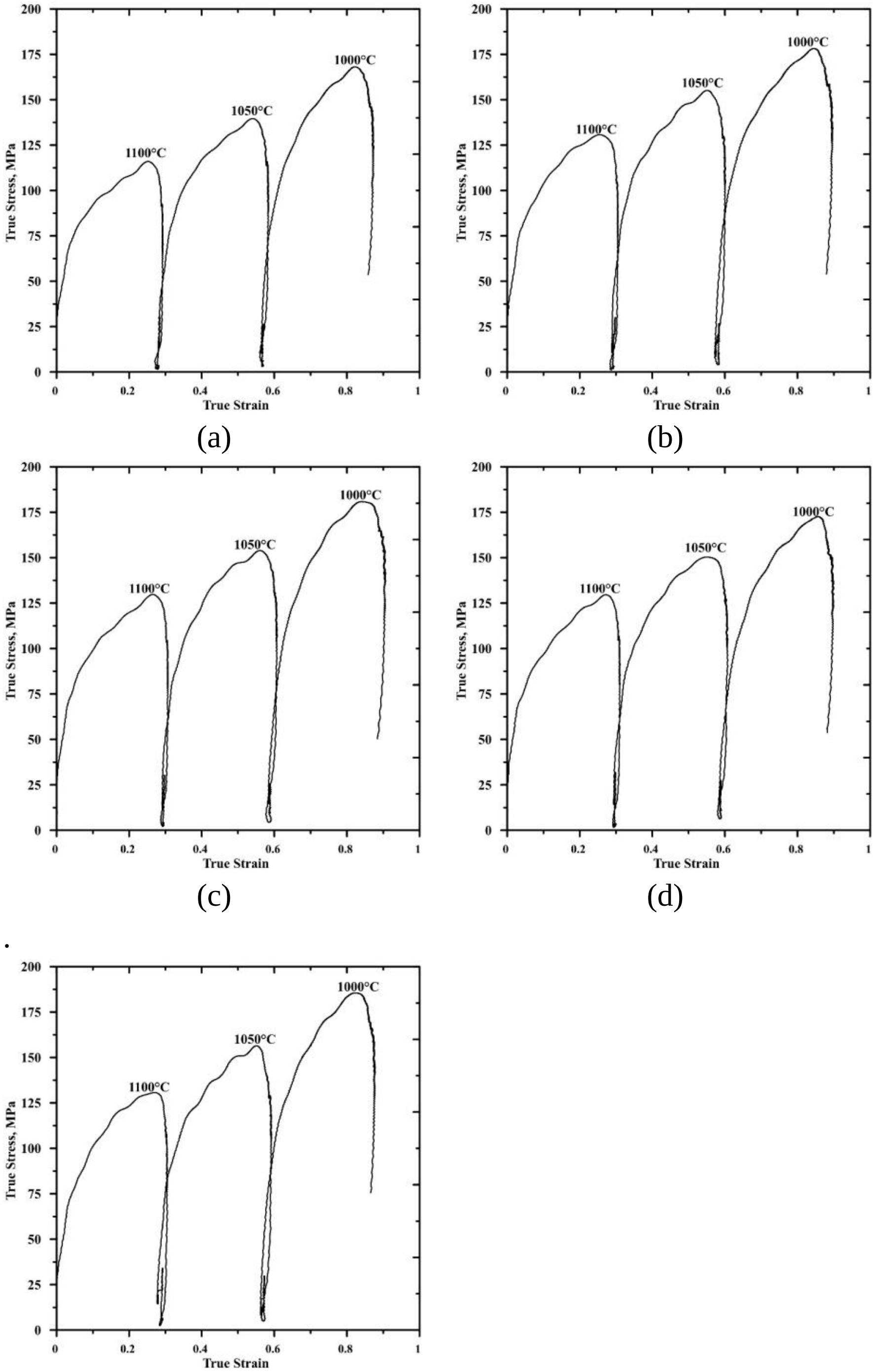

(a)

(b)

(c)

(d)

(e)

Figure B.1 True stress-true strain curves obtained from Gleeble® 3800 thermomechanical simulator (Roughing passes simulation) for (a) H0, (b) H4, (c) H8, (d) L4, and (e) L8.

Appendix C Finishing Passes Simulation: Flow curves, austenite grain microstructure, and transformed microstructure

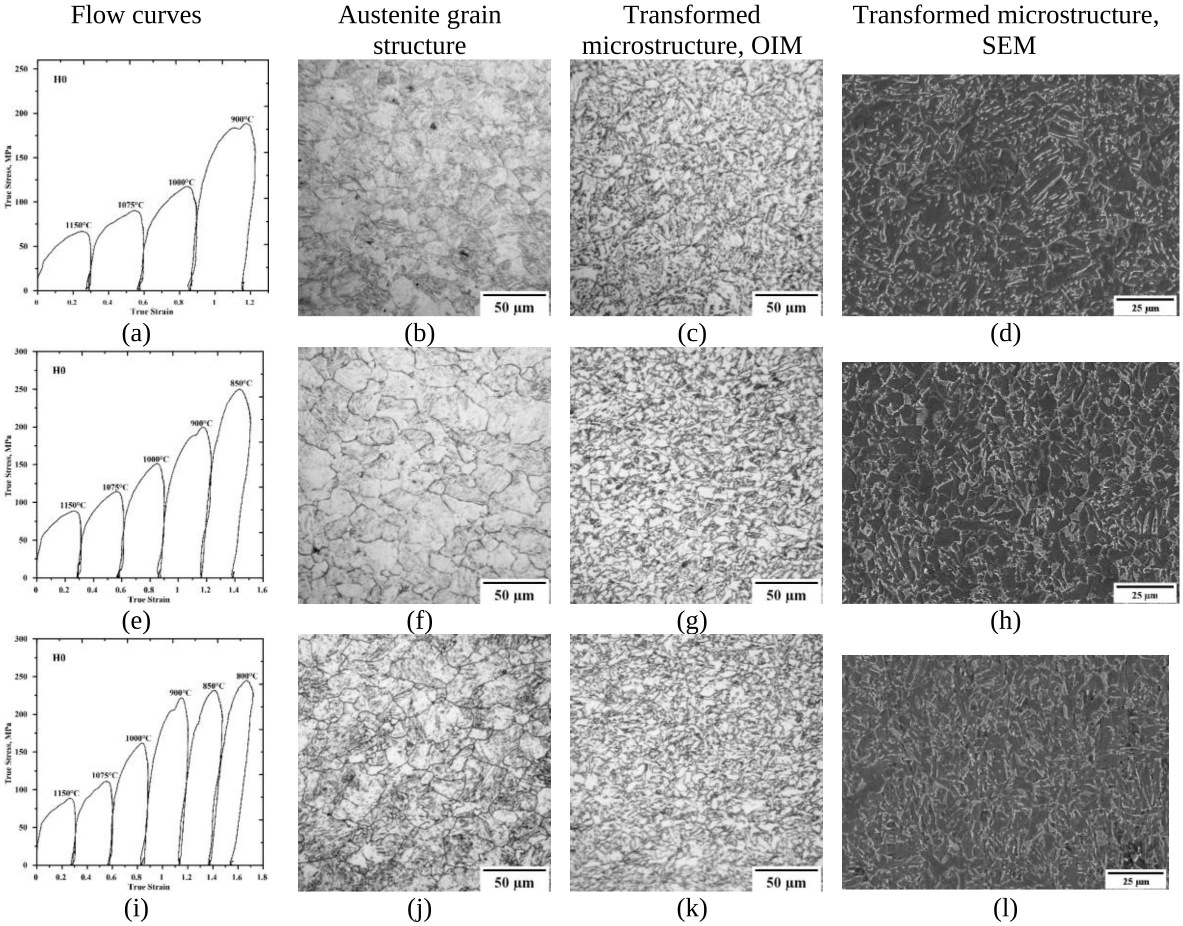

(a) (b) (c) (d)

(e) (f) (g) (h)

(i) (j) (k) (l)

Figure C.1 Change in the austenite and the transformed microstructure as a function of finishing temperature in <u>H0</u> steel; finishing passes simulation carried out following schedule II in Table 5.3.

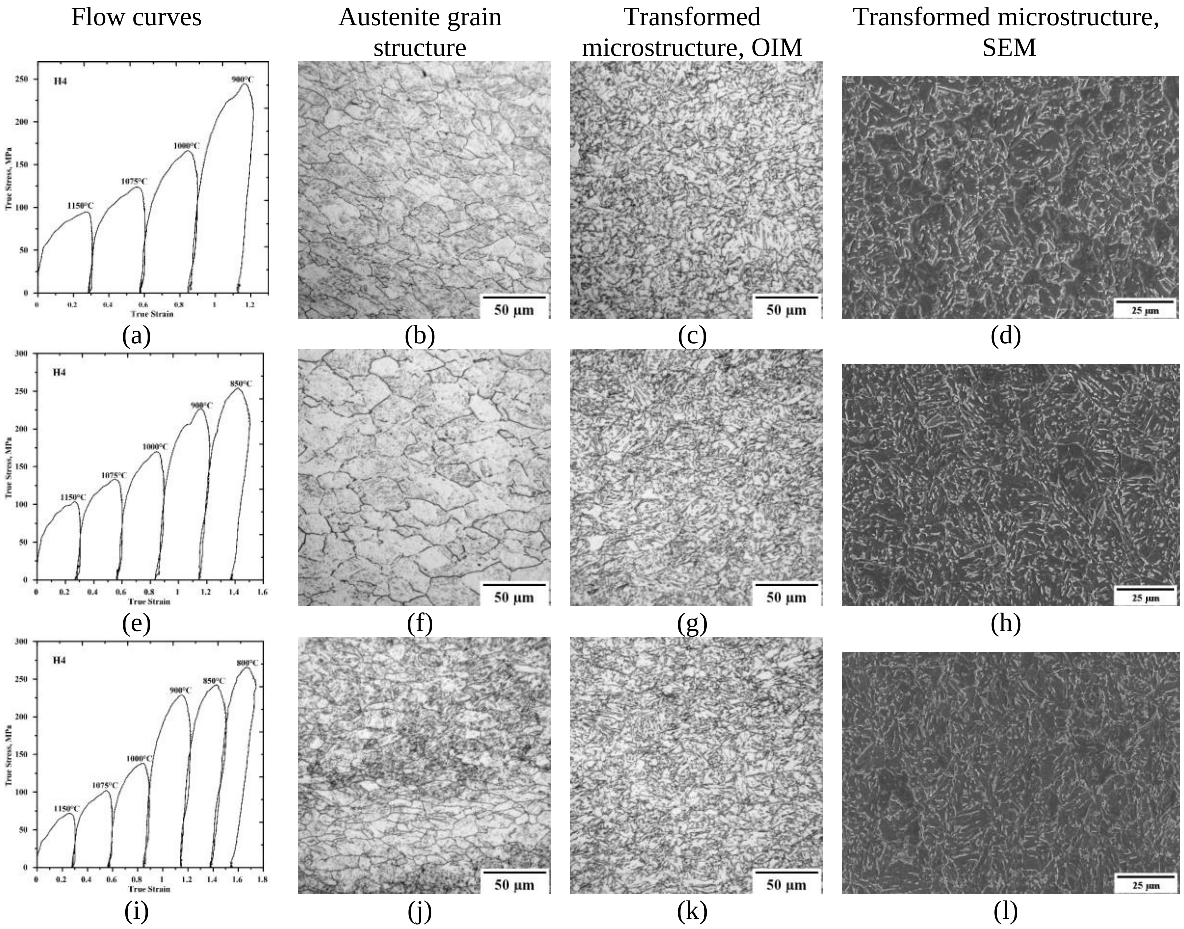

(a) (b) (c) (d)

(e) (f) (g) (h)

(i) (j) (k) (l)

Figure C.2 Change in the austenite and the transformed microstructure as a function of finishing temperature in H4 steel; finishing passes simulation carried out following schedule II in Table 5.3.

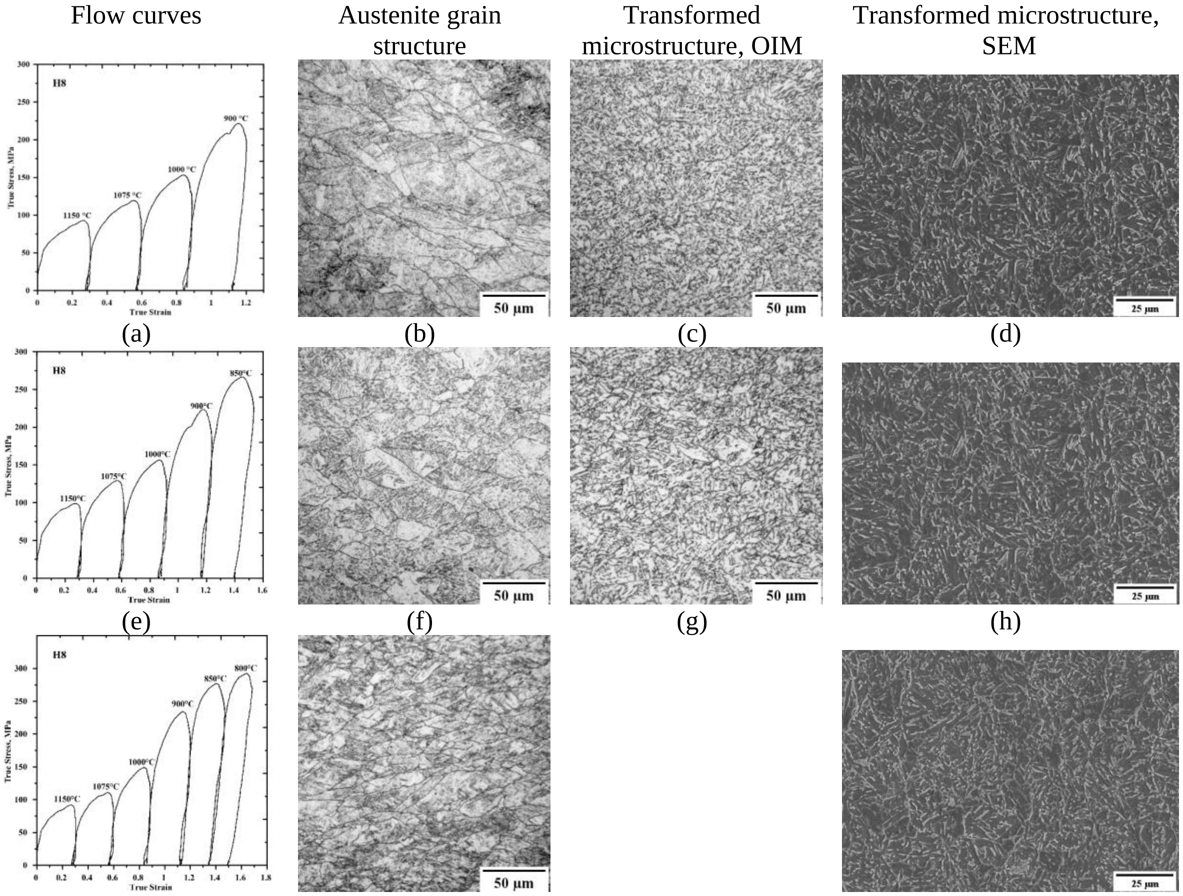

(a) (b) (c) (d)

(e) (f) (g) (h)

(i) (j) (l)

Figure C.4 Change in the austenite and the transformed microstructure as a function of finishing temperature in <u>H8</u> steel; finishing passes simulation carried out following schedule II in Table 5.3.

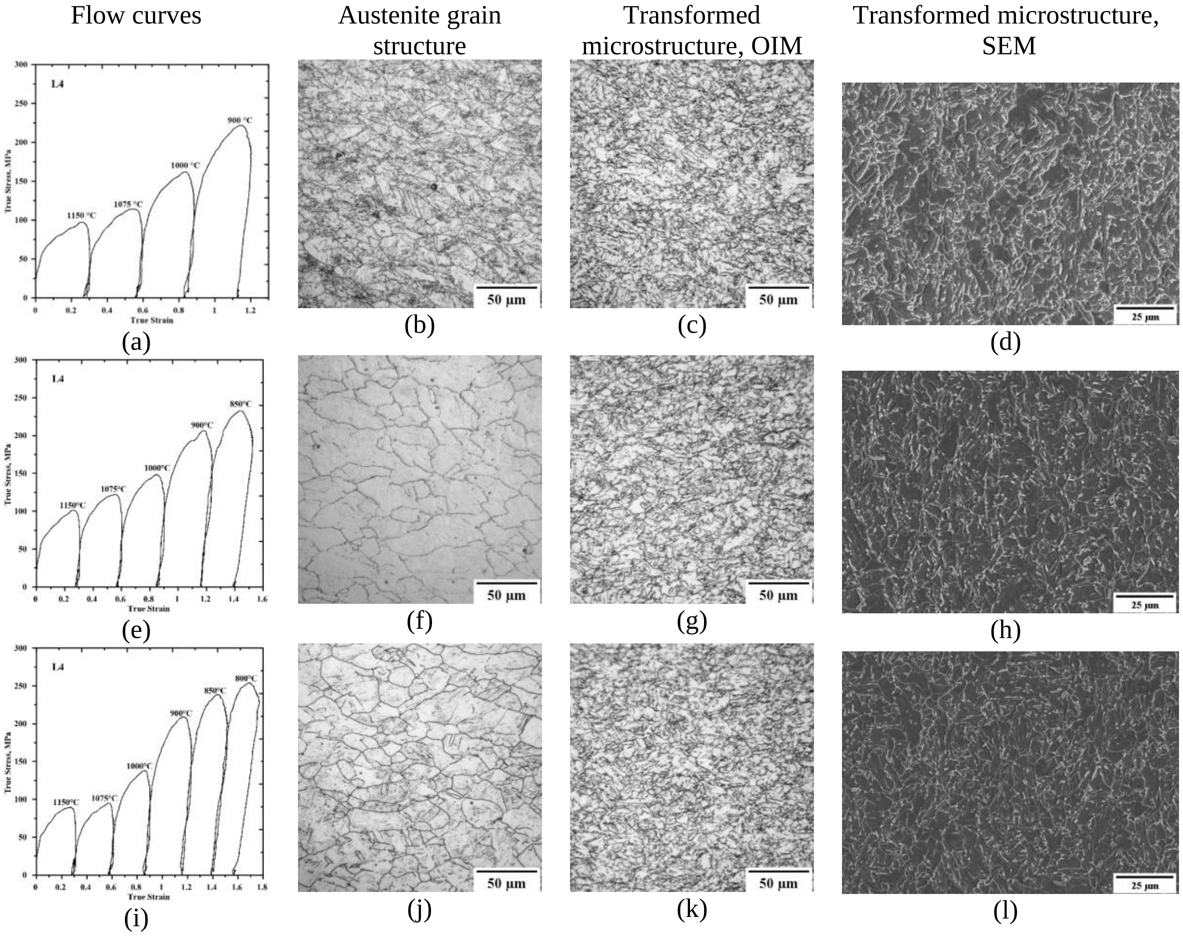

Figure C.6 Change in the austenite and the transformed microstructure as a function of finishing temperature in L4 steel; finishing passes simulation carried out following schedule II in Table 5.3.

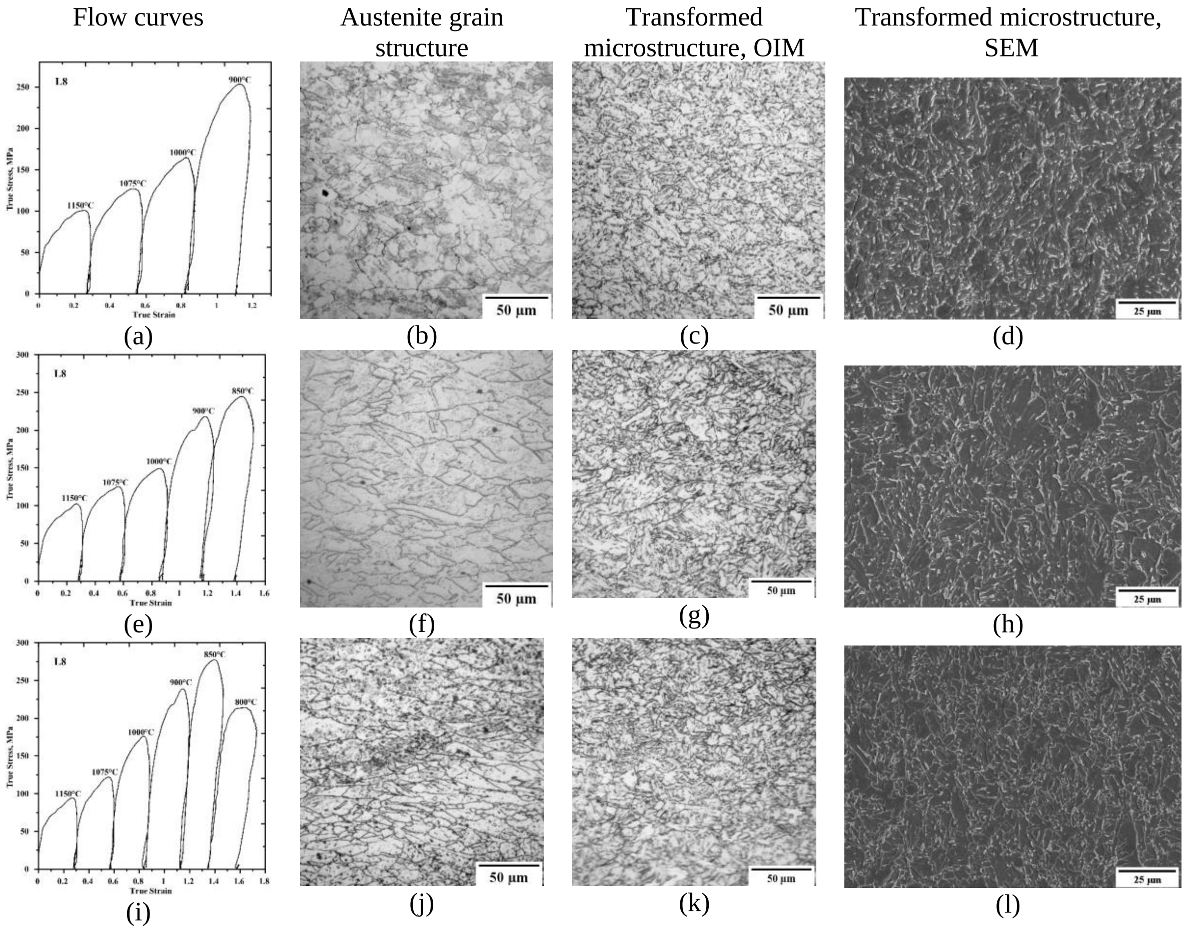

Figure C.8 Change in the austenite and the transformed microstructure as a function of finishing temperature in <u>L8</u> steel; finishing passes simulation carried out following schedule II in Table 5.3.

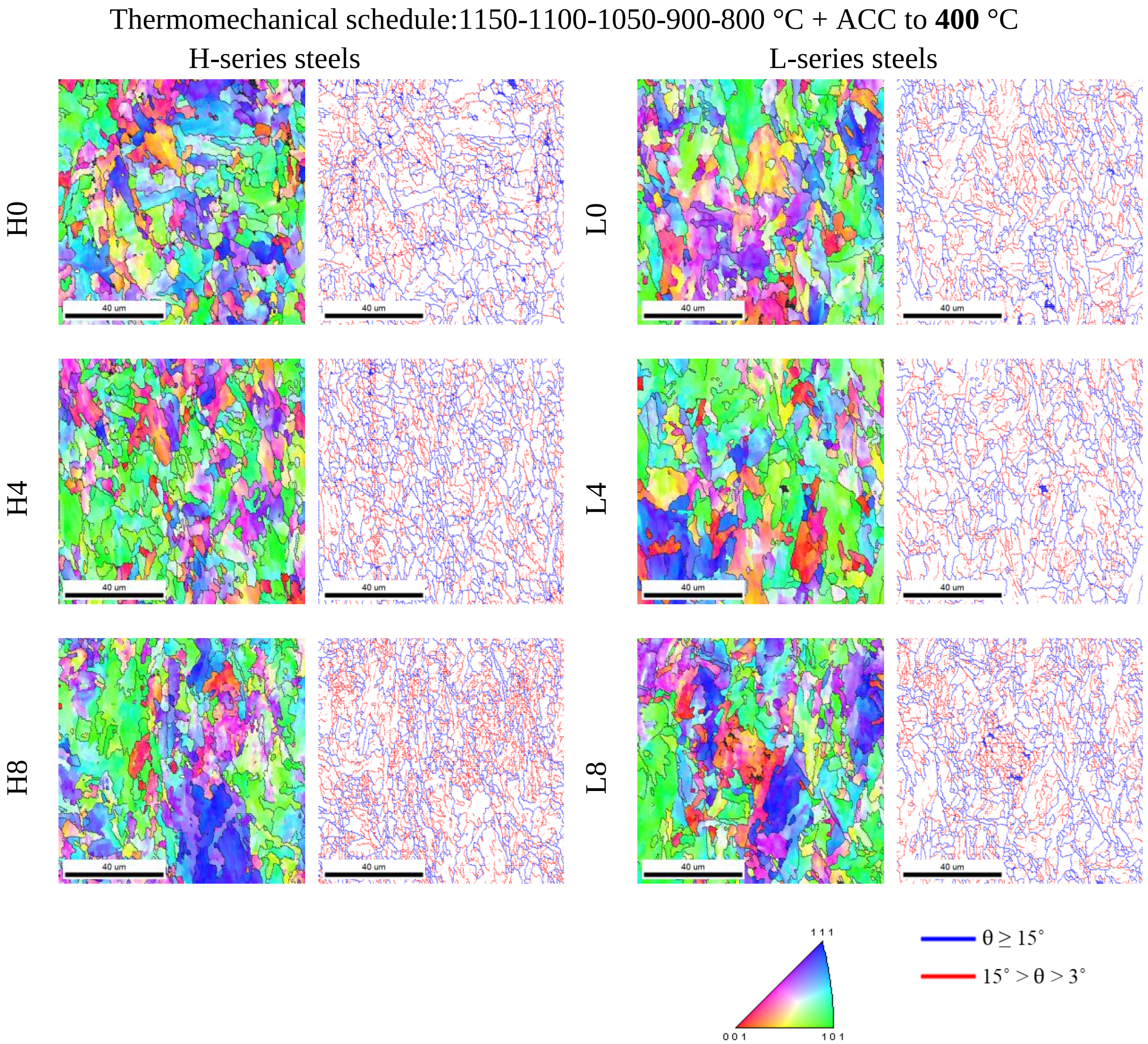

Figure C.8 Inverse pole figures (IPF) and misorientation boundary maps obtained by EBSD of all-experimental steels obtained after ACC simulation.

Appendix D Effect of Inhomogeneous Deformation on the Austenite grain structure

Figure E.1 shows a right cylinder before and after hot compression testing. Light optical micrographs taken from the center as well as from a region near the edge of a hot compressed sample are shown in Figure E.2. The effect of inhomogeneous deformation on the austenite grain structure in a hot compressed specimen is clear.

Figure E.1 Right cylinders before and after hot compression test.

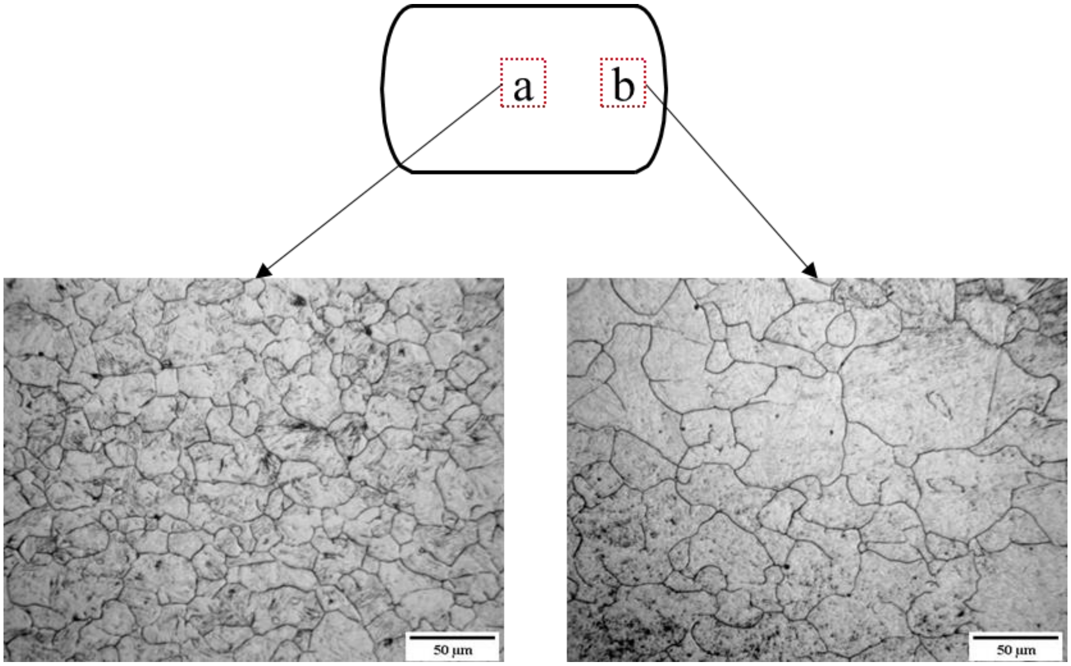

Figure E.2 Austenite grain structure taken from (a) the center region of a deformed sample and (b) a region near the edge.

Bibliography

[1] C. A. Beiser, "The Effect of Small Columbium Additions to semi-killed Medium Carbon Steels," in *Proc. of the Regional Tech. Meeting*, Buffalo, NY, USA, August 17–19 1959.

[2] K. J. Irvine, T. Gladman, J. Orr, and F. B. Pickering, "Controlled rolling of structural steels," *J Iron Steel Inst,* vol. 208, no. 8, pp. 717-726, 1970.

[3] H. Sekine and T. Maruyama, "Retardation of Recrystallization of Austenite During Hot Rolling of Nb-Containing Low-Carbon Steel," *Tetsu-to-Hagané,* vol. 58, no. 10, pp. 1424-1437, 1972.

[4] A. J. DeArdo, "Niobium in modern steels," *International Materials Reviews,* vol. 48, no. 6, pp. 371-402, 2003, doi: 10.1179/095066003225008833.

[5] S. Vervynckt, K. Verbeken, B. Lopez, and J. J. Jonas, "Modern HSLA steels and role of non-recrystallisation temperature," *International Materials Reviews*, vol. 57, no. 4, pp. 187-207, 2013, doi: 10.1179/1743280411y.0000000013.

[6] L. J. Cuddy, "Grain Refinement of Nb Steels by Control of Recrystallization during Hot Rolling," *Metallurgical Transactions A*, vol. 15, no. 1, pp. 87-98, 1984/01/01 1984, doi: 10.1007/BF02644390.

[7] T. Gladman, D. Dulieu, and I. D. McIvor, "Structure-Property Relationships in High-Strength Microalloyed Steels," in *Microalloying 75*, Washington D.C., M. Korchynsky, Ed., October 1-3 1975, New York: Union Carbide Corporation, 1977, pp. 32-55.

[8] I. Kozasu, C. Ouchi, S. Sampei, and T. Okita, "Hot Rolling as a High-Temperature Themo-Mechanical Process," in *Microalloying 75*, Washington D.C., M. Korchynsky, Ed., October 1-3 1975, New York: Union Carbide Corporation, 1977, pp. 120-135.

[9] F. B. Pickering, "High-Strength, Low-Alloy Steels- A Decade of Progress," in *Microalloying 75*, Washington D.C., M. Korchynsky, Ed., October 1-3 1975, New York: Union Carbide Corporation, 1977, pp. 9-30.

[10] T. Tanaka, "Controlled Rolling of Steel Plate and Strip," *International Metals Reviews*, vol. 26, no. 1, pp. 185-212, 1981/01/01 1981, doi: 10.1179/imtr.1981.26.1.185.

[11] L. J. Cuddy, "The Effect of Microalloy Concentration on the Recrystallization of Austenite During Hot Deformation " in *Thermomechanical Processing of Microalloyed Austenite*, Pittsburgh, PA USA, A. J. Deardo, G. A. Ratz, and P. J. Wray, Eds., Augest 17-19 1981, Warrendale, PA: The Metallurgical Society of AIME, 1982, pp. 129-139.

[12] C. Ouchi and T. Okita, "Austenitic Grain Refinement through Static Recrystallization Immediately after Hot Rolling," *Transactions of the Iron and Steel Institute of Japan,* vol. 24, no. 9, pp. 726-733, 1984, doi: 10.2355/isijinternational1966.24.726.

[13] D. G. Stalheim, "The Use of High Temperature Processing (HTP) Steel for High Strength Oil and Gas Transmission Pipeline Applications," *Iron & Steel,* vol. 40, no. 11, pp. 699-704, 2005.

[14] K. Hulka and H. G. Hillenbrand, "High Temperature Thermomechanical Processing: Background and Application," in *Microalloying 95,* Pittsburgh, PA, USA, M. Korchynsky, A. J. DeArdo, P. Repas, and G. Tither, Eds., June 11-14 1995: Iron and Steel Society, pp. 235-248.

[15] A. J. DeArdo, "Accelerated Cooling: A Physical Metallurgy Perspective," *Canadian Metallurgical Quarterly,* vol. 27, no. 2, pp. 141-154, 1988/04/01 1988, doi: 10.1179/cmq.1988.27.2.141.

[16] S. S. Hansen, J. B. V. Sande, and M. Cohen, "Niobium Carbonitride Precipitation and Austenite Recrystallization in Hot-Rolled Microalloyed Steels," *Metallurgical Transactions A,* vol. 11, no. 3, pp. 387-402, 1980/03/01 1980, doi: 10.1007/BF02654563.

[17] E. J. Palmiere, C. I. Garcia, and A. J. DeArdo, "The Influence of Niobium Supersaturation in Austenite on The Static Recrystallization Behavior of Low Carbon Microalloyed Steels," *Metallurgical and Materials Transactions A,* vol. 27, no. 4, pp. 951-960, 1996.

[18] J. Y. Koo *et al.*, "Metallurgical Design of Ultra-High Strength Steels For Gas Pipelines," in *The Thirteenth International Offshore and Polar Engineering Conference,* 2003, vol. All Days, ISOPE-I-03-333.

[19] A. J. DeArdo, "Modern thermomechanical processing of microalloyed steel: A physical metallurgy perspective," in *Microalloying 95*, Pittsburgh, PA, USA, M. Korchynsky, A. J. DeArdo, P. Repas, and G. Tither, Eds., June 11-14 1995: Iron and Steel Society, pp. 15-33.

[20] D. N. Crowther and B. Mintz, "Influence of Grain Size and Precipitation on Hot Ductility of Microalloyed Steels," *Materials science and technology,* vol. 2, no. 11, pp. 1099-1105, 1986.

[21] P. Cizek, B. P. Wynne, C. H. J. Davies, and P. D. Hodgson, "The Effect of Simulated Thermomechanical Processing on the Transformation Behavior and Microstructure of a Low-Carbon Mo-Nb Linepipe Steel," *Metallurgical and Materials Transactions A,* vol. 46A, no. 1, pp. 407-425, 2015, doi: 10.1007/s11661-014-2601-x.

[22] J. Zhao *et al.*, "Effect of microstructure on the crack propagation behavior of microalloyed 560MPa (X80) strip during ultra-fast cooling," *Materials Science and Engineering: A,* vol. 666, pp. 214-224, 2016, doi: 10.1016/j.msea.2016.04.073.

[23] A. J. Kaijalainen, P. P. Suikkanen, T. J. Limnell, L. P. Karjalainen, J. I. Kömi, and D. A. Porter, "Effect of austenite grain structure on the strength and toughness of direct-quenched martensite," *Journal of Alloys and Compounds*, vol. 577, pp. S642-S648, 2013/11/15/ 2013, doi: https://doi.org/10.1016/j.jallcom.2012.03.030.

[24] I. Tamura, H. Sekine, T. Tanaka, and C. Ouchi, "Chapter 1 - Introduction," in *Thermomechanical Processing of High-Strength Low-Alloy Steels*, I. Tamura, H. Sekine, T. Tanaka, and C. Ouchi Eds.: Butterworth-Heinemann, 1988, pp. 1-16.

[25] G. R. Speich, L. J. Cuddy, C. R. Gordon, and A. J. DeArdo, "Formation of Ferrite from Control-Rolled Austenite," *Phase transformations in ferrous alloys*, pp. 341-389, 1983.

[26] E. E. Underwood, "Quantitative Microscopy," New York, R. T. DeHoff and R. F. N., Eds., 1968: McGraw-Hill, p. 77.

[27] H. Sekine, T. Maruyama, H. Kageyama, and Y. Kawashima, "Grain Refinement Through Hot Holling and Cooling After Rolling," in *Thermomechanical Processing of Microalloyed Austenite*, Pittsburgh, PA USA, A. J. Deardo, G. A. Ratz, and P. J. Wray, Eds., Augest 17-19 1981, Warrendale, PA: The Metallurgical Society of AIME, 1982, pp. 141-160.

[28] T. Gladman, "The Physical Metallurgy of Microalloyed Steels," (in English), pp. 82-83, 1997.

[29] E. J. Palmiere, C. I. Garcia, and A. J. DeArdo, "Compositional and Microstructural Changes Which Attend Reheating and Grain Coarsening in Steels Containing Niobium," *Metallurgical and Materials Transactions A,* vol. 25, no. 2, pp. 277-286, 1994.

[30] T. Mori, M. Tokizane, K. Yamaguchi, E. Sunami, and Y. Nakazima, "Thermodynamic Properties of Niobium Carbides and Nitrides in Steels," *Tetsu-to-Hagane,* vol. 54, no. 7, pp. 763-776, 1968, doi: 10.2355/tetsutohagane1955.54.7_763.

[31] E. Turkdogan, "Causes and Effects of Nitride and Carbonitride Precipitation During Continuous Casting," *Iron Steelmaker*, vol. 16, no. 5, p. 61, 1989.

[32] K. J. Irvine, F. B. Pickering, and T. Gladman, "Grain-Refined C-Mn steels," *Iron Steel Inst. J,* vol. 205, no. 2, pp. 161-182, 1967.

[33] S. Akamatsu, M. Hasebe, T. Senuma, Y. Matsumura, and O. Kisue, "Thermodynamic Calculation of Solute Carbon and Nitrogen in Nb and Ti Added Extra-low Carbon Steels," *ISIJ International,* vol. 34, no. 1, pp. 9-16, 1994, doi: 10.2355/isijinternational.34.9.

[34] H. Sawamura and T. Mori, "THERMODYNAMIC INVESTIGATION OF NON-METALLIC INCLUSIONS IN STEEL (II) Behavior of Titanium-, Zirconium-, and Vanadium-Nitrides and Carbides and Their Effect on Austenitic Grain Size of Steel," *Tetsu-to-Hagane*, vol. 43, no. 1, pp. 31-38, 1957, doi: 10.2355/tetsutohagane1955.43.1_31.

[35] T. Zhou, R. J. O’malley, and H. S. Zurob, "Study of Grain-Growth Kinetics in Delta-Ferrite and Austenite with Application to Thin-Slab Cast Direct-Rolling Microalloyed Steels,"

Metallurgical and Materials Transactions A, vol. 41, no. 8, pp. 2112-2120, 2010, doi: 10.1007/s11661-010-0246-y.

[36] P. Uranga, A. I. Fernández, B. López, and J. M. Rodríguez-Ibabe, "Modeling of Austenite Grain Size Distribution in Nb Microalloyed Steels Processed by Thin Slab Casting and Direct Rolling (TSDR) Route," *ISIJ International*, vol. 44, no. 8, pp. 1416-1425, 2004, doi: 10.2355/isijinternational.44.1416.

[37] M. Hillert, "On the Theory of Normal and Abnormal Grain Growth," *Acta Metallurgica*, vol. 13, no. 3, pp. 227-238, 1965/03/01/ 1965, doi: https://doi.org/10.1016/0001-6160(65)90200-2.

[38] L. J. Cuddy and J. C. Raley, "Austenite grain coarsening in microalloyed steels," *Metallurgical Transactions A*, vol. 14, no. 10, pp. 1989-1995, 1983/10/01 1983, doi: 10.1007/BF02662366.

[39] S. Roy, D. Chakrabarti, and G. K. Dey, "Austenite Grain Structures in Ti- and Nb-Containing High-Strength Low-Alloy Steel During Slab Reheating," *Metallurgical and Materials Transactions A*, vol. 44, no. 2, pp. 717-728, 2012, doi: 10.1007/s11661-012-1409-9.

[40] L.-n. Duan, J.-m. Wang, Q.-y. Liu, X.-j. Sun, and J.-c. Cao, "Austenite Grain Growth Behavior of X80 Pipeline Steel in Heating Process," *Journal of Iron and Steel Research, International*, vol. 17, no. 3, pp. 62-66, 2010/03/01/ 2010, doi: https://doi.org/10.1016/S1006-706X(10)60074-X.

[41] J. Fernández, S. Illescas, and J. M. Guilemany, "Effect of microalloying elements on the austenitic grain growth in a low carbon HSLA steel," *Materials Letters*, vol. 61, no. 11, pp. 2389-2392, 2007/05/01/ 2007, doi: https://doi.org/10.1016/j.matlet.2006.09.021.

[42] H. J. McQueen and J. J. Jonas, "Recovery and Recrystallization during High Temperature Deformation," in *Treatise on Materials Science & Technology*, vol. 6, R. J. Arsenault Ed.: Elsevier, 1975, pp. 394-395.

[43] G. E. Dieter, "Mechanical Metallurgy," 3rd ed.: New York : McGraw-Hill, 1986, ch. 13, p. 433.

[44] J. J. Jonas, C. M. Sellars, and W. J. M. Tegart, "Strength and structure under hot-working conditions," *Metallurgical Reviews*, vol. 14, no. 1, pp. 1-24, 1969/01/01 1969, doi: 10.1179/mtlr.1969.14.1.1.

[45] G. Speich, L. Cuddy, C. Gordon, and A. DeArdo, "Formation of ferrite from control-rolled austenite," *Phase transformations in ferrous alloys*, pp. 341-389, 1983.

[46] C. Ouchi and T. Okita, "Dynamic Recrystallization Behavior of Austenite in Nb-Bearing High Strength Low Alloy Steels and Stainless Steel," *Transactions of the Iron and Steel Institute of Japan*, vol. 22, no. 7, pp. 543-551, 1982.

[47] A. Rohatgi, K. S. Vecchio, and G. T. Gray, "The influence of stacking fault energy on the mechanical behavior of Cu and Cu-Al alloys: deformation twinning, work hardening, and dynamic recovery," *Metallurgical and Materials Transactions A,* vol. 32, no. 1, pp. 135-145, 2001.

[48] F. J. Humphreys and M. Hatherly, *Recrystallization and Related Annealing Phenomena*. Elsevier, 2012.

[49] R. A. Petković, M. J. Luton, and J. J. Jonas, "Recovery and recrystallization of carbon steel between intervals of hot working," *Canadian metallurgical quarterly,* vol. 14, no. 2, pp. 137-145, 1975.

[50] A. Le Bon, J. Rofes-Vernis, and C. Rossard, "Recrystallization and Precipitation During Hot Working of a Nb-Bearing HSLA Steel," *Metal Science,* vol. 9, no. 1, pp. 36-40, 1975.

[51] E. J. Palmiere, "Suppression of Recrystallization During the Hot Deformation of Microalloyed Austenite," Ph.D Dissertation, University of Pittsburgh, 1991.

[52] H. Zhao and E. J. Palmiere, "Effect of austenite grain size on acicular ferrite transformation in a HSLA steel," *Materials Characterization,* vol. 145, pp. 479-489, 2018, doi: 10.1016/j.matchar.2018.09.013.

[53] L. J. Cuddy, "Microstructures Developed During Thermomechanical Treatment of HSLA Steels," *Metallurgical Transactions A,* vol. 12, no. 7, pp. 1313-1320, 1981.

[54] R. Esterl, M. Sonnleitner, and R. Schnitzer, "Microstructural Analysis of the Recrystallization Behavior of Low Alloyed Steels," *steel research international,* vol. 90, no. 3, 2019, doi: 10.1002/srin.201800500.

[55] I. Weiss and G. Fitzsimons, "The influence of Nb, V and N on the response of Austenite to Reheating and Hot Deformation in Microalloyed Steels," in *Proceedings of the International Conference on the Thermomechanical Processing of Microalloyed Austenite, edited by AJ DeArdo, AIME*, 1981, pp. 33-58.

[56] S. Yue, J. JJ, and B. KR, "Effect of Dynamic Recrystallization on Microstructural Evolution During Strip Rolling," *ISIJ international,* vol. 30, no. 3, pp. 216-225, 1990.

[57] I. Weiss and J. J. Jonas, "Interaction Between Recrystallization and Precipitation During the High Temperature Deformation of HSLA Steels," *Metallurgical Transactions A,* vol. 10, no. 7, pp. 831-840, 1979.

[58] L. J. Cuddy, J. J. Bauwin, and J. C. Raley, "Recrystallization of Austenite," *Metallurgical Transactions A,* vol. 11, no. 3, pp. 381-386, 1980.

[59] C. N. Homsher and C. J. Van Tyne, "Comparison of Two Physical Simulation Tests to Determine the No-Recrystallization Temperature in Hot Rolled Steel Plates," *Materials Performance and Characterization,* vol. 4, no. 3, 2015, doi: 10.1520/mpc20150002.

[60] J. G. Speer and S. S. Hansen, "Austenite Recrystallization and Carbonitride Precipitation in Niobium Microalloyed Steels," *Metallurgical Transactions A*, vol. 20, no. 1, pp. 25-38, 1989/01/01 1989, doi: 10.1007/BF02647491.

[61] M. SF and M. JE, "Static Recrystallization Modelling of Hot Deformed Steels Containing Severl Alloying Elements," *ISIJ international*, vol. 36, no. 8, pp. 1070-1076, 1996.

[62] M. Gómez, S. F. Medina, and P. Valles, "Determination of Driving and Pinning Forces for Static Recrystallization during Hot Rolling of a Niobium Microalloyed Steel," *ISIJ international*, vol. 45, no. 11, pp. 1711-1720, 2005.

[63] S. Vervynckt, K. Verbeken, P. Thibaux, M. Liebeherr, and Y. Houbaert, "Austenite Recrystallization–Precipitation Interaction in Niobium Microalloyed Steels," *ISIJ International*, vol. 49, no. 6, pp. 911-920, 2009, doi: 10.2355/isijinternational.49.911.

[64] V. Rajinikanth, T. Kumar, B. Mahato, S. Ghosh Chowdhury, and S. Sangal, "Effect of Strain-Induced Precipitation on the Austenite Non-recrystallization (Tnr) Behavior of a High Niobium Microalloyed Steel," *Metallurgical and Materials Transactions A*, vol. 50, no. 12, pp. 5816-5838, 2019, doi: 10.1007/s11661-019-05488-3.

[65] J. N. Cordea and R. E. Hook, "Recrystallization Behavior in Deformed Austenite of High Strength Low Alloy (HSLA) Steels," *Metallurgical Transactions*, vol. 1, no. 1, pp. 111-118, 1970/01/01 1970, doi: 10.1007/BF02819249.

[66] A. I. Fernández, P. Uranga, B. López, and R.-I. JM, "Static Recrystallization Behaviour of a Wide Range of Austenite Grain Sizes in Microalloyed Steels," *ISIJ international*, vol. 40, no. 9, pp. 893-901, 2000.

[67] L. F. Romano-Acosta, O. García-Rincon, J. P. Pedraza, and E. J. Palmiere, "Influence of thermomechanical processing parameters on critical temperatures to develop an Advanced High-Strength Steel microstructure," *Journal of Materials Science*, 2021, doi: 10.1007/s10853-021-06444-6.

[68] J. S. Perttula and L. P. Karjalainen, "Recrystallisation Rates in Austenite Measured by Double Compression and Stress Relaxation Methods," *Materials Science and Technology*, vol. 14, no. 7, pp. 626-630, 1998/07/01 1998, doi: 10.1179/mst.1998.14.7.626.

[69] M. Avrami, "Kinetics of Phase Change. I General Theory," *The Journal of chemical physics*, vol. 7, no. 12, pp. 1103-1112, 1939.

[70] A. I. Fernández, B. López, and J. M. Rodríguez-Ibabe, "Relationship between the austenite recrystallized fraction and the softening measured from the interrupted torsion test technique," *Scripta Materialia*, vol. 40, no. 5, pp. 543-549, 1999/02/05/ 1999, doi: https://doi.org/10.1016/S1359-6462(98)00452-7.

[71] J. E. Bailey and P. B. Hirsch, "The Recrystallization Process in Some Polycrystalline Metals," *Proc. R. Soc. Lond. A*, vol. 267, no. 1328, pp. 11-30, 1962.

[72] C. Zener, "Private communication to CS Smith," *Trans. AIME,* vol. 175, no. 15, p. ll, 1949.

[73] M. PA, M. Ferry, and T. Chandra, "Five Decades of the Zener Equation," *ISIJ international,* vol. 38, no. 9, pp. 913-924, 1998.

[74] T. Gladman, "On the theory of the effect of precipitate particles on grain growth in metals," *Proceedings of the Royal Society of London. Series A. Mathematical and Physical Sciences,* vol. 294, no. 1438, pp. 298-309, 1966.

[75] O. Kwon and A. J. DeArdo, "Interactions Between Recrystallization and Precipitation in Hot-Deformed Microalloyed Steels," *Acta Metallurgica et Materialia,* vol. 39, no. 4, pp. 529-538, 1991/04/01/ 1991, doi: https://doi.org/10.1016/0956-7151(91)90121-G.

[76] B. Dutta, E. Valdes, and C. M. Sellars, "Mechanism and Kinetics of Strain Induced Precipitation of Nb(C,N) in Austenite," *Acta Metallurgica et Materialia,* vol. 40, no. 4, pp. 653-662, 1992/04/01/ 1992, doi: https://doi.org/10.1016/0956-7151(92)90006-Z.

[77] S. Morito, H. Tanaka, R. Konishi, T. Furuhara, and T. Maki, "The morphology and crystallography of lath martensite in Fe-C alloys," *Acta Materialia,* vol. 51, no. 6, pp. 1789-1799, 2003/04/02/ 2003, doi: https://doi.org/10.1016/S1359-6454(02)00577-3.

[78] D. V. Edmonds and R. C. Cochrane, "Structure-Property Relationships in Bainitic Steels," *Metallurgical Transactions A,* vol. 21, no. 6, pp. 1527-1540, 1990/06/01 1990, doi: 10.1007/BF02672567.

[79] H. K. D. H. Bhadeshia and J. W. Christian, "Bainite in steels," *Metallurgical Transactions A,* vol. 21, no. 3, pp. 767-797, 1990/03/01 1990, doi: 10.1007/BF02656561.

[80] H. Zhao and E. J. Palmiere, "Effect of Austenite Deformation on the Microstructure Evolution and Grain Refinement Under Accelerated Cooling Conditions," *Metallurgical and Materials Transactions A,* vol. 48, no. 7, pp. 3389-3399, 2017, doi: 10.1007/s11661-017-3987-z.

[81] H. Zhao, B. P. Wynne, and E. J. Palmiere, "Conditions for the occurrence of acicular ferrite transformation in HSLA steels," *Journal of Materials Science,* vol. 53, no. 5, pp. 3785-3804, 2017, doi: 10.1007/s10853-017-1781-3.

[82] T. Araki, I. Kozasu, H. Tankechi, K. Shibata, M. Enomoto, and H. Tamehiro, "Atlas for Bainitic Microstructures," *ISIJ, Tokyo, Japan,* vol. 1, pp. 4-5, 1992.

[83] W. Wang, Y. Shan, and K. Yang, "Study of high strength pipeline steels with different microstructures," *Materials Science and Engineering: A,* vol. 502, no. 1, pp. 38-44, 2009/02/25/ 2009, doi: https://doi.org/10.1016/j.msea.2008.10.042.

[84] L. Lan, Z. Chang, X. Kong, C. Qiu, and D. Zhao, "Phase transformation, microstructure, and mechanical properties of X100 pipeline steels based on TMCP and HTP concepts," *Journal of Materials Science,* vol. 52, no. 3, pp. 1661-1678, 2016, doi: 10.1007/s10853-016-0459-6.

[85] B. Hwang, C. G. Lee, and T.-H. Lee, "Correlation of Microstructure and Mechanical Properties of Thermomechanically Processed Low-Carbon Steels Containing Boron and Copper," *Metallurgical and Materials Transactions A*, vol. 41, no. 1, p. 85, 2009/10/29 2009, doi: 10.1007/s11661-009-0070-4.

[86] F.-R. Xiao *et al.*, "Challenge of mechanical properties of an acicular ferrite pipeline steel," *Materials Science and Engineering: A*, vol. 431, no. 1-2, pp. 41-52, 2006, doi: 10.1016/j.msea.2006.05.029.

[87] R. A. Almatani and A. J. DeArdo, "Rational Alloy Design of Niobium-Bearing HSLA Steels," *Metals*, vol. 10, no. 3, p. 413, 2020.

[88] Danieli and C. SpA, "Start up Model for a Five Meter Plate Mill," A. J. DeArdo, Ed., ed. Italy, Buttrio, 2010.

[89] S. Vervynckt, K. Verbeken, P. Thibaux, and Y. Houbaert, "Characterization of the Austenite Recrystallization by Comparing Double Deformation and Stress Relaxation Tests," *steel research international*, vol. 81, no. 3, pp. 234-244, 2010, doi: 10.1002/srin.200900126.

[90] W. C. Oliver and G. M. Pharr, "An improved technique for determining hardness and elastic modulus using load and displacement sensing indentation experiments," *Journal of Materials Research*, vol. 7, no. 6, pp. 1564-1583, 1992, doi: 10.1557/JMR.1992.1564.

[91] Y. Ohmori and T. Maki, "Bainitic Transformation in View of Displacive Mechanism," *Materials Transactions, JIM*, vol. 32, no. 8, pp. 631-641, 1991, doi: 10.2320/matertrans1989.32.631.

[92] M.-C. Zhao, K. Yang, F.-R. Xiao, and Y.-Y. Shan, "Continuous cooling transformation of undeformed and deformed low carbon pipeline steels," *Materials Science and Engineering: A*, vol. 355, no. 1, pp. 126-136, 2003, doi: https://doi.org/10.1016/S0921-5093(03)00074-1.

[93] H. K. Sung, S. Y. Shin, B. Hwang, C. G. Lee, and S. Lee, "Effects of Cooling Conditions on Microstructure, Tensile Properties, and Charpy Impact Toughness of Low-Carbon High-Strength Bainitic Steels," *Metallurgical and Materials Transactions A*, vol. 44, no. 1, pp. 294-302, 2013/01/01 2013, doi: 10.1007/s11661-012-1372-5.

[94] S. G. Hong, K. B. Kang, and C. G. Park, "Strain-induced precipitation of NbC in Nb and Nb–Ti microalloyed HSLA steels," *Scripta Materialia*, vol. 46, no. 2, pp. 163-168, 2002/01/18/ 2002, doi: https://doi.org/10.1016/S1359-6462(01)01214-3.

[95] X. Ma, C. Miao, B. Langelier, and S. Subramanian, "Suppression of strain-induced precipitation of NbC by epitaxial growth of NbC on pre-existing TiN in Nb-Ti microalloyed steel," *Materials & Design*, vol. 132, pp. 244-249, 2017, doi: 10.1016/j.matdes.2017.07.006.

[96] D. C. Houghton, G. C. Weatherly, and J. D. Embury, "Characterization of Carbonitrides in Ti Bearing HSLA Steels," in *Thermomechanical Processing of Microalloyed Austenite*, Pittsburgh, PA USA, A. J. Deardo, G. A. Ratz, and P. J. Wray, Eds., Augest 17-19 1981, Warrendale, PA: The Metallurgical Society of AIME, 1982, pp. 267-292.

[97] M. A. Bepari, "Effects of Second-Phase Particles on Coarsening of Austenite in 0.15 Pct Carbon Steels," *Metallurgical Transactions A*, vol. 20, no. 1, pp. 13-16, 1989/01/01 1989, doi: 10.1007/BF02647489.

[98] D. Chakrabarti, C. Davis, and M. Strangwood, "Characterisation of bimodal grain structures in HSLA steels," *Materials Characterization*, vol. 58, no. 5, pp. 423-438, 2007/05/01/ 2007, doi: https://doi.org/10.1016/j.matchar.2006.06.014.

[99] C. Hutchinson, H. Zurob, C. Sinclair, and Y. Brechet, "The comparative effectiveness of Nb solute and NbC precipitates at impeding grain-boundary motion in Nb steels," *Scripta Materialia*, vol. 59, no. 6, pp. 635-637, 2008, doi: 10.1016/j.scriptamat.2008.05.036.

[100] A. Karmakar, S. Kundu, S. Roy, S. Neogy, D. Srivastava, and D. Chakrabarti, "Effect of microalloying elements on austenite grain growth in Nb–Ti and Nb–V steels," *Materials Science and Technology*, vol. 30, no. 6, pp. 653-664, 2014/05/01 2014, doi: 10.1179/1743284713Y.0000000386.

[101] S.-F. Tao, F.-M. Wang, G.-L. Sun, Z.-B. Yang, and C.-R. Li, "DICTRA Simulation of Holding Time Dependence of NbC Size and Experimental Study of Effect of NbC on Austenite Grain Growth," *Metallurgical and Materials Transactions A*, vol. 46, no. 8, pp. 3670-3678, 2015, doi: 10.1007/s11661-015-2922-4.

[102] L. M. Fu, H. R. Wang, W. Wang, and A. D. Shan, "Austenite grain growth prediction coupling with drag and pinning effects in low carbon Nb microalloyed steels," *Materials Science and Technology*, vol. 27, no. 6, pp. 996-1001, 2013, doi: 10.1179/1743284711y.0000000001.

[103] C. L. Davis and M. Strangwood, "Preliminary study of the inhomogeneous precipitate distributions in Nb-microalloyed plate steels," *Journal of Materials Science*, vol. 37, no. 6, pp. 1083-1090, 2002/03/01 2002, doi: 10.1023/A:1014342800399.

[104] M. I. Santella, "Grain Growth and High-Temperature Hot Rolling Behavior of Low-Alloy Steel Austenite," PhD Dissertation, University of Pittsburgh, Pittsburgh, PA, 1981.

[105] K. F. Al Hajeri, C. I. Garcia, M. Hua, and A. J. Deardo, "Particle-stimulated Nucleation of Ferrite in Heavy Steel Sections," *ISIJ International*, vol. 46, no. 8, pp. 1233-1240, 2006, doi: 10.2355/isijinternational.46.1233.

[106] L. P. Karjalainen, T. M. Maccagno, and J. J. Jonas, "Softening and Flow Stress Behaviour of Nb Microalloyed Steels during Hot Rolling Simulation," *ISIJ International*, vol. 35, no. 12, pp. 1523-1531, 1995, doi: 10.2355/isijinternational.35.1523.

[107] M. SF and A. Quispe, "Improved Model for Static Recrystallization Kinetics of Hot Deformed Austenite in Low Alloy and Nb/V Microalloyed Steels," *ISIJ international*, vol. 41, no. 7, pp. 774-781, 2001.

[108] S. Hong, K. Kang, and C. Park, "Strain-induced precipitation of NbC in Nb and Nb–Ti microalloyed HSLA steels," *Scripta materialia*, vol. 46, no. 2, pp. 163-168, 2002.

[109] S. Vervynckt, K. Verbeken, P. Thibaux, and Y. Houbaert, "Recrystallization–precipitation interaction during austenite hot deformation of a Nb microalloyed steel," *Materials Science and Engineering: A*, vol. 528, no. 16-17, pp. 5519-5528, 2011, doi: 10.1016/j.msea.2011.03.087.

[110] S. Akhlaghi and D. G. Ivey, "Precipitation Behaviour of a Grade 100 Structural Steel," *Canadian Metallurgical Quarterly*, vol. 41, no. 1, pp. 111-119, 2002/01/01 2002, doi: 10.1179/cmq.2002.41.1.111.

[111] R. Barbosa, F. Boratto, S. Yue, and J. J. Jonas, "The Influence of Chemical Composition on the Recrystallization Behavior of Microalloyed Steels," in *Processing, Microstructure and Properties of HSLA Steels*, Pittsburgh, PA USA, A. J. Deardo, Ed., November 3-5 1987, Warrendale, PA: TMS, 1982, pp. 51-61.

[112] D. Q. Bai, S. Yue, W. P. Sun, and J. J. Jonas, "Effect of Deformation Parameters on the No-Recrystallization Temperature in Nb-Bearing Steels," *Metallurgical and Materials Transactions A*, vol. 24, no. 10, pp. 2151-2159, 1993/10/01 1993, doi: 10.1007/BF02648589.

[113] B. Dutta and E. J. Palmiere, "Effect of Prestrain and Deformation Temperature on the Recrystallization Behavior of Steels Microalloyed with Niobium," *Metallurgical and Materials Transactions A*, vol. 34, no. 6, pp. 1237-1247, 2003/06/01 2003, doi: 10.1007/s11661-003-0234-6.

[114] F. Fletcher, "Meta-Analysis of Tnr Measurements: Determining New Empirical Models Based on Composition and Strain," in *Austenite Processing Symposium (Internal company presentation)*, 2008, pp. 1-14.

[115] C. N. Homsher, "Determination of the Non-Recrystallization Temperature (Tnr) in Multiple Microalloyed Steels," Master of Science, Colorado School of Mines, 2013.

[116] S. F. Medina, A. Quispe, and M. Gomez, "Model for Strain-Induced Precipitation Kinetics in Microalloyed Steels," *Metallurgical and Materials Transactions A*, vol. 45, no. 3, pp. 1524-1539, 2013, doi: 10.1007/s11661-013-2068-1.

[117] B. Dutta, E. J. Palmiere, and C. M. Sellars, "Modelling The Kinetics of Strain Induced Precipitation in Nb Microalloyed Steels," *Acta Materialia*, vol. 49, no. 5, pp. 785-794, 2001/03/14/ 2001, doi: https://doi.org/10.1016/S1359-6454(00)00389-X.

[118] J. S. Langer and k. Schwartz, "Kinetics of nucleation in near-critical fluids," *Physical Review A*, vol. 21, no. 3, p. 948, 1980.

[119] A. Costa e Silva, "Challenges and opportunities in thermodynamic and kinetic modeling microalloyed HSLA steels using computational thermodynamics," *Calphad,* vol. 68, 2020, doi: 10.1016/j.calphad.2019.101720.

[120] M. Fukuhara and A. Sanpei, "Elastic Moduli and Internal Friction of Low Carbon and Stainless Steels as a Function of Temperature," *ISIJ International,* vol. 33, no. 4, pp. 508-512, 1993, doi: 10.2355/isijinternational.33.508.

[121] R. K. Amin and F. B. Pickering, "Austenite Grain Coarsening and The Effect of Thermomechanical Processing on Austenite Recsrystallisation," in *Thermomechanical Processing of Microalloyed Austenite*, Pittsburgh, PA USA, A. J. Deardo, G. A. Ratz, and P. J. Wray, Eds., Augest 17-19 1981, Warrendale, PA: The Metallurgical Society of AIME, 1982, pp. 1-30.

[122] J. A. Dicello and A. D., "The Resistenace of HSLA Steels To Deformation During Hot Rolling," in *Thermomechanical Processing of Microalloyed Austenite*, Pittsburgh, PA USA, A. J. Deardo, G. A. Ratz, and P. J. Wray, Eds., Augest 17-19 1981, Warrendale, PA: The Metallurgical Society of AIME, 1982, pp. 529-552.

[123] T. Tanaka, T. Enami, M. Kimura, Y. Saito, and T. Hatomura, "Formation Mechanism of Mixed Austenite Grain Structure Accompanying Controlled-Rolling of Niobium-Bearing Steel," in *Thermomechanical Processing of Microalloyed Austenite*, Pittsburgh, PA USA, A. J. Deardo, G. A. Ratz, and P. J. Wray, Eds., Augest 17-19 1981, Warrendale, PA: The Metallurgical Society of AIME, 1982, pp. 195-215.

[124] S. Yamamoto, H. Yokoyama, K. Yamada, and M. Niikura, "Effects of the Austenite Grain Size and Deformation in the Unrecrystallized Austenite Region on Bainite Transformation Behavior and Microstructure," *ISIJ International,* vol. 35, no. 8, pp. 1020-1026, 1995, doi: 10.2355/isijinternational.35.1020.

[125] C. S. Chiou, J. R. Yang, and C. Y. Huang, "The effect of prior compressive deformation of austenite on toughness property in an ultra-low carbon bainitic steel," *Materials Chemistry and Physics,* vol. 69, no. 1, pp. 113-124, 2001/03/01/ 2001, doi: https://doi.org/10.1016/S0254-0584(00)00379-5.

[126] N. Isasti, D. Jorge-Badiola, M. L. Taheri, and P. Uranga, "Phase Transformation Study in Nb-Mo Microalloyed Steels Using Dilatometry and EBSD Quantification," *Metallurgical and Materials Transactions A,* vol. 44, no. 8, pp. 3552-3563, 2013/08/01 2013, doi: 10.1007/s11661-013-1738-3.

[127] G. R. Speich and T. M. Scoonover, "Continuous-Cooling-Transformation Behaviour and Strength of HSLA-80 (A710) Steel Plates," in *Processing, Microstructure and Properties of HSLA Steels*, Pittsburgh, PA USA, A. J. Deardo, Ed., November 3-5 1987, Warrendale, PA: TMS, 1982, pp. 263-286.

[128] C. Fossaert, G. Rees, T. Maurickx, and H. K. D. H. Bhadeshia, "The Effect of Niobium on the Hardenability of Microalloyed Austenite," *Metallurgical and Materials Transactions A*, vol. 26, no. 1, pp. 21-30, 1995/01/01 1995, doi: 10.1007/BF02669791.

[129] R. Y. Zhang and J. D. Boyd, "Bainite Transformation in Deformed Austenite," *Metallurgical and Materials Transactions A*, vol. 41, no. 6, pp. 1448-1459, 2010, doi: 10.1007/s11661-010-0190-x.

[130] B. L. Bramfitt and J. G. Speer, "A Perspective on the Morphology of Bainite," *Metallurgical transactions A*, vol. 21, no. 3, pp. 817-829, 1990.

[131] J. W. T. Reynolds, H. I. Aaronson, and G. Spanos, "A Summary of the Present Diffusionist Views on Bainite," *Materials Transactions, JIM*, vol. 32, no. 8, pp. 737-746, 1991, doi: 10.2320/matertrans1989.32.737.

[132] X. Liang and A. J. DeArdo, "A Study of the Influence of Thermomechanical Controlled Processing on the Microstructure of Bainite in High Strength Plate Steel," *Metallurgical and Materials Transactions A*, vol. 45, no. 11, pp. 5173-5184, 2014, doi: 10.1007/s11661-014-2444-5.

[133] S. Y. Han, S. Y. Shin, S. Lee, N. J. Kim, J.-H. Bae, and K. Kim, "Effects of Cooling Conditions on Tensile and Charpy Impact Properties of API X80 Linepipe Steels," *Metallurgical and Materials Transactions A*, vol. 41, no. 2, p. 329, 2009/12/19 2009, doi: 10.1007/s11661-009-0135-4.

[134] S. Y. Shin, B. Hwang, S. Lee, N. J. Kim, and S. S. Ahn, "Correlation of microstructure and charpy impact properties in API X70 and X80 line-pipe steels," *Materials Science and Engineering: A*, vol. 458, no. 1, pp. 281-289, 2007/06/15/ 2007, doi: https://doi.org/10.1016/j.msea.2006.12.097.

[135] M. Olasolo, P. Uranga, J. M. Rodriguez-Ibabe, and B. López, "Effect of austenite microstructure and cooling rate on transformation characteristics in a low carbon Nb–V microalloyed steel," *Materials Science and Engineering: A*, vol. 528, no. 6, pp. 2559-2569, 2011/03/15/ 2011, doi: https://doi.org/10.1016/j.msea.2010.11.078.

[136] B.-W. Choi, D.-H. Seo, J.-Y. Yoo, and J. Jang, "Predicting macroscopic plastic flow of high-performance, dual-phase steel through spherical nanoindentation on each microphase," *Journal of Materials Research*, vol. 24, no. 3, pp. 816-822, 2009/03/01 2009, doi: 10.1557/jmr.2009.0109.

[137] M. D. Taylor *et al.*, "Correlations between nanoindentation hardness and macroscopic mechanical properties in DP980 steels," *Materials Science and Engineering: A*, vol. 597, pp. 431-439, 2014/03/12/ 2014, doi: https://doi.org/10.1016/j.msea.2013.12.084.